Synthesis and characterization of tellurium based glasses for far infrared sensing and thermoelectric applications

Sho Cui

ANNÉE 2014

THÈSE / UNIVERSITÉ DE RENNES 1
sous le sceau de l'Université Européenne de Bretagne

pour le grade de

DOCTEUR DE L'UNIVERSITÉ DE RENNES 1

Mention : Sciences des Matériaux

Ecole doctorale Sciences de la Matière

présentée par

Shuo CUI

Préparée à l'unité de recherche 6226 ISCR
Institut des Sciences Chimiques de Rennes
UFR Sciences et Propriétés de la Matière

Synthesis and characterization of tellurium based glasses for far infrared sensing and thermoelectric applications

Thèse soutenue à Rennes
le 10 Décembre 2014

devant le jury composé de :

Xiang-Hua ZHANG
Directeur de Recherche CNRS, Université de Rennes1 / *président*

Monica FERRARIS
Professeur, École polytechnique de Turin / *rapporteur*

Antoine MAIGNAN
Directeur de Recherche CNRS, CRISMAT-Caen / *rapporteur*

Bruno BUREAU
Professeur, Université de Rennes1 / *directeur de thèse*

Catherine BOUSSARD-PLÉDEL
Ingénieur de Recherche CNRS, Université de Rennes1 / *co-directrice de thèse*

Jacques LUCAS
Professeur, Université de Rennes1 / *membre invité*

Acknowledgement

I would never have been able to finish my dissertation without the guidance of my committee members, help from my friends, and support from my family.

First and foremost I offer my sincerest gratitude to my supervisors, Catherine Boussard-Plédel and Bruno Bureau, for their patience, motivation, enthusiasm, and immense knowledge throughout my thesis, and also for all their kindness and assistance during my stay in France. One simply could not wish for a better or friendlier supervisor.

Besides my supervisors, I would like to thank many of my colleagues who also guided me through all these years. Jacques Lucas always give me new ideas and inspirations when I am confused. Without the help of Johann Troles and Laurent Brillant, I can never achieve the preparation of single mode fiber. The cooperation with Pierre Lucas, Pal Jovary and Carmelo Prestipino give me a chance to better understand the structure of tellurium-rich glasses. Mike Reece provide me a precious secondment and give me a clear idea of research on thermoelectric. I would also thank David le Coq, with whom we find glass ionic conductivity and far infrared transmittance together. Laurent Calvez was also bothered a lot by me due to many experimental and theoretical problems. He is like a Wikipedia for me, always ready to give and to learn the knowledge.

My sincere thanks also goes to Thierry Pain, Thierry Jouan and Franck Rojas. in providing the silica set-up, experimental equipment, or synthesizing the glasses, my experiments cannot proceed smoothly at all. I would also thank Thierry Guizouarn, Olivier Tougait and Blandine Lemardele, who also helps me a lot in the glass preparation and characterization.

During my stay in France, Hongli Ma and Xianghua Zhang also give me a lot of support and help me solve many difficulties in my daily life. Professor Hui Yang and Xianping Fan, my friends Ling Wang, Min Qian, and Xinxin Chen also provide me a powerful spiritual force.

I would also express my gratitude to my fellow labmates in the group of glass and ceramics: Giorgos Athanasiou, François Chevire, Virginie Nazabal, Franck Tessier, Ronan Lebullenger, Odile Merdrignac-Conanec, Marcel Poulain, Jean Rocherullé, Michel Cathelinaud, Didier François, Michel Lecroc, Corinne Perier, Julien Ari, Emeline Baudet, Antoine Brehault, Céline Caillaud, Radwan Chahal, Solenn Cozic, Noha Hakmeh, Florent Starecki, Claire Roiland, Minjia Wang, Yimin Wu, Gang Zhou, Yang Xu, Bai Xue, Bo Fan. In particular, I am grateful to Clement Conseil for enlightening me the first glance of research and Yinyao Liu for working together with me for 6 months.

Acknowledgement

The laboratory of glass and ceramics has provided the support and equipment I have needed to produce and complete my thesis and the GlaCERCo project has funded my studies.

Last but not the least, I would like to thank my parents Zhenguo Cui and Shuyun Wei for giving birth to me and my boyfriend and his parents Thomas Larhzaoui, Evelyne le Pape, and Samir Larhzaoui for their spiritual support.

French Abstract

Résumé en Français

Développement de Verres riches en tellure pour l'optique infrarouge et la thermoélectricité

Introduction

L'état vitreux est connu depuis des millénaires et reste un mystère à bien des égards pour ses propriétés thermique, physique ou structurale. Les verres peuvent être considérés comme des liquides figés, sans ordre à longue distance et caractérisés par une transition vitreuse. Leurs propriétés visco-élastiques les rendent thermo-formables, propriétés à l'origine de la plupart de leurs applications technologiques. Il est en effet facile et peu coûteux de mettre en forme un matériau vitreux pour fabriquer toute sorte d'objet, des plus ordinaires (vitrage, bouteille …) au plus sophistiqués (stockage nucléaire, fibres optiques). Les verres de notre environnement quotidien sont des verres d'oxydes, des silicates, constitués essentiellement de silice. Ils sont transparents à l'œil, supportent des températures élevées, sont très stables chimiquement et vieillissent bien au cours du temps. A côté de cette très large famille des verres à base de silice, il existe de nombreux autres systèmes, plus confidentiels, qui sont aptes à former du verre. Citons à titre d'exemple, d'abord des systèmes à bases d'oxydes tels que les phosphates, les borates, les aluminates, les germanates, liste non-exhaustive, ou toute combinaison entre ces éléments. Citons aussi d'autres types de matériaux totalement alternatifs ne comportant pas du tout d'oxygène tel que les verres d'halogénures (en particulier les fluorures) ou les verres de chalcogénures. La motivation essentielle à l'origine du développement de ces verres réside dans leur propriétés de transparence dans l'infrarouge, jusque dans le moyen infrarouge, là où les oxydes, en particulier les silicates, deviennent opaque aux rayons électromagnétiques. De ce point de vue, les verres de chalcogénure sont certainement ceux possédant le potentiel technologique le plus large.

Un verre dit "de chalcogénure" est majoritairement constitué d'un ou plusieurs chalcogène. Ces éléments, soufre, sélénium ou tellure, sont sous l'oxygène dans le tableau périodique. La plupart du temps, ces verres se présentent sous la forme de bloc noir, à l'aspect quasi-métallique, opaque à la lumière. Par contre, ils sont transparents sur une large gamme de longueurs d'onde pouvant s'étendre vers l'infrarouge lointain. Leur état vitreux leur confère par ailleurs des propriétés visco-élastiques qui les rend thermoformables à des températures facilement accessibles, typiquement dans une gamme de 200 à 400°C en fonction de leur composition. Leur développement a connu un essor remarquable au cours de la dernière décennie sous l'impulsion des militaires afin de développer des systèmes à vision

nocturne, typiquement des caméras dîtes infrarouges. Les lentilles de ces caméras, en verre de chalcogénures, sont beaucoup moins chères à produire car très simples à thermoformer. Depuis, de telles caméras équipent un nombre grandissant de voitures particulières pour aider les conducteurs à la conduite de nuit. Ces activités sont à l'origine de la création et du développement de la société Umicore-IR glass dans la région rennaise. Plus récemment, la mise en forme de fibres optiques en verre de chalcogénure a permis de développer des capteurs fonctionnant dans le moyen infrarouge. Leur mise en œuvre, en particulier pour des applications bio-médicales, s'est révélée riche en retombées potentielles et est à l'origine de la création d'une autre start-up, DIAFIR, également basée à Rennes.

De façon générale, la fenêtre de transmission de ces verres dépend du chalcogène majoritairement présent dans la composition vitreuse. Ainsi, les verres à base de soufre, le plus léger des 3 chalcogènes, sont ceux qui transmettent le moins loin dans l'infrarouge, jusqu'à 10µm sous forme de bloc de verre massif (pas plus de 6µm pour une fibre optique). Les verres au sélénium constituent certainement le meilleur compromis actuel, car ils sont très bons formateurs de verre d'une part, et transmettent jusqu'à 16 µm sous forme de massif ou 12 µm pour une fibre optique. Ce sont ces verres qui sont à l'origine des applications citées ci-avant.

Les verres de tellures sont donc bien sûr ceux qui potentiellement transmettent le plus loin, au-delà des fenêtres de transmission de l'atmosphère. Ainsi sous forme de verre massif, un pur tellurure peut transmettre jusqu'à 25 voire 30 µm, et environ 18µm pour une fibre optique. Ces verres ont été redécouverts et développés récemment pour de telles applications en optique sous l'impulsion des programmes spatiaux de l'ESA (Darwin) ou de la NASA. Ces programmes visent à détecter et caractériser des exo-planètes sur lesquelles des signes de vie seraient possibles. Ceci passe par la présence de molécules telles que l'eau, l'ozone ou le dioxyde de carbone dans l'atmosphère de ces planètes. Ces molécules peuvent être détectées grâce à leur signature infrarouge, ce qui nécessite le développement de fibre optique monomode fonctionnant sur une gamme de 4 à 20µm. Seuls les verres de tellure permettent de transmettre aussi loin, mais la difficulté réside dans le caractère fortement métallique du tellure qui est un moins bon formateur de verre que le sélénium. Ainsi, les verres de tellure sont historiquement connus pour aisément recristalliser, propriété à l'origine de leur développement pour le stockage optique grâce aux matériaux à changement de phase. Ainsi, parmi d'autres systèmes, il a récemment été mis au point au sein de l'équipe Verres et

Céramiques des verres de tellure suffisamment stables pour pouvoir envisager la fabrication de fibres optiques.

Ainsi, le **chapitre 1** de ce travail de thèse sera consacré à la préparation de fibres optiques double indice en verre Te-Ge-Se transmettant jusqu'à 16 µm. Le travail portera sur le développement d'une nouvelle méthode de préparation des préformes et sur l'amélioration des processus de purification du verre.

Récemment, il été montré que l'introduction d'AgI dans une composition riche en tellure permettait de fortement stabiliser le verre. Certaines compositions ne présentent même pas de pic de cristallisation lors d'une analyse thermique. L'objet du **chapitre 2**, est d'essayer de mieux comprendre le rôle joué par l'iodure d'argent dans un tel verre à travers l'exploration des propriétés physiques et structurales de différentes compositions vitreuses à base d'argent, d'iode ou d'iodure d'argent.

Le **chapitre 3** est consacré au développement de fibres optiques en verre du système $GeTe_4$-AgI. Il s'agira d'abaisser suffisamment les pertes optiques pour rendre ces fibres opérationnelles en tant que capteur dans le moyen infrarouge. Le bénéfice par rapport aux fibres au sélénium, actuellement en service, est d'étendre la gamme spectrale opérationnelle et gagner quelques µm d'ouverture, ce qui pourrait s'avérer décisif pour certaines applications notamment en médecine.

Ces 3 chapitres relatifs aux propriétés optiques de ces verres constituent la partie I de la thèse.

Comme il a été dit plus haut, les verres de tellures présentent également un caractère semi métallique, bien sûr à cause de leur forte teneur en tellure lui-même élément semi-conducteur. Ceci nous a incité à également explorer le potentiel de ces verres pour des applications en tant que matériaux thermoélectriques. En effet, un verre est intrinsèquement un mauvais conducteur de la chaleur à cause du désordre structural le caractérisant. Un verre, mauvais conducteur thermique et bon conducteur électrique, constitue donc un point de départ intéressant pour développer des composés pour la thermoélectricité. Précisons que, comme pour l'optique, l'intérêt final d'un matériau fonctionnel vitreux sera sa capacité à être facilement mise en forme par comparaison à son homologue cristallisé. Des travaux ont déjà été réalisés sur ce thème à Rennes et ailleurs, qui tendent à confirmer le potentiel de ces matériaux sous forme strictement vitreuses ou de vitro-céramiques. Ces travaux de thèse sont également l'occasion de proposer des compléments et des pistes d'études nouvelles sur ce thème. Il s'agit de la partie II du travail.

Ainsi, le **chapitre 4** sera consacré à l'étude de verres au sein des systèmes Te-As-Cu, Se-As-Cu et (Te/Se)-(As/Sb/Bi)-(Cu/Ag). Leurs propriétés thermiques, électroniques seront étudiées de façon systématique pour essayer d'identifier des candidats intéressants. Des essais de cristallisation seront également menés afin d'augmenter la conductivité électrique.

Enfin, une approche alternative sera proposée dans le **chapitre 5**. Il s'agira de fabriquer des matériaux composites, vitro-céramisés, à partir de verre de tellure d'une part et de tellure de bismuth cristallisé d'autre part. Le broyage planétaire et le Spark Plasma Sintering (SPS) seront mis en œuvre pour mettre en forme ces matériaux composites.

PARTIE I: Verres à base de tellure pour l'optique infrarouge

Chapitre 1

Verres du système Te-Ge-Se pour l'infrarouge lointain.

Le projet DARWIN de l'Agence Spatiale Européenne et son pendant américain de la NASA appelé TPF pour Terrestrial Planet Finder, visent à détecter des planètes situées en dehors de notre système solaire (exo-planètes) et porteuses potentielles d'une vie. La présences de molécules d'eau, d'ozone ou de dioxyde de carbone dans l'atmosphère de ces planètes est la signature recherchée indiquant qu'une forme de vie puisse s'y développer. Ces molécules absorbent dans le moyen infrarouge respectivement à 6, 9 et 15 µm. Notre rôle en sciences des matériaux consiste à développer des fibres optiques permettant la détection de ces signaux. Nous devons donc développer des fibres optiques transparentes au-delà de 15 µm (idéalement jusqu'à 20 µm) et monomodes pour permettre de filtrer la luminosité des étoiles environnantes polluant le signal infrarouge en provenance des exo planètes. Pour atteindre cet objectif, les verres riches en tellure s'imposent naturellement puisqu'ils sont les seuls à transmettre la lumière jusqu'à de telles longueurs d'onde. Il faut cependant stabiliser ces matériaux pour rendre possible la mise en forme d'objets sophistiqués tels que ces fibres optiques monomodes sans que le verre ne cristallise. Ainsi, il a déjà été montré que les verres du système Te-Ge-Se constituaient des candidats intéressants dès lors que le taux de sélénium reste limité, inférieur à quelques pourcents.

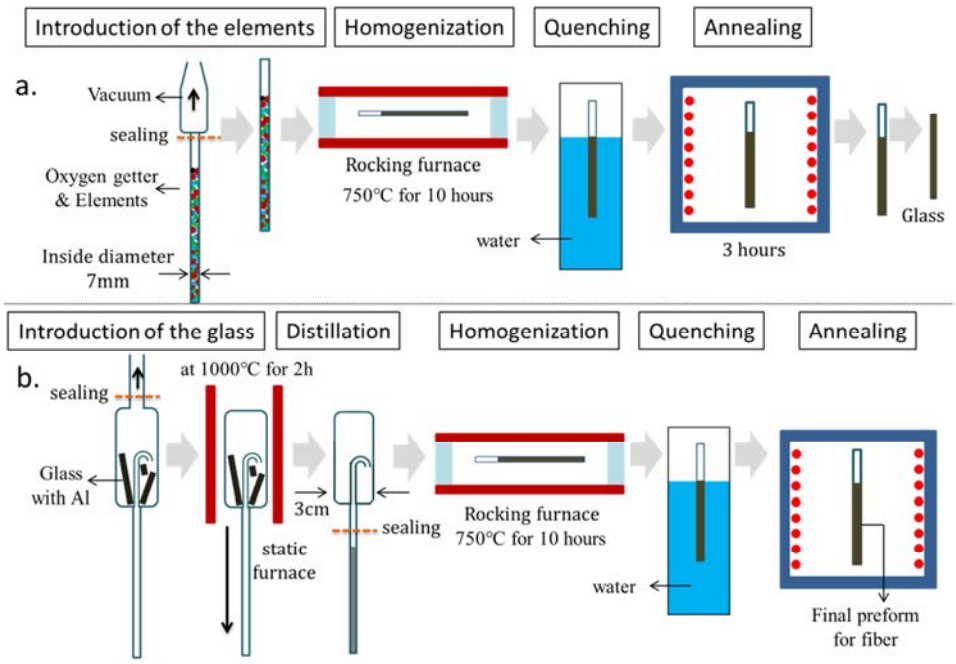

Figure 1 Schéma de purification du Te-Ge-Se en deux étapes : purification chimique (a) et distillation (b)

Pour obtenir des fibres ultra-transparentes, il est nécessaire en amont d'effectuer un travail poussé de purification du verre. Au cours de la thèse une procédure nouvelle de purification en deux étapes a été développée. Elle consiste à effectuer séparément la réaction d'oxydo-réduction avec l'aluminium captant les oxydes résiduels et la distillation du matériau, tel que l'illustre la figure 1. Grâce à ce nouveau processus, les pertes optiques de la fibre optique mono-indice ont été abaissées à un niveau inédit de l'ordre de 6 dB.m-1 à 10.5 µm, ce qui constitue de notre point de vue une limite en dessous de laquelle il sera difficile de descendre à cause de la concentration importante en porteurs de charges inhérente à la présence du tellure semi-conducteur.

Par ailleurs, la méthode classique dite du « rod in tube » (barreau dans tube) pour fabriquer la fibre optique n'est pas adaptée car elle implique une multitude d'opérations successives pour réduire le diamètre du cœur. Ces opérations sont autant de risque potentiel de générer des défauts aux interfaces. Aussi une méthode alternative de fabrication a été mise au point, basée sur le moulage du tube et présentée sur la figure 2.

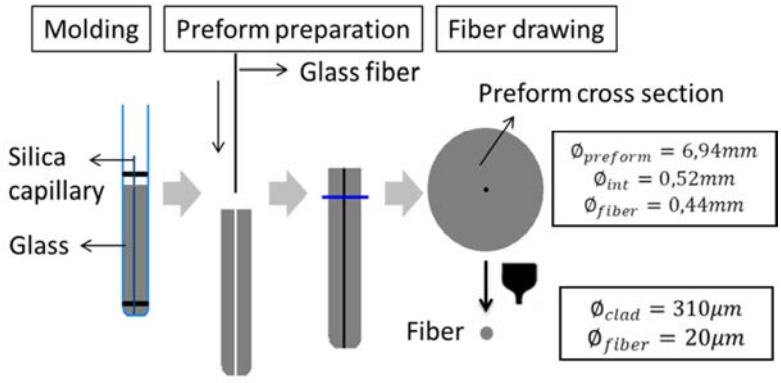

Figure 2 Fabrication de fibres optique double-indice par la méthode capillaire

Grâce à cette méthode une fibre optique double-indice a été préparée à partir des deux verres de compositions $Te_{76}Ge_{21}Se_3$ et $Te_{71}Ge_{21}Se_8$ pour la gaine et le cœur respectivement. Les pertes optiques s'établissent autour de 11.5dB/m à 10.7 µm et la fibre transmet effectivement la lumière jusqu'à 16 µm. Le profil du faisceau lumineux en sortie de fibre optique a été caractérisé grâce à une caméra infrarouge et à un laser CO_2 comme source. Un alliage d'étain et de gallium a été déposé sur la fibre afin de vider les modes se propageant dans la gaine. Alors le profil en sortie de fibre est parfaitement cylindrique comme le montrent les enregistrements de la figure 3. Le profil en 3 dimensions montre quant à lui clairement un profil gaussien conforme aux résultats espérés signant une propagation de type monomode dans la fibre optique.

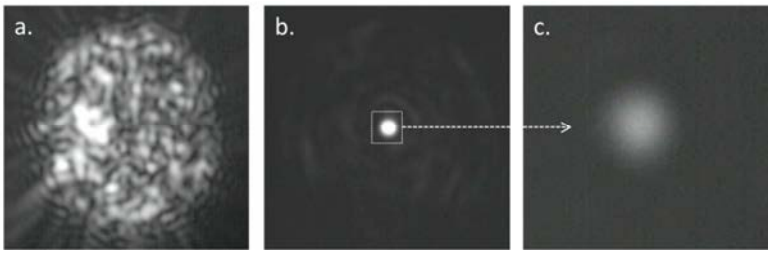

Figure 3 Images du signal à la sortie avant (a.) et après (b. & c.) revêtement en GeSn.

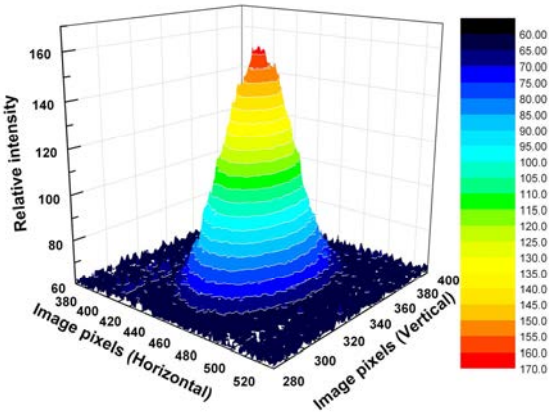

Figure 4 Distribution de la lumière en 3 dimensions pour la fibre en $Te_{76}Ge_{21}Se_3/Te_{71}Ge_{21}Se_8$.

Ce résultat très encourageant reste cependant surprenant à ce stade car la configuration choisie initialement, compositions des verres et le diamètre de cœur, n'est pas sensé correspondre à une propagation de type monomode ! Des travaux restent donc encore à réaliser pour stabiliser les nouvelles méthodes de purification et de fabrication, et assoir la reproductibilité de l'ensemble du processus.

Chapitre 2

Étude du rôle joué par AgI, Ag et I dans des verres de tellure.

Il a récemment été montré que l'ajout d'iodure d'argent AgI joue un rôle extrêmement positif sur la stabilité des verres de tellure, en particulier à partir de $GeTe_4$. En particulier, aucun pic de cristallisation n'est observé sur les courbes d'analyse thermique alors que ces verres cristallisent habituellement très facilement. Pourtant le rôle joué par AgI est assez mystérieux et aucune explication ne permet à ce jour de comprendre l'effet décisif de ce sel sur la stabilité du verre. Dans ce chapitre on se propose de regarder l'influence de l'iode, de l'argent et de l'iodure d'argent pris séparément sur les propriétés physique et structural de ces verres. A titre d'exemple, nous pouvons observer sur la figure 5 les courbes d'analyse thermique de certaines compositions qui montrent l'absence de cristallisation uniquement lorsque l'on ajoute AgI en quantité suffisante, de 10 à 20% molaire.

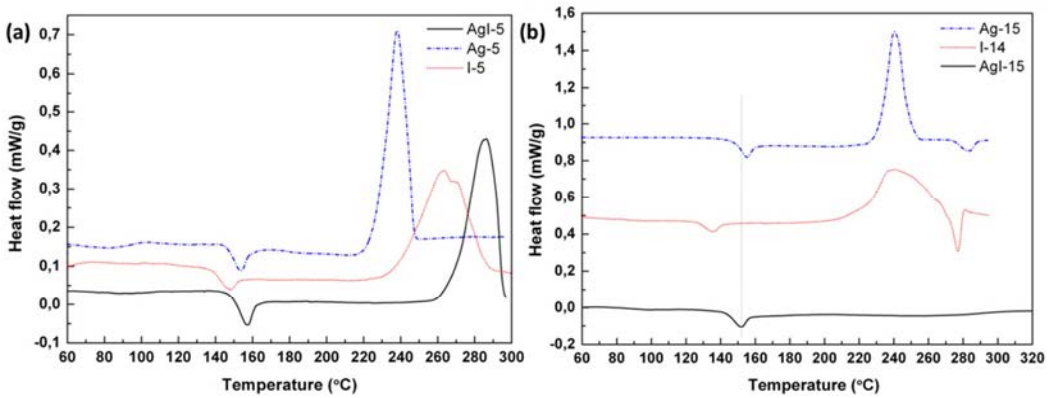

Figure 5 Comparaison des DSC de verres $GeTe_4$ dopé avec 5% (a) et 15%[1] (b) d'Ag, I et AgI.

Sur la figure 6 sont reportées les conductivités électriques mesurées par sonde 4 points d'une part et impédancemètrie d'autre part. Ces résultats montrent des processus de conductivités très différents pour les verres contenant de l'argent pour lesquels la conductivité est exclusivement électronique et croît avec le taux d'Ag, alors que la situation est plus complexe pour les compositions contenant AgI. D'abord, la conductivité globale diminue jusqu'à 15% de sel ionique, car l'iode tend à capter les électrons de conduction apportés par le tellure. Ensuite la conductivité croît au-delà car les ions Ag^+ deviennent mobiles dans un réseau plus ouvert car structuralement l'iode tant à ouvrir le réseau.

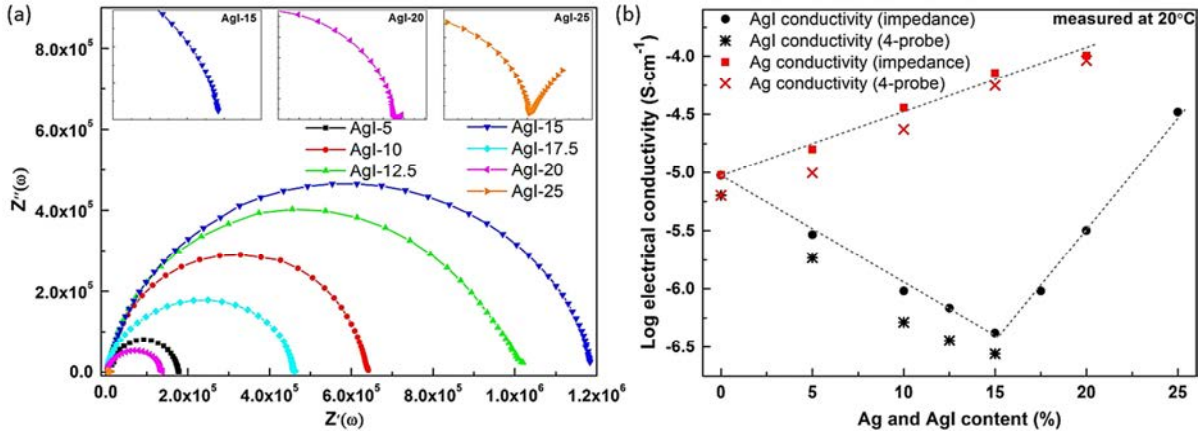

Figure 6 Diagramme de Nyquist du $(GeTe_4)_{100-x}AgI_x$ à 10°C (a) et comparaison de la conductivité électrique entre le $(GeTe_4)_{100-x}$xAgx et le $(GeTe_4)_{100-x}AgI_x$ (b).

Pour confirmer cette analyse, une étude structurale a pu être menée grâce à Pal Jovari, chercheur à Budapest, par analyse reverse Monte Carlo de diagramme X et EXAFS. Ce travail montre que l'argent joue d'abord un rôle de formateur de verre, en coordinence 3, et se lie grâce à des liaisons covalentes majoritairement au tellure. Ensuite, pour les concentrations

[1] A noter qu'il n'y a pas de verre avec 15% de l'iode. Verre avec 14% de l'iode a été choisi dont la composition est très proche.

plus élevées en AgI, on retrouve de l'argent avec de l'iode dans la première sphère de coordination en quantité plus importante. L'argent est alors davantage à l'état ionique Ag^+ dans les interstices du réseau. Ce résultat est en accord avec l'évolution des conductivités observées plus haut. Par ailleurs l'iode reste effectivement coordonné à un seul élément et tend à dépolymériser le réseau. Un modèle structural a été proposé à partir de ces résultats (figure 7).

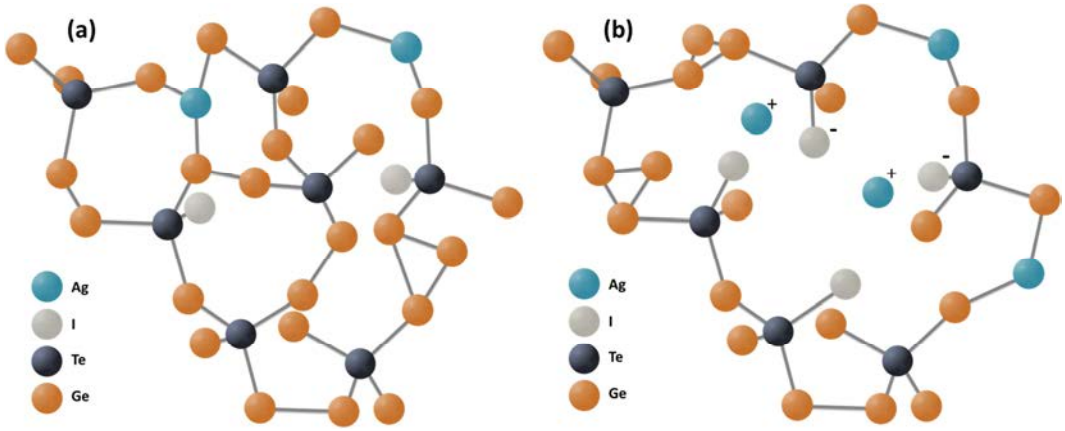

Figure 7 Structure du $(GeTe_4)_{100-x}AgI_x$ avec moins (a) ou plus (b) de 15% d'AgI

D'un point de vu plus finalisé, ces verres ont été également caractérisés optiquement à de plus grandes longueurs d'onde à l'Université du Littoral à Dunkerque. Sur la figure 8, sont reportées les courbes de transmission qui montrent que ces verres laisse passer la lumière jusqu'à 38 µm. C'est à notre connaissance les seuls verres transmettant aussi loin dans l'infrarouge lointain, les rendants intéressants pour réaliser des fenêtres optiques, par exemple pour des applications spatiales.

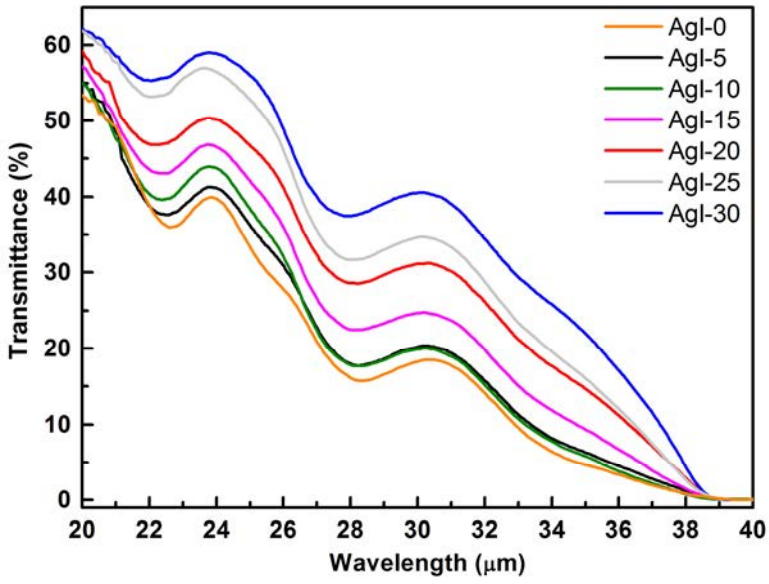

Figure 8 Transmittance dans l'infrarouge lointain du $(GeTe_4)_{100-x}AgI_x$..

Chapitre 3

Fibres optiques en verre du système $GeTe_4$-AgI pour la spectroscopie moyen infrarouge

L'objectif de ce chapitre est de développer des fibres optiques à partir des verres du système $GeTe_4$-AgI afin de mettre en œuvre des expériences de détection infrarouge par spectroscopie par ondes évanescentes. Comme il a été montré précédemment, ces verres sont particulièrement intéressants pour fabriquer des fibres optiques car ils re-cristallisent difficilement. Pourtant, les expériences passées ne se sont pas révélées si simples, et les fibres obtenues étaient caractérisées par des pertes optiques importantes de l'ordre de 20 $dB.m^{-1}$. L'essentiel de ces pertes semblent parvenir de défauts de surface et en particulier de la présence de cristaux de composition GeI_4 en surface. Un gros travail de polissage mécanique des préformes a été mis en œuvre pour remédier à ce problème (figure 9).

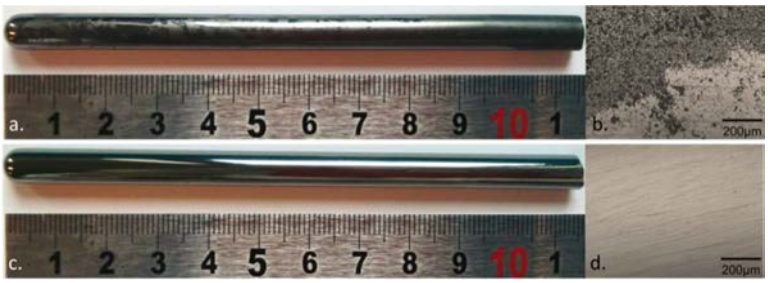

Figure 9 Photos microscopique et macroscopique de la préforme de fibre optique en $(Ge_{0.21}Te_{0.79})_{90}AgI_{10}$ avant (a et b) et après (c et d) polissage

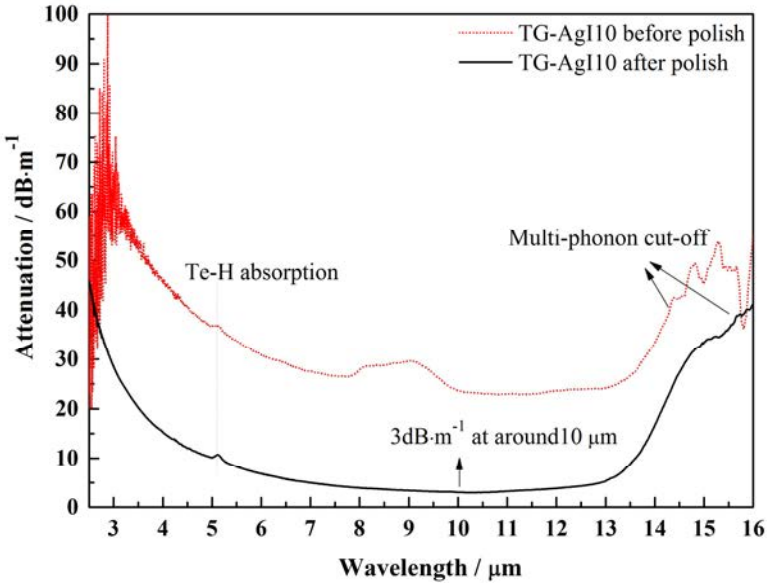

Figure 10 Pertes optiques de la fibre en $(Ge_{0.21}Te_{0.79})_{90}AgI_{10}$ obtenue avec (ligne noir) ou sans (ligne rouge en pointillé) polissage mécanique.

Grâce à ce traitement, les pertes ont été substantiellement abaissées à 3 dB.m^{-1} à 10 µm, mesurées sur une fibre mono-indice (figure 10). Il s'agit à notre connaissance des pertes les plus basses jamais mesurées dans une fibre optique en verre de tellure. Ces fibres ont également été effilées localement pour diminuer le diamètre de la fibre à hauteur de la tête de mesure du capteur par onde évanescente. Cette manipulation est une difficulté supplémentaire en particulier pour un verre de tellure, mais il a déjà été montré qu'elle était décisive en termes de sensibilité du capteur. Cette fibre effilée a ainsi été utilisée pour détecter quelques substances cibles telles que le dichlorométhane ou le chloroforme. La figure 11 présente une comparaison de spectres FEWS acquis avec une telle fibre et ceux acquis grâce à la fibre en verre $Te_2As_3Se_5$ actuellement mise en service par la société DIAFIR. La nouvelle fibre en verre $GeTe_4$-AgI permet d'acquérir le signal jusqu'à 16 µm contre 12 µm jusqu'alors, permettant ainsi l'observation des bandes d'absorption C-Cl par exemple. On vérifie également le gain en sensibilité lorsque le diamètre de la fibre diminue.

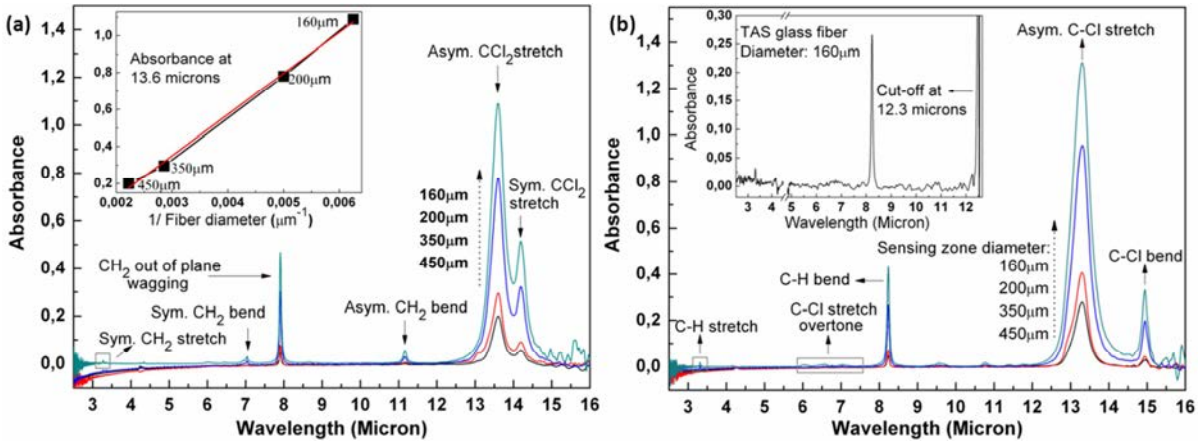

Figure 11 Détection du dichloromethane (a) et du chloroform (b) en utilisant les fibres en $(Ge_{0.21}Te_{0.79})_{90}AgI_{10}$

Pour illustrer le potentiel de ces fibres sur une problématique concrète, les spectres du toluène en concentration variable dans l'iso-octane ont été enregistrés. On distingue clairement les deux bandes d'absorption dues à des vibrations C-H « hors plan » à 13.7 et 14.4 µm. Ces bandes signent la présence du toluène avec un seuil de détection de l'ordre 0.5 % en volume. Le toluène est utilisé comme additif dans l'essence pour optimiser le taux d'octane. Notons que l'on retrouve une loi de proportionalité entre l'absorbance et la concentration jusqu'à 10% de toluène, permettant ainsi son dosage.

De façon générale, l'apport de ces fibres pour la spectroscopie par ondes évanescente est très significatif et pourrait s'avérer décisif lors de la mise en œuvre de ces capteurs pour des

problématiques biomédicales, principal débouché pour cette spectroscopie. De nombreuses études sont en cours (sérum, lait, beurre, essence …) pour démontrer le potentiel de ces fibres par comparaison aux fibres optiques en séléniure.

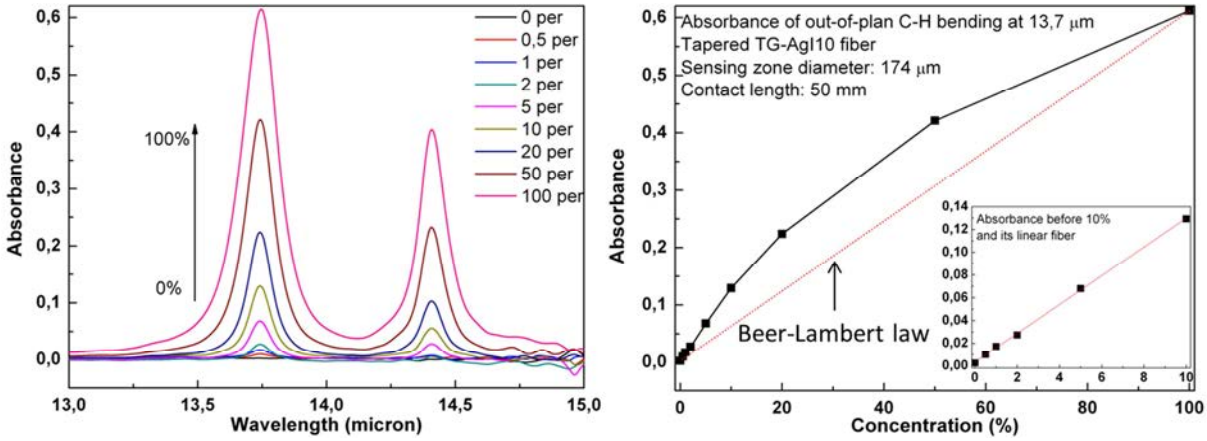

Figure 12 Variation de l'absorption du toluène en fonction de la concentration capté par la fibre en TG-AgI10 effilé. L'encart représente l'absorption du toluène moins 10% et sa régression linéaire.

PARTIE II: Verres à base de tellure pour la thermoélectricité

Chapitre 4

Développement de verres de tellures comme matéraiux thermoélectrique.

Un matériau thermoélectrique transforme un gradient de température en courant et inversement, le passage d'un courant dû à une différence de potentiel en un gradient de température. Les verres de chalcogénure sont, comme tous les verres, de mauvais conducteurs thermiques (environ 0.5W/m^{-1}K^{-1}) et sont caractérisés par un coefficient Seebeck important (plus de 500µV/K). Parmi ces verres, les tellurures sont les meilleurs conducteurs électroniques, et des verres des systèmes Cu-Ge-Te, Cu-Si-Te, Cu-Ga-Te ou Cu-As-Te ont déjà fait l'objet de travaux antérieurs. Par rapport à cet état de l'art, des progrès restent à réaliser pour accroître encore la conductivité électronique de ces verres et essayer de les rendre concurrentiels par rapport au Bi_2Te_3, matériaux cristallisé de référence pour ce type d'application.

De nouvelles compositions de verres du système Te-As-Se-Cu ont été préparés et leur résistivités mesurées (figure 13). Plus le verre est riche en sélénium, plus le domaine vitreux s'accroit et plus le taux de cuivre peut augmenter. Cependant, ceci ne permet pas d'abaisser les résistivités et les verres les plus intéressants restent les purs tellurures. Il s'avère finalement que la composition la plus intéressante soit $Te_{45}As_{30}Cu_{25}$ présentant une résistivité de 18Ω·cm.

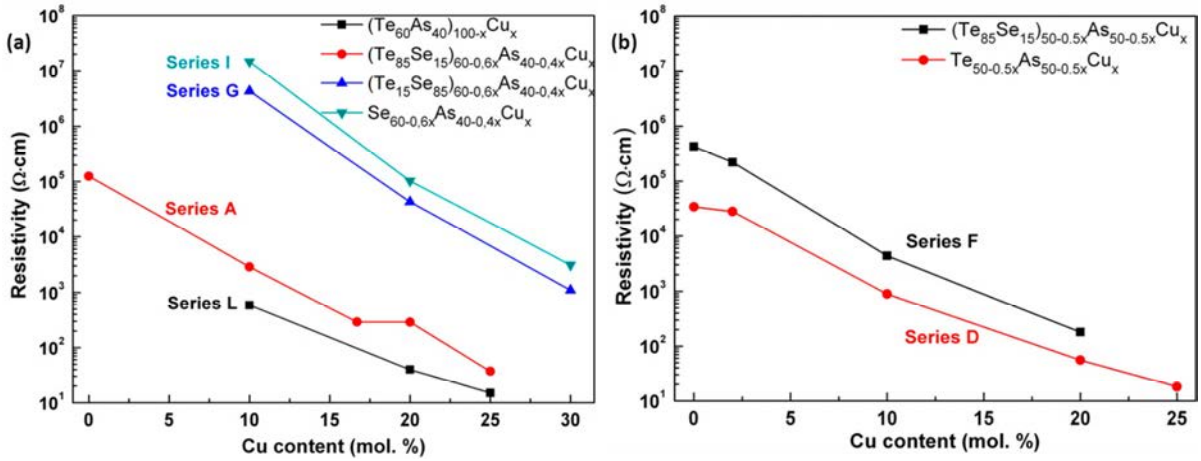

Figure 13 Comparaison des résistances du Te-As-Cu, Te-Se-As-Cu et du Se-As-Cu

A partir de cette composition, des vitro-céramiques ont été préparées par recuit du verre. Les résultats sont regroupés sur la figure 14. Un recuit de 15h à Tg+30°C permet d'obtenir une vitrocéramique assez homogène et d'abaisser la résistivité à 6 Ω.cm après avoir poli la

surface de l'échantillon, puis 2 Ω.cm à Tg+40°C. Il est donc possible de contrôler l'évolution de la résistivité en jouant avec les paramètres de cristallisation.

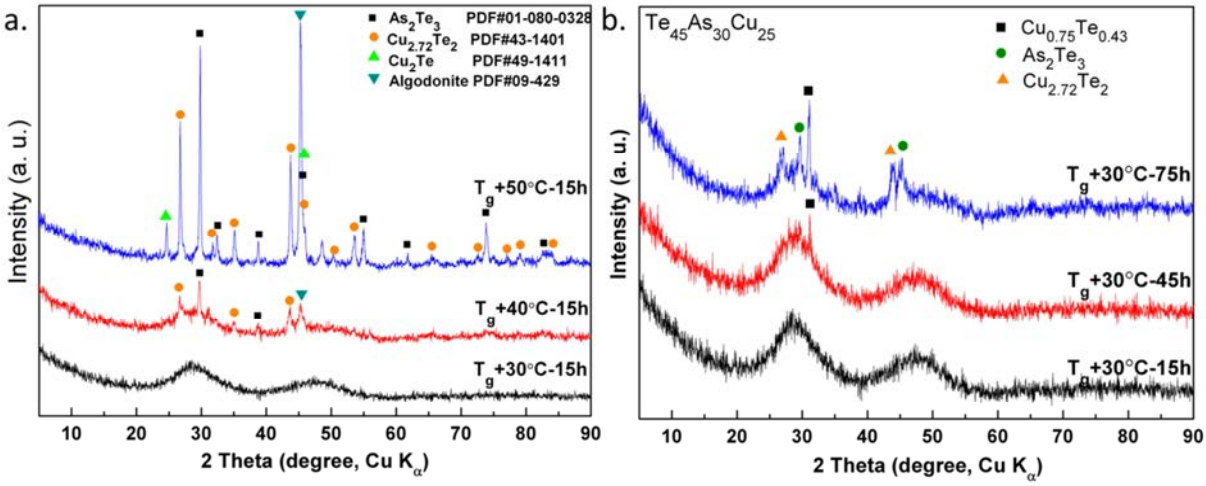

Figure 14 DRX du $Te_{45}As_{30}Cu_{25}$ après traitement thermique à différentes températures pendant 15 h (a.) et à T_g+30°C pour différentes durées (b.)

Cependant, en polissant à différentes profondeurs un barreau de vitrocéramiques, il s'avère que les valeurs mesurées sont différentes et que donc le taux de cristallisation n'est pas homogène du cœur à la surface du barreau (figure 15). Ce résultat décevant nous a poussés à envisager une voie alternative de préparation de matériaux composites.

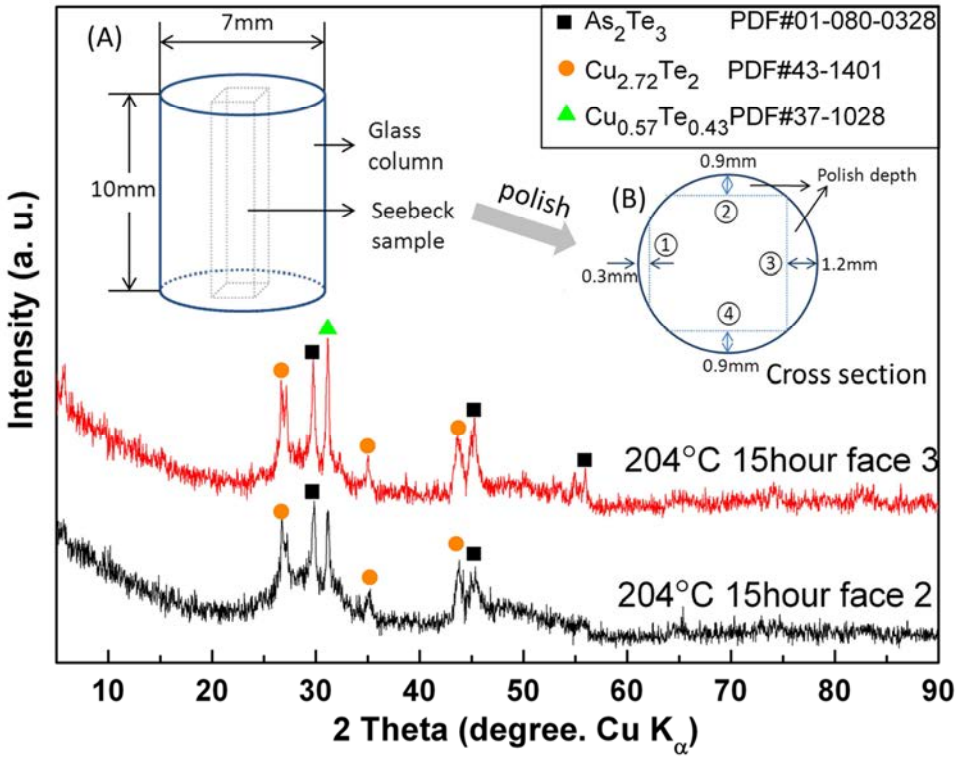

Figure 15 DRX des différentes faces d'une tige de $Te_{45}As_{30}Cu_{25}$ après polissage. L'échantillon a subi un traitement thermique a 204°C durant 15 h.

Chapitre 5

Préparation de matériaux composites par pressage à chaud et Spark Plasma Sintering

La stratégie consiste à préparer des matériaux composites, mélanges de verre et de cristal, par broyage planétaire puis pressage ou SPS. Le verre permet de faciliter la mise en forme des matériaux, d'abaisser les températures de synthèse et de diffuser les phonons.

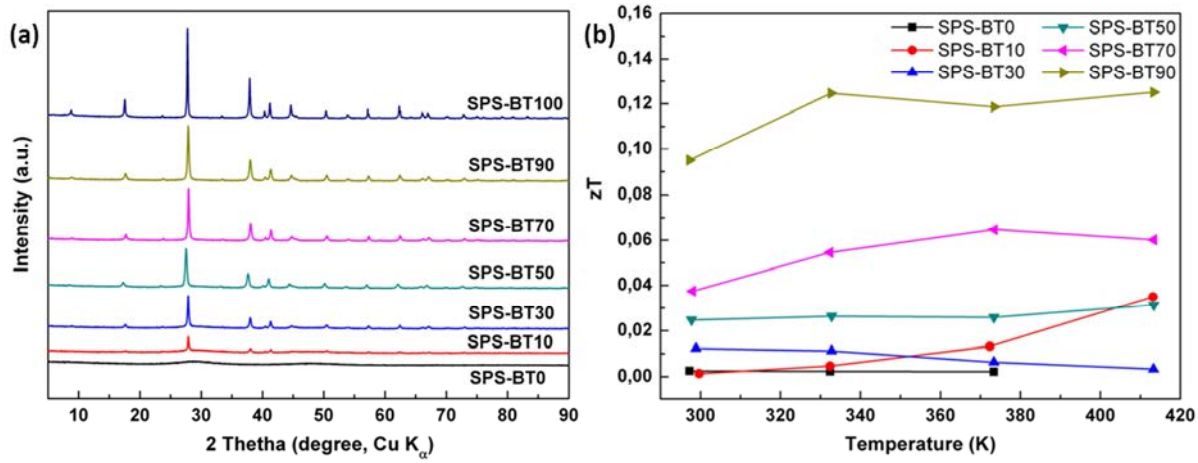

Figure 16 DRX (a) et ZT (b) du $(Te_{0.85}Se_{0.15})_{45}As_{30}Cu_{25}$ avec différents pourcentages de Bi_2Te_3

Les premiers essais se sont portés sur un mélange entre le verre $(Te_{85}Se_{15})_{45}As_{30}Cu_{25}$ et Bi_2Te_3 cristallisé. Le pressage à chaud s'est vite révélé insuffisant pour compacter les matériaux. Par SPS il a été possible de préparer une série de composites vitro-céramisés en substituant continument l'un et l'autre des éléments (figure 16). L'ensemble des caractérisations thermoélectriques a été réalisé pour aboutir au ZT présenté sur la même figure. Celui-ci augmente avec le taux de cristallites Bi_2Te_3 dans le verre. Le verre contenant 90% de Bi_2Te_3 présente donc le ZT=0.12 le plus élevé. Cette valeur est beaucoup plus faible que celle de Bi_2Te_3, mais le matériau final présente l'avantage de pouvoir être facilement mise en forme. Par ailleurs, le verre est un conducteur de type p alors que Bi_2Te_3 est de type n. Le mélange de ces 2 composés n'est donc pas optimal pour améliorer les conductivités et nous nous sommes orientés vers le composé $Bi_{0.5}Sb_{1.5}Te_3$ (BST) qui lui est conducteur de type p comme le verre.

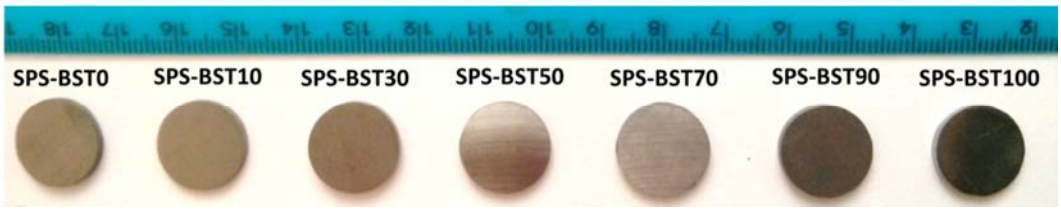

Figure 17 Composites de $(Te_{0.85}Se_{0.15})_{45}As_{30}Cu_{25}$ / $Bi_{0.5}Sb_{1.5}Te_3$ fabriqué par la méthode SPS.

Les composites obtenus sont photographiés sur la figure 17. Ils ont été complétement caractérisés (résistivité, densités, Seebeck, analyse thermique) de façon à calculer les ZT reportés sur la figure 18. Les valeurs les plus intéressantes sont curieusement obtenues pour l'échantillon contenant 30 % de BST. La valeur de ZT peut ainsi atteindre 0.35 ce qui est encourageant bien qu'inférieur au ZT du BST seul (1.4). Cependant la densification des matériaux n'est pas parfaite et le BST initial pas parfaitement cristallisé. Une marge de progression existe donc pour cette étude.

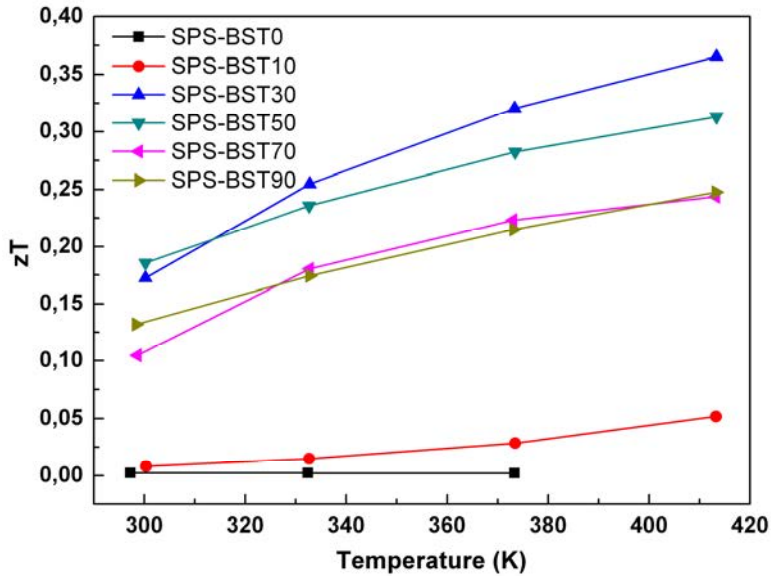

Figure 18 Facteur de mérite thermoélectrique du composites $(Te_{0.85}Se_{0.15})_{45}As_{30}Cu_{25}$ /$Bi_{0.5}Sb_{1.5}Te_3$.

Conclusion

Des résultats très encourageants ont été obtenus quant au développement des verres de tellure pour l'optique moyen-infrarouge.

Il a ainsi été montré que des fibres monomodes transmettant la lumière jusqu'à 16 µm pouvaient être obtenues. La technologie reste cependant à stabiliser pour bien maîtriser les paramètres géométriques de la fibre. Il s'agit d'un résultat qui pourrait être décisif dans le cadre du projet DARWIN de l'ESA, actuellement en veille.

Les verres $GeTe_4$-AgI sont particulièrement intéressants car ils cristallisent difficilement. Une étude de leurs propriétés de conduction couplée à une analyse reverse Monte Carlo de données de diffraction sur grands instruments, permet de faire des hypothèses fortes sur leur organisation structurale et leur mode de fonctionnement.

Par ailleurs ces verres ont permis de fabriquer des fibres performantes, la plus faible atténuation jamais mesurée à 3 $dB.m^{-1}$, pour la spectroscopie par ondes évanescentes. Pour la première fois il est possible d'enregistrer un spectre jusqu'à 16 µm contre 12 µm pour les fibres actuellement en service. Il s'agit d'une avancée majeure qui aura des conséquences très positives lors de leur mise en œuvre pour des stratégies bio-médicales en particulier.

Enfin, il a également été montré que ces verres pouvait être intéressants pour réaliser des fenêtres optiques transparentes jusqu'à 38 µm dans l'infrarouge lointain.

Très clairement, les conclusions sont plus mitigées concernant la thermoélectricité.

En ce qui concerne les matériaux massifs de type As-(Te/Se)-Cu, il semble difficile d'abaisser les résistivités en-deçà de 15 Ω.cm pour les verres et 2 Ω.cm pour les vitrocéramiques. Ce dernier résultat est intéressant, mais les vitrocéramiques obtenues ne sont pas très homogènes.

Enfin, la stratégie « matériaux composites » plus exploratoire demande des développements supplémentaires. Les composites issus du mélange verre de tellure/BST, tous deux conducteurs de type p, sont potentiellement intéressants mais les conditions de synthèse doivent être réexaminées pour densifier davantage les matériaux.

Table of Contents

Chapter 2

Addition of Silver, Iodine and Silver Iodide in $GeTe_4$ Glass

Chapter 3

Te-Ge-AgI glass for far-infrared biochemical sensing

Chapter 4

Te-Based Glass: a New Class of Material for Thermoelectric Application

General Introduction

Glass is one of the oldest materials known to man. It is often transparent in the visible and fragile. In material science, the glass holds a special place and its formation still a kind of mystery. It is regarded as a frozen liquid with an amorphous structural network and displays glass transition phenomenon.

The viscoelastic versus temperature property of glasses makes them especially interesting for thermal formability. In addition, the glass has an optical transparent window which strongly depends on the compositions. These two unique properties make glass a good candidate for various applications, such as lenses and optical sensor.

There are several glass families. The most familiar type of glass, used for centuries in windows and drinking vessels, is oxide glass, composed of SiO_2, Na_2O, and CaO etc. Other glass families, such as halide glasses including fluoride glasses, got their heyday in the 1980s and 1990s thanks to their transparency in the near infrared range.

A chalcogenide glass is a glass containing one or more chalcogen elements (e.g. sulfur, selenium or tellurium). It is developed primarily for its optical properties in the mid-infrared region where all the other glasses are opaque and blind. The modern technological applications of chalcogenide glasses are widespread. Examples include infrared detectors, moldable infrared optics such as lenses, and infrared optical fibers. In addition, due to their low phonon energy, these glasses could also be utilized for the applications of fiber laser or optical amplifier in the infrared range.

In chalcogenide glasses, the added elements, such as arsenic (As), gallium (Ga), germanium (Ge), antimony (Sb) and metal halide, are used to tailor the property of the glass (e.g. glass stability and free electrons concentration). For example, the infrared transmission window depends on the molar mass of glass components.

Selenide glasses exhibit excellent infrared transmission in the 3 to 15 µm region as bulk. Due to their superior thermo-mechanical properties, these glasses could be easily shaped into optical devices such as lenses and optical fibers. As the fundamental absorption domain caused by vibrations of most of chemical and biological molecules is located in the mid-infrared region, selenide glass fibers have been developed along the past decade of research for infrared sensing up to 12 µm based on an original spectroscopic method named Fiber Evanescent Wave Spectroscopy (FEWS). However, due to the limited optical window, the selenide glasses and fibers cannot be applied for applications further in the mid-infrared beyond 12 µm.

As tellurium (Te) is the heaviest chalcogen element, telluride glass can transmit longer wavelength in the infrared region compared with sulfur and selenium based glasses. For this reason, tellurium-based glasses are good candidates to integrate the envisaged optical system for Darwin project of the European Space Agency (ESA), aiming at the discovery of the signatures of life in the universe. This asks for fibers transparent from 6μm to 20μm to detect the possible presence of water (6μm), ozone (9μm) and carbon dioxide (15μm) on extrasolar planets by infrared spectral analysis of their atmospheres. To detect the very low signal from planets, the invasive signal from stars should be suppressed using nulling interference, which asks for the development of single mode fiber. ESA has defined two transmission bands, the first (6-12 μm) to detect infrared signatures of H_2O and O_3 and the second to detect signature of CO_2 (15μm). A chalcogenide glass fiber based on the Te-As-Se composition is suitable for the short wavelength band. For the long wavelength beyond 12 μm, tellurium based glass has to be used to elaborate a single mode fiber, but this achievement is still not yet available.

In addition, in order to test the fundamental vibrations (stretching and bending) of molecules and biomolecules whose main absorption bands are beyond 12 μm, such as benzene and chloroform, optical sensor with extended spectral range have to be developed based on telluride glass fiber.

Nevertheless, due to the strong metallic character of tellurium, Te-based glasses are difficult to control and vitrify. Different strategies have already been considered to enhance glass stabilization by introducing some other, rather heavy, elements in the mixture. For the two applications mentioned above, the requirement of glass stabilization is very demanding in order to obtain a fiber without surface crystallization during fiber drawing process. Se-doped and AgI-doped $GeTe_4$ glasses are up to now the best tellurium-based glasses with sufficient thermal stability. The $GeTe_4$ glass containing 10% of silver iodine is particularly good, showing no crystallization peak by thermal analysis. However, the glass structure is still not clear to explain this phenomenon.

On this basis, Chapter 1 aims at the preparation of Te-Ge-Se single mode fiber working beyond 12 μm for the Darwin project. The novel purification procedure and molding method which are suitable for tellurium-based glass will be explored. The optical and thermal properties of the glass will be detailed. The light propagation property of the fiber prepared will be also tested and discussed.

Chapter 2 is dedicated to the exploration of the particular good thermal stability of the AgI-doped $GeTe_4$ glasses. A series of physical properties, such as density, electrical

resistivity, optical transmittance and atomic coordination numbers of Ag-doped, I-doped and AgI-doped $GeTe_4$ glass will be studied to propose a reasonable glass structure model which can explain the glass property from a microstructural point of view.

At this time, it is quite difficult to obtain fibers from the AgI-doped $GeTe_4$ glass and their optical losses are still larger than 20 dB/m, which is unacceptable for any application. The aim of the Chapter 3 is to find the root reason of this poor physical property and try to prepare single index glass fiber with reasonable optical losses for the potential application as an infrared sensing probe working beyond 12μm for biochemical species.

On the other hand, tellurium-based glasses are the glasses with the highest electrical conductivity. They also exhibit dramatically high Seebeck coefficient and low thermal conductivity due to the intrinsic property of the glass. They are therefore quite interesting TE materials, and recently, the potential of Te-based glasses in this area has been shown. Nowadays, energy crisis is one of the most important social issues in today's society, and new sources of energy are being sought. The complete absence of moving parts and the lack of substance such as fluorinated cooling agents make TE devices highly attractive.

Compared with the commonly used TE material bismuth telluride, the electrical conductivity of tellurium-based glass is still not sufficient for application. Thus the main aim of the present work is to increase the electrical conductivity of the telluride glasses without a decrease of the Seebeck coefficient and thermal conductivity.

In Chapter 4, the principle of thermoelectricity will be presented. A large scale of glass compositions, such as Te-As-Cu, Se-As-Cu, and Te-As-Se-Cu (Ag), will be explored. Their thermal and electrical properties will be detailed in order to find glasses with maximum electrical conductivity.

On this basis, Chapter 5 focuses on the further improvement of thermoelectric performance. Some composites of glass with bismuth telluride will be prepared using hot-pressing and spark plasma sintering. A series of characterization including Seebeck coefficient, electrical resistivity, and thermal conductivity will be performed for the calculation of figure of merit.

Chapter 1.

Te-Ge-Se Glass System for Far-Infrared Sensing

1.1 Introduction

Chalcogenide glasses are based on sulfur, selenium and tellurium elements, and have been studied for several decades regarding to different applications. Among them, selenide glasses exhibit excellent infrared transmission in the 3 to 15 µm region[1-3]. Due to their superior thermo-mechanical properties, these glasses could be easily shaped into optical devices such as lenses[4] and optical fibers[5]. Along the past decade of research, selenide glass fibers have been proved to be suitable for infrared sensing up to 12 µm[6,7] based on an original spectroscopic method named Fiber Evanescent Wave Spectroscopy (FEWS)[8]. As the fundamental absorption domain caused by vibrations of most of chemical and biological molecules is located at infrared region[9], Se-based is particularly suitable for applications such as the detection of: molecular substances[10], environmental pollutants[11] and in-situ chemical reactions[7] by close contact between fiber and the specimen.

However, due to the limited optical window of selenide glasses fiber[12], the strongest vibration absorption peaks of many molecules beyond 12 µm cannot be detected. Meanwhile, to monitor the terrestrial planets and analyze the possibility of extraterrestrial life, two atmospheric windows are identified and used. Selenide optical fiber can be used in the first window (6-12 µm) to detect infrared signatures of H_2O (6 µm) and O_3 (9 µm). Therefore, new optical fibers working in the second (12-18 µm) window and detect the signature of CO_2 (15 µm) in Darwin mission[13] (European Space Agency) or Terrestrial Planet Finder[14] (National Aeronautics and Space Administration) should be developed.

Compared with selenium-based glasses, the transparency of tellurium-based glasses to infrared radiation generally increases towards smaller wavenumbers. This owns to its higher atomic masses and smaller bonding force constants, which lead to lower vibration absorption frequencies. According to our previous study, Te-based bulk glass can transmit infrared signal up to 25 µm[15-18], which is larger than Se-based glass. It can be predicted that the optical fiber drawn from Te-based glass can transmit infrared signal beyond 12 µm[19]. Therefore, for both exoplanets detection and FEWS applications, Te-based glass fibers should be developed. In this chapter, the main task is to develop Te-based glass fibers for extra solar terrestrial planets detection. To characterize the chemical signatures of life on planet, the light from a parent star should be suppressed. This asks for the development of single mode fiber in order to carry out interferometry measurements, called nulling interferometry. Hence, our aim in this chapter is a successful fabrication of Te-based single mode glass fibers.

Here, it should be mentioned that, although Se and Te have the same hexagonal structure, it is well known that, in contrast to Se, which is a good glass-forming element, Te is impossible to vitrify even when using fast quenching. Indeed, the Te melt, which has a low viscosity, possesses a strong metallic character. Recently, several tellurium based glass systems have already been reported in the literature. The strategy most commonly used is to add gallium (Ga)[15], iodine (I)[16], silver iodine (AgI)[20,21] or a small amount of selenium (Se)[22-24] to enhance the stability of the glass. Nevertheless, the requirement of glass stabilization is very demanding in order to obtain a fiber without surface crystallization during fiber drawing process. Indeed, the temperature difference (ΔT) between glass transition temperature (T_g) and crystallization temperature (T_x) should be larger than 120 ˚C[25], which eliminates most of the potential candidates. Thus, the development of Te-based glass exhibiting a good thermal stability together with composition easy to control is essential. In that frame, it has been demonstrated that the Te-Ge-Se glasses, with a few percent of selenium[24], are good candidates.

To obtain a high quality double index fiber, the starting bulk glass should be highly purified. In this chapter, bulk Te-Ge-Se (TGS) glasses were prepared using different purification procedures. Thermal stability and optical transmittance of bulk glasses will be detailed. In order to select the optimum purification method, single index fibers were prepared by drawing preforms following different purification procedures. Another difficulty to deal with is the high crystallization tendency of the glass during fiber drawing process. The traditional rod-in-tube method is not suitable for the preparation of such Te-based single mode fiber due to the numerous steps of casting and drawing. As a result, a new method of preparation of the preforms has been developed. Based on this new technique, double index fibers were designed and prepared. Their characterizations, such as optical losses and light propagation, are also presented and discussed.

1.2 The Darwin project description

In recent years, space programs whose goal is to detect extra solar terrestrial planets have emerged. Two typical examples are the « Terrestrial Planet Finder » (TPF) led by « National Aeronautics and Space Administration » (NASA) and Darwin project led by «European Space Agency» (ESA). Both projects have the same goals: (1) to block the light from a parent star in order to detect its much smaller, dimmer planets; (2) to characterize the surfaces and atmospheres of newfound planets, and look for the chemical signatures of life. To achieve

these two goals, a telescope flotilla operating in the thermal infrared spectral region is required. The reasons are as follows:

a) In the visible spectrum an Earth-like planet is outshone by its star by a factor of a billion. However, in the infrared, the difference is less by a few orders of magnitude.

b) The simultaneous presence of water, ozone and carbon dioxide in the atmosphere appears to be a reliable signature of life, whose absorption bands are located at 6μm, 9μm and 15μm respectively.

In order to develop an infrared sensor with capability for imaging and spectroscopy, wavefront errors have to be reduced to a very high degree in order to achieve the required nulling quality. The nulling interferometer configuration consists in creating destructive interferences to suppress the invasive signal from stars and to permit to detect the very low signal from its planet (Figure 1.1).

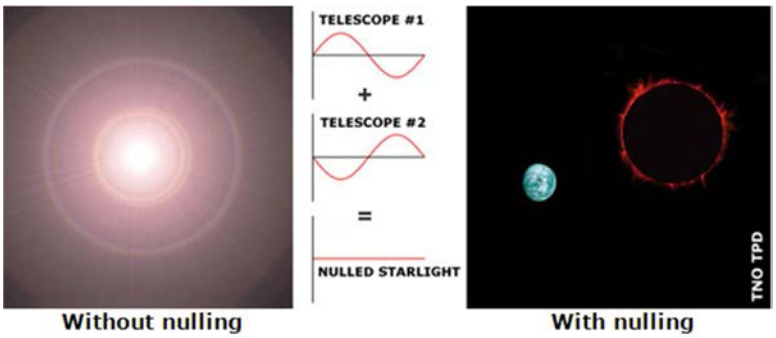

Figure 1.1 Scheme of nulling principle for the detection of signal from planet

In this system, phase shifts would be introduced into two beams, so that light from the central star would suffer destructive interference and cancel itself out. However, light from any orbiting planets would not cancel out, as the planets are offset slightly from the star's position. This would allow planets to be detected, despite the much brighter signal from the star. However, achieving optimum performance from the interferometers requires that the wavefronts of light reaching the interferometer are free of distortions. This can only be achieved by using single mode fibers, which are excellent wavefront filters.

For the Darwin mission, the operational wavelength range is 6-20μm. Within the current ESA project, this is covered by a dual-band fiber system. A chalcogenide glass fiber based on the Te-As-Se (TAS)[26] composition is selected to be used for the short wavelength band. For the long wavelength beyond 12 μm, tellurium based glass is proposed but is still not yet available.

1.3 Bulk glass synthesis and characterization

In order to successfully prepare high quality Te-based single mode glass fibers, high purity glass preforms which are stable enough against crystallization to allow the manufacturing of optical fiber should be prepared. In an optical fiber, any tiny defect and impurity absorption could be greatly amplified due to the long-distance propagation of light. Therefore, the requests for glass stability, synthesis and purification procedure are very critical. The characterization of bulk glasses, including glass stoichiometry, stability, and optical transmittance before and after purification, should be confirmed so as to obtain high quality preforms for fiber drawing.

1.3.1 Selection of the glass composition

Despite being close neighbors on the Periodic Table and having similar electronic structure, Se and Te are totally opposite in terms of their ability to form glassy materials. The main difference between Se and Te is the nature of the bonding responsible for the interchain cohesion[27]. For Se, the bonding is of Van der Waals origin and can be easily destroyed by thermal agitation, generating a viscous liquid. On the contrary, Te exhibits a much stronger metallic character, and its free electrons (electrical resistivity $\rho=5.4\times10^{-3}\Omega\cdot m$[28]) are several orders of magnitude higher than Se ($\rho=1.0\times10^{3}\sim20\times10^{3}\Omega\cdot m$[29]). This intrinsic property makes it impossible to be in a vitreous state even by fast quenching.

One way to prevent the nucleation and crystallization tendency of Te is to reduce the number of free electrons. This strategy has been achieved by grafting halogen atoms along the Te chains as demonstrated in the discovery of the so-called TeX glasses[30,31]. However, due to the low dimensionality of the glassy framework, this series of glass shows low thermal and weak mechanical properties and is not suitable for the fabrication of optical devices working at room temperature.

Following the same strategy, some interesting glass compositions containing large amounts of tellurium, have been identified with better thermal and mechanical properties than the above TeX glasses thanks to the higher dimensionality of their network provided by $GeTe_4$ tetrahedral structural units. The bulk infrared transmittance spectra of Te-Ge-Ga, Te-Ge-I, Te-Ge-Se, and Te-Ge-AgI glass systems, which have been recently investigated in our laboratory since 2006, are shown in Figure 1.2.

The Te-Ge-Ga glass system was the first reported Te-based ternary glass system with glasses containing 70 to 80% of Te for bulk[15,32] and fiber optics[33]. The bulk glasses present

an exceptional optical-transmission window, lying between 2 and 28 μm[15]. The lowest optical loss calculated from bulk transmittance of $Te_{75}Ga_{10}Ge_{15}$ glass is close to 0.6 dB/cm in the wavelength range of 6–20 μm[32]. However, as the maximum ΔT is limited, this composition shows a high tendency to crystallize during fiber drawing process.

Indeed, surface crystallization in fiber drawing process is quite a common problem for Te-based glass. To shape a glass into optical fibers with a limited risk of nucleation of metallic Te nanoparticles, the temperature difference ΔT between glass transition temperature and crystallization temperature should be more than 120°C.

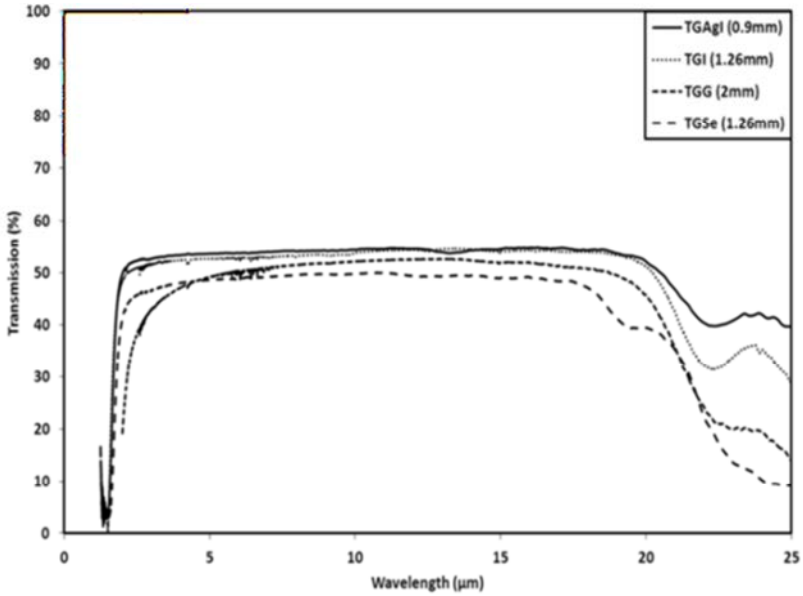

Figure 1.2 IR transmission window of different rich Tellurium based glasses reported in literature[20].

Hence, Te-Ge-I[16] system was developed since 2007. The optimally stable glass was found to be $Ge_{20}Te_{73}I_7$ with a ΔT value of 124°C. However, as the glass forming zone of this ternary system is very narrow, a small deviation from the ideal composition due to the volatility of iodine during synthesis can lead to rapid loss of stability of the glassy materials. For double index fiber, it is extremely vital to control the composition deviations between core and clad to get single mode propagation. Therefore, glasses containing volatile elements such as iodine should be avoided for double index fiber, especially single mode fiber for outer space application.

In order to overcome those issues, more recently, glasses from the ternary systems Te-Ge-Se[22-24] and Te-Ge-AgI[20,21] exhibiting broad infrared transmission and superior stability (ΔT>120°C) have been explored. For Te-Ge-AgI system, even though the volatility of iodine can be greatly decreased by the addition of Ag, the glass composition still cannot be precisely

controlled due to the loss of a small amount of iodine. As a result, Te-Ge-AgI is not proper for double index fiber preparation. This Te-Ge-AgI system, due to its good thermal stability, mechanical formability, large transmission window and high infrared sensitivity, is especially suitable for infrared sensing based on FEWS, which will be introduced in the next chapter.

Glasses from the Te-Ge-Se (TGS) system with a few percentage of Se have already shown an attractive stability (ΔT=120°C), and a good control of the glass composition due to the lack of volatile element. The Te-Ge-Se ternary phase diagram including the glass forming region is shown in Figure 1.3. In this chapter, the $Ge_{21}Te_{79}Se_3$ (TGS3) glass will be used for the preparation of single index fiber.

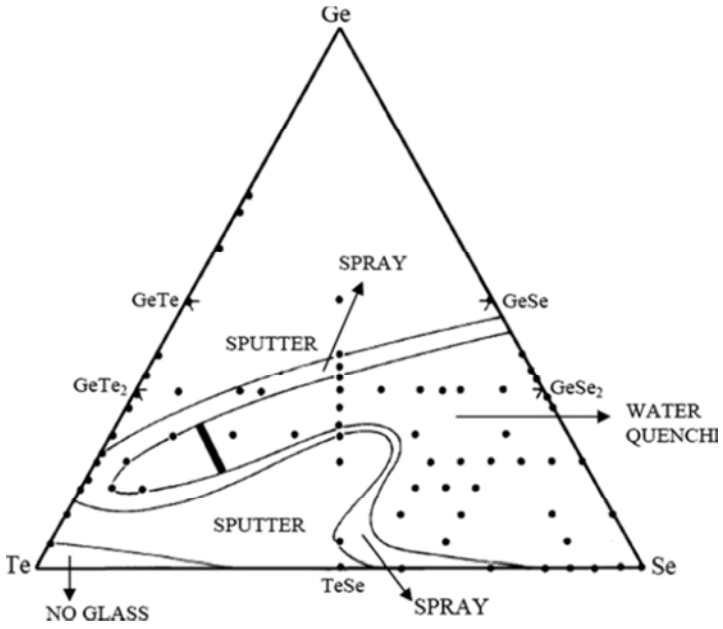

Figure 1.3 Glass formation area in the Te-Ge-Se ternary system[34].

For TGS glasses, the refractive index can be easily modified by the substitution of Te by Se. This opens a way toward the fabrication of double index optical fiber. A double index optical fiber[23] with its core and clad composition to be $Ge_{21}Te_{79}Se_3$ and $Ge_{21}Te_{74}Se_8$ (TGS8) respectively has been prepared by traditional rod-in-tube method[35]. This method is only suitable for the preparation of single step-index multimode fiber with large core size. However, a single mode fiber usually has a relatively small core (with a diameter of less than 30 μm). As a result, several steps of casting and drawing process are required to achieve the targeted core diameter. During this procedure, the crystallization of Te-based glass is almost inevitable. In this work, according to the evolution of the glass refractive index versus the ratio Se/Te, multi-mode (TGS3/TGS8) and single-mode double index fibers will be prepared by a novel “capillary” method. Note that single mode fiber often has a small refractive index difference between core and clad. Multi-mode fiber with the same core diameter but a higher

refractive index contrast is prepared firstly for monitoring composition diffusion and controlling fiber drawing parameters. The design of core and clad compositions of single mode fiber will be explained later.

1.3.2 Influence of glass purity on optical properties

As explained before, the optical properties of Te-based glasses are very sensitive to the existence of impurities. Especially for optical fiber, the absorption of any tiny defect and impurity could be greatly amplified due to the long-distance propagation of light. The presence of defects in the glass structure (e.g. vacancies, over/under coordinated atoms) and/or dopants and impurities can produce localized energy states taking place within the forbidden gap. The presence of such states, thus, enables optical absorption at frequencies within the transmission window. When such absorption processes are at frequencies resonant with the operational wavelength of the fiber, such structural elements present a significant problem in the development of low-loss fiber optic system. Among the impurities, the most common light-absorbing species are oxide, water (hydroxyl -OH), and hydride within the glass structure, and their presence result in significant absorption (Table 1.1).

Table 1.1 Typical absorption bands position of impurities in chalcogenide glass

Absorption band [μm]	2.9	4.0	4.5	4.9	5.1	6.3	13.0
Impurity	OH-	S-H	Se-H	Se-H	Te-H	H_2O	Ge-O

As an illustration, the optical losses of $Te_{20}As_{30}Se_{50}$ (TAS) single index optical fibers are shown in Figure 1.4. Then the attenuation curves of fibers drawn from preforms with and without purification are obtained. Clearly, the quality of the purification steps is essential to get some low-loss fibers.

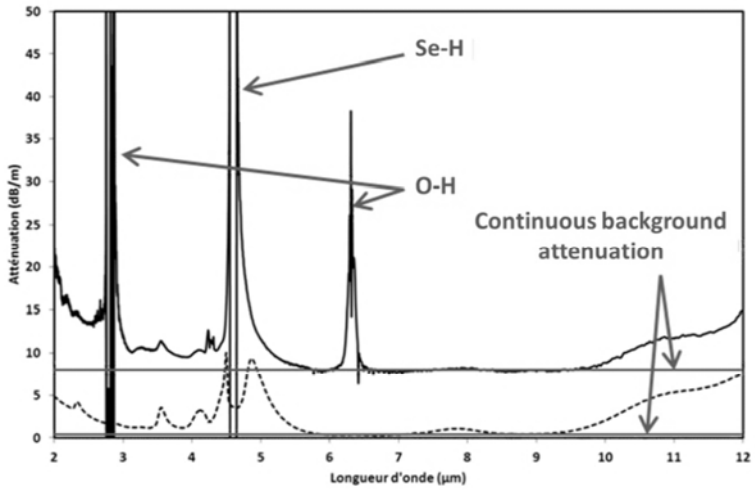

Figure 1.4 The fiber optical losses of $Te_{20}As_{30}Se_{50}$ glasses and single index fibers with (dotted line) and without (solid line) purification[36].

1.3.3 Purification of the starting elements

The high purity elements (5N, 6N) used for the experiments are stored in a glove box under the protection of argon. However, free of H_2O (0 ppm) and O_2 (0 ppm) is not enough, because this characterization of purity does not take into account the solid state oxides. In addition, a special technique for purification of starting elements should be implemented to avoid the vibration absorptions of oxide, hydride, hydroxyl, etc.

In this work, Te (6N, Nippon Mining & Metals Co.), due to its high purity, requires no extra purification. For germanium (5N, Umicore Electro-Optic Materials), as both Ge and GeO_2 exhibit a high melting temperature T_m (T_m(Ge)= 938.25˚C and T_m(GeO_2)=1115˚C), it is difficult to do the purification. Both the two elements will be purified during glass synthesis, using aluminum (5N) as absorbent to trap oxygen as aluminum oxide, alumina. The mechanism of selenium purification is based on the difference of vapor pressure between Se (0.24 mm Hg at 300 ˚C) and SeO_2 (200.05 mm Hg at 300 ˚C). During heating, SeO_2 will become vapor and escape from selenium.

To do this purification, we introduce, in a glove box, selenium in a silica ampoule previously cleaned and dried under vacuum (Figure 1.5). As SeO_2 is not adhesive to silica tube, to avoid the drop back of SeO_2, upper part of the purification chamber should be narrowed. After the seal of inlet, the set-up is settled under vacuum. In order to capture the impurities escape from Se, a silica trap immersed in liquid nitrogen is settled before the vacuum pump and acts as a kind of ‘filter’ to protect the pump. Then the furnace temperature is gradually increased to 240˚C (controlled by thermocouple) and maintained at this temperature for 4 hours. The ampoule is then cooled, sealed, and opened in glove box.

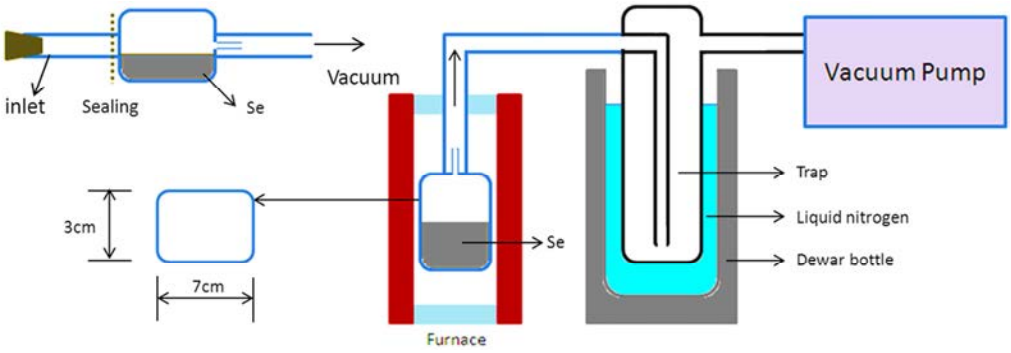

Figure 1.5 Selenium purification scheme

1.3.4 Synthesis of the bulk glass

For the preparation of high-quality optical fiber, the purification of the glass starting elements is not sufficient. Additional purification of the glass needs to be implemented. In

order to check the purification efficiency, a comparison of TGS glasses with and without purification has been done by the traditional melting-quenching technique. In order to avoid introduction of extra pollution, all the glasses have to be synthesized in clean silica glass ampoules under vacuum.

1.3.4.1 Synthesis of glasses without purification

For Te-based glasses synthesis, it is essential to operate in closed systems under anaerobic condition because of the high vapor pressure of chalcogenide melt and the tendency to react with oxygen, particularly at higher temperatures. Consequently, chalcogenide glasses have been produced by melting the corresponding element mixtures in silica glass ampoules under vacuum. The setup should be cleaned with hydrofluoric acid to remove the silica dust, rinsed thoroughly with distilled water and dried under vacuum. A rocking furnace with fixed oscillation frequency and amplitude is used for homogenization of melts. The schematic diagram of glass preparation process is shown in Figure 1.2.

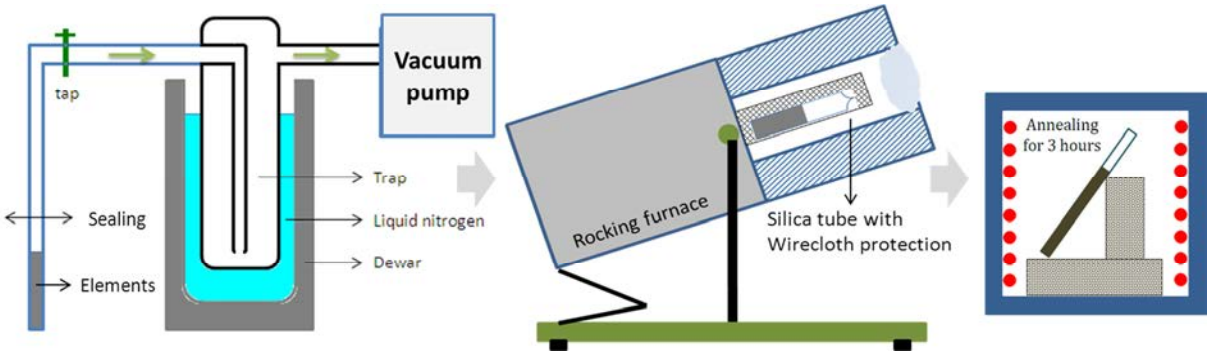

Figure 1.6 The schematic diagram of glass preparation process.

To avoid oxidation, raw elements were weighted under the protection of argon and transferred to a quartz tube which can be closed by a tap in glove box. In view of the low stability of the TGS glass compared to Se-based glasses, the internal diameter of the silica tube is lowered to 7mm. The tube was then connected to a trap immersed in liquid nitrogen and evacuated (10^{-5} millibar) using a mechanical-diffusion pump system for 2 hours. The silica tube containing the raw elements was sealed and put into a rocking furnace afterwards. After homogenization at 750˚C for 10 hours, the TGS glass was quenched at 500˚C in water and annealing at 160˚C for 3 hours in a chamber furnace. The thermal profile is shown in Figure 1.7. By this way, a rod 7 mm in diameter and 15 cm long is obtained

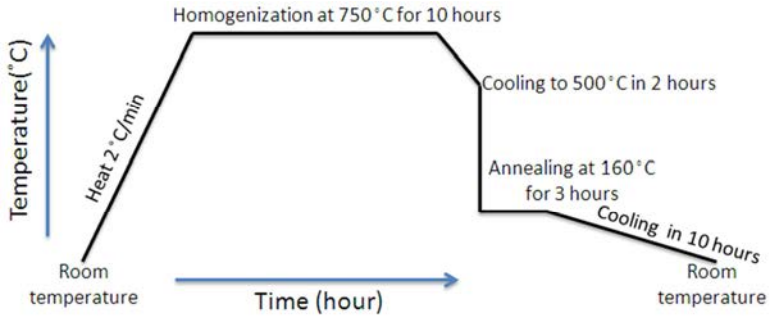

Figure 1.7 Thermal profile for the synthesis of TGS glass.

1.3.4.2 Synthesis of glasses by one-step purification process

As germanium is really difficult to be purified due to the high melting temperature of both Ge and GeO_2, extra purification have to be implemented during the glass preform preparation procedure. For Te-based chalcogenide glasses, aluminum is a well-known oxygen getter [37,38] and can have a redox reaction with other oxide.

$$\mathbf{Al + MO \rightarrow Al_2O_3 + M} \qquad \textbf{(1.1)}$$

This is due to the strong reducing behavior of aluminum compared to other metals M. The generated alumina Al_2O_3 remains in the chamber during distillation procedure due to its high melting temperature (2072°C) and extremely low vapor pressure. In order to analyze the distillation procedure, the melting temperature T_m, boiling temperature T_b, and the temperatures needed for the indicated pressure of Te, Ge, Se and Al are listed in Table 1.2.

Table 1.2 Melting, boiling temperatures and vapor pressure of Te, Ge, Se and Al elements

Element	Melting temperature [°C]	Boiling temperature [°C]	Temperature in °C for the indicated pressure[39]	
			1 Pa	100 kPa
Te	449.51	988	--	992.4
Ge	938.25	2833	1371	2831
Se	221	685	227	685
Al	660.32	2470	1209	2517

According to this table, during the distillation at 1000°C, the vapor pressure of both Te and Se are larger than 100 kPa, making them quite easy to be distilled. Germanium, owing to its high melting temperature (938.25°C) and low vapor pressure (<1 Pa at 1000°C), needs a longer distillation time. Note that the temperatures needed for the vapor pressure of Ge and Al reaching one Pascal are 1371°C and 1209°C respectively. As a result, the elemental Al which is not completely reacted with oxygen can be distillated to the reaction tube and induce extra impurity. Therefore, it is important to add the proper amount of Al to be sure that the

majority of Al will react with the oxide to form Al_2O_3. According to previous results, 100 ppm of Al is the best rate[40].

In this work, the glass was synthesized using a one-step purification method as shown in Figure 1.8. A silica setup with a chamber connected to the reaction tube was used for glass preparation. Te, Ge, and Se mixed with 100 ppm Al wt. were distilled at 1000°C for 2 hours. The hot metal vapor goes through a filter towards a reaction silica tube of 7 mm internal diameter thanks to the pressure gradient created by a temperature difference. The reaction tube was sealed again with distillated elements inside and heated according to the procedure shown in Figure 1.8.

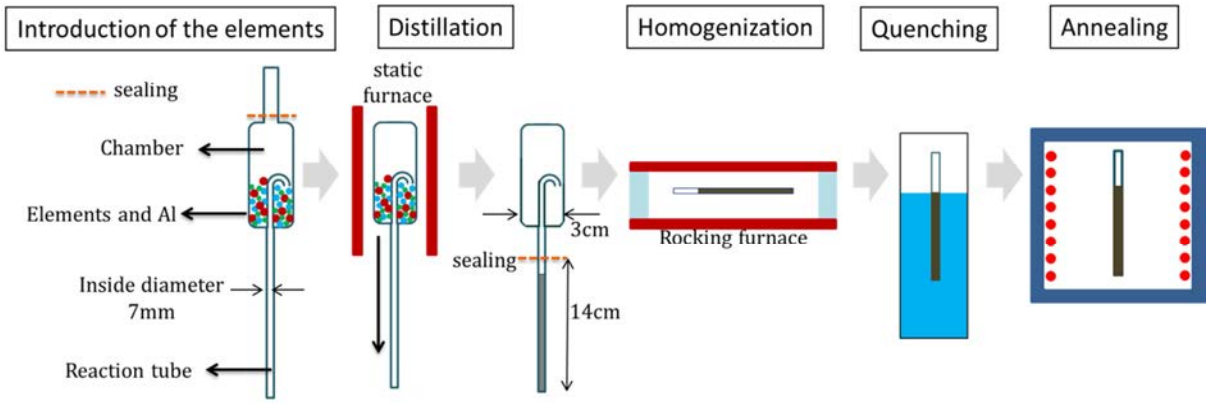

Figure 1.8 Schematic diagram of one-step purification process

1.3.4.3 Synthesis of glasses by two-steps purification process

During the one-step purification procedure, the elements distillation and the redox reaction between aluminum trapper and oxide occurred simultaneously. In order to obtain a better contact between aluminum trapper and the mixture, a new two-steps purification method has been developed as shown in Figure 1.9.

The initial elements together with Al are firstly sealed into silica tube. The glass containing 100 ppm of aluminum is prepared by traditional melting-quenching technique. Therefore oxide in the glass constituent elements could well react with Al during the chemical purification process. Then, the mixture containing alumina is transferred to another silica chamber for distillation in order to trap alumina. All the parameters for glass synthesis and distillation process are the same as for the first method. The final glass, obtained after annealing, can be directly used as glass preform for single index fiber drawing.

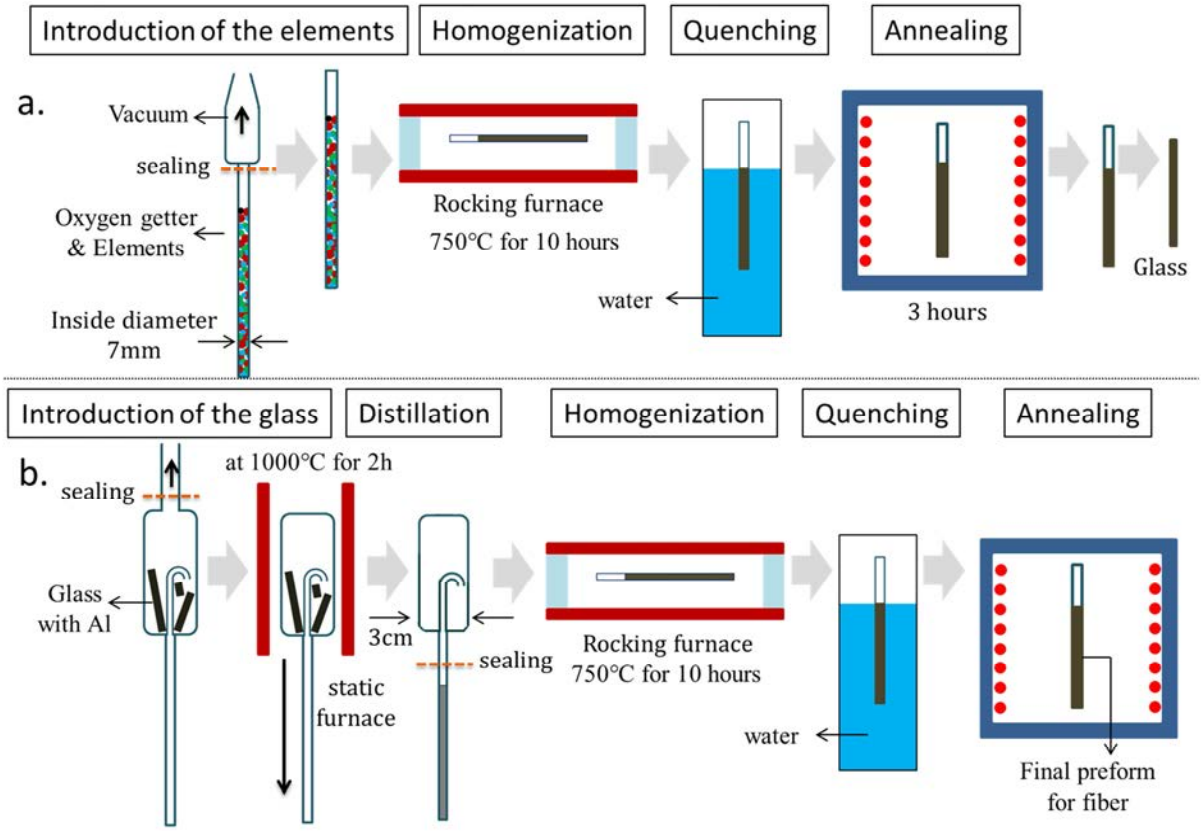

Figure 1.9 Schematic diagram of two-steps purification procedure of Te-Ge-Se glasses: chemical purification (a.) and distillation (b.)

1.3.5 Characterization of bulk glass

1.3.5.1 Elemental Analysis of TGS Glass by EDS

Energy-Dispersive X-ray Spectroscopy (EDS) is a qualitative and quantitative X-ray micro-analytical technique that can provide information on the chemical composition of a sample for elements with atomic number (Z) >3. The incident beam injects an electron in an inner shell and create an electron hole in the orbital, resulting in a high-energy unstable configuration for the atom. An electron from an outer, higher-energy orbital then fills the hole, and the excess energy is emitted in the form of characteristic X-ray. The number and energy of the characteristic X-rays emitted from a specimen can be measured by an energy-dispersive spectrometer, which allows measuring the elemental composition of the specimen. The schematic principle diagram and a typical EDS spectrum (Jeol JSM 7000F, Oxford Instruments) of a TGS glass are shown in Figure 1.10. The measurement accuracy is ±1%.

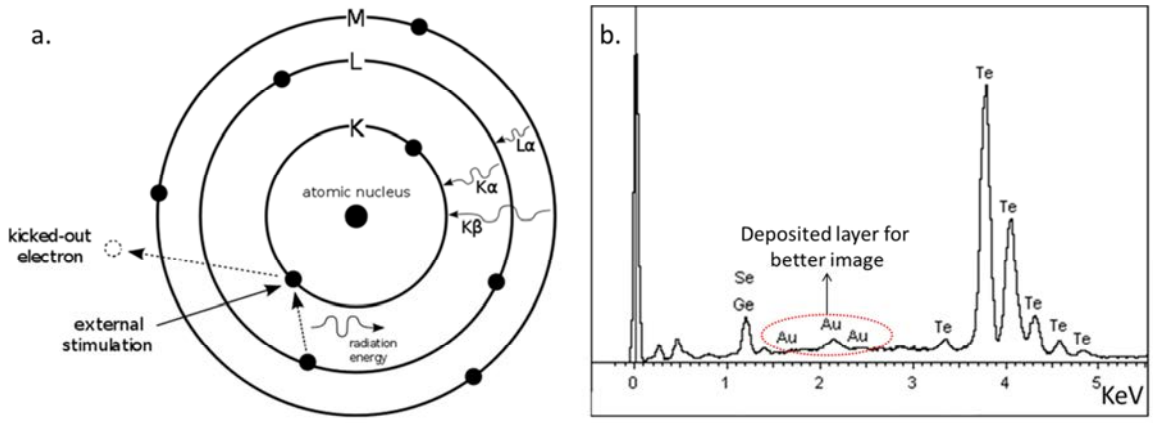

Figure 1.10 The schematic principle diagram of EDS (a) and a typical TGS glass EDS spectrum (b).

For the glass preform preparation, it should be emphasized here that the final configuration of the optical fiber requires a control of the composition of the glasses during the synthesis. During the purification steps, a compromise must be found between efficient purification and conservation of the stoichiometry of the glass. By EDS, the actual composition of two-steps purified TGS3 glass is confirmed to be $Ge_{20.1}Te_{76.6}Se_{3.3}$, which is consistent with the initial composition.

1.3.5.2 Thermal stability of glasses using different purification methods

Differential scanning calorimetry (DSC) is a thermo analytical technique for which the difference in the amount of heat required to increase the temperature of a sample and a reference is measured as a function of temperature. Any phase change, chemical reaction or transformation of the sample is accompanied by a thermal change and can be detected and analyzed by this technique. In the glass science field, DSC is a well-known technique to determine the glass transition temperature (T_g), crystallization temperature (T_x), and melting point (T_m). T_g is characterized by an endothermic gap of the baseline corresponding to a C_p jump, crystallization results in an exothermic phenomenon whereas the melting gives rise to an endothermic peak (Figure 1.11 a).

Thermal analysis of the TGS3 glasses prepared with one or two-step purification methods were achieved by TA Instruments Auto Q20. The aim is to check the thermal stability of the samples (Figure 1.11 b). The DSC were performed under an argon flow at a heating rate of 10°C/min from 50°C to 310°C.

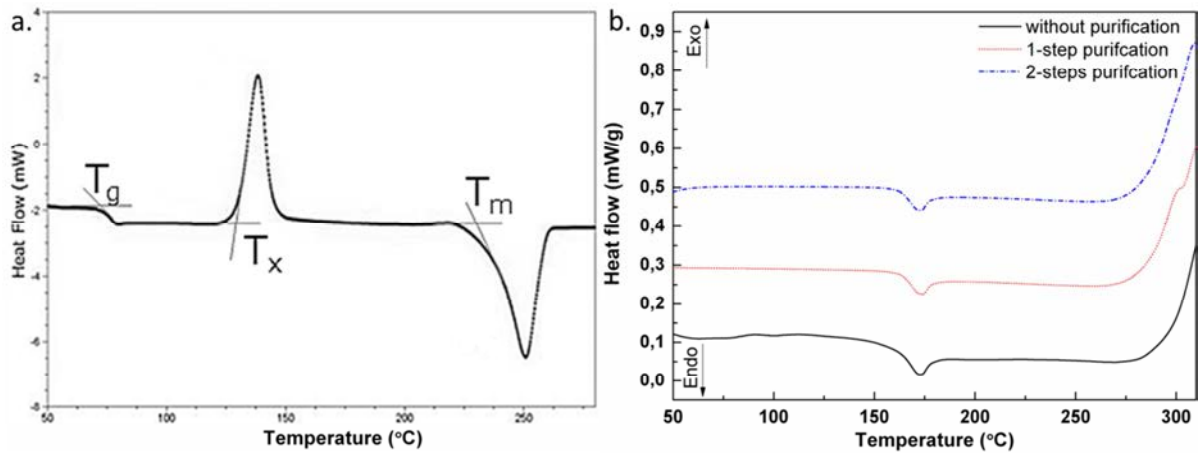

Figure 1.11 DSC curves of a typical glassy state material (a) and TGS3 glasses prepared without and with one-step and two-steps purification methods (b)

The both glasses show similar T_g and T_x values. The temperature difference ΔT is larger than 120°C. This signifies that the different purification steps do not alter the thermal stability of the final glass and the glass is stable enough for fiber drawing. Nevertheless, at this stage, it is still too early to choose the better purification procedure.

1.3.5.3 Optical transmittance

In optics and spectroscopy, transmittance is the fraction of incident light at a specified wavelength transmitted through a sample. The principle of infrared transmission measurement is based on the comparison of the optical signal detected before (I_o) and after (I_t) passing through the sample. The transmittance is given as a percentage, and can be defined as:

$$T(\%) = 100 \times \frac{I_t}{I_o} \quad \textbf{(1.2)}$$

A glass transmission spectrum is obtained when the measurement is performed over a wide range of wavelengths. By analyzing the peaks shown in the spectrum, the chemical bond absorbing the light can be identified. As shown in Figure 1.12a, the reflection of the beam at each interface is not negligible if refractive index difference between two different media is high. To give account of the Fresnel losses, the equation 1.3 has to be considered when incident light is perpendicular to the surface of the sample.

$$R = \left|\frac{n_1 - n_2}{n_1 + n_2}\right|^2 \quad \textbf{(1.3)}$$

where, R is reflection coefficient; n_1 and n_2 are refractive indices of the two contact media.

Note that reflection by a glass comes from the front side as well as the back side, and that some of the light bounces back and forth a number of times between the two sides. The combined reflection coefficient (R_c) for this case is shown in Eq. (1.4), when interference can be neglected.

$$R_c = \frac{2R}{(1+R)} \tag{1.4}$$

For tellurium based glasses, R_c is calculated to be around 40% according to the refractive indices of air (1.003) and the glass (>3). The influence of Fresnel reflection on the transmission spectrum of glasses with different refractive indices is shown in Figure 1.12 b.

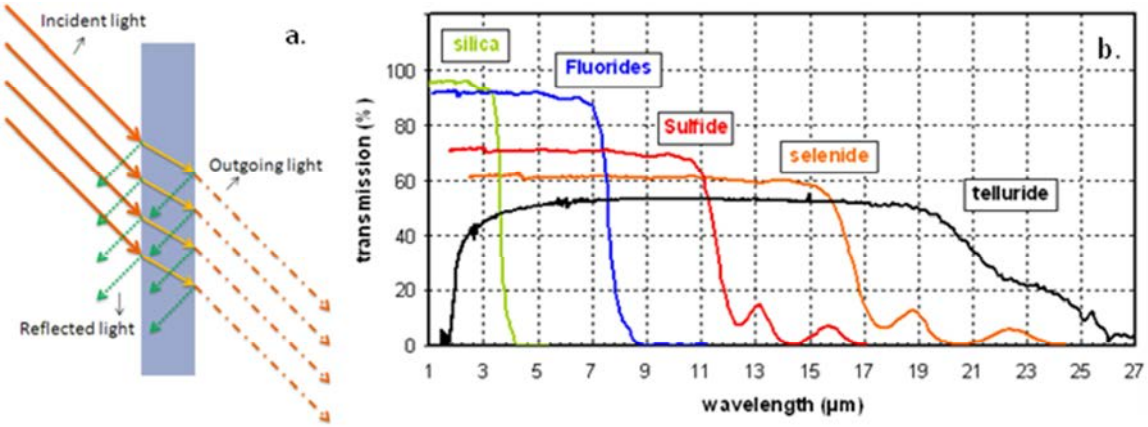

Figure 1.12 The scheme of Fresnel reflection (a.) and the typical transmission spectrum of glasses with different refractive indices (b.)

For all glasses, the transmission limit at short wavelengths is due to electronic transitions from valence band to conduction band. The cut-off at large wavelengths (multi-phonon absorption) is the result of fundamental vibrations of chemical bonds constituting the glassy network. The vibration frequency (υ) for a diatomic molecule AB is expressed as follows,

$$\upsilon = \frac{1}{2\pi} * \sqrt{\frac{\kappa}{\mu}} \tag{1.5}$$

where $\mu = \frac{m_A m_B}{m_A + m_B}$ is the reduced mass, k is force constant, m_A and m_B are atomic masses.

As a result, a glass based on heavier atoms exhibits smaller vibration frequencies. Therefore, telluride glass show a wider transmission window extended to far infrared region compared to sulfide and selenide glasses (Figure 1.12 b).

In order to check the multi-phonon cut-off wavelength of the TGS3 glass, the infrared transmittance was measured using an optical polished glass disk with thickness around 1.0 mm. In Figure 1.13, optical transmittance spectra of bulk glasses before and after two-

steps purification are compared. This comparison demonstrates the benefit of the two-step purification procedure.

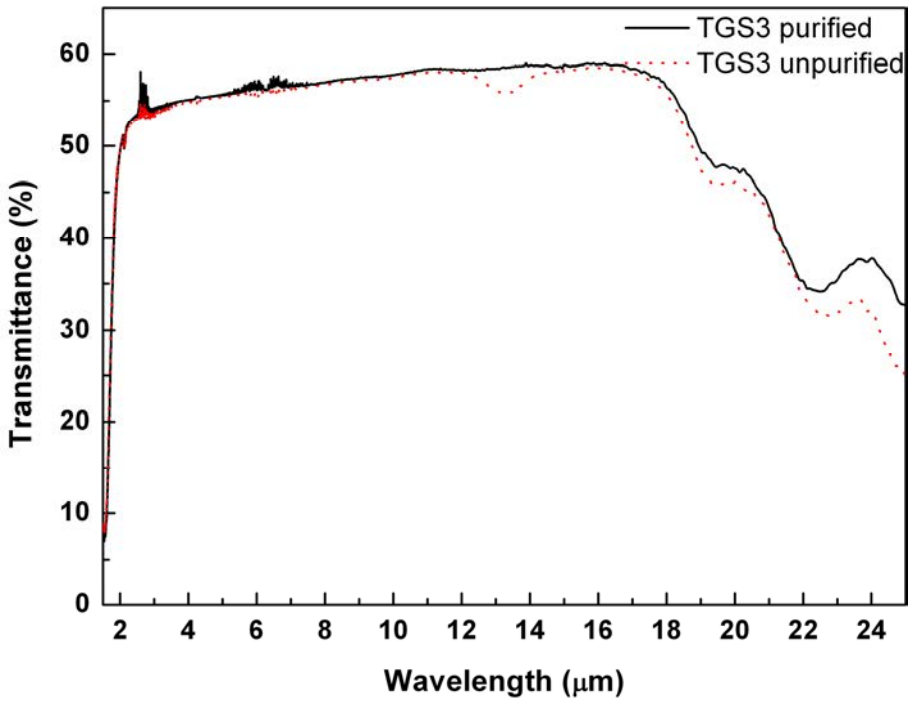

Figure 1.13 Infrared transmittance of TGS3 glasses without purification (red dotted line) and with two-steps purification (black line).

In particular, it can be observed that after this purification, the Ge-O absorption broad band at 13 μm has been totally removed. Also, purified TGS3 glass shows a very flat transmission window from 3 μm up to 18 μm. The absorption shoulders at 19 μm and 22 μm are caused by Ge-Se and Ge-Te vibration respectively.

1.4 Single index fiber preparation and characterization

1.4.1 Fiber drawing principle and process

The fabrication of the fibers was carried out under a helium controlled atmosphere thanks to a home-made fiber tower. The photograph of the fiber drawing tower and schematic diagram of fiber drawing process are shown in Figure 1.14.

To prepare a chalcogenide optical fiber, the glass preform is settled vertically in the ring furnace chamber. To avoid the presence of H_2O and O_2 in atmosphere, the chamber should be purged under a flow of argon at 3 L/min for at least 2 hours. Before drawing fiber, the gas flow needs to be converted into He (3 L/min) for a better thermal conductivity. Two successive sweeps at 120°C are operated to remove the last traces of moisture present on the

surface of the preform. Then glass is then heated to its softening point and the first glass drop is generated by the effect of its own weight. Then the fiber is stretched and fixed on the drum. Once the fiber is fixed, by changing the processing parameters such as preform descent speed (V_p) and drum rotation speed (V_d), fibers with various diameters can be prepared in the range 500 to 40 μm typically.

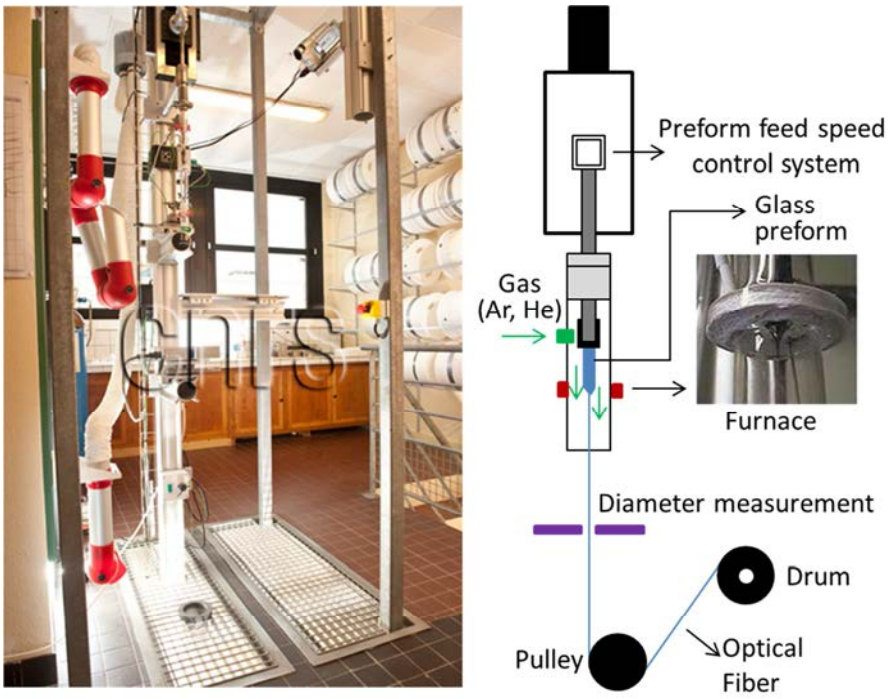

Figure 1.14 The photograph of fiber drawing tower (left) and schematic diagram of fiber drawing process (right).

Basically, V_p and V_d can be determined from a simple principle, the volumes of glass preform and of the obtained fiber remaining equal:

$$\frac{\pi \emptyset_p^2}{4} V_p = \frac{\pi \emptyset_f^2}{4} V_d \quad \textbf{(1.6)}$$

Here, $\emptyset_p$ and $\emptyset_f$ are the diameters of the preform and the fiber respectively. Typically, V_p is several millimeters per minute. In the process of fiber drawing, by fixing V_p and adjusting V_d ($0.1 \sim 10 m/min$), one can easily control the fiber diameter.

Optical fibers have been drawn from glass preforms prepared using one or two steps of purification as described above. The final diameter of the fiber was controlled to be 440 μm. The typical fiber drawing parameters of the TGS glasses are listed in Table 1.3.

Table 1.3 Typical parameters for TGS glass fiber drawing

Parameters before fiber drawing			
Preform diamter :	7.0 mm		
Flow of argon :	3 L/min	Flow time :	2 hours
Parameters during fiber drawing			
Helium flow (<200°C) :	3 L/min	Water elimination temp.	120 °C
Helium flow (>200°C) :	2.5 L/min	Fiber drawing temp.	265 °C
Preform speed :	2 mm/min	Speed of drum :	0.50 m/min
Tension :	15 grams	Heating rate :	10 °C/min
Fiber diameter :	440 µm		

The glass preform, first drop and single index fiber are shown in Figure 1.15. After drawing, fiber surface remains shiny and shows no visible crystallization.

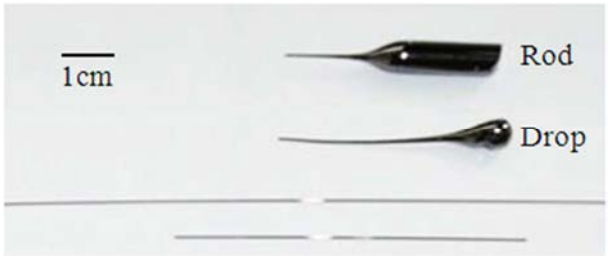

Figure 1.15 Photograph of TGS3 fiber and preform after drawing

1.4.2 Fiber optical properties characterization

When light propagates in an optical fiber, a part of the optical energy is lost by interaction with the glassy material. As the light transmits much longer in fiber than in a bulk glass disc, the losses are much higher at the output of the optical fiber. The measurement of the optical losses is essential to characterize the optical behavior of the fibers. Empirical research has shown that the power losses in an optical fiber are caused primarily by both scattering and absorption. Indeed, beside intrinsic absorption loss, the impurities such as hydroxyl group and oxides can induce extra light losses in a fiber at some wavelengths. Therefore, due to the high sensitivity of optical fibers to the presence of any impurity, optical attenuation measurement is the most efficient method to evaluate the glass quality after purification.

1.4.2.1 Cutback technique

The cutback method is the most common way to measure the attenuation (Fig.I.18). The method consists in comparing the output powers of different fiber lengths by cutting the fiber step by step. On this basis, the fiber attenuation coefficient (α) can be calculated from

$$\alpha = \frac{10}{L_1 - L_2} \lg \frac{I_2}{I_1} \quad \textbf{(1.7)}$$

where L_1 and L_2 represent the fiber lengths before and after cut, I_1 and I_2 represent the output powers before and after cut respectively.

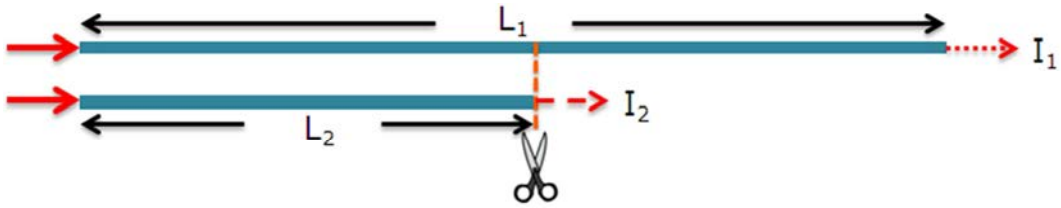

Figure 1.16 Schematic diagram of cutback method for fiber attenuation test.

1.4.2.2 Optical losses of fibers after 1-step and 2-steps purification processes

The optical losses were measured thanks to a Bruker Vector 27 FT-IR Spectrometer and the output signal of the fiber is focused on a mercury cadmium telluride (MCT) detector cooled by liquid nitrogen. The optical losses of TGS3 fibers with one and two-steps purifications were calculated from Equation (1.7) and compared in the Figure 1.17.

Clearly, with the two-steps purification methods, the minimum of optical attenuation has been significantly decreased from 11.5dB/m to 6.5dB/m at around 10.5 μm. This value is almost the limitation for a telluride glass fiber due to large quantity of free electrons at room temperature inherent to the semi-conducting behavior of the tellurium. Combined with previous DSC results, it can be drawn that by using two-steps purification, glass stability could be well maintained and the optical loss of single index fiber could be greatly decreased.

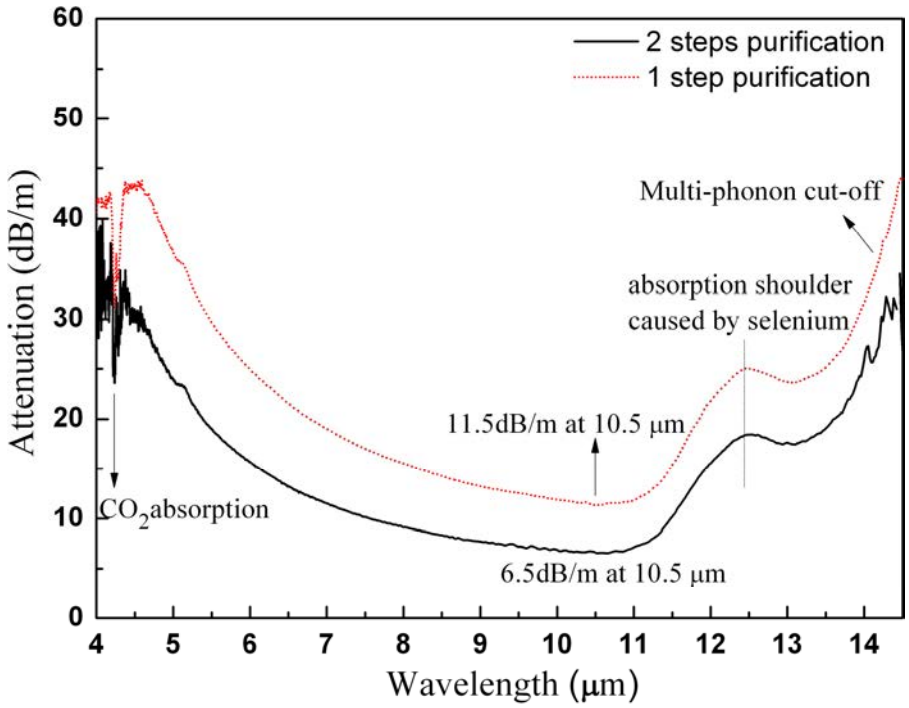

Figure 1.17 Optical losses of single index TGS3 fibers obtained from the preform using one-step and two-steps purification methods.

On the other hand, compared to Se-based glass fiber (Figure 1.4), this Te-based glass fiber shows a transmission extending further in the mid-infrared up to 14.5 μm. By adding Se, which is a famous glass network former, the TGS3 glass stability is greatly enhanced compared to $GeTe_4$ glass. However, as a lighter element, the presence of Se induces an obvious absorption shoulder around 12.5 μm. Other intrinsic absorptions, such as phonon cut-off, are caused by the glasses constituent elements and cannot be eliminated.

1.5 Double index fiber preparation and characterization

1.5.1 Fiber design for single-mode and multi-mode propagation

Light propagation in double index fiber

Optical fibers are widely used in fiber-optic communications, illumination and other applications including sensors and fiber lasers. Most often, an optical fiber is composed of a core, a cladding and generally a protective coating. There are two types of optical fiber: multimode and single-mode. The core diameter of a multimode fiber is generally larger than for a single-mode fiber, making the light to have several propagation modes. Multimode fibers can be classified into graded-index and step-index, depending on the reflection index distribution between the core and the clad. On graded-index fiber, the change is gradual, while on step-index fiber, the change is abrupt. For both the two kinds of multimode fibers, the light transfer routes are different between low-order and high-order mode, generating dispersion. For single-mode fiber, as the light has only one way of travelling inside the fiber core, dispersion is really limited. The typical fiber structures and light propagation behavior are shown in Figure 1.18.

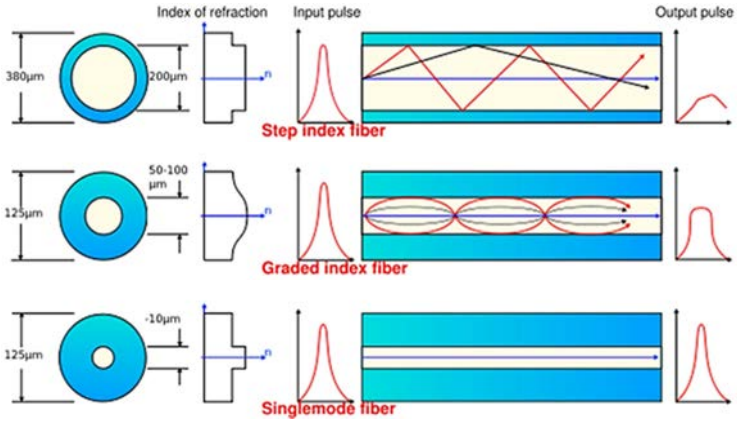

Figure 1.18 Differences among graded-index multimode, step-index multimode and single-mode optical fibers.

The design principles of single-mode fiber

For the single-mode propagation, the normalized frequency V of the fiber should be less than 2.405. In this case, only one mode called fundamental mode can propagate. Indeed, the value 2.405 is the first zero of the Bessel function $J_0(u)$. In practice, the V value of a specific fiber can be calculated from

$$V = \frac{\pi d_{core}}{\lambda} NA \quad \textbf{(1.8)}$$

where d_{core} is the core diameter, λ is the wavelength of the light passing through the fiber core. NA is the abbreviation of numerical aperture and can be calculated from the refractive index of core n_{core} and clad n_{clad}.

$$NA = \sqrt{n_{core}^2 - n_{clad}^2} \quad \textbf{(1.9)}$$

For chalcogenide double index fiber, considering the complexity of double index fiber preparation and the composition control of both core and clad, the commonly used parameters to design single-mode fiber are listed in Table 1.4.

Table 1.4 Commonly used parameters of telluride single-mode fiber

NA	$\Delta n\ (n_{core} - n_{clad})$	d_{core}
0.4~0.2	8.0×10^{-3}~1.5×10^{-3}	20~40 μm

Fiber composition design for single-mode and multimode propagation

The most common type of single mode fiber has a core diameter much smaller than multimode fibers and is designed for use in the near infrared from silica glass. In order to design step-index multimode and single-mode fiber the refractive indexes of the glass have to be known. Thus, the evolution of the refractive index of the TGS glasses versus the ratio Se/Te was measured from the optical transmission property of the glass (Figure 1.19 a). It is the easiest method to evaluate the refractive indexes, but the accuracy is no more than 10^{-3}.

It is clear that by substituting Te by Se, the refractive index of the glass can be modified in a controlled way. By linear fitting the refractive index at 10 μm (Figure 1.19 b), glass refractive index evolution with Se can be expressed by

$$n_{glass} = -0.0137 c_{Se} + 3.4216 \quad \textbf{(1.10)}$$

Based on this, the glass refractive index n_{glass} can be directly calculated using the concentration of selenium c_{Se} (%). On the basis of this finding, $Te_{76}Ge_{21}Se_3$ and

$Te_{75.5}Ge_{21}Se_{3.5}$ (TGS3.5) compositions were selected as the core and clad compositions of the single-mode fiber. Indeed, n_{glass} are estimated to be 3.380 and 3.374 respectively. When the core diameter is around 25 μm, the wavelength threshold value is calculated to be around 7 μm using Eq. (1.8) and (1.9). When the operating wavelength is larger than 7 μm, the TGS3/TGS3.5 step index fiber is single-mode fiber.

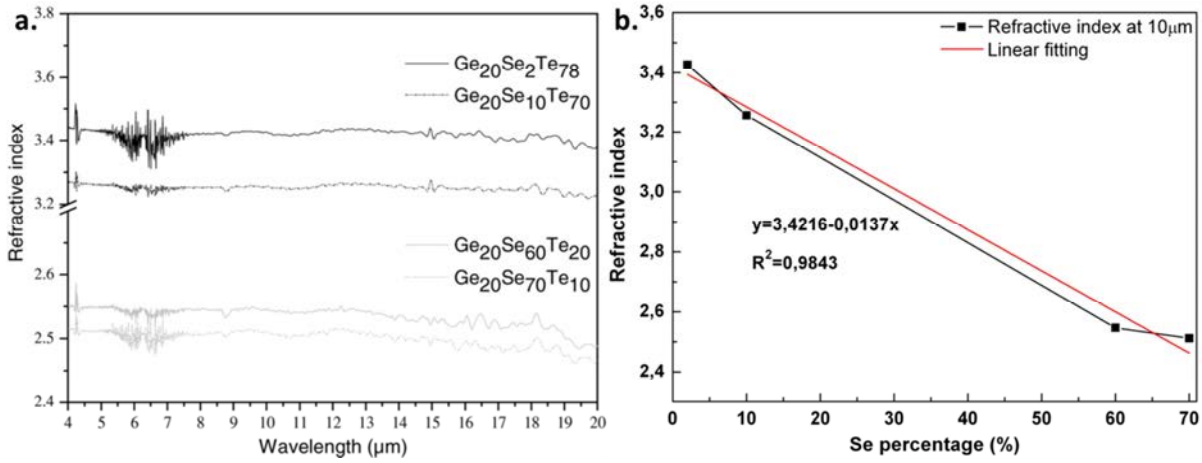

Figure 1.19 Refractive index evolution of Te-Ge-Se glasses versus Se/Te ratio[23]

For step-index multimode fibers, the compositions selected to manufacture the core and clad are TGS3 and TGS8 respectively, ensuring a Δn between core and clad equal to 0.07 in the working wavelength range. This quite large Δn was chosen on purpose in order to be sure that this multimode step index fiber will properly guide infrared light. Recently, TGS3/TGS8 multimode fiber with a large core (200 μm) has been successfully prepared[23]. Here, the core and clad diameters used for single mode propagation were also used to prepare the multimode fiber. Nevertheless, the ultimate goal is to design a single-mode optical fiber.

1.5.2 Capillary method introduction

1.5.2.1 Drawing backs of rod-in-tube method

Due to the high crystallization tendency of Te-based glasses, the key step for double index fiber is the successful production of preform without crystallization. For selenide glass, the common method used to design double index fiber is the so-called "rod in tube" technique. It requires several steps, including draw of the rod, and preparation of the tube by rotational casting, and draw of the preform with rod inside the tube. Depending on the desired final dimensions, the second and third steps can be repeated several times. However, as "rod in tube" technique asks for several times of casting and drawing process in order to get the desired core diameter (Figure 1.20 a) for single mode propagation, it is not suitable for the

glass having a high tendency to crystallize. From a previous study, it has been shown that after the casting process, crystals will appear on the surface of telluride glass (Figure 1.20 b). Hence, a new technique needs to be developed to decrease the tendency of crystallization during preform preparation and fiber drawing proceeds for Te-based glasses.

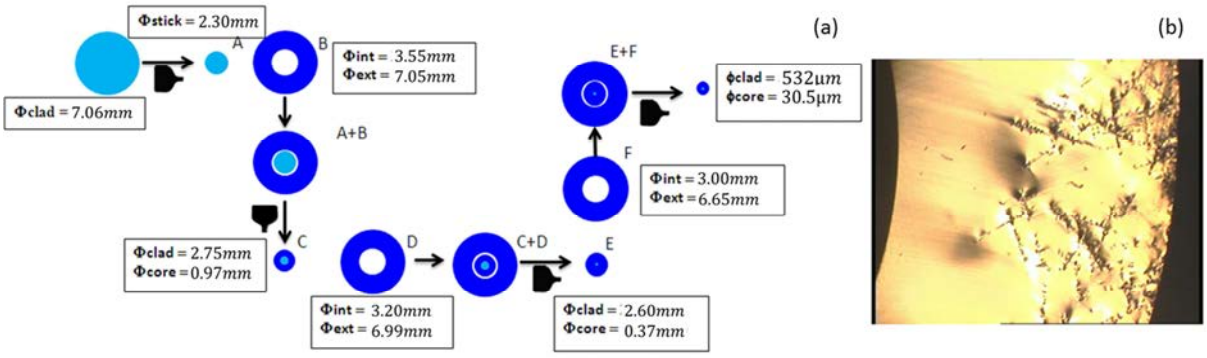

Figure 1.20 Schematic diagram of rod-in-tube method (a) and Optical microscope image of Te-based glass after casting (b)

1.5.2.2 Strategy of capillary method

Capillary method, which has been developed for the fabrication of microstructured optical fibers[41], comes into our sight. A microstructure fiber which can guide light similar to double index fiber is drawn from a preform constituted by a series of hexagonal capillaries. An array of silica capillaries are used to mold the chalcogenide glass and are removed by hydrofluoric acid (HF) before fiber drawing.

For the preparation of the double index fiber, a modified capillary method is applied (Figure 1.21). A cylindrical glass set-up with only one silica capillary in the center was used to mold melted telluride glass. After quenching and annealing, the glass preform for clad was immersed in HF for 30 minutes to remove the silica capillary, and then thoroughly cleaned in deionized water. The fiber, drawn from a glass with a higher refractive index, was then introduced in the capillary and drawn again together with the jacket tube to prepare double index fiber.

By using this method, one step is enough to get the preform for double index fiber. Compared to traditional rod-in-tube method, this new technique prevents from drawing the rod several times and minimizes the crystallization tendency. Thanks to this method, the fibers with their core and clad compositions to be TGS3/TGS8 and TGS3/TGS3.5 respectively were successfully drawn.

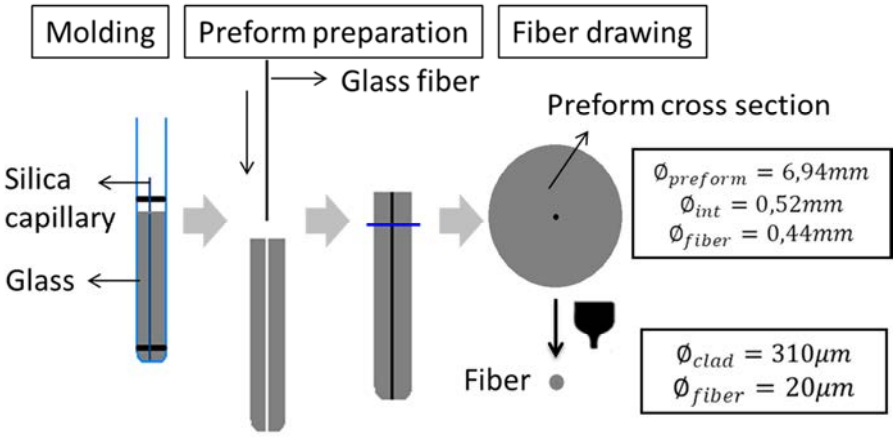

Figure 1.21 Capillary method for the fabrication of double index fiber.

1.5.2.3 Feasibility study of the capillary method

Capillary morphology controlling

The preparation of high-quality double index fiber strongly depends on the the quality of the preform. Therefore, the morphology of the silica capillary used for preform molding, such as its straightness and the shape of its cross section, should be checked. The silica capillary surface quality and its cross-section shape can be seen in Figure 1.22.

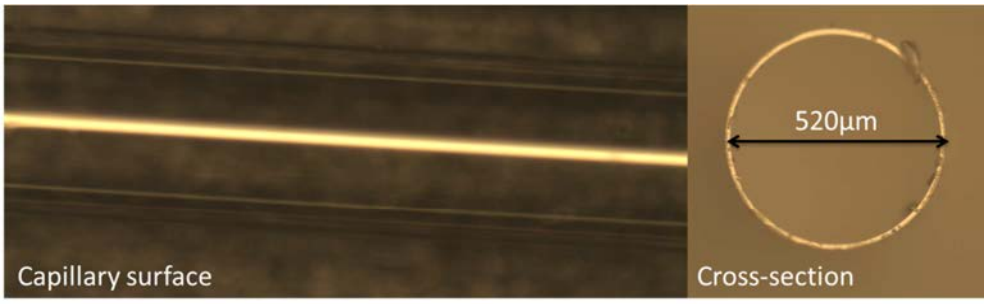

Figure 1.22 Optical microscope images of silica capillary surface and cross-section

After repeated observations, it can be concluded that the capillary used in the molding experiment shows a perfect cylindrical shape and a circular cross section. The capillary diameter is precisely to be 520 µm. In addition, the capillary surface is shiny without visible defects.

Influence of hydrofluoric acid on glass surface

In the industrial field, hydrogen fluoride (HF) is used commonly to etch silicon dioxide. In this study, HF is also used to remove the silica capillary by immersing the molded telluride

glass preform inside the hydrofluoric acid for 30 minutes. The reaction between HF and SiO_2 can be described as

$$4HF + SiO_2 = SiF_4 + 2H_2O \quad \textbf{(1.11)}$$

As an acid with a strong causticity, the effect of HF on chalcogenide glass needs to be studied to confirm that the etching process would not induce corrosion and other surface defects. Optical transmittance measurement is an effective method. TGS8 glass, as a clad composition for multimode fiber preparation, is cut and optical polished. The infrared transmittance spectra of glass disk after immersion in hydrofluoric acid for different time were tested and shown in Figure 1.23.

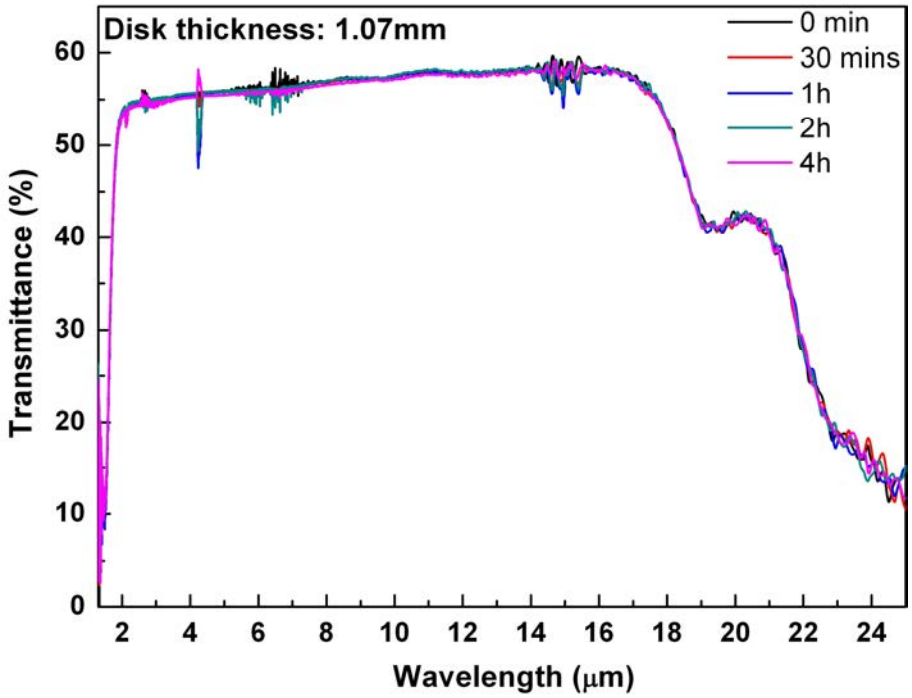

Figure 1.23 Infrared transmittance spectra of optical polished TGS8 glass disks before and after immersion in hydrofluoric acid for different time.

It can be seen that after contact with HF up to 4 hours, the transmittance spectra are exactly the same. The cut-on wavelength and the transmittance value at shorter wavelength, which are sensitive to micro scale defects, show no variation. This indicates that the TGS glasses are stable in HF acid.

To confirm our conclusion, optical microscope photos of glass surface after different reaction time with HF are also shown in Figure 1.24. The results also show that HF would not corrode the surface of chalcogenide glass when the contact time is limited (less than 4 hours).

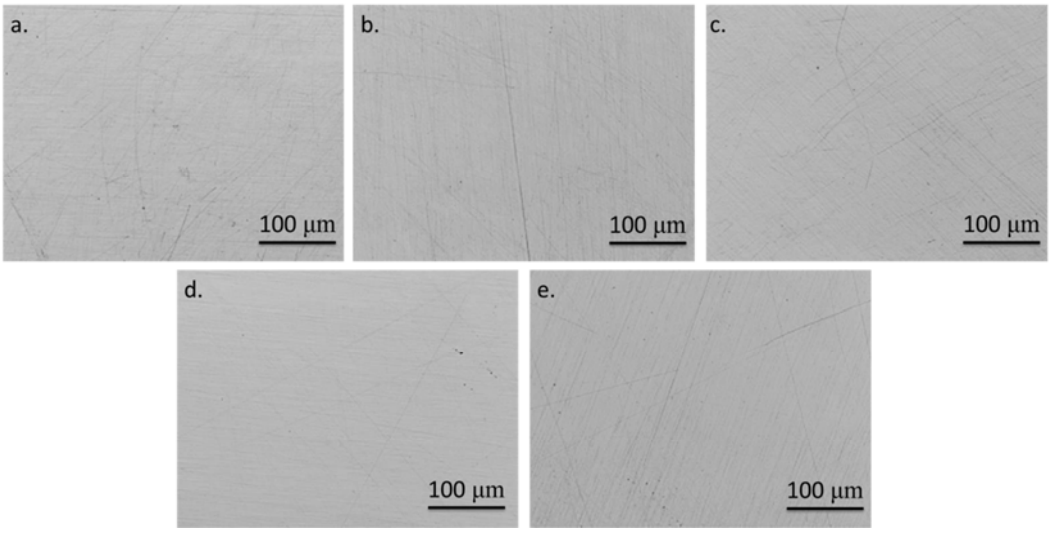

Figure 1.24 Optical microscope images of TGS8 glass disks reacted with HF for 0 minute (a), 30 minutes (b), 1 hour (c), 2 hours (d), and 4 hours (e).

1.5.3 Multimode TGS3/TGS8 fiber investigation

As explained above, to carry out the Darwin project, it is necessary to develop a single mode optical fiber transmitting signal beyond 12 µm. TGS glasses with a few percentage of Se, due to its proper thermal stability (ΔT=120°C) and the simplicity of refractive index adjustment, are good candidates. Due to a better stability of TGS8 caused by a higher proportion of selenium, TGS3 and TGS8 are chosen as core and clad compositions respectively to evaluate the suitability of the novel capillary method for single-mode optical fiber preparation.

1.5.3.1 Double index fiber preparation

To prepare a preform for double index fiber, a TGS3 fresh fiber (450µm) should be thread into the hole (520µm) of the TGS8 preform. Pictures of the TGS3/TGS8 preform obtained are presented in Figure 1.25. To avoid trace amounts of water molecules at the glass surface, beside an argon purge of the chamber, it is also essential to introduce a small flow of He between TGS3.5 fiber and TGS3 preform. After two hours of purging, the double index fiber with its core and clad to be 20µm and 310µm respectively was obtained by drawing the two-glass preform.

During the fiber drawing process, the parameters, such as furnace temperature and helium flow, were kept exactly the same as for the preparation of TGS3 single-index fiber. Spaces between fiber and preform were eliminated upon drawing thanks to a vacuum system.

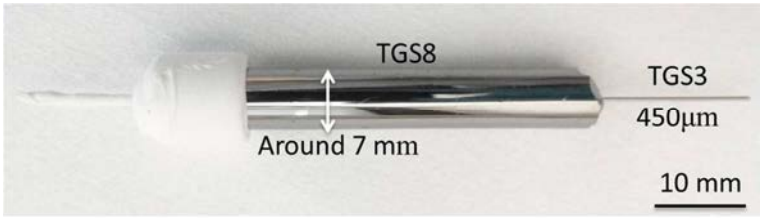

Figure 1.25 Photograph of TGS3/TGS8 preform ready for drawing.

1.5.3.2 Losses of TGS3/TGS8 optical fiber

The optical loss of TGS3/TGS8 fiber was measured using the cut-back method. However, to obtain the optical losses precisely at high attenuation regions, the fiber should be quite short so as to get enough optical signals for attenuation calculation. Therefore, the precise attenuation curve of the TGS3/TGS8 double index fiber was tested by cutting the fiber of different lengths: longer for low attenuation region and shorter for high attenuation region. The combined attenuation curve is shown in Figure 1.26. The attenuation curve of TGS3 single index fiber, which is used as the core of this double index fiber, is also displayed for comparison. The fiber lengths before and after cutting are listed in Table 1.5.

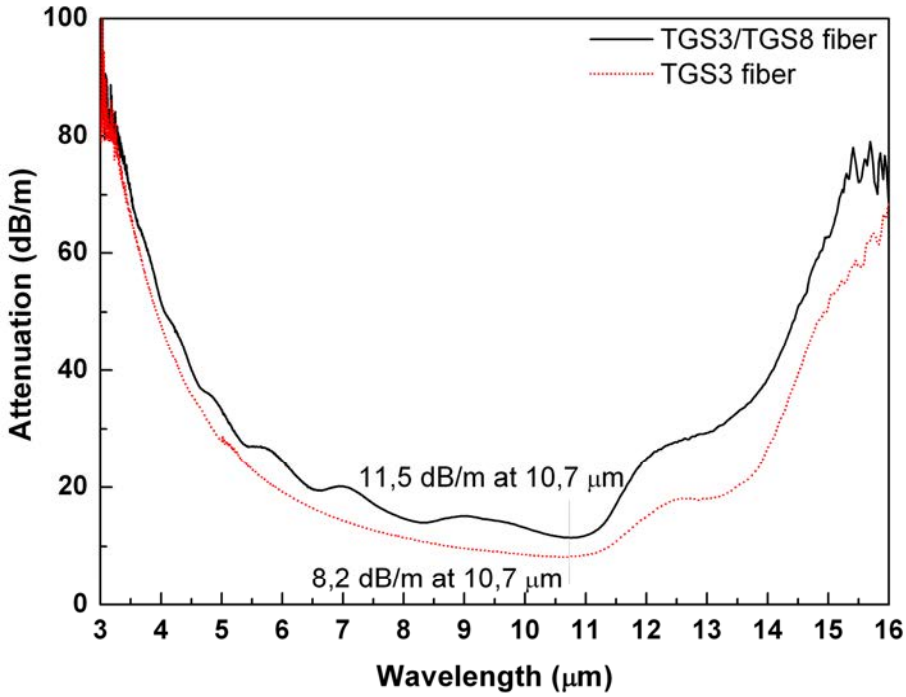

Figure 1.26 Optical loss of TGS3/TGS8 double index fiber.

Table 1.5 The length details of TGS3 and TGS3/TGS8 fibers used for cutback method

Fiber type	Fiber length details for cutback method		
	<5 µm	5-13 µm	>13µm
TGS3/TGS8	35-19 cm	80-35 cm	35-19 cm
TGS3	38-20 cm	121-38 cm	38-20 cm

This double index Te-based glass fiber shows a large signal transmission region up to 16 μm. This is much broader than for selenide glass fibers which stop transmitting signal beyond 12 μm for the best of them. Compared with the optical attenuation value (8.2 dB/m at 10.7 μm) of TGS3 single index fiber, TGS3/TGS8 double index fiber shows stronger optical loss (11.5 dB/m at 10.7 μm). Meanwhile, a series of broad band absorption peaks between 3 and 11 μm are observed. The potential explanation could be the light scattering caused by defects between the core and clad during the light reflection process.

1.5.3.3 Composition distribution study of TGS3/TGS8 fiber cross-section

According to previous experience in the preparation of all solid microstructured fiber by using capillary method, inappropriate fiber drawing parameters may cause:

a) A composition diffusion between core and clad.
b) A cross-sectional shape change of the core.
c) A space between core and clad.

For TGS3/TGS8 double index fiber, due to the large refractive indices difference, the interface between core and clad can be clearly observed using both optical microscope and scanning electron microscope (Figure 1.27). After fiber drawing, the core kept a regular circle shape and the space between TGS3 fiber and TGS8 preform was totally eliminated. As a result, all the fiber drawing parameters, such as temperature and vacuum between core and clad, were confirmed to be proper. Nevertheless, defects at the interface can be observed, confirming our previous prediction from the extra absorption peaks in attenuation curve.

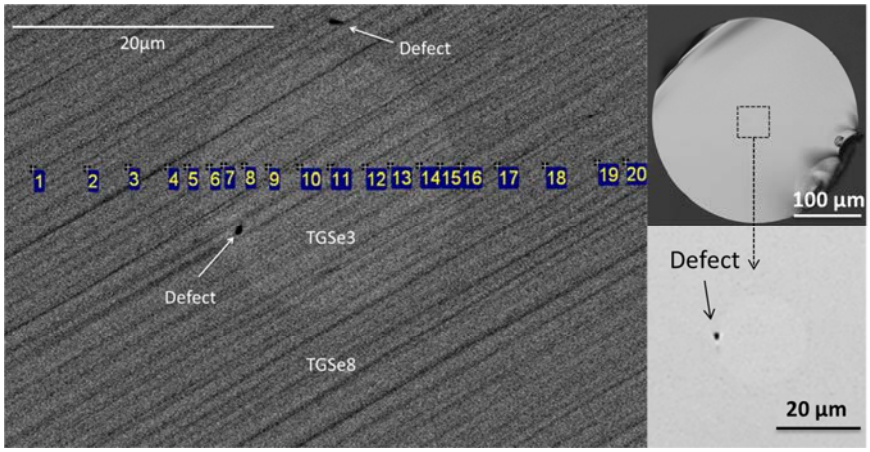

Figure 1.27 Electron microscopy (left) and optical microscopy (right) images of TGS3/TGS8 fiber cross section.

To investigate the composition distribution, EDS of 20 points along a straight line through the center of the core were implemented. The actual composition evolution and the theoretical values (dotted line) are compared in Figure 1.28.

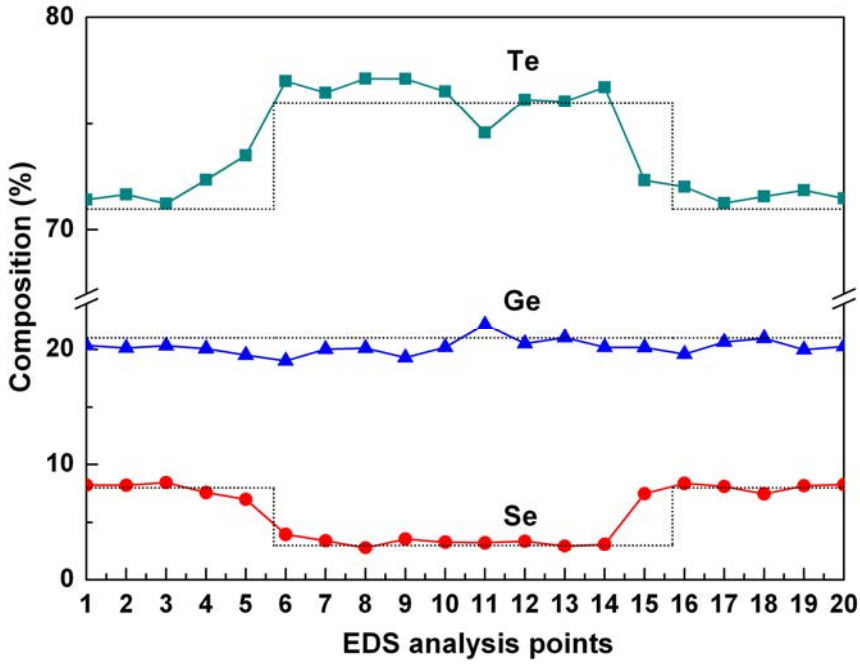

Figure 1.28 Real and theoretical (dotted line) composition distributions comparison of TGS3/TGS8 fiber cross section.

The actual and the theoretical values are in good agreement. As expected, the glass composition shows a significant change at the interface between the core and the clad. The fluctuations along the line are due to the accuracy of the EDS measurement (~1%).

1.5.3.4 Propagation characteristics of the TGS3/TGS8 fiber

To control the propagation of light in the core of the prepared TGS3/TGS8 double index fiber, a coherent light source should be used. The principle of the measurement consists in the injection of an infrared interference light at 10.3 μm emitted by a tunable CO_2 laser. The infrared light was focused and injected into the fiber core with the help of ZnSe lens. The signal at the output of the fiber was observed with a camera (FLIR ThermaCAM E300) equipped with an infrared detector operating in the 7 to13 μm range at room temperature. A germanium lens is placed near the output of the fiber in order to ensure a focalization on the camera sensor (Figure 1.29).

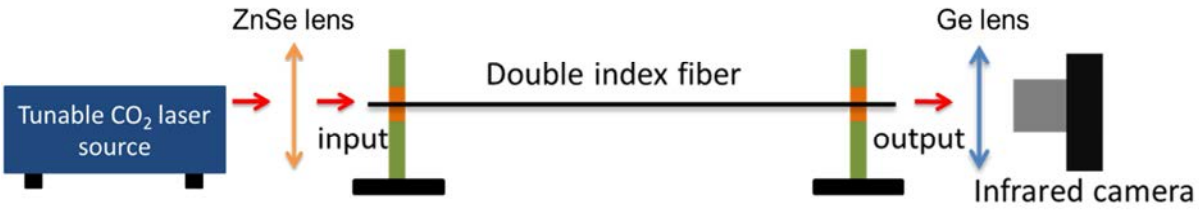

Figure 1.29 Set-up used for the control of the propagation in a TGS3.5/TGS3 double index fiber

The total fiber length is around 20 cm. In order to remove the cladding modes which are confined in the clad due to its much higher refractive index than the surrounding medium, a liquid GaSn alloy was applied on the fiber external surface. The images of output signal before and after GaSn coating are shown in Figure 1.30.

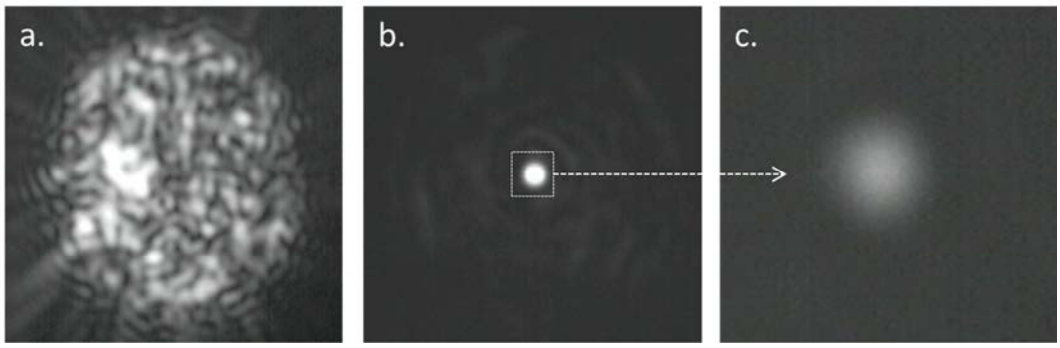

Figure 1.30 The images of output signal before (a.) and after (b. & c.) GeSn coating.

Before the application of Ga-Sn alloy (Figure 1.30 a), a large quantity of light was confined in the clad. During the multiple-path transmission, each mode undergoes a random phase shift. As a result, random interference of the modes in clad occurs, so that the sum of the complex amplitudes of the modes has a random intensity. That is what we have observed in the output image of fiber without Ga-Sn coating.

After removing the confined cladding mode by application of a liquid GaSn alloy (Figure 1.30 b), only the light propagating in the core could be clearly observed. A small amount of light propagating in the clad could also been seen. These confined cladding modes are the diffusion of the light in the core due to the defects at interface.

By taking an enlarged image of the core (Figure 1.30 c), it can be seen that the output light show a regular round shape. This phenomenon is very similar to single-mode propagation, which shows a fundamental mode bell-shaped spatial distribution similar to the Gaussian distribution[42]. The 2D profiles of light distribution in both horizontal (X axis) and vertical (Y axis) direction were studied in Figure 1.31.

Due to the removal of multimodes confined in fiber clad and the image amplification generated by germanium lens, it is quite difficult to monitor the border of fiber cross section. Therefore, the beam width cannot be calculated. In Figure 1.31, Horizontal and vertical axes represent image pixels and light relative intensity respectively, and they themselves have no practical meaning. By fitting, it is clear that the light intensities in both directions follow some Gaussian distributions.

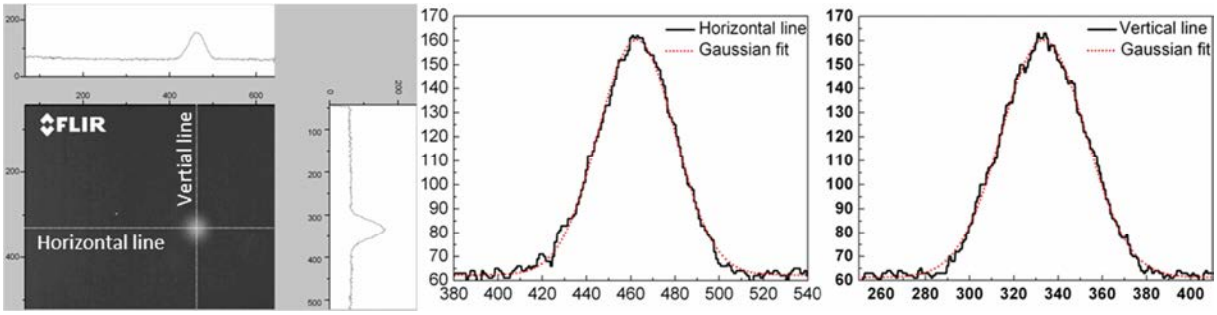

Figure 1.31 2D profiles of light distribution and their Gaussian fit.

For a single-mode fiber, on one hand, the image must be circular. On the other hand, the profile built in 3D from the distribution of observed intensities must follow a Gaussian distribution. To confirm this phenomenon, 3D profile of observed light intensities is studied and shown in Figure 1.32.

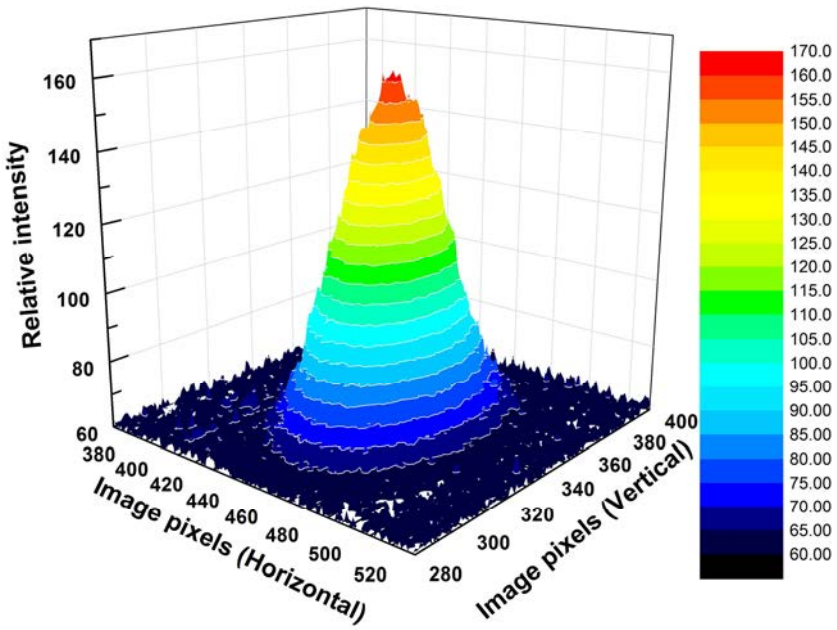

Figure 1.32 3D light distribution in TGS3/TGS8 fiber.

Similar to 2D profile, this 3D profile also follows an obvious Gaussian distribution. Indeed, the light distribution of TGS3/TGS8 fiber is in compliance with the two principles mentioned above. Therefore, although this double index fiber was designed to be a

multimode fiber, it shows an experimental single mode behavior. Indeed, the normalized frequency (V) of TGS3/TGS8 fiber is calculated to be 4.136, which is not so far from 2.405. The exact number of mode cannot be easily calculated, because the equations using V to calculate the mode numbers of multimode fiber are not proper for fibers carrying only a few modes.

1.5.4 A first attempt of single mode TGS3/TGS3.5 preparation

Based on the positive results obtained from TGS3/TGS8 multimode fiber, the first attempt of single mode optical preparation using capillary method was carried out. TGS3 and TGS3.5 are chosen as core and clad compositions respectively.

1.5.4.1 Double index fiber preparation

The preform preparation process and fiber drawing parameters were kept exactly the same as for TGSe3/TGSe8 multimode fiber. The TGS3/TGS3.5 double index optical fiber was successfully prepared with its core and clad to be 20μm and 310μm respectively. Due to the composition similarity of TGS3 and TGS3.5 glasses, the refractive indices of the two are similar. Thus, the interface between core and clad is impossible to be observed by both SEM and optical microscope.

1.5.4.2 Optical fiber losses

To monitor impurities and defects inside the fiber and at the interface between core and clad, optical loss of the TGS3/TGS3.5 double index fiber was measured using the cutback technique (Figure 1.33).

In order to obtain accurate values in both strong and low attenuation region, the optical loss between 5 μm and 13 μm was obtained by cutting the fiber from 124 cm to 35 cm. Meanwhile, the value before 5 μm and beyond 13 μm was calculated from the output signal intensity of fibers with their length to be 35 cm to 19 cm respectively.

Similar to the TGS3/TGS8 multimode fiber, the TGS3/TGS3.5 double-index glass optical fiber also show a broad signal transmission band from 3 μm up to 16 μm (Figure 1.33). Selenium absorption shoulder at around 12.5 μm can also be observed. The minimum attenuation value is 7.5dB/m at 10.5 μm. However, the series of broad band absorption peaks between 3 and 11 μm caused by the defects between the core and clad in TGS3/TGS8 multimode fiber are not visible here.

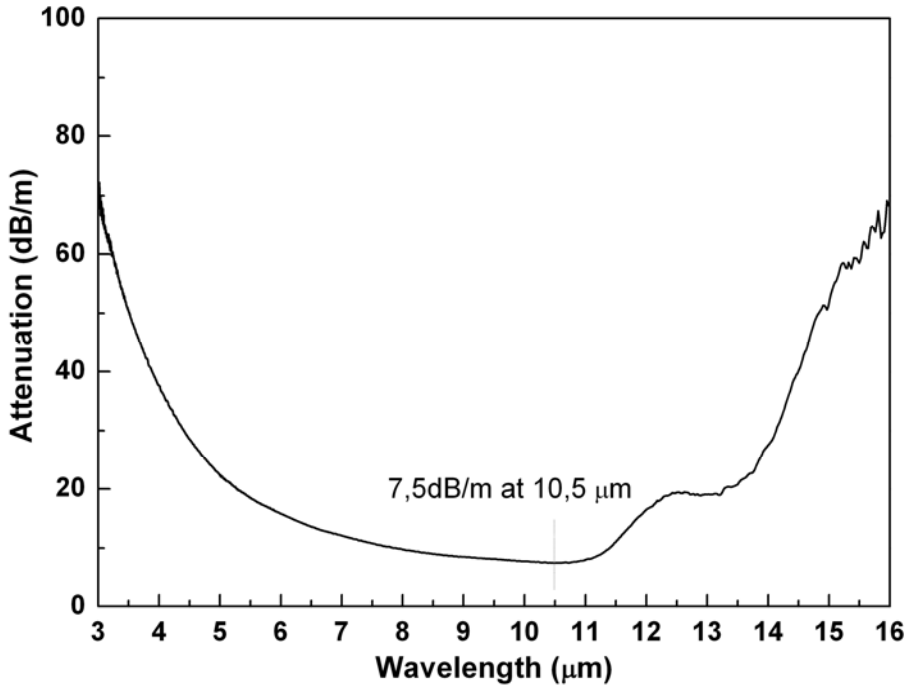

Figure 1.33 Optical loss of TGS3/TGS3.5 double index fiber.

1.5.4.3 Propagation characteristics of the TGS3/TGS3.5 fiber

To characterize the light propagation property of the TGS3/TGS3.5 double index fiber, the tunable CO_2 laser at 10.3 μm was also used. The set-up schematic diagram has already been introduced in Figure 1.29. However, almost no light in the core could be detected. After the application of liquid Ga–Sn alloy on the fiber external surface, all confined light in the clad were totally removed, and no output light could be detected.

To confirm this phenomenon, the fiber optical propagation image was also studied with a Bruker Tensor 27 Fourier Transform Infrared (FTIR) spectrometer and a FLIR ThermaCAM E300 infrared camera. The set-up schematic diagrams are shown in Figure 1.34.

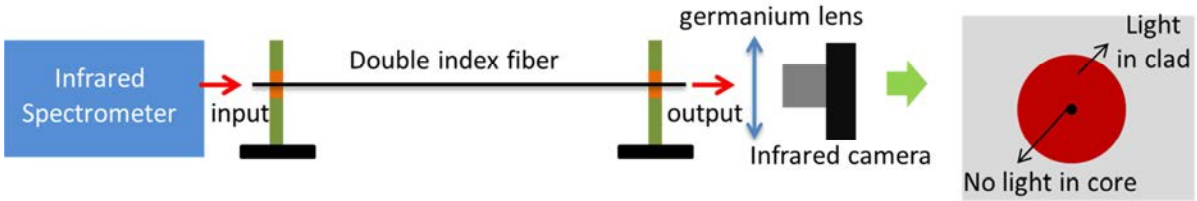

Figure 1.34 Principle of optical propagation measurement of TGS3.5/TGS3 double index fiber using non-coherent light source.

Similarly, at the output of the fiber, no light is detected in the center of the fiber with the infrared camera. Moreover, the diameter of the dark area is larger than the core diameter. This phenomenon is perhaps caused by crystallization or defects at the core and clad interface.

Note that both the glass thermal stability and the fiber attenuation are quite sensitive to the existence of small percentage of crystals. To confirm our prediction, TGS3 glass is chosen as an example for further investigation. The evolution of thermal stability from bulk glass to fiber will be explored. Optical losses of fibers obtained from different fiber drawing procedures will be also measured.

1.5.5 Thermal stability investigation of TGS glass and fiber

Compared to Se-based glasses, Te-based glasses possess an intrinsic tendency to crystallize due to the long chain structure and free electrons of Te. However, in order to prepared Te-based double index fiber using the capillary method, the core should be drawn at least two times. Therefore, the comparison of thermal stability between bulk glass and optical fiber should be studied. In this chapter, TGS3 glass, as an example, will be systematically studied.

1.5.5.1 Comparison of the thermal stability of TGS3 glass and fiber

Small pieces of TGS3 bulk glass and fiber were chosen for DSC test in order to confirm the glass thermal stability before and after fiber drawing process.

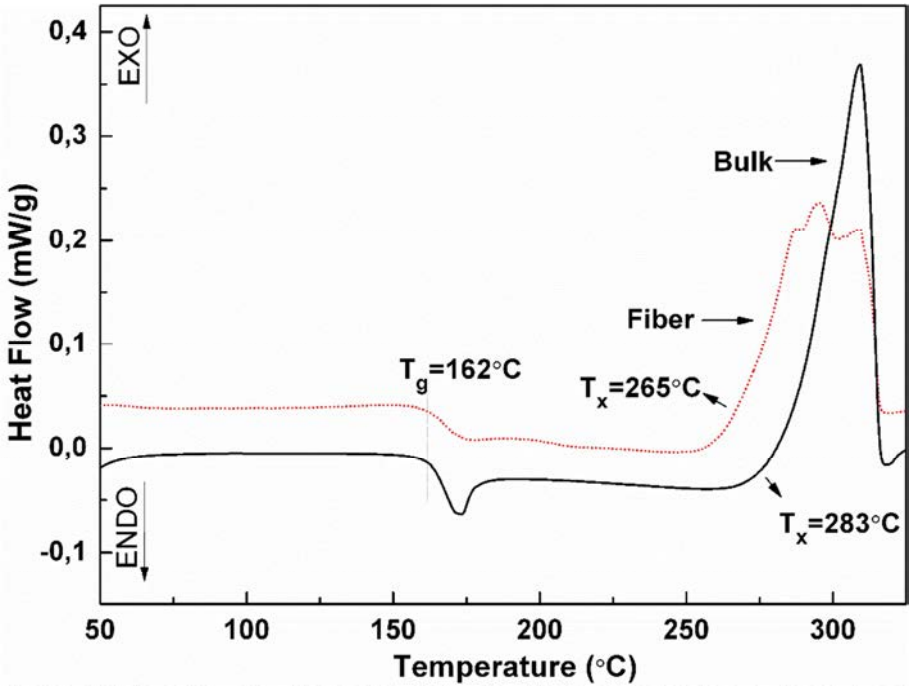

Figure 1.35 The DSC curves of TGS3 bulk glass and fiber

It could be obtained from the DSC curves (Figure 1.35) that after fiber drawing process, T_g is maintained at the same value as for the starting glass. However, T_x decreased from 283°C to 265°C. Therefore, ΔT decreased from 121°C to 103°C, and the glass fiber became quite

instable for a second drawing. This phenomenon could be attributed to glass composition change or surface nucleation and crystallization during fiber drawing process. As the composition of the core in TGS3/TGS8 multimode fiber was confirmed to have no obvious change by EDS (Figure 1.28), the glass stability reduction is likely caused by the surface nucleation and crystallization. This prediction is reasonable, as surface crystallization has been already observed in some unsuccessful TGS3/TGS8 multimode fiber preparation.

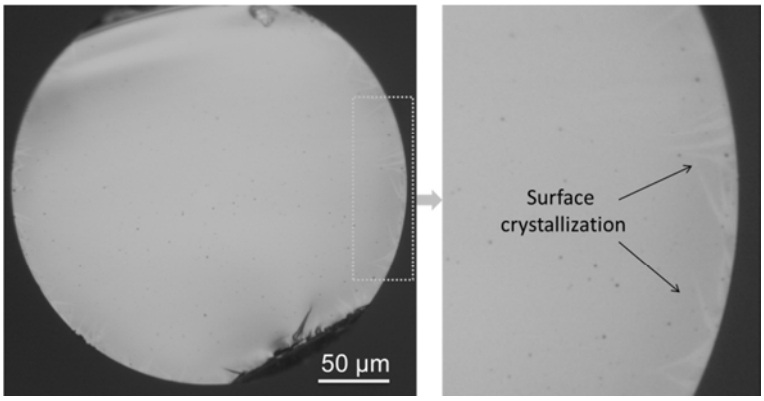

Figure 1.36 Surface crystallization of TGS3/TGS8 multimode fiber

From Figure 1.36, it can be observed that the nucleation first appears on surface and then grows into the glass, forming micro-scale crystals. Nevertheless, in the nucleation step, the nano-sized nucleus cannot be easily observed. But it can significantly alter the glass stability. Therefore, fiber drawing parameters should be controlled more precisely in order to solve this problem.

1.5.5.2 Influence of the fiber drawing times on TGS3 glass stability

Two-steps fiber drawing process

According to the prediction, the heat during fiber drawing process could make the fiber surface crystallized and destroy the glass stability. In order to study the influence of fiber drawing times on TGS3 glass stability, the preform was firstly drawn into a stick ($\emptyset = 2.5mm$) and then into a fiber (Figure 1.37).

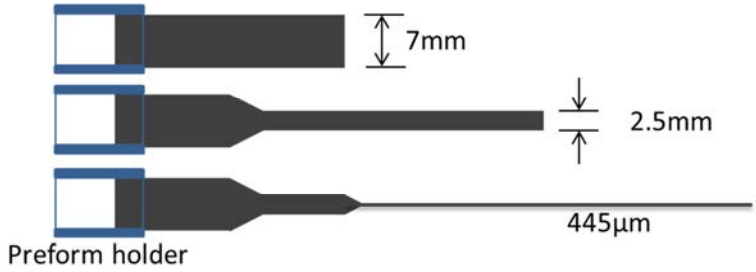

Figure 1.37 Schematic diagram of two-steps fiber drawing process

This new procedure is called “two-steps fiber drawing process”. The fiber drawing parameters are listed below (Table 1.6 & Table 1.7).

Table 1.6 Parameters for TGS3 stick drawing

Parameters before fiber drawing			
Preform diamter :	6.9 mm		
Flow of argon :	3 L/min	Flow time :	2 hours
Parameters during stick drawing			
Helium flow (<200°C) :	3 L/min	Water elimination temp.	120 °C
Helium flow (>200°C) :	2.5 L/min	Fiber drawing temp.	300 °C
Preform speed :	13 mm/min	Speed of drum :	0.10 m/min
Tension :	130 grams	Heating rate :	10 °C/min
Stick diameter :	2.5 mm		

Table 1.7 Parameters for TGS3 fiber drawing from stick

Parameters before fiber drawing			
Stick diamter :	2.5 mm		
Flow of argon :	3 L/min	Flow time :	2 hours
Parameters during fiber drawing			
Helium flow (<200°C) :	3 L/min	Water elimination temp.	120 °C
Helium flow (>200°C) :	2.5 L/min	Fiber drawing temp.	265 °C
Preform speed :	5 mm/min	Speed of drum :	0.15 m/min
Tension :	15 grams	Heating rate :	10 °C/min
Fiber diameter :	450 µm		

By comparing the two tables, we can conclude that both the heating temperatures and tension used for the elaboration of stick are much higher than for the fiber. Indeed, for the preparation of a stick, the preform feed speed is increased. This means that the temperature must be increased in order to maintain the viscosity of glass preform proper for the fibering. At the same time, as the diameter of the stick is much larger than fiber, a larger tension is quite normal to be observed.

Thermal stability and optical properties of two-steps drawing TGS3 fiber

The optical loss and stability of this fiber were compared with the fiber drawn directly from the same preform.

To verify the thermal stability, DSC curves (Figure 1.38) of the TGS3 bulk, the stick and the fiber obtained after two drawing were measured and compared. Compared with glass preform and stick, T_x of glass fiber has been decreased for more than 20°C, generating an obvious ΔT decrease. Indeed, the preform high surface energy caused by broken bonds may induce a surface crystallization during fiber drawing. Compared with stick, this surface

crystallization has a larger influence on fiber thermal stability due to a higher surface ratio, inducing an obvious T_x value variation.

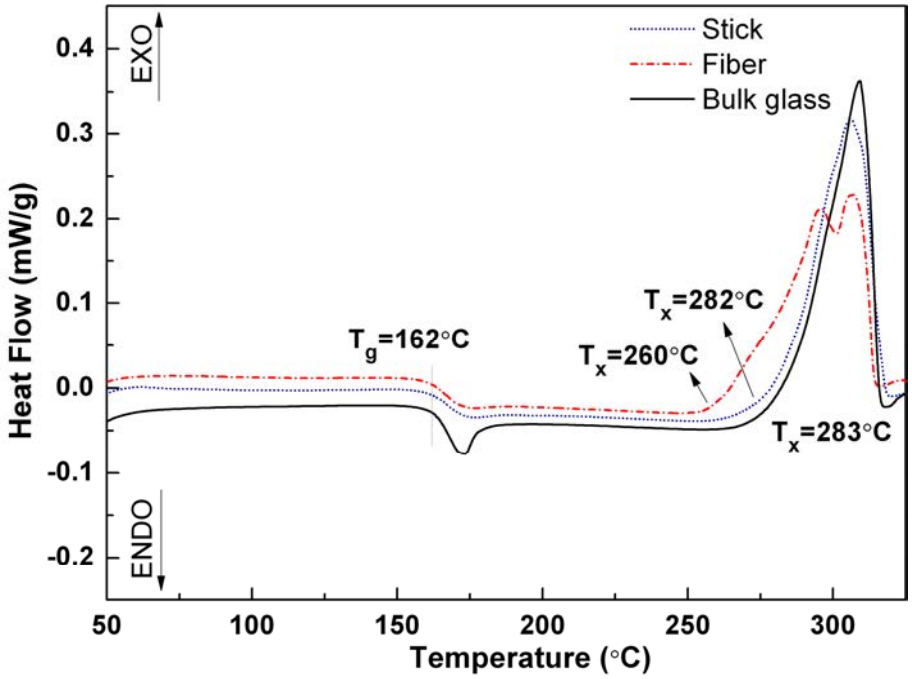

Figure 1.38 The glass stability comparison of TGS3 bulk, stick and fiber.

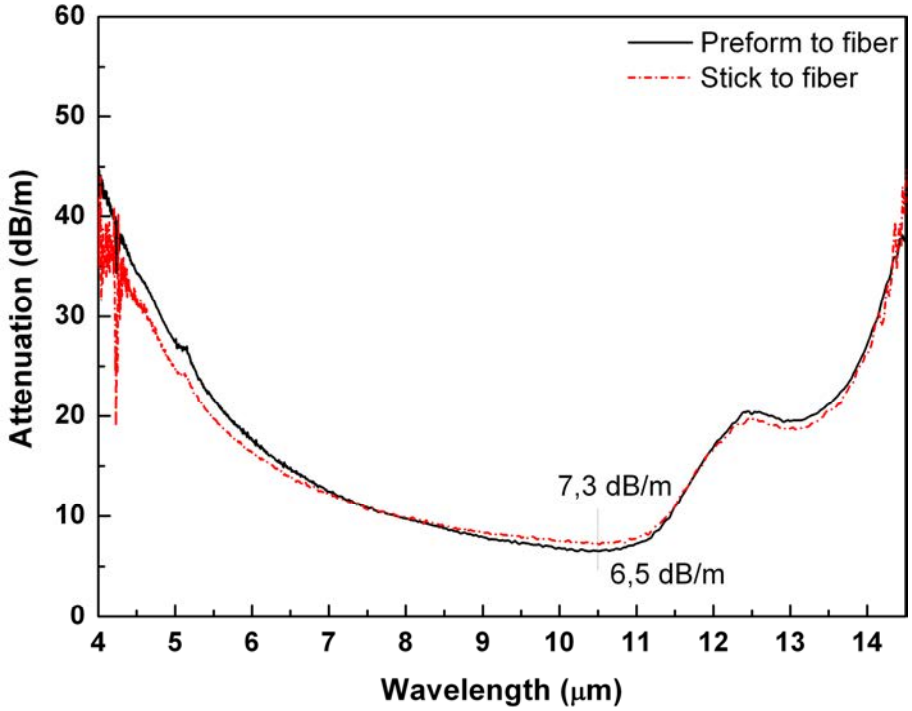

Figure 1.39 Optical losses of TGS3 glass fibers obtained from the same preform after one-step and two-steps fiber drawing.

To check the influence of the fiber drawing procedures on optical losses, a new fiber was drawn directly from the same preform using parameters listed in Table 1.3. The light

attenuation of the two TGS3 fibers obtained by drawing the preform and stick respectively were also tested (Figure 1.39). Comparing optical losses of the two fibers, there is no obvious differences. The most possible explanation is that the precipitated crystals are nano-scale and their growth is stopped when the fiber goes out of the furnace heating region. These nano-scale crystals will not cause obvious scattering of infrared light at the wavelength larger than 4μm. However, as nucleation agents, they can significantly reduce the glass thermal stability.

1.5.5.3 Influence of preform speed on TGS3 glass stability

For telluride glass, during the fiber drawing process, staying too much time in the heating zone could cause the surface crystallization. From previous studies, it was found that there was no obvious thermal stability change when the glass preform was passing through the heating zone fast and drawn into glass stick. Therefore, beside normal preform speed of 2 mm/min, 5 mm/min was also used to decrease the duration of the preform in heating zone, and thereby reduce the possibility of surface crystallization. However, the fiber drawing temperature is 20 °C more, generating a larger temperature gradient to accelerate heat conduction. DSC curves (Figure 1.40) and optical losses (Figure 1.41) of the fibers were characterized respectively.

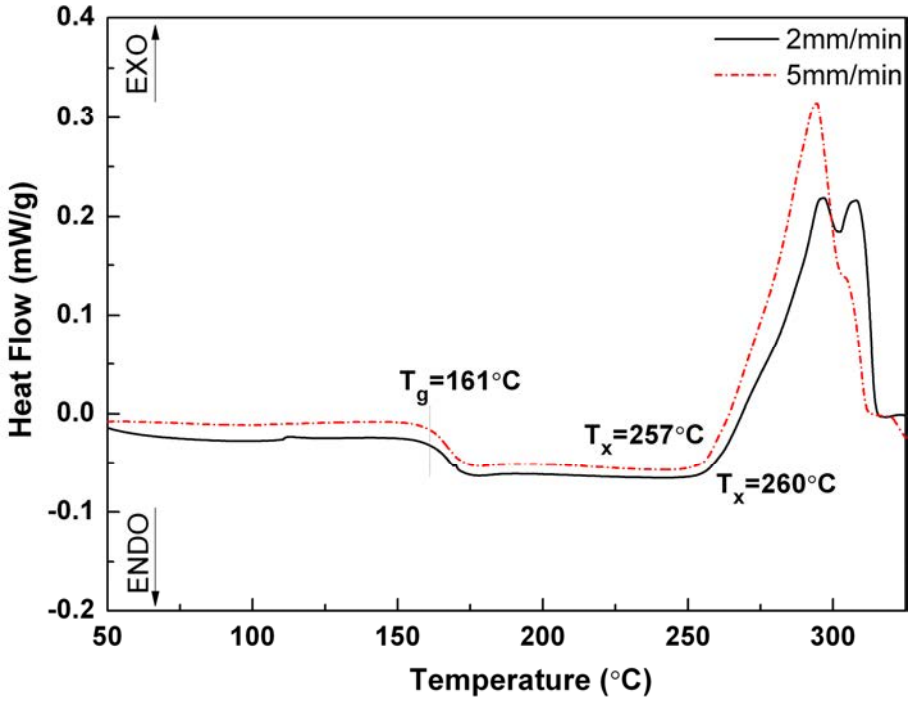

Figure 1.40 The glass stability comparison of TGS3 fibers drawn with different preform feed speed.

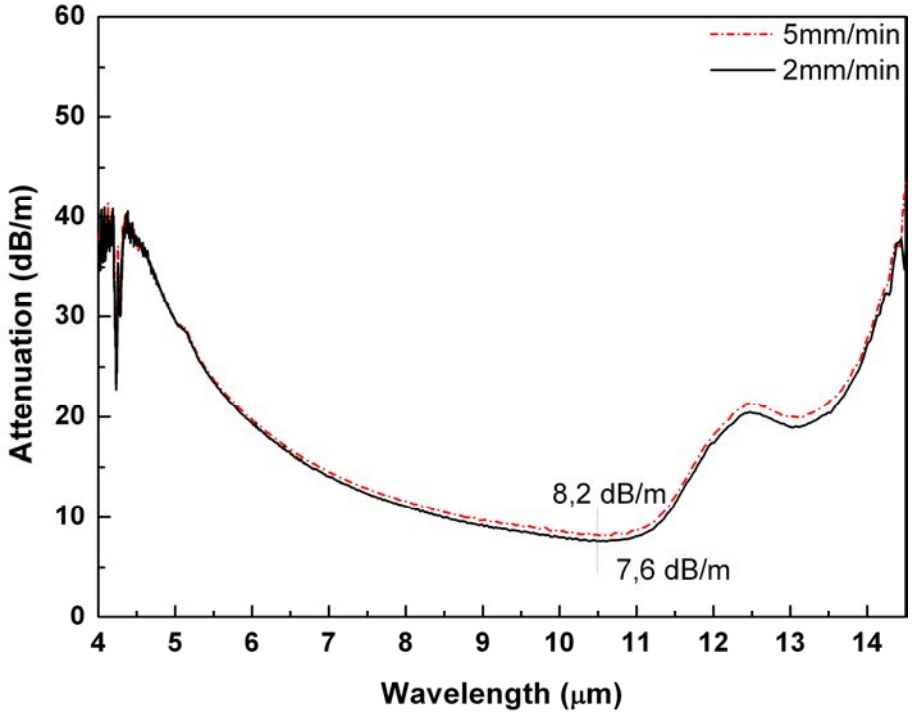

Figure 1.41 The optical losses of TGSe3 fibers. The speeds of preforms were 2mm/min and 5mm/min respectively.

It can be seen that the increase of preform speed could not cause significant changes in both the glass thermal stability and the fiber optical losses. Therefore, it is not a good way to maintain the glass thermal stability by fiber drawing using higher preform speed.

In general, we can conclude from this part of our study that the thermal stabilities of TGS3 fibers prepared using different fiber drawing procedures are all reduced compared with bulk glass. This phenomenon is probably caused by surface nucleation and crystallization. In a double index fiber, the light is guided inside the core by the total reflection at the core/clad interface. Therefore, the crystallization of TGS3 fiber, which will be drawn into fiber core, is not negligible. However, TGS3/TGS8 double index fiber has already been successfully prepared. As a result, we can predict that by coordinating fiber drawing parameters precisely and carefully polishing preform surface in the future, it is quite possible to prepare the good single mode fiber.

1.6 Conclusion

Both Darwin mission (European Space Agency) and Terrestrial Planet Finder (National Aeronautics and Space Administration) aim at the spectral analysis of the atmosphere of exoplanets to detect the traces of water, ozone and carbon dioxide whose signatures in the infrared are 6, 9 and 15 microns respectively. For detection of infrared signal beyond 12 μm, Te-Ge-Se ternary glasses with limited Se content (≤ 8%) have been selected thanks to their proper thermal stability and to the simplicity of composition control.

To obtain high quality preforms for fiber drawing, the thermal stability and optical properties of glasses prepared without purification and with one-step or two-steps purifications have been analyzed and compared. In order to provide a good contact between raw material and aluminum absorbent, two-steps chemical-distillation purification was successfully developed. Thanks to this new purification technique, the optical losses of TGSe3 fiber have been lowered significantly. The minimum of attenuation is now about 6dB/m located at 10.5 microns, which is almost the limit for telluride glass fiber due to large quantity of free electrons at room temperature.

Then, in order to get single mode fiber transmitting properly the light, a new way to make the preform, called capillary method, has also been developed alternatively to the classical rod in tube method. Thus, high purity TGS3/TGS8 double index fiber with its minimum attenuation to be 11.5dB/m at 10.7 μm has been successfully fabricated. The fiber propagation property has been checked with a tunable CO_2 laser and a FLIR ThermaCAM E300 infrared camera. After removing the confined cladding mode, the output light shows a regular round shape and the intensity profile exhibit a Gaussian shape. Although this double index fiber was designed to be a multimode fiber, it shows an obvious experimental single mode character.

Based on this promising result, a new fiber designed to be single mode has been prepared and characterized. This new achievement was not successful since it has not been possible to detect any optical signal at the output of the fiber. It has been shown that this failure was probably due to defects and crystallization generated at the interface during two-times fiber drawing process.

Thus, these exhaustive and systematic works have enabled to pave the way toward the manufacturing of a single mode fiber. Effort will focus on the preform polishing in order to limit crystallization effect during the fibering process.

Reference

[1] L. Calvez, H. Ma, J. Lucas, X. Zhang. Selenium-Based Glasses and Glass Ceramics Transmitting Light from the Visible to the Far-IR. Advanced Materials. 2007, 19 (1): 129-132

[2] J. Savage, P. Webber, A. Pitt. An Assessment of Ge-Sb-Se Glasses as 8 to 12μm Infra-Red Optical Materials. Journal of Materials Science. 1978, 13 (4): 859-864

[3] J.A. Savage. Optical Properties of Chalcogenide Glasses. Journal of Non-Crystalline Solids. 1982, 47 (1): 101-115

[4] X. Zhang, Y. Guimond, Y. Bellec. Production of Complex Chalcogenide Glass Optics by Molding for Thermal Imaging. Journal of Non-Crystalline Solids. 2003, 326: 519-523

[5] T. Kanamori, Y. Terunuma, S. Takahashi, T. Miyashita. Chalcogenide Glass Fibers for Mid-Infrared Transmission. Lightwave Technology, Journal of. 1984, 2 (5): 607-613

[6] J.S. Sanghera, I.D. Aggarwal. Active and Passive Chalcogenide Glass Optical Fibers for IR Applications: A Review. J. Non-Cryst. Solids. 1999, 256–257 (0): 6-16

[7] D. Le Coq, K. Michel, J. Keirsse, C. Boussard-Plédel, G. Fonteneau, B. Bureau, J.-M. Le Quéré, O. Sire, J. Lucas. Infrared Glass Fibers for *in-Situ* Sensing, Chemical and Biochemical Reactions. Comptes Rendus Chimie. 2002, 5 (12): 907-913

[8] A. Messica, A. Greenstein, A. Katzir. Theory of Fiber-Optic, Evanescent-Wave Spectroscopy and Sensors. Applied optics. 1996, 35 (13): 2274-2284

[9] D. Lin-Vien, N.B. Colthup, W.G. Fateley, J.G. Grasselli. The Handbook of Infrared and Raman Characteristic Frequencies of Organic Molecules. Elsevier, 1991

[10] F. Charpentier, J. Troles, Q. Coulombier, L. Brilland, P. Houizot, F. Smektala, C. Boussard-Plédel, V. Nazabal, N. Thibaud, K. Le Pierrès, G. Renversez, B. Bureau. CO_2 Detection Using Microstructured Chalcogenide Fibers. Sensor Letters. 2009, 7 (5): 745-749

[11] K. Michel, B. Bureau, C. Pouvreau, J.C. Sangleboeuf, C. Boussard-Plédel, T. Jouan, T. Rouxel, J.L. Adam, K. Staubmann, H. Steinner, T. Baumann, A. Katzir, J. Bayona, W. Konz. Development of a Chalcogenide Glass Fiber Device for in Situ Pollutant Detection. J. Non-Cryst. Solids. 2003, 326–327 (0): 434-438

[12] J. Troles, V. Shiryaev, M. Churbanov, P. Houizot, L. Brilland, F. Desevedavy, F. Charpentier, T. Pain, G. Snopatin, J. Adam. $GeSe_4$ Glass Fibres with Low Optical Losses in the Mid-IR. Optical Materials. 2009, 32 (1): 212-215

[13] L. Kaltenegger, M. Fridlund. The Darwin Mission: Search for Extra-Solar Planets. Advances in Space Research. 2005, 36 (6): 1114-1122

[14] C.A. Beichman. Terrestrial Planet Finder: The Search for Life-Bearing Planets around Other Stars. In: Astronomical Telescopes & Instrumentation: International Society for Optics and Photonics, 1998: 719-723

[15] S. Danto, P. Houizot, C. Boussard-Plèdel, X.H. Zhang, F. Smektala, J. Lucas. A Family of Far-Infrared-Transmitting Glasses in the Ga–Ge–Te System for Space Applications. Adv. Funct. Mater. 2006, 16 (14): 1847-1852

[16] A.A. Wilhelm, C. Boussard-Plédel, Q. Coulombier, J. Lucas, B. Bureau, P. Lucas. Development of Far-Infrared-Transmitting Te Based Glasses Suitable for Carbon Dioxide Detection and Space Optics. Adv. Mater. 2007, 19 (22): 3796-3800

[17] Z. Yang, P. Lucas. Tellurium Based Far Infrared Transmitting Glasses. J. Am. Ceram. Soc. 2009, 92 (12): 2920-2923

[18] X. Zhang, H. Ma, C. Blanchetière, J. Lucas. Low Loss Optical Fibres of the Tellurium Halide-Based Glasses, the Tex Glasses. J. Non-Cryst. Solids. 1993, 161: 327-330

[19] P. Lucas, Z. Yang, M.K. Fah, T. Luo, S. Jiang, C. Boussard-Pledel, M.-L. Anne, B. Bureau. Telluride Glasses for Far Infrared Photonic Applications. Optical Materials Express. 2013, 3 (8): 1049-1058

[20] C. Conseil, J.-C. Bastien, C. Boussard-Plédel, X.-H. Zhang, P. Lucas, S. Dai, J. Lucas, B. Bureau. Te-Based Chalcohalide Glasses for Far-Infrared Optical Fiber. Opt. Mater. Express. 2012, 2 (11): 1470-1477

[21] X. Wang, Q. Nie, G. Wang, J. Sun, B. Song, S. Dai, X. Zhang, B. Bureau, C. Boussard, C. Conseil, H. Ma. Investigations of Ge–Te–AgI Chalcogenide Glass for Far-Infrared Application. Spectrochim. Acta, Part A. 2012, 86 (0): 586-589

[22] S. Maurugeon, B. Bureau, C. Boussard-Plédel, A.J. Faber, X.H. Zhang, W. Geliesen, J. Lucas. Te-Rich Ge–Te–Se Glass for the CO_2 Infrared Detection at 15μm. J. Non-Cryst. Solids. 2009, 355 (37–42): 2074-2078

[23] S. Maurugeon, C. Boussard-Plédel, J. Troles, A.J. Faber, P. Lucas, X.H. Zhang, J. Lucas, B. Bureau. Telluride Glass Step Index Fiber for the Far Infrared. J. Lightwave Technol. 2010, 28 (23): 3358-3363

[24] S. Maurugeon, B. Bureau, C. Boussard-Plédel, A.J. Faber, P. Lucas, X.H. Zhang, J. Lucas. Selenium Modified $GeTe_4$ Based Glasses Optical Fibers for Far-Infrared Sensing. Opt. Mater. 2011, 33 (4): 660-663

[25] C. Conseil, V.S. Shiryaev, S. Cui, C. Boussard-Pledel, J. Troles, A.P. Velmuzhov, A.M. Potapov, A.I. Suchkov, M.F. Churbanov, B. Bureau. Preparation of High Purity Te-Rich Ge-Te-Se Fibers for 5-15 μm Infrared Range. Journal of Lightwave Technology. 2013, 31 (11): 1703-1707

[26] C. Conseil, Q. Coulombier, C. Boussard-Plédel, J. Troles, L. Brilland, G. Renversez, D. Mechin, B. Bureau, J.L. Adam, J. Lucas. Chalcogenide Step Index and Microstructured Single Mode Fibers. J. Non-Cryst. Solids. 2011, 357 (11–13): 2480-2483

[27] B. Bureau, C. Boussard-Pledel, P. Lucas, X. Zhang, J. Lucas. Forming Glasses from Se and Te. Molecules. 2009, 14 (11): 4337-4350

[28] A. Nussbaum. Electrical Properties of Pure Tellurium and Tellurium-Selenium Alloys. Physical Review. 1954, 94 (2): 337

[29] K. Plessner. Conductivity, Hall Effect and Thermo-Electric Power of Selenium Single Crystals. Proceedings of the Physical Society. Section B. 1951, 64 (8): 671

[30] X.H. Zhang, G. Fonteneau, J. Lucas. Tellurium Halide Glasses. New Materials for Transmission in the 8–12 μm Range. Journal of Non-Crystalline Solids. 1988, 104 (1): 38-44

[31] J. Lucas, X.H. Zhang. The Tellurium Halide Glasses. Journal of Non-Crystalline Solids. 1990, 125 (1–2): 1-16

[32] S. Zhang, X.H. Zhang, M. Barillot, L. Calvez, C. Boussard, B. Bureau, J. Lucas, V. Kirschner, G. Parent. Purification of $Te_{75}Ga_{10}Ge_{15}$ Glass for Far Infrared Transmitting Optics for Space Application. Opt. Mater. 2010, 32 (9): 1055-1059

[33] P. Lucas, C. Boussard-Pledel, A. Wilhelm, S. Danto, X.-H. Zhang, P. Houizot, S. Maurugeon, C. Conseil, B. Bureau. The Development of Advanced Optical Fibers for Long-Wave Infrared Transmission. Fibers. 2013, 1 (3): 110-118

[34] S.B. Bhanu Prashanth, S. Asokan. Composition Dependent Electrical Switching in Glasses–the Influence of Network Rigidity and Thermal Properties. Solid State Communications. 2008, 147 (11–12): 452-456

[35] J.L. Adam, X.H. Zhang. Chalcogenide Glasses Preparation, Properties and Applications. Sawston, Cambridge, UK: Woodhead Publishing Limited, 2014

[36] C. Conseil. Verres À Base De Tellure Pour L'optique Infrarouge Et La Thermoélectricité: Rennes 1. 2012

[37] V. Shiryaev, J.-L. Adam, X. Zhang, C. Boussard-Plédel, J. Lucas, M. Churbanov. Infrared Fibers Based on Te–As–Se Glass System with Low Optical Losses. Journal of Non-Crystalline Solids. 2004, 336 (2): 113-119

[38] V.S. Shiryaev, C. Boussard-Plédel, P. Houizot, T. Jouan, J.L. Adam, J. Lucas. Single-Mode Infrared Fibers Based on TeAsSe Glass System. Materials Science and Engineering: B. 2006, 127 (2–3): 138-143

[39] E.R. Cohen, D.R. Lide, G.L. Trigg. Aip Physics Desk Reference. New York, NY, USA: Springer, 2003

[40] S. Maurugeon. Fibres Infrarouges Pour L'optique Spatiale: Rennes 1. 2009

[41] L. Brilland, F. Smektala, G. Renversez, T. Chartier, J. Troles, T. Nguyen, N. Traynor, A. Monteville. Fabrication of Complex Structures of Holey Fibers in Chalcogenide Glass. Optics express. 2006, 14 (3): 1280-1285

[42] M.C. Teich, B. Saleh. Fundamentals of Photonics. Canada, Wiley Interscience. 1991: 3

Chapter 2.

Addition of Silver, Iodine and Silver Iodide in $GeTe_4$ Glass

2.1 Introduction

For numerous molecules, the fingerprinting region of the fundamental vibration is located between 2.5 and 25 μm. Due to the complex and specific absorption bands of molecules associated to their unique structure, the pattern in the fingerprinting region is completely different and could therefore be used to identify the compound. That is the reason why mid-infrared spectroscopy is a well-known and widely used technique for the detection, the identification and the monitoring of (bio-) chemical molecular species. Chalcogenide optical fibers, thanks to their flexibility and far-infrared transmission ability, are very convenient devices for remote[1], real-time[2] and *in-situ*[3] analysis. Selenide optical fibers have been used along the past ten years to carry out Fiber Evanescent Spectroscopy (FEWS) in different fields of activities. Nevertheless, to obtain richer information beyond 12 μm, which is the transmittance limitation of Se-based fiber [4-6], Te-based glass have to be developed. Such fibers also permit the detection of CO_2, which absorbs at 15 μm on planets located far from our solar system in the frame of space programs exploring terrestrial planet, as introduced in chapter 1. To meet the requirements of the final users Te-based glasses have to be stable enough to be reshaped at high temperature into optical fibers for example. For fiber drawing process, the temperature difference ΔT between T_g and T_x has to be larger than 120 °C.

Te-Ge-Se glass system (TGS glass), see chapter 1, has been proved to be a good candidate [7-9]. Nevertheless, the few percentages of Se in this system can cause significant Ge-Se absorption band limiting the mid-infrared transmission owing to its light atom weight. Indeed, this can generate a negative impact on the fiber cut-off wavelength due to the long light propagation distance in an optical fiber. Meanwhile, we have also observed in the first chapter that for TGS glass fiber, a small content of surface nucleation and crystallization cannot be avoided during fiber drawing process. As a result, new stable pure telluride glass systems without Se should be explored.

Based on previous results, iodine can effectively enhance the glass forming ability of Te-based glass[10]. Indeed, as electronegative element, it is clear that iodine plays a benefit role to trap the electronic charges [10,11]. Indeed, iodine has a [Kr] $4d^{10}\ 5s^2\ 5p^5$ electron configuration. Its electronegativity is 2.66, which is larger than most of other glass forming elements, such as Te (2.1) and Ge (2.01). During the glass synthesis procedure, iodine will tend to trap one electron to form [Kr] $4d^{10}\ 5s^2\ 5p^6$ stable full configuration, acting as a kind of electron absorber. This behavior should decrease the free electron concentration, and as a result make

the glass more stable. Moreover, iodine is a heavy element and will not impede the mid-infrared transparency.

It must be mentioned that while the presence of iodine is beneficial for stabilizing the glass, it also has an intrinsic volatility and would like to escape from glass during synthesis[12], making the glass composition difficult to be controlled. To improve this drawback, adding iodine as a form of salt appeared as a promising strategy. Thus, the Te-Ge-AgI glass system has been explored recently [13-15]. This new glass system has a very good thermal stability. In fact, DSC curves of glasses with 10, 15 and 20% of AgI show no obvious crystallization peak[13], which has never been found in other Te-based glass systems. In order to better understand the role played by Ag and I into the glassy network, $GeTe_4$ initial glass has been doped with Ag, I and AgI separately.

A series of $(GeTe_4)_{100-x}M_x$ (M=Ag, I, and AgI) glasses were synthesized using traditional melt quenching method. Their basic physical properties were measured, including thermal stability, density, electrical and ionic conductivity, in correlation with some glass local structure investigations. The motivation is to try to find some explanation to their especially good thermal stability. Meanwhile, their optical properties, i.e. infrared transmittance spectra and optical band gap were also studied in order to develop its potential applications in optics.

2.2 Selection of glass compositions

The $(GeTe_4)_{100-x}AgI_x$ (TG-AgI) glass system has a better thermal stability than any other Te-based glass systems. Indeed, DSC curves of the glasses with 10, 15 and 20% AgI show no visible crystallization. To better understand the benefit of the introduction of AgI in the glass composition, a large range of glass compositions have been prepared including composition with smaller AgI concentration. Meanwhile, $(GeTe_4)_{100-x}Ag_x$ (TG-Ag) and $(GeTe_4)_{100-x}I_x$ (TG-I) glasses were also prepared for comparison. A detailed list of the glass composition is shown in Table 2.1. The actual compositions of the synthesized glasses were also verified by EDS. To simplify the expression, glasses are named after AgI, Ag and I doping concentration.

Table 2.1 Compositions of $(GeTe_4)_{100-x}M_x$ (M=Ag, I, and AgI) glasses

	Sample name	Formula	Cal. composition	Actual composition (obtained by EDS)
$(GeTe_4)_{100-x}AgI_x$ **(TG-AgI)** glass system (x=0, 5,10, 12.5, 15, 17.5, 20, 25, and 30)	AgI-0	$GeTe_4$	$Ge_{20}Te_{80}$	$Ge_{20.7}Te_{79.3}$
	AgI-5	$(GeTe_4)_{95}AgI_5$	$Ge_{18.1}Te_{72.4}Ag_{4.8}I_{4.8}$	$Ge_{18.0}Te_{72.5}Ag_{4.9}I_{4.6}$
	AgI-10	$(GeTe_4)_{90}AgI_{10}$	$Ge_{16.4}Te_{65.5}Ag_{9.1}I_{9.1}$	$Ge_{16.1}Te_{66.1}Ag_{8.8}I_{9.0}$
	AgI-12.5	$(GeTe_4)_{87.5}AgI_{12.5}$	$Ge_{15.6}Te_{62.2}Ag_{11.1}I_{11.1}$	$Ge_{15.4}Te_{62.6}Ag_{11.2}I_{10.8}$
	AgI-15	$(GeTe_4)_{85}AgI_{15}$	$Ge_{14.8}Te_{59.1}Ag_{13}I_{13}$	$Ge_{13.8}Te_{60}Ag_{13.5}I_{12.7}$
	AgI-17.5	$(GeTe_4)_{82.5}AgI_{17.5}$	$Ge_{14}Te_{56.2}Ag_{14.9}I_{14.9}$	$Ge_{14.1}Te_{57.3}Ag_{15.4}I_{13.2}$
	AgI-20	$(GeTe_4)_{80}AgI_{20}$	$Ge_{13.3}Te_{53.3}Ag_{16.7}I_{16.7}$	$Ge_{12.8}Te_{54}Ag_{16.9}I_{16.3}$
	AgI-25	$(GeTe_4)_{75}AgI_{25}$	$Ge_{12}Te_{48}Ag_{20}I_{20}$	$Ge_{12.1}Te_{48}Ag_{20.8}I_{19.1}$
	AgI-30	$(GeTe_4)_{70}AgI_{30}$	$Ge_{10.8}Te_{43}Ag_{23.1}I_{23.1}$	--
$(GeTe_4)_{100-x}Ag_x$ **(TG-Ag)** glass system (x=0, 5,10, 15, and 20)	Ag-0	$GeTe_4$	$Ge_{20}Te_{80}$	$Ge_{20.7}Te_{79.3}$
	Ag-5	$(GeTe_4)_{95}Ag_5$	$Ge_{19}Te_{76}Ag_5$	$Ge_{19.1}Te_{75.4}Ag_{5.4}$
	Ag-10	$(GeTe_4)_{90}Ag_{10}$	$Ge_{18}Te_{72}Ag_{10}$	$Ge_{17.9}Te_{71.9}Ag_{10.2}$
	Ag-15	$(GeTe_4)_{85}Ag_{15}$	$Ge_{17}Te_{68}Ag_{15}$	$Ge_{17.5}Te_{67.4}Ag_{15.1}$
	Ag-20	$(GeTe_4)_{80}Ag_{20}$	$Ge_{16}Te_{64}Ag_{20}$	$Ge_{15.4}Te_{64.0}Ag_{20.6}$
$(GeTe_4)_{100-x}I_x$ **(TG-I)** glass system (x=0, 5, and 14)	I-0	$GeTe_4$	$Ge_{20}Te_{80}$	$Ge_{20.7}Te_{79.3}$
	I-5	$(GeTe_4)_{95.5}I_5$	$Ge_{19}Te_{76}I_5$	$Ge_{18.5}Te_{77.0}I_{4.5}$
	I-14	$(GeTe_4)_{86}I_{14}$	$Ge_{17.2}Te_{68.8}I_{14}$	$Ge_{17}Te_{69.4}I_{13.6}$

For Ag-doped glasses, due to the extra free electrons introduced with silver, the glasses become more and more unstable. The $(GeTe_4)_{75}Ag_{25}$ cannot form vitreous state even quenched in ice water. Excluding this composition, all the other glasses with Ag content up to 20% give rise to a glassy state. The final compositions were checked by EDS and are close to the initial one.

For I-doped glasses, the original concentration of iodine added into I-5 and I-14 glasses during weighing were 10% and 16% respectively. However, as a volatile element, iodine has a significant loss during vacuum and glass synthesis period[12]. Moreover, compared with final composition, the loss quantity of iodine is totally out of control and cannot be predicted. That is why the I-doped glasses were properly named after the measurement of the actual iodine concentration.

For the TG-AgI series, the actual percentage of both Ge and I are always a bit lower compared to the designed glass stoichiometry. The fundamental reason is the generation of germanium iodide (GeI_4) during glass synthesis due to its low melting (T_m=144°C) and boiling (T_b=350°C) temperature. After quenching, small amount of yellow-orange crystals condensed on the top of the silica tube. The SEM image of this crystal is shown in Figure 2.1.

By EDS analysis at the same region, the composition is confirmed to be $Ge_{21.7}I_{78.3}$. Nevertheless, by adding iodine as a form of salt, the composition controllability of TG-AgI glasses are much better. After synthesis, the most of the iodine atoms were kept inside the glass structure.

Based on the preparation of $(GeTe_4)_{100-x}M_x$ (M=Ag, I, and AgI) glasses, a series of characterizations i.e. thermal stability, density, electrical and ionic conductivity were applied to explore the effects of Ag, I, and AgI inside $GeTe_4$ glasses and propose a structure model of $(GeTe_4)_{100-x}$ AgI_x glasses. Optical properties such as infrared transmittance and optical band gap were also investigated.

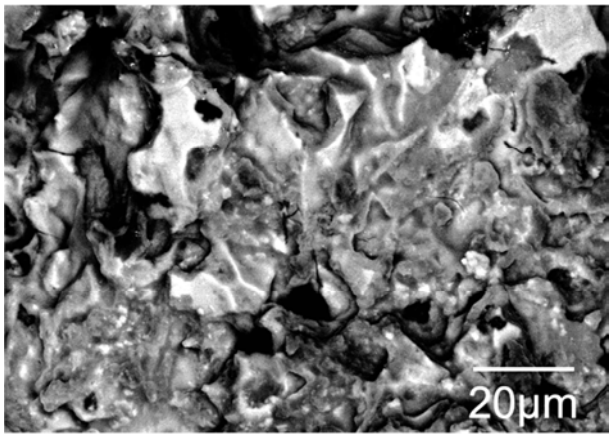

Figure 2.1 SEM image of GeI_4 crystal

2.3 Glass thermal stability study

2.3.1 DSC measurement of $(GeTe_4)_{100-x}M_x$ (M=Ag, I, and AgI) glasses

By measuring ΔT between T_g and T_x and the amount of heat released during crystallization using DSC, the glass thermal stability can be evaluated. The scanning calorimetry of the $(GeTe_4)_{100-x}M_x$ (M=Ag, I, and AgI) glasses were achieved by TA Instruments Auto Q20 at a heating rate of 10°C/min.

2.3.1.1 Thermal stability of $(GeTe_4)_{100-x}Ag_x$ glasses

DSC curves of TG-Ag glasses are shown in Figure 2.2.

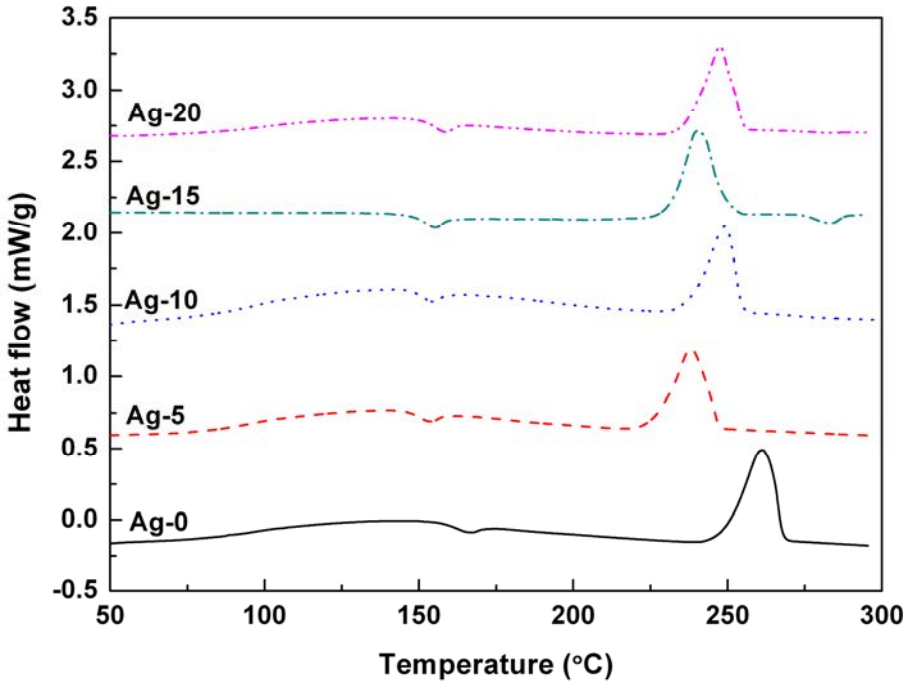

Figure 2.2 DSC curves of $(GeTe_4)_{100-x}Ag_x$ glasses

In Figure 2.2, all the TG-Ag glasses are found to exhibit a single glass transition peak and a single crystallization peak upon heating. The large exothermic peak together with the small ΔT shows that these glasses are rather instable against crystallization. The exact values of T_g and T_x are listed in Table 2.2. By adding Ag into $GeTe_4$ glasses, T_g firstly show drop and then increase gradually. This phenomenon has also been observed by K. Ramesh[16] in $Ge_{15}Te_{85-x}Ag_x$ glass system. In addition, ΔT values of Ag-5 glass is 81.7 °C, which is almost the limitation of the glass can be prepared by melt quenching method. By adding more Ag, glass should be more unstable owning to a higher free electron concentration. However, the content of Ag in $GeTe_4$ glass can be up to 20 mol. %. According to reference[16], this is because Ag in germanium telluride glasses forms its own connected structures and constrains the structural network more gradually, which maintains the glass-forming ability of Ag-Ge-Te system.

Table 2.2 T_g, T_x and ΔT of $(GeTe_4)_{100-x}Ag_x$ glasses

	T_g [°C]	T_x [°C]	ΔT [°C]
Ag-0	157.4	248.8	91.4
Ag-5	145.9	227.6	81.7
Ag-10	147.7	238.6	90.9
Ag-15	147.7	231.1	83.4
Ag-20	150.4	237.4	87.0

2.3.1.2 Thermal stability of $(GeTe_4)_{100-x}I_x$ glasses

Due to its [Kr] $4d^{10}$ $5s^2$ $5p^6$ electron configuration, iodine often plays the role of terminal atom in chalcogenide glass[10]. In this ternary system, iodine is expected to take the place of Te and connect with Ge, breaking the Te-Te chains and randomly cutting the rings. As Te-Te homo-atomic bonds often act as a kind of nucleation agent and cause crystallization during heating, the incorporation of iodine into structure should improve the glass stability.

Meanwhile, the network connectivity caused by iodine gives some flexibility to the network[10] and as a result decreases the glass transition temperature[17]. This phenomenon has also been clearly observed in T_g evolution from I-0 to I-14 (Figure 2.3). From Table 2.3, it can be found that by adding iodine, the T_g shows an obvious decrease from 157.4°C to 137.9°C and then 126.3°C. Also, ΔT value becomes higher and the crystallization peak intensity rather decreases and spreads over a wider range of temperature. These observations mean that iodine actually improves the glass thermal stability. Nevertheless, even for the richer composition in iodine, the crystallization peaks remain visible and quite large.

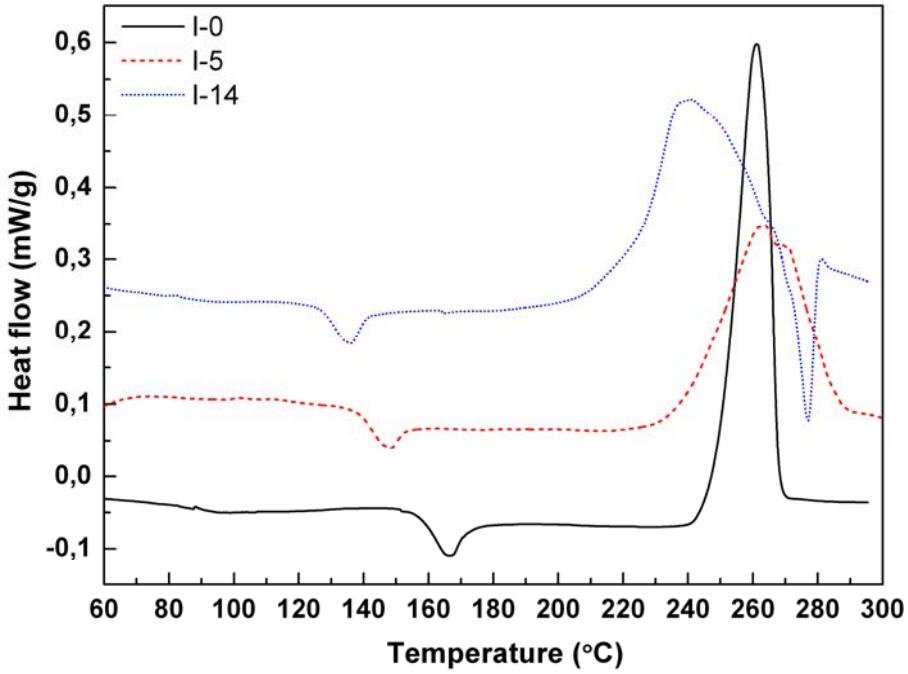

Figure 2.3 DSC curves of $(GeTe_4)_{100-x}I_x$ glasses

Table 2.3 T_g, T_x and ΔT of $(GeTe_4)_{100-x}I_x$ glasses

	T_g[°C]	T_x[°C]	ΔT[°C]
I-0	157.4	248.8	91.4
I-5	137.9	237.9	100
I-14	126.3	222.2	95.9

2.3.1.3 Thermal stability of $(GeTe_4)_{100-x}AgI_x$ glasses

To explore the thermal stability evolution of TG-AgI glasses with AgI content up to 30 mol. %, DSC curves were measured (Figure 2.4). T_g, T_x, and ΔT values are listed in Table 2.4. Compared to AgI-0 glass, only 5% of AgI already greatly enhances glass thermal stability. The TG-AgI glasses start to show no visible crystallization peak when AgI content is more than 10%. This is consistent with previous results [13,15]. For AgI-30, the glass started to show again a small crystallization peak, but the exothermic crystallization peak is very weak and even much smaller than T_g.

VS Shiryaev[15] attributed this behavior to the incorporation of iodine atoms into glass structure breaking Te-Te bonds. This structural feature of Ge-Te-AgI glasses ensures a sufficient limitation of degree of freedom to prevent the rearrangement of glass network into regular crystalline structure. Nevertheless, this explanation is also valuable to describe the TG-I glasses for which the crystallization phenomena are clearly visible. Something special happens when iodine and silver are introduced simultaneously which needs to be understood.

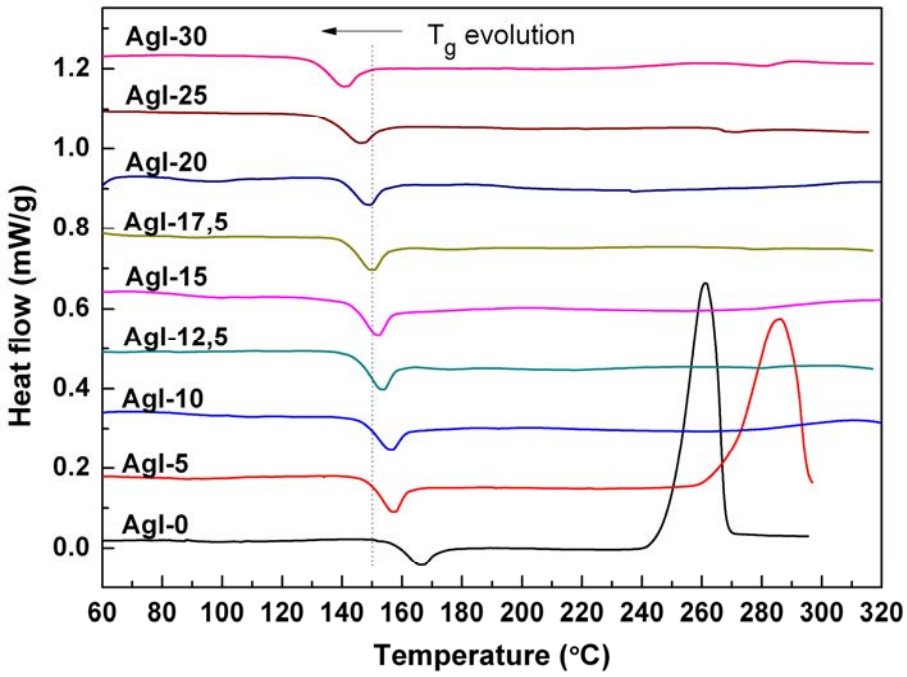

Figure 2.4 DSC curves of $(GeTe_4)_{100-x}AgI_x$ glasses

Also, the Figure 2.4 and Table 2.4 show a T_g monotonic decrease as AgI content increases. As for the TG-I glasses, this is caused by the introduction of iodine which make the glass network more floppy.

Table 2.4 T_g, T_x and ΔT of $(GeTe_4)_{100-x}AgI_x$ glasses

Sample	T_g[°C]	T_x[°C]	ΔT[°C]
AgI-0	157.4	248.8	91.4
AgI-5	148.1	268.3	120.2
AgI-10	146.3	--	--
AgI-12.5	144.4	--	--
AgI-15	143.0	--	--
AgI-17.5	140.7	--	--
AgI-20	139.6	--	--
AgI-25	134.3	--	--
AgI-30	130.2	228.6	98.4

2.3.2 Thermal stability comparison of Ag, I and AgI-doped glasses

From previous result, one can find that the effects of Ag and I separately and AgI as a salt on glass thermal stability are quite different. In order to have a better understanding, the thermal stability of $(GeTe_4)_{100-x}M_x$ (M=Ag, I, and AgI) glasses need to be directly compared and discussed.

2.3.2.1 Influence of iodine and AgI on T_g

In Figure 2.5, one can observe that T_g of both TG-AgI and TG-I have a clear declining trend as dopant concentration increases owing to the glass network disconnectivity caused by iodine. Especially for AgI-doped $GeTe_4$ glasses, experimental values show a quite good agreement with linear fit (R^2=0.9656). As a result, the fitting formula can be used to predict the glass transition temperature of TG-AgI glasses with other dopant concentrations less than 30%. This will be really practical for synthesis of TG-AgI glasses in the future.

However, T_g of glasses with the same mole fraction of AgI and I are quite different. For TG-AgI glasses, their T_g values reduce more slowly than TG-I glasses. According to literature[16], Ag in Ge-Te-Ag glass system can forms its own connected structures and constrains the structural network more gradually. As a result, we can propose that in our TG-AgI glass system, silver can constrain the glass structure to some extend and slow down the destruction of glass network caused by iodine.

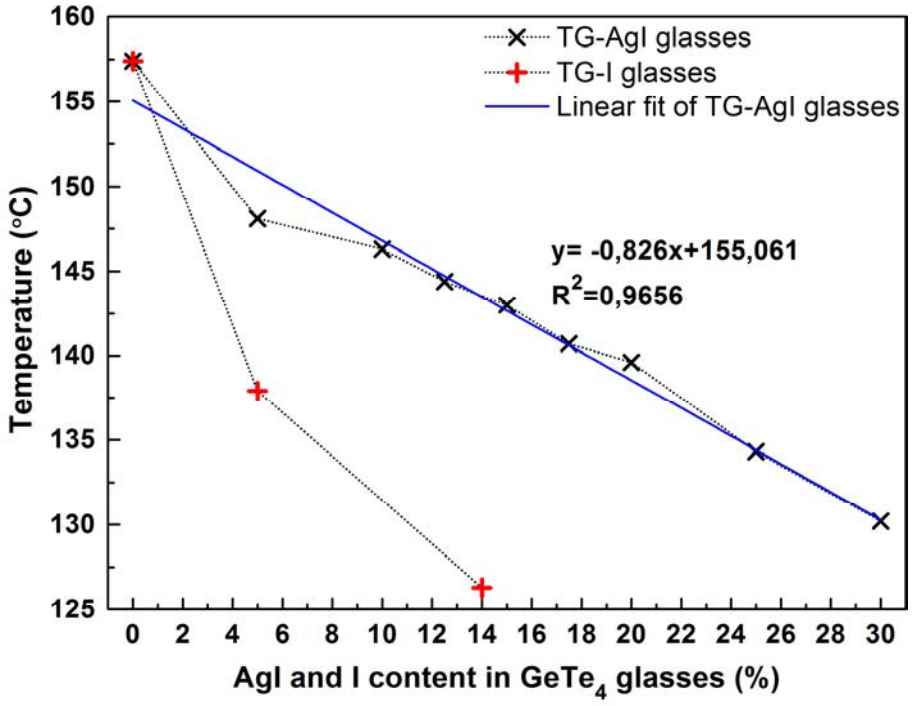

Figure 2.5 T_g evolutions of AgI and I-doped $GeTe_4$ glasses and their linear fit

2.3.2.2 Glass thermal stability comparison

In order to have a more intuitive view on impact of Ag, I and AgI on glass stability, $GeTe_4$ glasses doped with 5% and 15% of Ag, I and AgI were compared (Figure 2.6). Note that there is no I-15 sample; I-14 glass was chosen whose composition is very close.

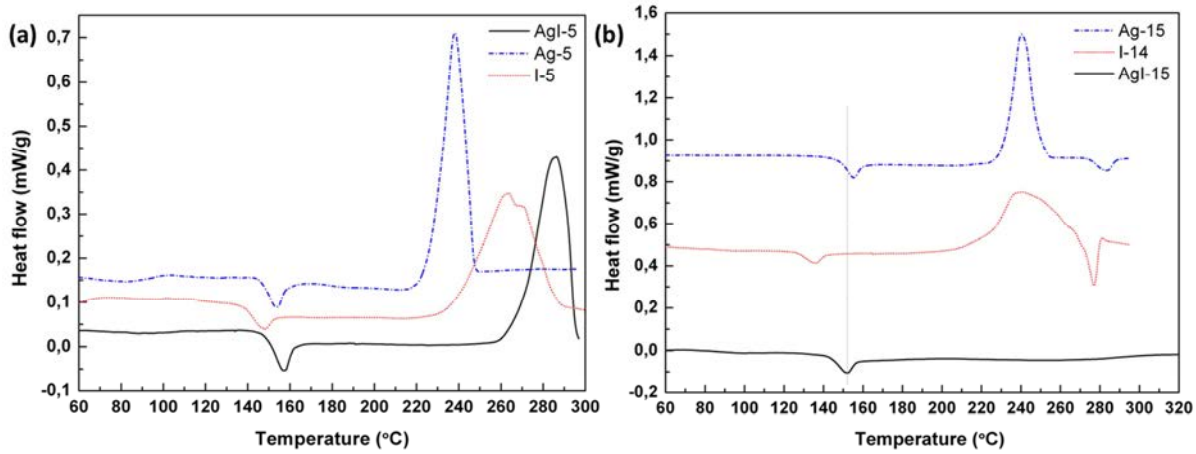

Figure 2.6 DSC curves comparison of Ag-5, I-5, and AgI-5 glasses (a) and Ag-15, I-14, and AgI-15 (b) glasses

One can see from Figure 2.6 that glasses with only 5% of Ag, I and AgI possess quite different thermal properties. AgI-5 glass shows its thermal stability higher than any of Ag-5 and I-5 glasses. This phenomenon is more obvious in Figure 2.6 b. AgI-15 glass has no

visible T_x. In comparison, Ag-15 and I-14 glasses both show obvious T_x exothermic peaks. Hence, the good glass forming ability of TG-AgI glass is caused by the synergy effects of Ag and I. Clearly, to get this absence of any crystallization effect it is important to introduce simultaneously iodine and silver into the glass composition. Note that the internal structure of material determines its performance. To explain this synergy effect of Ag and I from the perspective of the microscopic structure, a series of physical properties should be investigated for building a glass structure model.

2.4 Physical properties of Te-Ge-X (X=Ag, I, and AgI) glasses

The properties of telluride glass, like all materials, are dictated by the types of atoms present, the types of bonding between the atoms, and the way the atoms are packed together. The type of bonding and structure helps determine what type of properties a material will have. Hence, it is crucial to determine the connections between the microscopic structure and macroscopic properties of glasses. In this part, several typical physical properties will be explored in order to propose a reasonable glass structure model to explain the evolution of glass macroscopic properties.

2.4.1 Density, molar volume and packing density of glass

2.4.1.1 Measuring principle introduction

Density measurements

Glass density ($\rho_{density}$) was measured at room temperature depending on Archimedes' principle, using ethanol (99.5 vol. %) as the immersion liquid. The density was obtained by employing the relation,

$$\rho_{density} = \frac{m_{air} \times \rho_{eth}}{m_{air} - m_{eth}} \quad \textbf{(2.1)}$$

where m_{air} is the weight of glass sample in air, m_{eth} is the height of glass sample in ethanol, and ρ_{eth} is density of ethanol (0.79089 g·cm^{-3} at 20 °C).

Molar volume and mass density calculations

To obtain molar volume, the molecular weight *M* of the glass should firstly be calculated. A typical equation to calculate $A_xB_y(CD)_z$ glass molecular weight is,

$$M = M_A \frac{x}{x+y+2z} + M_B \frac{y}{x+y+2z} + M_C \frac{z}{x+y+2z} + M_D \frac{z}{x+y+2z} \quad \textbf{(2.2)}$$

where the fractional parts represent the proportion of each element of the total element, M_A M_B M_C, and M_D are atom weights. On this basis, the molar volume V_{molar} of the glass samples can be calculated from following expression,

$$V_{molar} = \frac{M}{\rho_{density}} \quad \textbf{(2.3)}$$

The mass density, which is also called number density, is defined as atom number per unit volume. It can be easily calculated from V_{molar} and Avogadro constant NA.

$$n = \frac{NA}{V_{molar}} = \frac{\rho_{density} \cdot NA}{M} \quad \textbf{(2.4)}$$

Packing density calculations

Packing density ρ_p is different from density $\rho_{density}$ and mass density n. It has taken into account the different dimensions of the types of atoms. Actually, packing density signifies the fraction of volume occupied by atoms, and is more suitable than the mass densities for structural studies. The packing density is calculated according to,

$$\rho_p = \frac{\frac{4}{3}\pi \sum r_i^3 c_i NA}{V_{molar}} \quad \textbf{(2.5)}$$

where r_i is atom radius, c_i is element percentage, and NA is Avogadro constant. Since the chalcogenide glasses are made from chemicals with similar electronegativities, these chalcogenide glasses possess predominantly covalent bonds[18]. To calculate ρ_p, the atom radius r_i of each elements is shown in Table 2.5.

Table 2.5 Elements covalent radius[1]

Elements	Tellurium	Germanium	Silver	Iodine
Radius* [pm]	136	122	134	133

2.4.1.2 Relationship between density and glass structure

The density of a substance is its mass per unit of volume. It depends on the element percentage, atom weight, and mass density. As a result, even though density is a characteristic property, it cannot reveal any material internal structure. Mass density n

[1] All the radius data come from database: http://chemglobe.org/

excludes the influence of element category and percentage. Packing density ρ_p takes into account the different dimensions of the types of atoms. Therefore, both n and ρ_p studies are helpful for glass structure analysis. M, $\rho_{density}$, and the calculated V_{molar}, n, and ρ_p of $(GeTe_4)_{100-x}M_x$ (M=Ag, I, and AgI) glasses are listed in Table 2.6.

Table 2.6 Glass molecular weight, density, and other calculated parameters

Sample	Molecular weight M	Density $\rho_{density}$ [g/cm^3]	Molar volume V_{molar}[cm^3/mol]	Mass density n [10^{22}/cm^3]	Packing density ρ_p [%]
AgI-0	116.608	5.499	21.205	2.840	28.259
AgI-5	116.682	5.587	20.885	2.883	28.694
AgI-10	116.749	5.662	20.620	2.920	29.070
AgI-12.5	116.781	5.680	20.560	2.929	29.156
AgI-15	116.811	5.719	20.425	2.948	29.351
AgI-17.5	116.839	5.728	20.398	2.952	29.392
AgI-20	116.867	5.760	20.289	2.968	29.551
AgI-25	116.919	5.828	20.062	3.002	29.889
Ag-0	116.608	5.499	21.205	2.840	28.259
Ag-5	116.171	5.734	20.260	2.972	29.596
Ag-10	115.734	5.858	19.757	3.048	30.370
Ag-15	115.297	6.023	19.143	3.146	31.364
Ag-20	114.860	6.190	18.556	3.245	32.377
I-0	116.608	5.499	21.205	2.840	28.259
I-5	117.123	5.408	21.657	2.781	27.656
I-14	118.049	5.275	22.379	2.691	26.741

Density evolution

The density measurement is considered to be a very important tool to detect the structural changes in the glass network. The density is supposed to change abruptly when the structure of the glass is slightly changed. The densities of $(GeTe_4)_{100-x}M_x$ (M=Ag, I, and AgI) glasses with different dopant concentration are measured using Archimedes' principle and shown in Figure 2.7.

As dopant concentration increases, glass densities vary linearly. The density of both AgI-doped and Ag-doped glasses show an obvious enhancement. Meanwhile, we can observe that the molecular weight of GT-AgI is almost unchanged; GT-Ag glass molecular weight even shows a significant decrease. On the contrary, the GT-I glasses with more iodine has a higher molecular weight. However the glass density is decreasing. Therefore, we can conclude that the glass structure is strongly modified by Ag, I and AgI, making glass density variation different from molecular weight change.

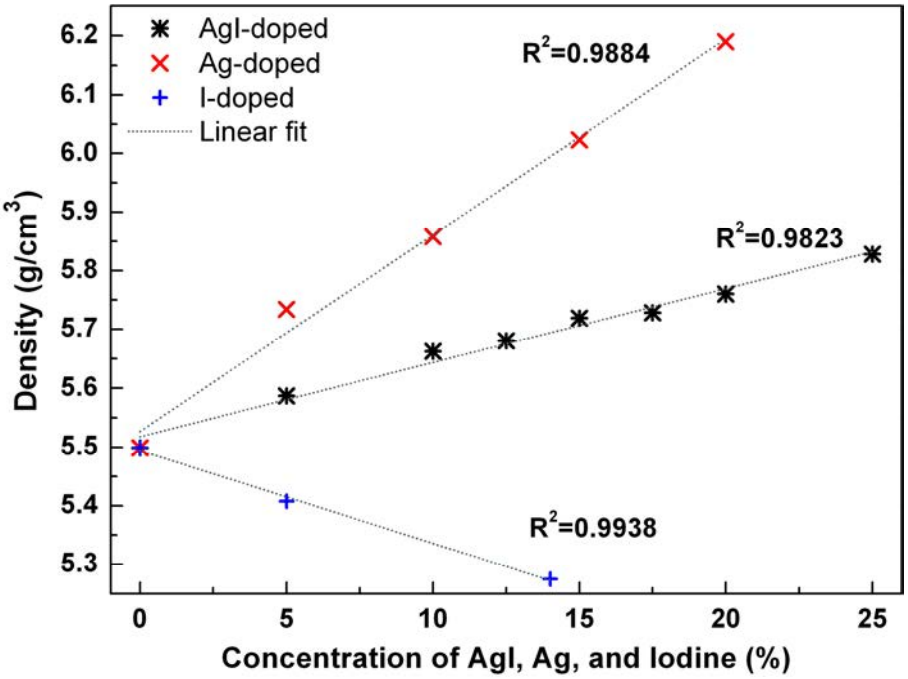

Figure 2.7 Density of $(GeTe_4)_{100-x}M_x$ (M=Ag, I, and AgI) glasses

Glass molar volume and mass density

To exclude the influence of the glass composition on our structural analysis, Equations (2.3) and (2.4) were used to calculate glass molar volume and mass density. Based on the definitions, V_{molar}, and n are actually talking about the same issue: glass structure. As the product of V_{molar} multiple n is Avogadro constant, the evolutions of V_{molar} and n are always opposite in Figure 2.8.

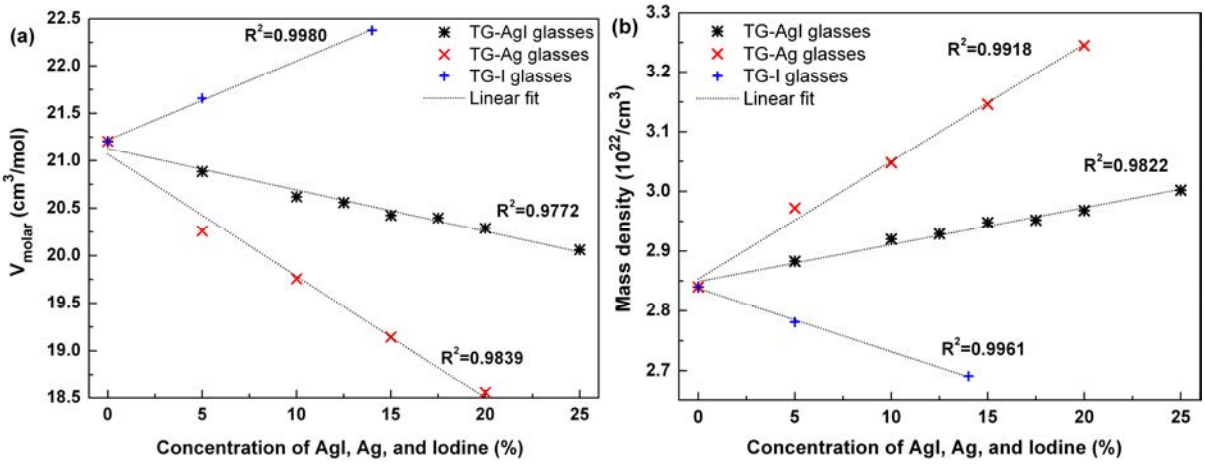

Figure 2.8 Molar volume (a) and mass density (b) of $(GeTe_4)_{100-x}M_x$ (M=Ag, I, and AgI) glasses

According to Figure 2.8, the increase of iodine concentration in TG-I glasses decreases atom number per unit volume, leading to an increase of the molar volume. The influence of

Ag is opposite. Glass became more constrained after doping, indicating that the Ag atoms rather act as glass former. AgI-doped glass, due to double effects of Ag and I, show a more gradual parameter variation. This is consistent with the previous inferences.

However, it is quite difficult to confirm our conclusion by just using V_{molar} and n. For example, it is not possible to identify the structural role played by iodine: the mass density decreases because iodine break of Ge-Te skeleton or simply because of the iodine large radius? As a result, the different dimensions of the types of atoms must be taken into account. This is the reason of the packing density investigation.

Packing density

The packing densities of the glasses (Figure 2.9) were calculated using the covalent atomic radii listed in Table 2.5.

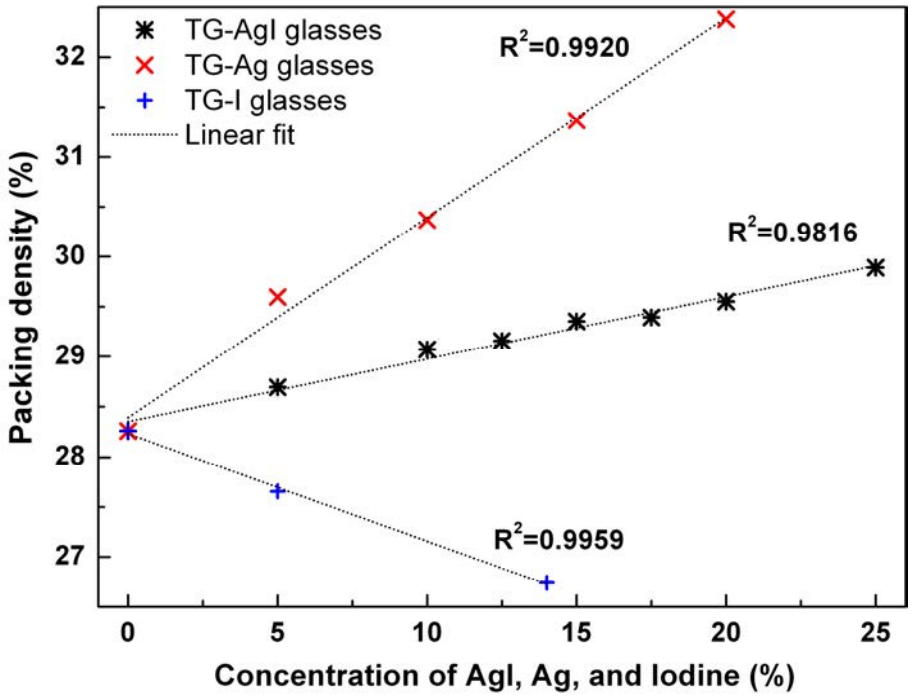

Figure 2.9 Packing density of $(GeTe_4)_{100-x}M_x$ (M=Ag, I, and AgI) glasses

Compared with glass mass density (Figure 2.8 b), the packing density evolution is quite similar due to atomic radius similarity. Thus, the possibility of Ge-Te-I glass structure expansion caused by atoms with a larger radius can be excluded. Therefore, it can be concluded that iodine acts as a structure terminator and effectively breaks the Ge-Te skeleton. Meanwhile, as previously discussed, silver acts as glass former by forming bonds with the vitreous skeleton.

2.4.2 Glass electrical conductivity results

Chalcogenide glasses are famous semiconductor materials with their band gap varying from less than 1 eV up to 3 eV depending on the composition. From S-based to Te-based glasses, due to the bond strength decreases, the degree of orbital overlap decline, generating a smaller band gap. As electrons are easier to be excited to conduction band by thermal energy in a narrow band gap material, band gap is a major factor determining the electrical conductivity of a solid. Indeed, Te-based glass, as the most conductive vitreous material, has already shown to be a promising material for thermoelectric application[19].

2.4.2.1 Electrical conductivity measurement

Glass electrical conductivity is the reciprocal of its resistivity. In our experiment, the resistivity was measured by the method of four point probes. “Four point probes” is an easy method to test sheet electrical resistivity. A current is passed through the outer probes and induces a voltage in the inner voltage probes (Figure 2.10).

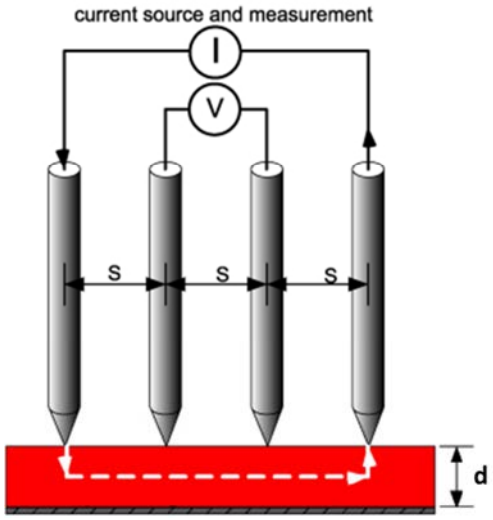

Figure 2.10 Mechanism of resistivity measurement by using a four point probe

The bulk resistivity ρ could be measured using the voltage (V) and current (I) readings from the probe and sample thickness (d).

$$\rho[\Omega \cdot cm] = \frac{\pi}{ln2} d \frac{V}{I} = \frac{0.5324Vd}{I} \quad \textbf{(2.6)}$$

The simple formula above works when the wafer thickness less than half the probe spacing (t < s/2). Conductivity σ is defined as the inverse of resistivity:

$$\sigma[S \cdot cm^{-1}] = \frac{1}{\rho} \quad \textbf{(2.7)}$$

2.4.2.2 Glass electrical conductivity analysis

The relationship between electrical conductivity logarithmic value and dopant concentration is shown in Figure 2.11.

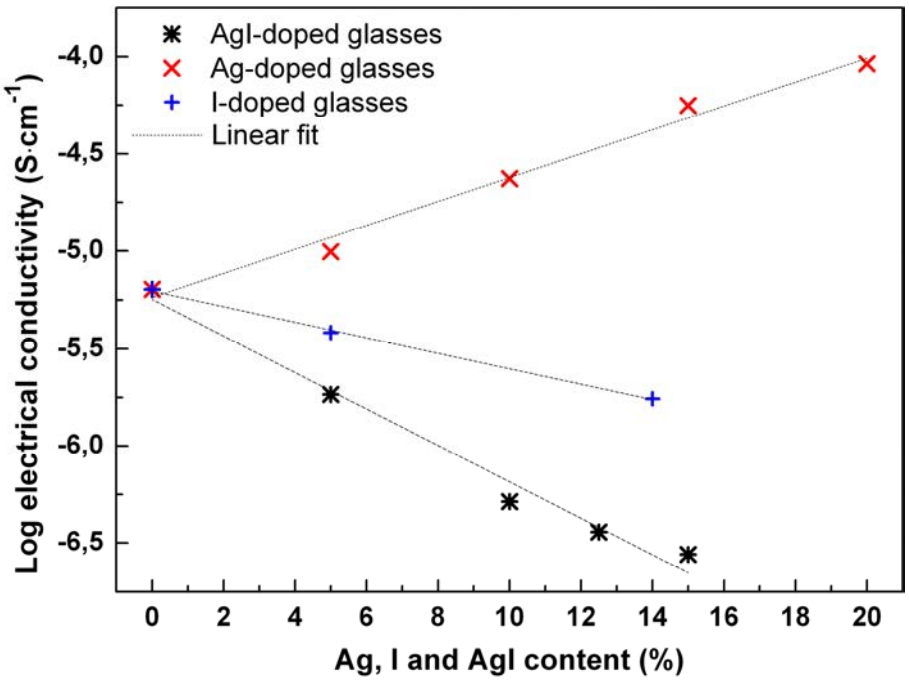

Figure 2.11 Glass electrical conductivity evolution

It is quite interesting to find out that σ of AgI-doped glasses are lower than both I-doped and Ag-doped $GeTe_4$ glasses with the same dopant concentration. In Ge-I polar covalent bond, electrons prefer to stay around iodine nucleus which has a higher electronegativity. This behavior can change the electron cloud distribution and make iodine has a slight negative charge. That is why the GT-I glasses show a lower σ than $GeTe_4$ glass. In GT-Ag glasses, the free electrons contribution from silver can go to glass network and increase σ. However, GT-AgI glasses have the lowest electrical conductivity. This phenomenon is induced by charge interactions between iodine and silver atoms blocking the trapped electron going back to glass network. It could also be the consequences of a better assimilation of iodine by the vitreous network compare to the GT-I glasses.

2.4.3 Glass conductivity by impedance spectroscopy

In 1921, Tubandt et al. found that solid AgI had extraordinary high ionic conductivity. At temperatures above 147 °C, AgI exhibits a phase transition from β phase to α phase. This high-temperature phase has an ionic conductivity similar to that of its liquid phase. Up to now, Fast-ion-conducting glasses comprise a class of solid electrolytes. They have attracted

much attention for the last decade because of their potential applications in the solid-state batteries, fuel cell technologies and other electrochemical devices [20-23]. It has been proved that ionic conductivity of borate and chalcogenide glasses can be enhanced by orders of magnitude upon increasing the concentration of silver iodide with relatively small and polarizable cations [24,25].

As a result, it is quite interesting to investigate the electrical properties of TG-Ag and TG-AgI glasses, for providing more information to glass structure analysis and finding their potential applications as solid-state electrochemical devices.

2.4.3.1 Basics of electrochemical impedance spectroscopy

In a linear (or pseudo-linear) system, the current response to a sinusoidal potential will be a sinusoid at the same frequency but shifted in phase. An expression analogous to Ohm's Law allows us to calculate the impedance of the system as a complex number:

$$Z(\omega) = \frac{E_t}{I_t} = \frac{E_0 \exp(j\omega t)}{I_0 \exp(j\omega t + \varphi)} = Z_0 \exp(j\varphi) = Z_0(\cos\varphi - j\sin\varphi) \quad \textbf{(2.8)}$$

where ω is the radial frequency; φ is phase shift; j is imaginary number. In a Nyquist impedance plot (Figure 2.12), the real part (Z′(ω)) of the impedance is plotted against the imaginary part (Z″(ω)) for data collected at a series of frequencies.

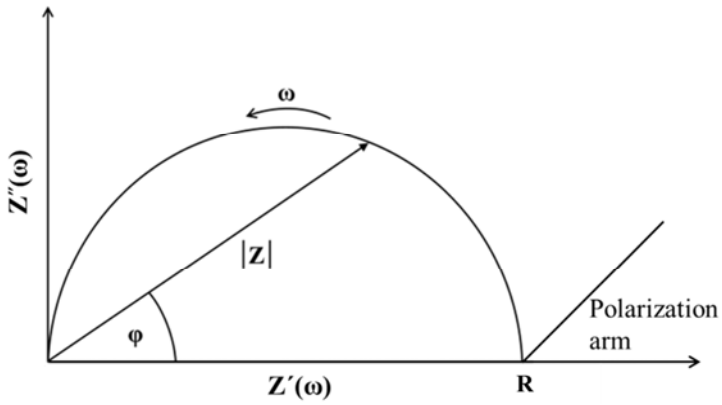

Figure 2.12 A typical Nyquist impedance plot

When the transport of charge carriers is dominated by ionic charge carriers, ionic diffusion also can create impedance. This potential perturbation frequency dependent impedance is quite small at high frequencies, and become bigger at low frequencies. On a Nyquist Plot, besides a standard semicircle at the high frequency section, the impedance caused by ionic charge carriers appears as a diagonal line away from the Z′(ω) axis.

To obtain a Nyquist Plot, the annealed glass disk with optical polished surface was used as solid electrolyte. The measurement cell was made by depositing gold electrodes on two parallel faces by a sputtering technique. The typical thickness and diameter of the disks are 1 mm and 7 mm, respectively. Electrochemical impedance of the electrochemical cell was measured using an Autolab workstation (PGSTAT302N) from 10°C up to 60°C with its frequency from 800kHz to 1Hz and shown as complex plane impedance spectrum. Then, the resistive impedance of the bulk electrolyte R was determined from the cross point of the fitted arc with the horizontal line. Actually, the electrical impedance measured here includes the impedance caused by both electrons and ions.

2.4.3.2 Ionic conduction contribution

Figure 2.13 depicts the electrochemical impedance spectroscopy of AgI-10 and AgI-20 glasses at different temperatures in Cartesian coordinates. Z´(ω) and Z˝(ω) are the real and the imaginary components of the impedance. Then the bulk electrolyte impedance *R* was determined by extrapolating the semicircle to the Z´(ω) axis at low-frequency area. The cross point (where the Z˝(ω) value equals to zero) gives the value of the resistance.

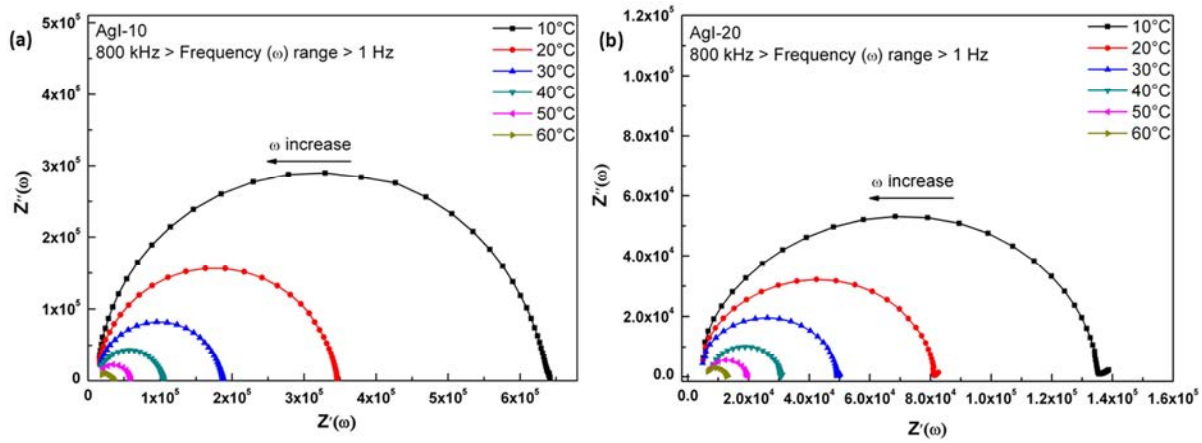

Figure 2.13 Electrochemical impedance spectroscopy of $(GeTe_4)_{90}AgI_{10}$ (a) and $(GeTe_4)_{80}AgI_{20}$ (b) glasses at different temperatures.

Compare the impedance spectroscopy of AgI-10 and AgI-20 glasses, it can be observed that AgI-20 glass at low frequency region, the beginning of a polarization arm appears and turn away gradually from the Z´(ω) axis. The occurrence of this polarization arm indicates a diffusion-controlled process[26]. At this low frequency region, the diffusion of active species can generate a space charge accumulation on the sample-electrode interface during potential oscillation. This is a typical feature of ion conductance. As a result, a transition of TG-AgI glasses from electronic to ionic conductors by increasing AgI content is predicted.

For comparison, the electrochemical impedance spectroscopies of $(GeTe_4)_{100-x}Ag_x$ glasses were also measured at different temperatures. All the impedance arcs are similar to Figure 2.13a, with no tail, indicating an electronic conductivity.

To have a clear view of this charge carrier evolution, the impedance spectroscopy of TG-AgI glasses at 10°C were compared in Figure 2.14. The enlarged figure of AgI-15, AgI-20, and AgI-25 glasses at low frequency region was also shown as insets.

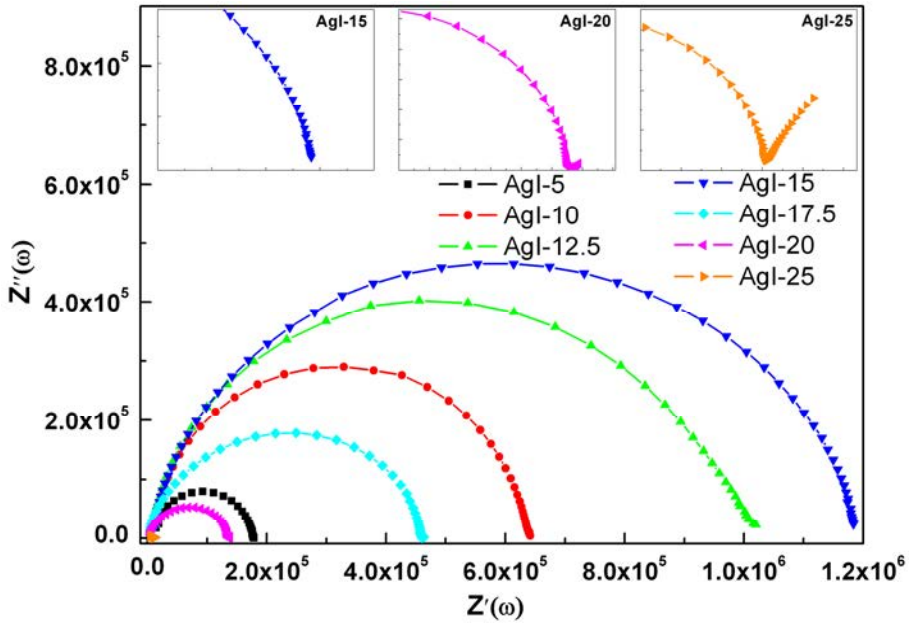

Figure 2.14 Electrochemical impedance spectroscopy of $(GeTe_4)_{100-x}AgI_x$ glasses at 10°C.

It is clear that the ionic conductivity start to appear when AgI content is more than 15%. In addition, the polarization arms become more obvious by adding AgI, signifying an increase of ion diffusion.

2.4.3.3 Electronic versus ionic conductivity investigation

Indeed, the total glass conductivity values at different temperatures can be calculated according to,

$$\sigma = \frac{F}{R_\infty} = \frac{d}{\pi r^2 R} \tag{2.9}$$

where F is the cell constant calculated by dividing disk thickness d by its surface area πr^2.

On this basis, the room temperature (20°C) σ of TG-AgI and TG-Ag glasses were shown in Figure 2.15 to compare the electrical properties of the two glass systems and at the same time find the AgI concentration threshold during the conductivity type transition. Electrical conductivities $\sigma_{4-probe}$ measured by four probe method were also listed for comparison.

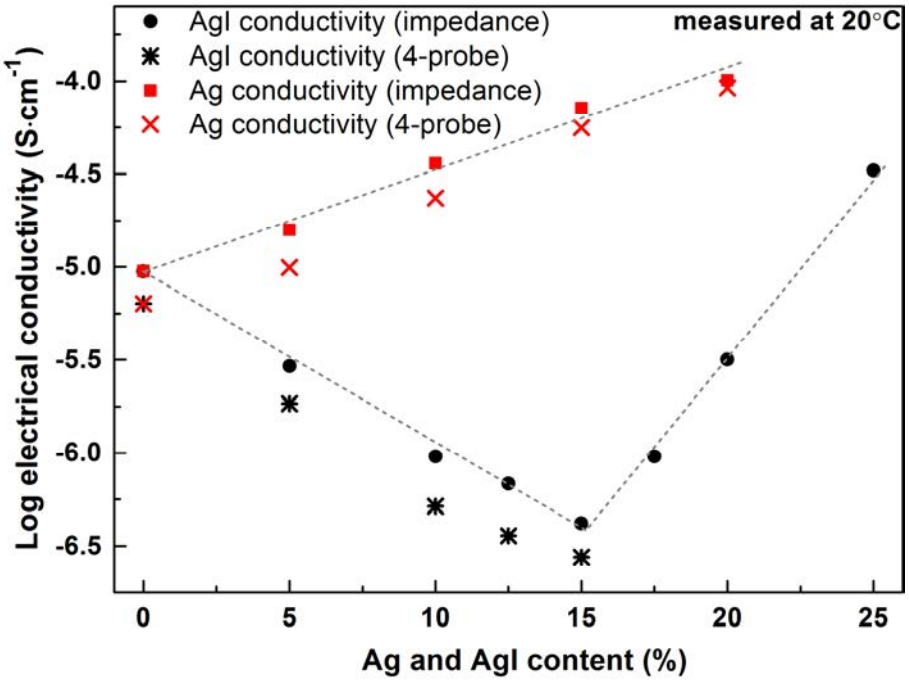

Figure 2.15 Conductivity evolutions of Ag and AgI-doped glasses

In Figure 2.15, the electrical conductivities obtained by both methods have the same order of magnitude. This consistency confirmed the reliability of the σ measurement. For TG-AgI glasses, both σ and $\sigma_{4-probe}$ show monotone decrease as dopant concentration increase when AgI is less than 15%. For TG-AgI (AgI≥15%) glasses, σ measured by impedance spectroscopy increases with AgI content. This σ transition trend can be only explained by the appearance of novel charge carrier: Ag^+ ions. This could also explain the blocking of $\sigma_{4-probe}$ measurement when AgI is larger than 15%. Actually, under the applied electrical potential, the free ions diffused following the potential direction and accumulated at the glass surface around the probe. Such an uneven distribution of charge could generate a new potential inside the glass which can offset the applied potential and block the charge carrier transfer. $(GeTe_4)_{100-x}Ag_x$ glasses, similar to $(As_{40}Te_{60})_{100-x}Ag_x$ glasses[27,28], exhibit an electronic nature. By adding Ag up to 20%, electrical are increased almost 10 times.

2.4.3.4 Temperature dependence of glass conductivity

As shown in Figure 2.13, the intersection point of both the two glasses moves to lower impedance as temperature increases, indicating an increase of conductivity. This is usual phenomenon for both electronic and ionic conductors[29,30] because both the two conductions are thermally activated process usually visualized as jumping over energy barriers. The temperature dependence of the total conductivity σ obeys an Arrhenius law,

$$\sigma = \frac{\sigma_0}{T}\exp(-\frac{E_a}{kT}) \quad \textbf{(2.10)}$$

where σ_0 is the pre-exponential factor, E_a is the activation energy, k is the Boltzmann constant, and T is the temperature. The value of σ_0 and E_a were obtained from the exponential fit of the data to Equation (2.10). The σ data and the exponential fitting of both TG-AgI and TG-Ag glasses are shown in Figure 2.16 and Figure 2.17 respectively.

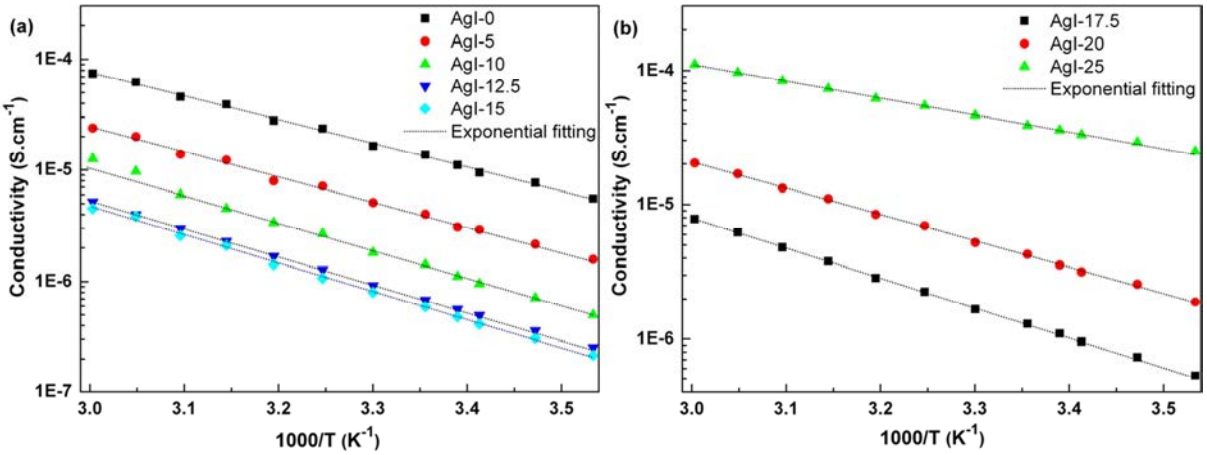

Figure 2.16 Temperature dependence of $(GeTe_4)_{100-x}AgI_x$ glass electrical conductivity, from 0 to 15% of AgI on the left, and from 15 to 25% on the right.

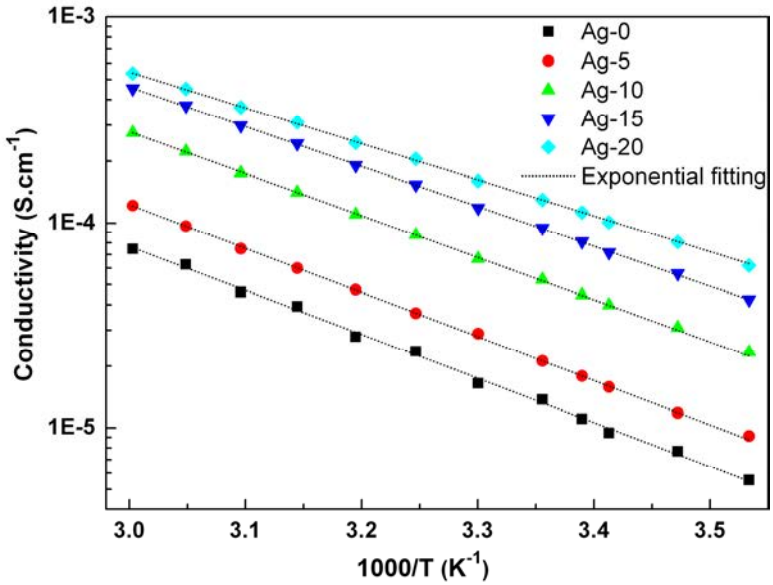

Figure 2.17 Temperature dependence of $(GeTe_4)_{100-x}Ag_x$ glass electrical conductivity

The fitted equation agrees reasonably well with the results obtained from experiments. The conductivity values of TG-AgI and TG-Ag glasses all obey the Arrhenius law in the measuring temperature range. The values of σ_0 and E_a were obtained from the exponential fit of the data to Equation (2.10). Figure 2.18 presents both the activation energy E_a and the pre-exponential factor σ_0 as a function of dopant percentage x.

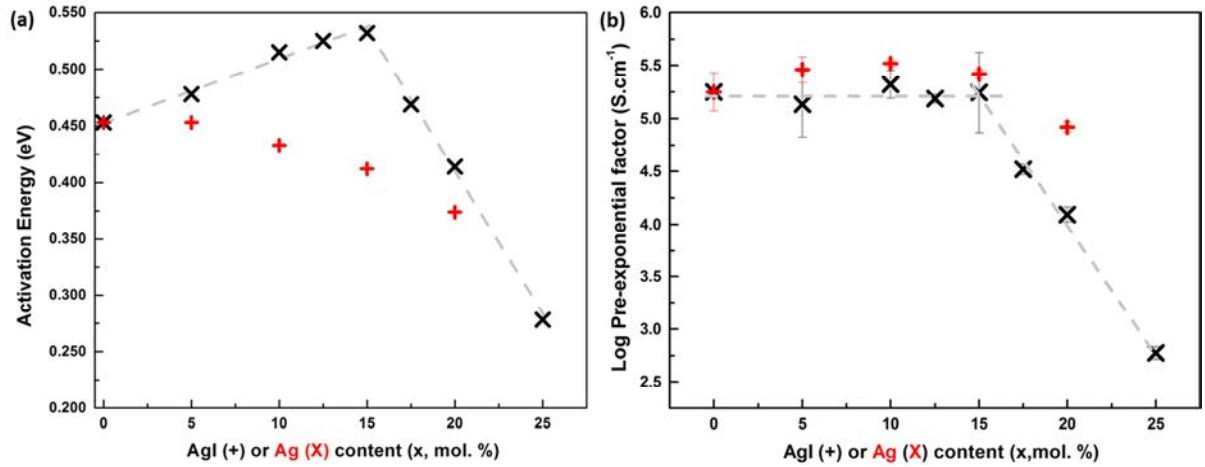

Figure 2.18 the activation energy E_a (a) and pre-exponential factor σ_0 (b) of $(GeTe_4)_{100-x}AgI_x$ and $(GeTe_4)_{100-x}Ag_x$ glasses vs. dopant content.

In chemistry, E_a is a term introduced in 1889 by the Swedish scientist Svante Arrhenius that means the minimum energy that must be input to a chemical system with potential reactants to cause a chemical reaction. At a more advanced level, the Arrhenius Activation energy term from the Arrhenius equation is best regarded as an experimental parameter measuring the energetically feasibility for a given process. For electrical conductivity, E_a is the activation energy of the current carrier jump process[31]. E_a of TG-AgI glasses first increase due to the suppression of the electronic conduction, then decrease because of the concentration increase of ions as charge carriers. $(GeTe_4)_{100-x}Ag_x$ glasses, as electronic conductor, due to the electron concentration increase caused by Ag doping, should show a continuous decrease of $E_a$values. Note that for electronic conductors, E_a values have to be correlated to the electronic band gap of the material, which is also supposed to correspond to the optical band gap. Therefore, these results will be discussed later in section 2.5.2.

The theoretical significance of pre-exponential term σ_0 in the Arrhenius conductivity equation is difficult to judge. Many believe that σ_0 is proportional to the amount of mobile charges [30,32]. Some authors stated that σ_0 is composition independent [33-35]. Here, the conductive mechanism of TG-Ag glass is unchanged, and σ_0 does not change significantly with the composition. For TG-AgI glasses, σ_0 also shows an obvious inflection point when AgI content is 15% owning to the charge carrier evolution. When glass is electronic conductor, σ_0 is composition independent. In contrast, σ_0 clearly decreases when the ionic conductivity dominates. This is rather consistent because electronic charge carriers are not involved anymore in this conduction phenomenon.

Compare E_a and σ_0 values with glass conductivity, it can be found that σ_0 variation cannot determine σ evolution. Indeed, the temperature dependence of σ is mainly dominated by the exponential term in Equation (3), and the influence of the pre-exponential term is extremely weak.

2.4.4 $(GeTe_4)_{100-x}AgI_x$ glass structure model

Studies of the structure of the glass network, including the local structure unit, the bonding nature and chemical ordering, are essential for understanding the characteristic properties of the glass. The Ge-Te bulk glasses together with several third element additions are known to be good candidates for optical data storage and mid-infrared transmission devices. Previous works based on extended-X-ray absorption spectroscopy (EXAFS) and other structural analysis methods have built the structural models of both Ag-doped and I-doped germanium telluride glasses, as depicted in Figure 2.19.

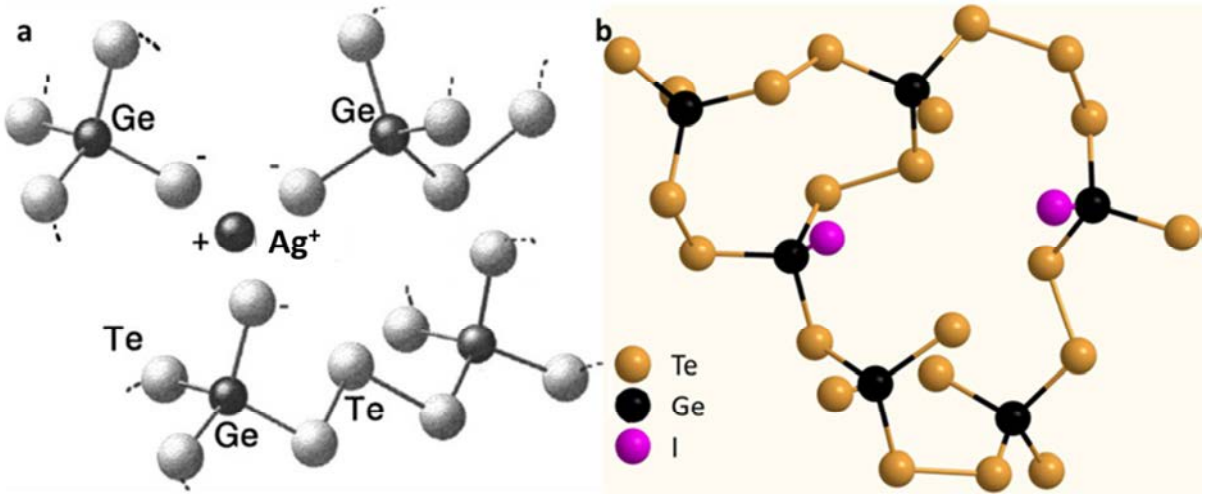

Figure 2.19 Structure models of $Ge_{15}Te_{80}Ag_5$ [36] (a) and $Ge_{20}Te_{73}I_7$ [37] (b) glasses

The both above models are in good agreement with the solid state chemist's intuition: Silver goes into the glass network and connects to Te; Iodine connects with Ge and form terminal atoms at the end of Ge-Te chains and therefore serves its purpose of opening up the network by generating larger rings without breaking the continuity of the structure.

Actually, the structure of $(GeTe_4)_{85}AgI_{15}$ and $(GeTe_4)_{75}AgI_{25}$ glasses have also been studied thanks to the contribution of Pál Jóvári using X-ray and neutron diffraction and EXAFS very recently. Large scale structural models have been obtained by fitting simultaneously the experimental datasets in the framework of the reverse Monte Carlo simulation technique. Hopefully, the results of this study are being published. The

coordination numbers are summarized and compared with the relevant values of $GeTe_4$ in Table 2.7.

Table 2.7 Coordination numbers in $(GeTe_4)_{100-x}AgI_x$ (x=0, 15, 25) glasses

	$GeTe_4$	$(GeTe_4)_{0.85}(AgI)_{0.15}$	$(GeTe_4)_{0.75}(AgI)_{0.25}$
Ge-Te	4.02	3.93	3.77
Te-Ge	1.00	0.98	0.94
Te-Te	1.10	1.46	1.82
Ge-I		0.13	0.17
Te-Ag		0.11	0.21
Te-I		–	–
Ag-Te		2.44	2.50
Ag-Ag		–	0.29
Ag-I		0.18	0.40
I-Ge		0.72	0.51
I-Te		–	–
I-Ag		0.18	0.41
N_{Ge}	4.02	4.06	3.91
N_{Te}	2.10	2.55	2.97
N_I		0.90	0.91
N_{Ag}		2.62	3.19
<N>	2.48	2.78	2.97

The total coordination number of Ag in TG-AgI glasses is around 3 depending on the AgI content. This signifies that Ag atoms take part in the construction of the telluride glassy network by surrounding itself mainly by Te neighbors. Meanwhile, iodine prefers to be linked to germanium. From $GeTe_4$ to $(GeTe_4)_{75}AgI_{25}$, the Te-Te coordination number increases from 1.1 to 1.82, and the total coordination number of Te (N_{Te}) increases from 2.10 to 2.97. Therefore, the increase of N_{Te} is mostly due to the increase of the Te-Te coordination number. It means the addition of AgI to $GeTe_4$ glass switches Te atoms from twofold- to threefold-coordinated. This strong structural evolution could explain the absence of crystallization. Indeed, it is the crystalline phase of Te which crystallizes and this phase is built up with chains of two-fold coordinated tellurium atoms. In that case, Te-Te-Te sequences act as nucleating agent. So, the predominance of three fold coordinated Te in the structure could prevent the glass from crystallizing. In addition, by adding AgI, the average coordination number <N> increases from 2.48 to 2.97. This higher <N> value may be responsible for a better thermal stability of AgI doped $GeTe_4$ glasses due to a high structure complexity. Indeed, in TG-AgI glasses, iodine can effectively cut the vitreous skeleton by connecting to Ge, generating a lower T_g. As a result, the glass structure is more flexible and become more constrained by local structural adjustment. This structural adjustment can make the <N> value higher and increase the glass density and packing density. Meanwhile, due to

the strong localization of the electrons caused by Ag-Te and Ge-I bonds, the decrease of free electrons is also beneficial to the improvement of glass thermal stability.

Note also that Ag is rather linked to Te by covalent type bonds for x=15% and the surplus of Ag for x=25% becomes rather bonded to iodine by ionic bonds. This observation is in good agreement with the sharp increase of the ionic conductivity beyond x= 15%.

In general, the structural analyze as summarized in table 2.10 rather meet our expectation. On this basis, a structural model is proposed in Figure 2.19 for the GT-AgI glasses. Silver goes into the glass network by connecting tellurium atoms, and then iodine. Iodine act as an electron absorber and a glass network terminator.

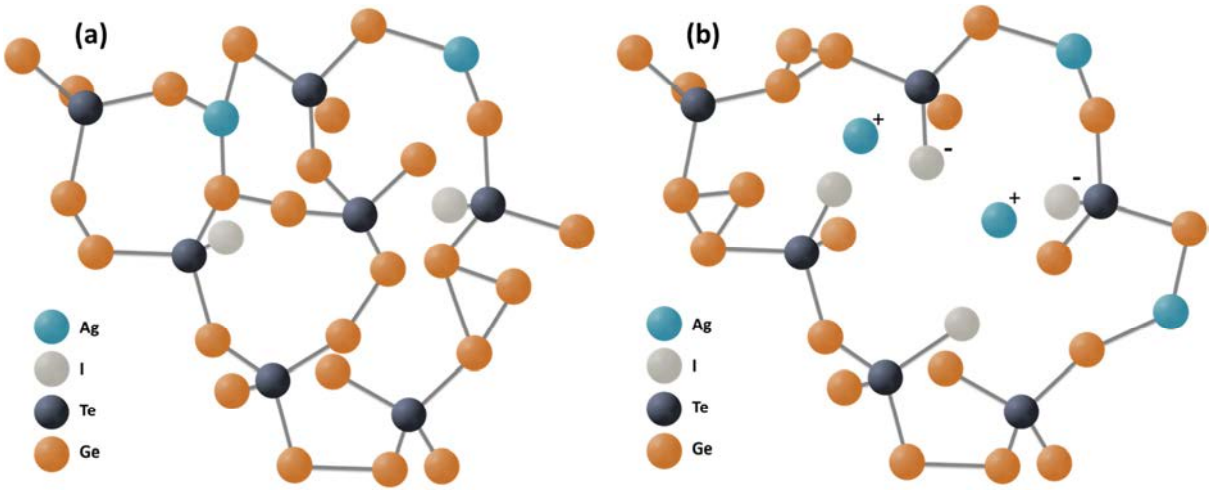

Figure 2.20 Structure model for the $(GeTe_4)_{100-x}AgI_x$ glass with AgI content less (a) and more (b) than 15%.

2.5 Effects of glass composition on the optical properties

To understand the influence of glass microstructure on its optical properties, the glass infrared transmittance T and optical band gap E_{opt}, are investigated.

2.5.1 Broadband infrared transmittance and refractive index

2.5.1.1 Transmittance dependence on refractive index

In optics, the Fresnel equations deduced by Augustin-Jean Fresnel, describe the behavior of light when moving between media of differing refractive indices. It can be used to calculate the reflection and refraction of light at uniform planar interfaces. According to the introduction of our first chapter, the combined reflection coefficient R_c has a direct relationship with the refractive indices n of the dielectric medium.

For our telluride glasses, the absorption loss caused by the 1mm of light transmission is negligible. As a result, the relationship between R_c caused by sample front side as well as back side and its transmission coefficient (T) follows the relationship:

$$R_c + T = 1 \tag{2.11}$$

Based on Eq. 1.3 and Eq. 1.4, an equation between glass refractive index n_1 and bulk transmittance T can be derived (Eq. (2.12)).

$$\begin{aligned} T &= 1 - R_c = 1 - \frac{2R}{(1+R)} \\ &= 1 - \frac{2\left|\frac{n_1 - n_2}{n_1 + n_2}\right|^2}{\left(1 + \left|\frac{n_1 - n_2}{n_1 + n_2}\right|^2\right)} = \frac{2n_1 n_2}{n_1^2 + n_2^2} \end{aligned} \tag{2.12}$$

Owning to the intrinsic high refractive indices of chalcogenide glasses, especially selenide (~2.7)[38] and telluride (~3.3)[39] glasses, the light reflection caused by Fresnel effect is not negligible. By using the approximate value of air reflection index ($n_2 = 1$), the graphical dependence of glass optical transmittance as a function of the refractive index is shown in Figure 2.21.

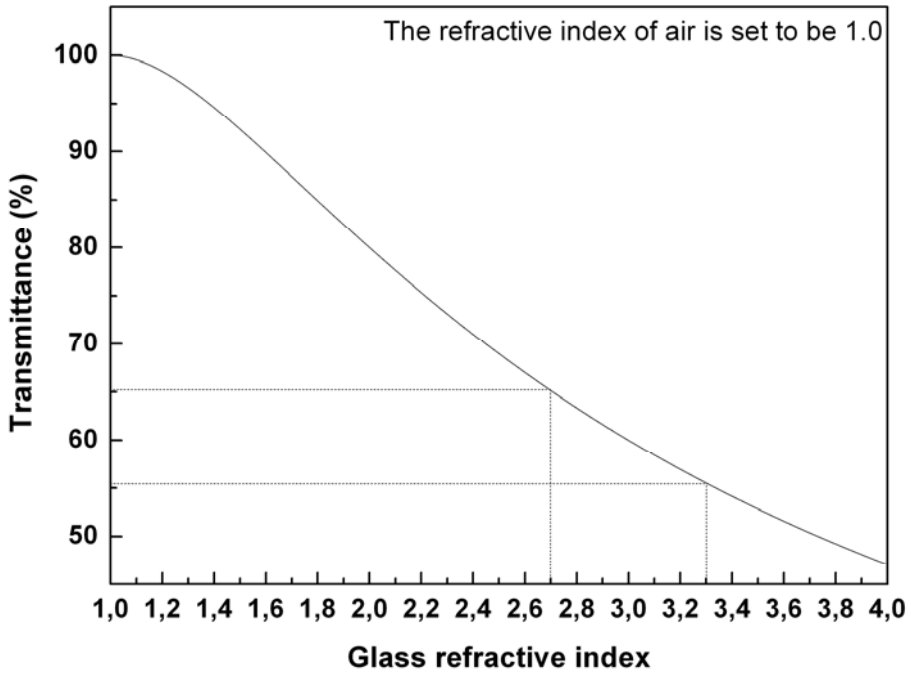

Figure 2.21 Relationship between glass optical transmittance and its refraction index

As n_1 increases, more lights are reflected at the glass-air interfaces, inducing a lower transmittance. As a result, by measuring the optical transmittance of bulk glasses, the refractive index can be calculated. However, the accuracy of glass transmittance

measurement depends greatly on the flatness and parallelism of two faces. The experimental error is not small enough to obtain accurate refractive index value. Therefore, this method can only provide a rough tendency.

2.5.1.2 Infrared transmittance of $(GeTe_4)_{100-x}AgI_x$ glasses

Figure 2.22a shows the infrared transmittance of GT-AgI glasses from 1 to 25 μm. Due to the poor sensitivity of DTGS detector in the near-infrared region (< 2.5 μm), a Perkin-Elmer Lambda 950 UV-VIS-NIR spectrophotometer was used in the wavelength range from 1 to 2.5 μm in order to determine the cut-on wavelengths of the glasses.

All the TG-AgI glasses show a wide flat transmittance from 2.0 μm up to 20.0 μm. As the glass has been synthesized without any additional purification, absorption caused by Ge-O at 13.2 μm can be clearly observed. In addition, the transmittance shows an upward trend with the AgI content, signifying a decrease of glass refractive indices. The glass refractive index can be estimated using Equation (2.12), (Figure 2.22 b).

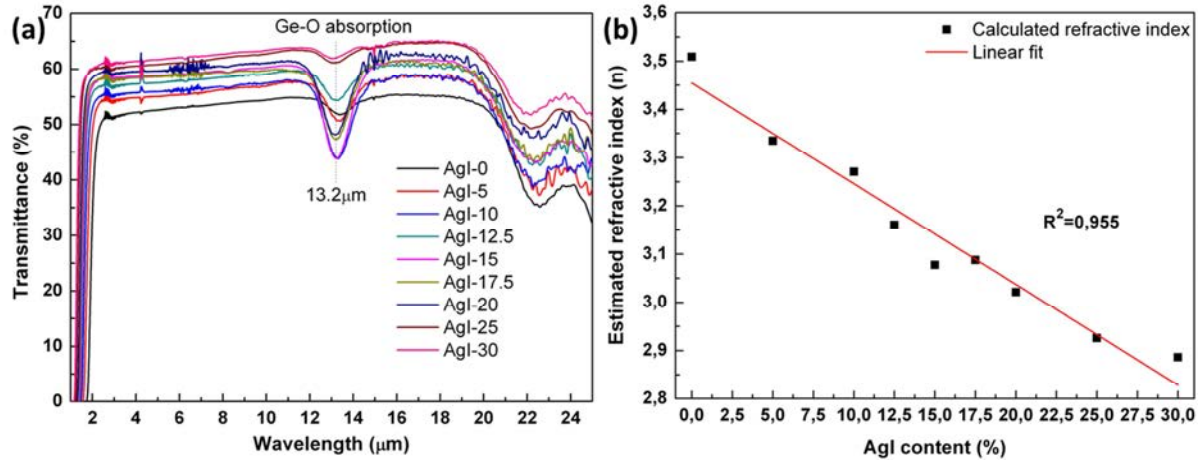

Figure 2.22 IR transmittance (a) and refractive indices (b) of $(GeTe_4)_{100-x}AgI_x$ glasses

Increase in AgI content yields a linear decrease of the refractive index. This monotonicity has also been observed in other iodine-containing chalcogenide glasses [40-43]. Actually, the refractive index of chalcogenide glass can be lowered by combining them with element of the halogen group. Here, this decrease may be connected to the role of network terminator played by iodine. Nevertheless this trend is quite unusual in view of the increase of the density and of the packing density. On the other hand, this trend can be explained by a stronger localization of the electron for the richer in AgI glass compositions, as shown by the decrease of the electronic conductivity.

2.5.1.3 IR transmittance of $(GeTe4)_{100-x}Ag_x$ glasses

The infrared transmittances of $(GeTe4)_{100-x}Ag_x$ glasses are shown in Figure 2.23.

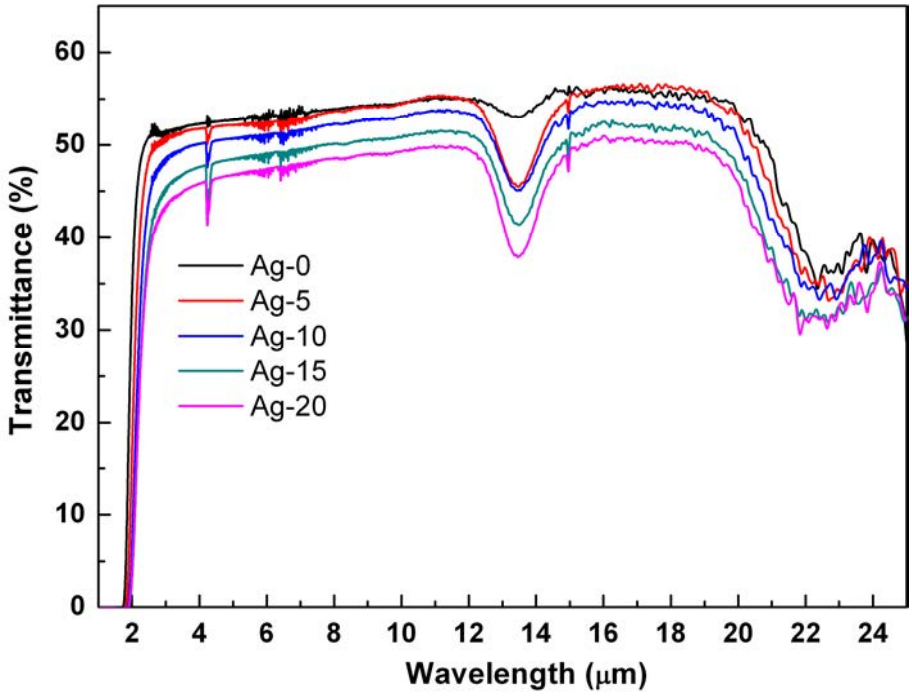

Figure 2.23 IR transmittance of $(GeTe_4)_{100-x}Ag_x$ glasses

Similar to GT-AgI glasses, the GT-Ag glasses also show a broadband infrared transmission from 2 to 25 μm with a Ge-O absorption band at 13.2 μm. Meanwhile, a monotonous optical transmittance decrease occurs as Ag content increasing, indicating a refractive index enhancement. This phenomenon has been reported also in other Ag-doped chalcogenide glass systems[40,44].

It is well known that refractive index is determined by electron shell polarizability as well as by its packing density in the substance structure. By adding heavier and easier polarizable atoms or enhance the packing density of glass structure, the refractive index can be generally increased. According to the structural analysis of GT-Ag glass system[36], the Ag atom promotes the cross-linking of the structural network. Thus, as shown in paragraph 2.4.1.2, the packing density of the glasses increases with the addition of Ag, and the electronic conductivity increases (paragraph 2.4.2.2), in full agreement with the increase of the refractive indexes.

Concerning AgI-doped glasses, the Ge-Te network de-reticulation caused by iodine induced a refractive index decrease. Thus, the effect of silver and iodine on $GeTe_4$ glass refractive index is opposite, and iodine plays a major role when the two elements coexist in the glass.

2.5.2 Optical band gap evolution

An obvious evolution of cut-on wavelength can be observed in previous transmittance spectra of both TG-AgI and TG-Ag glasses. It should be mentioned that the glass optical transmittance has a direct relationship with optical band gap E_{opt}, which describes the minimum energy required for optical excitation of a material. The band gap wavelength is given when the absorption coefficient α of the glass reaches 10 cm^{-1}.[45] To convert transmittance to absorption coefficient, the spectra should be firstly normalized to exclude the influence of reflection. The absorption coefficient could be calculated using:

$$\alpha = -\frac{\ln T}{d} \tag{2.13}$$

where T and d represent transmittance and bulk thickness respectively.

2.5.2.1 Optical band gap of $(GeTe_4)_{100-x}Ag_x$ glasses

Based on Equation (2.13), the optical absorption coefficients of TG-Ag glasses are shown in Figure 2.24 together with glass near-IR transmittance spectra.

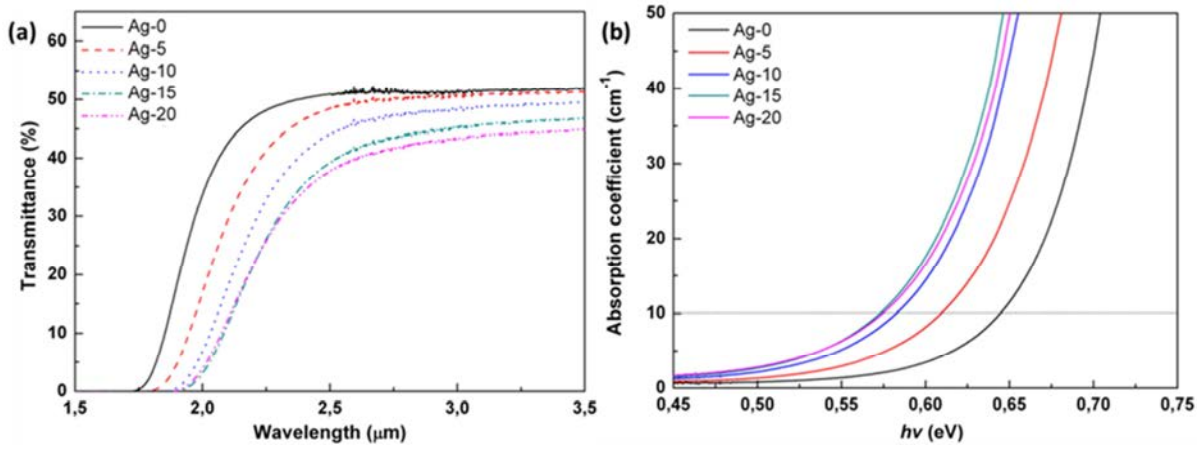

Figure 2.24 Enlarged transmittance spectra (a) and optical absorption coefficients (b) of $(GeTe_4)_{100-x}Ag_x$ glasses.

For GT-Ag glasses, a transmission edge redshift occurs when the Ag content increases. The optical band gap values were determined when α reaches 10 cm^{-1}. The observed decreased in the optical band gap with increase of Ag concentration was attributed to the structural transformation. Actually, Ag enters the glass structure and forms its own connected structure. In this constrained network structure, silver, as a famous electronic conductor, may cause an increase in disorder and create impurity energy levels in the band gap. Due to the high doping concentration, the density of states of these dopants increase and forms a

continuum of states just like in the bands and effectively the band gap decreases. This trend is in agreement with the electronic conductivity activation energy (Figure 2.18), which is supposed to be directly connected to the optical band gap. Nevertheless, it is noticeable that the band gap stop to decrease beyond x=15. This observation disagrees with the measurements of the electronic conductivity which continuously increase even for the highest percentage of Ag.

2.5.2.2 Optical band gap of $(GeTe_4)_{100-x}AgI_x$ glasses

Both the near-IR transmittance spectra and the calculated optical absorption coefficients of TG-AgI glasses are shown in Figure 2.25.

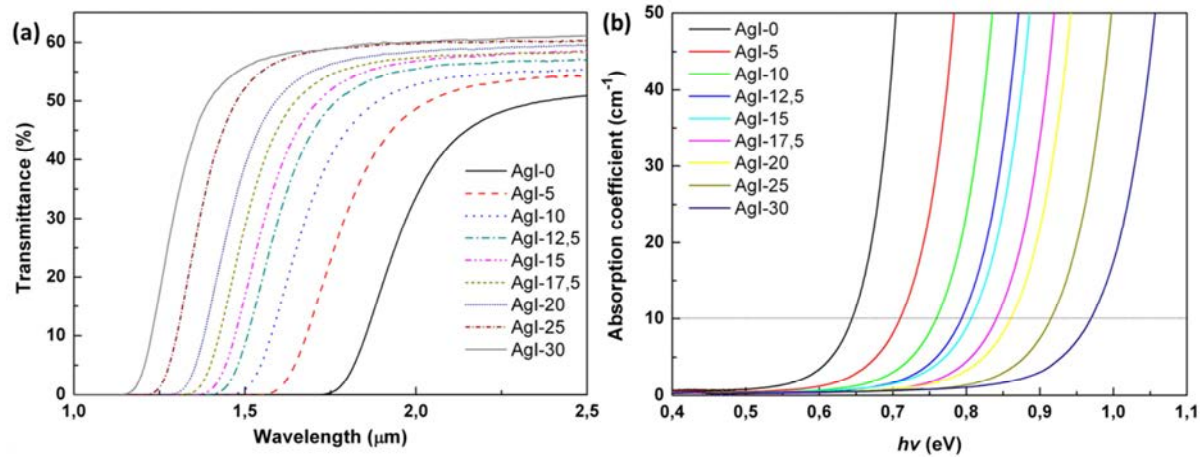

Figure 2.25 Enlarged transmittance spectra (a) and optical absorption coefficients (b) of $(GeTe_4)_{100-x}AgI_x$ glasses.

For GT-AgI glasses, the transmission edge showed an obvious blueshift from AgI-0 to AgI-30. By adding AgI, E_{opt} was enlarged. Iodine, an electronegative element, plays a positive role to trap the electronic charges. As a result, the extra electron energy levels in band gap will be decreased, generating a larger optical band gap. Indeed, the effect of Ag and I on the E_{opt} of glass is totally opposite. Once again, as for the index evolution, the effect of iodine supersedes that of silver in TG-AgI glasses.

The dependence of TG-AgI glass optical band gap as a function of doping concentration is shown in Figure 2.26. A linear relationship is observed. This gives the possibility of determining analytically the percentage of particular components in the glasses of the general formula GT-AgI that would result in the predefined value of optical band gap in the interval from 0.645 to 0.969 eV.

Note also that E_{opt} increase agrees the increase of the activation energy calculated from the electrical conductivity for x<15% for which the electronic contribution govern the total conductivity behavior (Figure 2.18). On the other hand when the ionic conductivity becomes predominant (x>15%), E_{opt} keeps increasing and the activation energy caused by ion diffusion start to decrease. The both E_{opt} and E_a data cannot be correlated anymore.

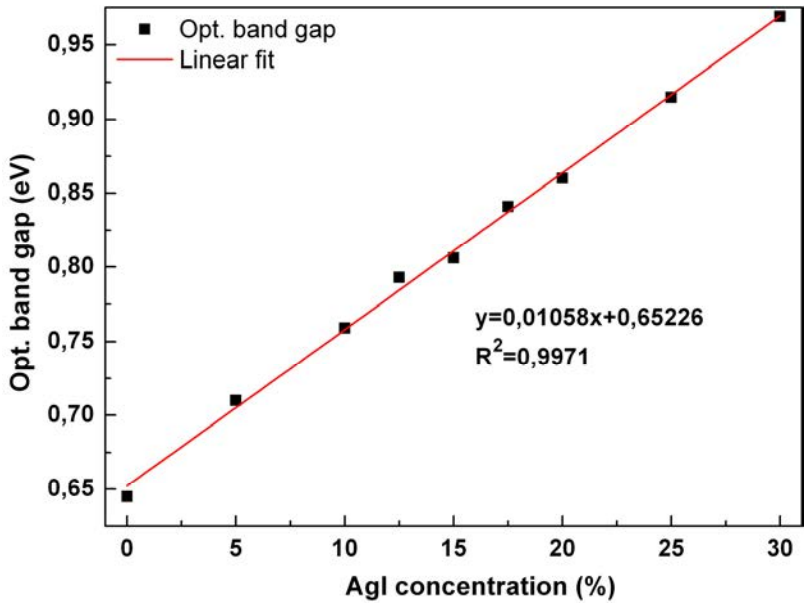

Figure 2.26 Linear relationship between AgI content and TG-AgI glass optical band gap

2.5.2.3 Comparison of glasses with the same dopant concentration

For comparison, the short-wavelength transmission edges and optical absorption coefficients of TG-Ag5, TG-I5, and TG-AgI5 glasses are also shown in Figure 2.27.

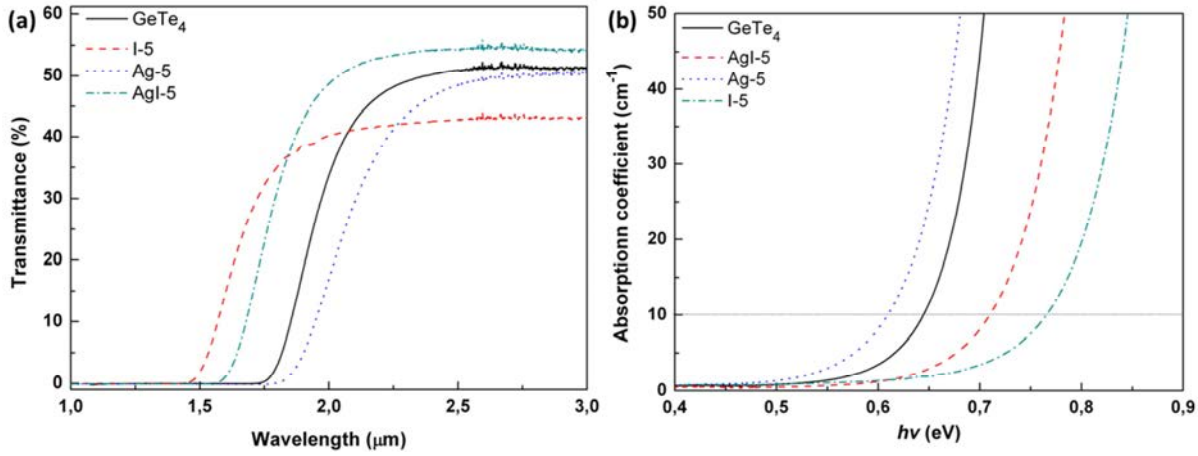

Figure 2.27 Enlarged transmittance spectra (a) and optical absorption coefficients (b) of $(GeTe_4)_{95}M_5$ (M=Ag, I, and AgI) glasses.

It can be confirmed that in transmittance spectra, Ag produces a spectral redshift, but iodine produces a larger blueshift. As a result, GT-AgI glass transmission edge shows a

blueshift on the basis of the Ag and I combined effect, and the band gap decrease caused by silver is over-compensated by iodine which increases the band gap. This is consistent with the previous prediction. All the E_{opt} values are listed in Table 2.8.

Table 2.8 Optical band gap of $(GeTe_4)_{100-x}M_x$ (M=Ag, I, and AgI) glasses

Sample	E_{opt} [eV]	Sample	E_{opt} [eV]
AgI-0	0.645	Ag-0	0.645
AgI-5	0.710	Ag-5	0.609
AgI-10	0.759	Ag-10	0.583
AgI-12.5	0.793	Ag-15	0.573
AgI-15	0.806	Ag-20	0.575
AgI-17.5	0.841	I-0	0.645
AgI-20	0.860	I-5	0.765
AgI-25	0.915	I-14	--
AgI-30	0.969		

2.6 Far infrared spectra of $(GeTe_4)_{100-x}AgI_x$ glasses

In previous infrared spectra, GT-AgI glasses still have a relative high transmittance up to 25 μm compared to other tellurium glasses. Therefore, the infrared transmission definitive limitation is interesting to check.. In order to achieve this goal, the far-infrared transmittance spectra up to 50 μm shown in Figure 2.28 were measured by Bruker Vertex 80V spectrometer in cooperation with D. Le Coq and P. Masselin from the University of Dunkerque.

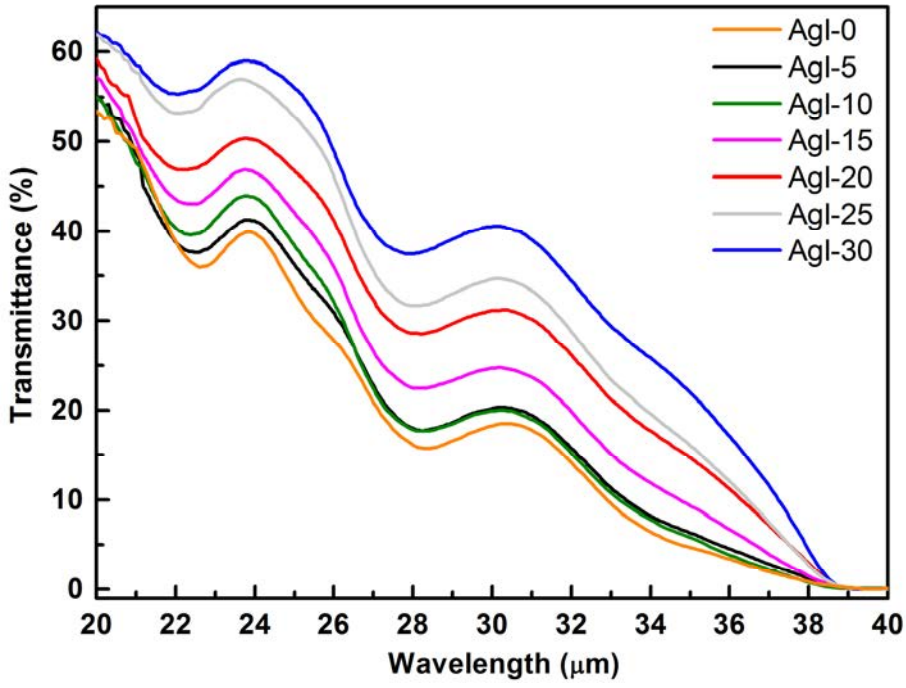

Figure 2.28 Far-IR transmittance of $(GeTe_4)_{100-x}AgI_x$ glasses.

It is very interesting to observe that all these glasses can transmit optical signals up to over 35 μm. The two absorption peaks at around 21 μm (476 cm^{-1}) and 28 μm (357 cm^{-1}) respectively can be explained by the symmetric stretching mode of the $GeTe_4$ tetrahedral. The frequency ω of the fundamental $GeTe_4$ symmetric stretching mode A_1 measured by Raman is around 120 cm^{-1}.[46-48] As this A_1 mode is both Raman and IR active, it is also applicable for IR spectrum analysis. Splitting of this fundamental frequency to harmonics (such as$\omega_2 = 240\ cm^{-1}$, $\omega_3 = 360\ cm^{-1}$and $\omega_4 = 480\ cm^{-1}$) could also cause absorptions. Moreover, the high-order harmonic has a smaller probability of occurrence, and as a result cause limited vibration absorption. For TG-AgI glasses, ω_2, ω_3 and ω_4 roughly correspond to the absorption peaks observed in the FTIR spectra. This indicates that the multi-phonon cut-off of TG-AgI glasses is mainly due to the Ge-Te network vibrations.

Moreover, the light transmission capability is enhanced obviously as AgI percentage increasing. The transmittance at 30 μm of AgI-30 is around 40%. Considering the Fresnel reflection losses caused by its high refractive index, this value is quite attractive for future application as optical lens beyond 25 μm.

Up to now, the most common material used as an infrared optical window up to 40 μm is Cesium Iodide crystal. CsI is a very soft material and it is difficult to obtain well-polished surfaces. Besides, it is water-soluble and can be damaged by moisture in the atmosphere. Another candidate is CdTe crystal, which can transmit infrared signal up to 32 μm. As Cadmium is classified among thevery toxic elements, this material is rather avoided. The GT-AgI glasses, due to their proper hardness, excellent thermal stability and good far-infrared transmission properties, are possible to be reshaped to optical lenses. A typical future application could be in far-infrared astronomy by monitoring emissions from very cold matter (140 Kelvins or less), such as cold clouds of gas and dust in our own galaxy, as well as in nearby galaxies.

2.7 Conclusion

In this chapter, a series of $(GeTe_4)_{100-x}M_x$ (M is Ag, I, or AgI) glasses were synthesized using traditional melt quenching method. The aims are to explore the effect of Ag, I separately and AgI as a salt in $GeTe_4$ glass on glass properties. To achieve this goal, glass physical properties were investigated, including thermal stability, density, electrical and ionic conductivity. Also, a glass structural model is proposed thanks to XRD and EXAFS measurement analyzed by reverse Monte Carlo in close collaboration with Pal Jovary from Budapest. Finally, the glass optical properties, such as infrared transmittance spectra and optical band gap were also studied.

According to these works, it is confirmed that, in the $(GeTe_4)_{100-x}AgI_x$ glasses, as previously observed for the $(GeTe_4)_{100-x}Ag_x$, silver acts as glass former, embedded in the covalent network, rather bonded to Te. On the other hand, for the richest composition in AgI (beyond 15%), the structural data show that silver start to act as modifier, occupy the interstices of the network, engaged rather ionic bond with iodine. It is in good agreement with the ionic conductivity measurements which show an increase of the ionic conductivity for these compositions.

As far as iodine is concerned, the main conclusion is that it acts as an electron absorber and a glass network terminator. By adding AgI, the glass network is opened up gradually, and the glasses switch from an electronic conductor to ionic conductor. Thus, when AgI content is s larger than 15%, the ion diffusion channels are large enough and a clear breaking point can be observed for total conductivity, activation energy, and pre-exponential factor.

It is also noticeable that in general for electronic and optical properties, iodine and silver taken separately act in opposite side. For the $(GeTe_4)_{100-x}AgI_x$ glasses, iodine rather impose it behavior to silver (electronic conductivity, band gap, indexes). Finally, introduce iodine as such a salt is clearly good strategy because iodine do not escape from the melt or from the final glass, the optical transmission in the mid-infrared are conserved and the thermal stability is much higher.

Concerning this last point, the structural data are also helpful to propose some explanation. Silver as glass former makes the glass network more complex in term of nature of bond and coordination numbers. They are mainly bonded to Te. Also, tellurium switches from two to three fold coordinated. Moreover, iodine atoms trap the electron at the origin of the π bonds which rigidify the skeleton of the crystalline phase of the pure tellurium. These structural

features help us to understand why tellurium do not crystallized anymore from this glassy network.

At the end of the chapter, the experiments carried out in Dunkerque show that these vitreous materials could also be very useful for far infrared transmission. To our knowledge, they are the first glass transmitting so far in the infrared. Thus, the GT-AgI glasses are very promising materials both as optical fibers for the mid-infrared means, and as lenses for the far-infrared range.

Reference

[1] J. Heo, M. Rodrigues, S.J. Saggese, G.H. Sigel Jr. Remote Fiber-Optic Chemical Sensing Using Evanescent–Wave Interactions in Chalcogenide Glass Fibers. Applied optics. 1991, 30 (27): 3944-3951

[2] M.L. Anne, E.L.G.L. Salle, B. Bureau, J. Tristant, F. Brochot, C. Boussard-Plédel, H.L. Ma, X.H. Zhang, J.L. Adam. Polymerisation of an Industrial Resin Monitored by Infrared Fiber Evanescent Wave Spectroscopy. Sensors and Actuators B: Chemical. 2009, 137 (2): 687-691

[3] D. Le Coq, K. Michel, J. Keirsse, C. Boussard-Plédel, G. Fonteneau, B. Bureau, J.-M. Le Quéré, O. Sire, J. Lucas. Infrared Glass Fibers for in-Situ Sensing, Chemical and Biochemical Reactions. Comptes Rendus Chimie. 2002, 5 (12): 907-913

[4] V.Q. Nguyen, J.S. Sanghera, B. Cole, P. Pureza, F.H. Kung, I.D. Aggarwal. Fabrication of Arsenic Sulfide Optical Fiber with Low Hydrogen Impurities. J. Am. Ceram. Soc. 2002, 85 (8): 2056-2058

[5] J.S. Sanghera, I.D. Aggarwal. Active and Passive Chalcogenide Glass Optical Fibers for IR Applications: A Review. J. Non-Cryst. Solids. 1999, 256–257 (0): 6-16

[6] C. Conseil, Q. Coulombier, C. Boussard-Plédel, J. Troles, L. Brilland, G. Renversez, D. Mechin, B. Bureau, J.L. Adam, J. Lucas. Chalcogenide Step Index and Microstructured Single Mode Fibers. J. Non-Cryst. Solids. 2011, 357 (11–13): 2480-2483

[7] S. Maurugeon, B. Bureau, C. Boussard-Plédel, A.J. Faber, X.H. Zhang, W. Geliesen, J. Lucas. Te-Rich Ge–Te–Se Glass for the CO_2 Infrared Detection at 15μm. J. Non-Cryst. Solids. 2009, 355 (37–42): 2074-2078

[8] S. Maurugeon, C. Boussard-Plédel, J. Troles, A.J. Faber, P. Lucas, X.H. Zhang, J. Lucas, B. Bureau. Telluride Glass Step Index Fiber for the Far Infrared. J. Lightwave Technol. 2010, 28 (23): 3358-3363

[9] S. Maurugeon, B. Bureau, C. Boussard-Plédel, A.J. Faber, P. Lucas, X.H. Zhang, J. Lucas. Selenium Modified $GeTe_4$ Based Glasses Optical Fibers for Far-Infrared Sensing. Opt. Mater. 2011, 33 (4): 660-663

[10] A.A. Wilhelm, C. Boussard-Plédel, Q. Coulombier, J. Lucas, B. Bureau, P. Lucas. Development of Far-Infrared-Transmitting Te Based Glasses Suitable for Carbon Dioxide Detection and Space Optics. Adv. Mater. 2007, 19 (22): 3796-3800

[11] Z. Yang, P. Lucas. Tellurium Based Far Infrared Transmitting Glasses. J. Am. Ceram. Soc. 2009, 92 (12): 2920-2923

[12] S. Dai, G. Wang, Q. Nie, X. Wang, X. Shen, T. Xu, L. Ying, J. Sun, K. Bai, X. Zhang. Effect of CuI on the Formation and Properties of Te-Based Far Infrared Transmitting Chalcogenide Glasses. Infrared Physics & Technology. 2010, 53 (5): 392-395

[13] C. Conseil, J.-C. Bastien, C. Boussard-Plédel, X.-H. Zhang, P. Lucas, S. Dai, J. Lucas, B. Bureau. Te-Based Chalcohalide Glasses for Far-Infrared Optical Fiber. Opt. Mater. Express. 2012, 2 (11): 1470-1477

[14] X. Wang, Q. Nie, G. Wang, J. Sun, B. Song, S. Dai, X. Zhang, B. Bureau, C. Boussard, C. Conseil, H. Ma. Investigations of Ge–Te–AgI Chalcogenide Glass for Far-Infrared Application. Spectrochim. Acta, Part A. 2012, 86 (0): 586-589

[15] V.S. Shiryaev, A.P. Velmuzhov, M.F. Churbanov, A.D. Plekhovich, C. Boussard-Plédel, J. Troles, C. Conseil, V.G. Plotnichenko. Preparation and Investigation of High Purity

Ge–Te–AgI Glasses for Optical Application. Journal of Non-Crystalline Solids. 2013, 377 (0): 1-7

[16] K. Ramesh, S. Asokan, K. Sangunni, E. Gopal. Glass Formation in Germanium Telluride Glasses Containing Metallic Additives. Journal of Physics and Chemistry of Solids. 2000, 61 (1): 95-101

[17] R.J. MacKinnon, J. Heo, G.H. Sigel Jr. Optical and Physical Effects of Iodine in Chalcohalide Glasses. In: OE/LASE'90, 14-19 Jan., Los Angeles, CA: International Society for Optics and Photonics, 1990: 101-108

[18] V.Q. Nguyen, J.S. Sanghera, I.D. Aggarwal, I.K. Lloyd. Physical Properties of Chalcogenide and Chalcohalide Glasses. Journal of the American Ceramic Society. 2000, 83 (4): 855-859

[19] P. Lucas, C. Conseil, Z. Yang, Q. Hao, S. Cui, C. Boussard-Pledel, B. Bureau, F. Gascoin, C. Caillaud, O. Gulbiten, T. Guizouarn, P. Baruah, Q. Li, J. Lucas. Thermoelectric Bulk Glasses Based on the Cu-As-Te-Se System. Journal of Materials Chemistry A. 2013, 1 (31): 8917-8925

[20] T. Minami. Fast Ion Conducting Glasses. Journal of Non-Crystalline Solids. 1985, 73 (1): 273-284

[21] H.L. Tuller, M. Barsoum. Glass Solid Electrolytes: Past, Present and near Future-the Year 2004. Journal of Non-Crystalline Solids. 1985, 73 (1): 331-350

[22] M. Tatsumisago, T. Saito, T. Minami. Fabrication of Mesoscopic Composites Composed of A-AgI and AgI-Based Superionic Glass. Thermochimica acta. 1996, 280: 333-341

[23] T. Usuki, S. Saito, K. Nakajima, O. Uemura, Y. Kameda, T. Kamiyama, M. Sakurai. Structural and Electrical Properties of AgI Dispersed as-Chalcogenide Glasses. Journal of Non-Crystalline Solids. 2002, 312: 570-574

[24] C. Varsamis, E. Kamitsos, G.D. Chryssikos. Structure of Fast-Ion-Conducting AgI-Doped Borate Glasses in Bulk and Thin Film Forms. Physical Review B. 1999, 60 (6): 3885

[25] Y. Kowada, H. Adachi, M. Tatsumisago, T. Minami. Electronic States of Ag Ions in AgI-Based Superionic Conducting Glasses. Journal of Non-Crystalline Solids. 1998, 232: 497-501

[26] T.-C. Wen, W.-C. Chen. Gelled Composite Electrolyte Comprising Thermoplastic Polyurethane and Poly (Ethylene Oxide) for Lithium Batteries. Journal of power sources. 2001, 92 (1): 139-148

[27] Z. Borisova. Glassy Semiconductors. New York: Plenum, 1981

[28] A. Giridhar, S. Mahadevan. Silver as a Dopant and as a Constituent in As-Ag-Te Glasses: Electrical Conductivity. Journal of Non-Crystalline Solids. 1996, 197 (2–3): 228-234

[29] S. Stehlik, J. Kolar, M. Bartos, M. Vlcek, M. Frumar, V. Zima, T. Wagner. Conductivity in Ag–As–S (Se, Te) Chalcogenide Glasses. Solid State Ionics. 2010, 181 (37): 1625-1630

[30] M. Ureña, A. Piarristeguy, M. Fontana, B. Arcondo. Ionic Conductivity (Ag^+) in AgGeSe Glasses. Solid State Ionics. 2005, 176 (5): 505-512

[31] C.P. Poole Jr. Encyclopedic Dictionary of Condensed Matter Physics. Academic Press, 2004

[32] C. Julien, G. Nazri. Solid State Batteries: Materials Design and Optimization: Materials Design and Optimization. London: Kluwer academic publishers, 1994

[33] C. Moynihan, D. Gavin, R. Syed. Pre-Exponential Term in the Arrhenius Equation for Electrical Conductivity of Glass. Le Journal de Physique Colloques. 1982, 43 (C9): C9-395-C399-398

[34] M. Kawasaki, J. Kawamura, Y. Nakamura, M. Aniya. Ionic Conductivity of $Ag_x(GeSe_3)_{1-x}(0\leq X\leq 0.571)$ Glasses. Solid State Ionics. 1999, 123 (1): 259-269

[35] A. Pradel, N. Kuwata, M. Ribes. Ion Transport and Structure in Chalcogenide Glasses. Journal of Physics: Condensed Matter. 2003, 15 (16): S1561

[36] M. Sakurai, F. Kakinuma, E. Matsubara, K. Suzuki. Partial Structure Analysis of Amorphous $Ge_{15}Te_{80}M_5$ (M= Cu, Ag and In). Journal of Non-Crystalline Solids. 2002, 312: 585-588

[37] P. Lucas, Z. Yang, M.K. Fah, T. Luo, S. Jiang, C. Boussard-Pledel, M.-L. Anne, B. Bureau. Telluride Glasses for Far Infrared Photonic Applications. Optical Materials Express. 2013, 3 (8): 1049-1058

[38] L.G. Aio, A.M. Efimov, V.F. Kokorina. Refractive Index of Chalcogenide Glasses over a Wide Range of Compositions. Journal of Non-Crystalline Solids. 1978, 27 (3): 299-307

[39] S. Danto, P. Houizot, C. Boussard-Plèdel, X.H. Zhang, F. Smektala, J. Lucas. A Family of Far-Infrared-Transmitting Glasses in the Ga–Ge–Te System for Space Applications. Adv. Funct. Mater. 2006, 16 (14): 1847-1852

[40] L. Zhenhua, G. Frischat. The Formation and Infrared Optical Properties of Some Chalcogenide and Chalcohalide Glasses. Journal of Non-Crystalline Solids. 1993, 163 (2): 169-176

[41] J. Heo, J.D. Mackenzie. Chalcohalide Glasses: I. Synthesis and Properties of Ge-S-Br and Ge-S-I Glasses. Journal of Non-Crystalline Solids. 1989, 111 (1): 29-35

[42] S. Lukic, S. Skuban, D. Petrovic, A. Petrovic, M. Garic. Characteristics of Complex Non-Crystalline Chalcogenides from the Ge-As-S-Se-I System. Journal of Optoelectronics and Advanced Materials. 2004, 6: 755-768

[43] M.M. El-Hawary, R. El-Mallawany, A.M. Abousehly, H.H. Hegazy. Infrared Transmission of Chalcohalide Glasses in the Ge–Se–Te–I System. Infrared Physics & Technology. 2012, 55 (4): 256-262

[44] M. Frumar, T. Wagner. Ag Doped Chalcogenide Glasses and Their Applications. Current Opinion in Solid State and Materials Science. 2003, 7 (2): 117-126

[45] M. Baazouzi, M.-T. Soltani, M. Hamzaoui, M. Poulain, J. Troles. Optical Properties of Alkali-Antimonite Glasses and Purified Processes for Fiber Drawing. Optical Materials. 2013, 36 (2): 500-504

[46] G.B. Fisher, J. Tauc, Y. Verhelle. Amorphous and Liquid Semiconductors. London: Taylor & Francis, 1974: 1259

[47] K. Andrikopoulos, S. Yannopoulos, A. Kolobov, P. Fons, J. Tominaga. Raman Scattering Study of Gete and $Ge_2Sb_2Te_5$ Phase-Change Materials. Journal of Physics and Chemistry of Solids. 2007, 68 (5): 1074-1078

[48] S. Sen, E. Gjersing, B. Aitken. Physical Properties of $Ge_xAs_{2x}Te_{100-3x}$ Glasses and Raman Spectroscopic Analysis of Their Short-Range Structure. Journal of Non-Crystalline Solids. 2010, 356 (41): 2083-2088

Chapter 3.

Te-Ge-AgI Glass for Far-Infrared Biochemical Sensing

3.1 Introduction

Chalcogenide glasses, based on sulfur, selenium, tellurium and other additional elements, are good candidates for designing sensors working in the infrared range, especially as optical fibers[1-5]. The leading mechanism is to take advantage of the evanescent wave generated at fiber surface to capture the excitation of the vibrations of chemical bonds within the molecules in contact with the fiber. For numerous molecules and biomolecules, the fingerprint region, which covers a series of complex and specific absorption bands, is located between 2.5 and 25 μm. However, for S and Se-rich chalcogenide glass fibers, light atomic weight causes the multi-phonon cut-off wavelength to be around 6 μm[6,7] and 12 μm[6,8,9], respectively. This is a strong and detrimental limitation. Te-rich chalcogenide glasses, due to the Te atom heaviness, exhibit the ability to transmit light in the middle and far infrared ranges up to 28 μm[10-13] and therefore has drawn tremendous interests. In order to test the fundamental vibrations (stretching and bending) of molecules and biomolecules whose main absorption bands are beyond 12 μm, such as benzene[14] and chloroform [15], optical sensor of high selectivity and sensitivity should be developed based on telluride glass fiber. Meanwhile, as described in the first chapter, development of telluride glass fiber is also relevant in the field of extraterrestrial exploration. Carbon dioxide, which is one of the markers of potential life on telluric exoplanets, can be more easily analyzed by monitoring infrared absorption peak at 15 μm. Thus, telluride glass fibers have also to be fabricated for remote detection of CO_2 in Darwin mission (ESA) or Terrestrial Planet Finder (NASA) [9,16,17].

Nevertheless, due to the strong metallic character of tellurium, Te-based glasses are difficult to control and vitrify. Different strategies have already been considered to enhance glass stabilization by introducing some other elements in $GeTe_4$, such as selenium (Te-Ge-Se)[17-19], iodine (Te-Ge-I)[11], and gallium (Te-Ge-Ga)[10]. Nevertheless, the requirement of glass stabilization is very demanding in order to obtain a fiber without surface crystallization during fiber drawing process, and most of these systems cannot provide glasses easy to draw. Te-Ge-Se glass, with which an experimental single-mode fiber has been successfully prepared using capillary method, is a good candidate. However, the existence of selenium in the Te-based glass can block the light in the far infrared range due to the light atom weight of Se. As a result, Te-Ge-AgI, as a pure telluride glass system, has been developed.

Very recently, $GeTe_4$ glass containing 10 % of silver iodine showed no crystallization peak by thermal analysis and appeared as an interesting candidate [20-22]. However, it was

quite difficult to obtain fibers from the glass preforms and their optical losses were larger than 20 dB/m, which is unacceptable for any application.

The aim of the present work is to develop a protocol of purification in order to obtain stable glasses which could be drawn into fibers with lower attenuations. Moreover, they could be drawn into optical tapered fibers in order to implement Fiber Evanescent Wave Spectroscopy (FEWS) experiments. Molecules such as dichloromethane, chloroform and toluene are selected for sensing due to their strong absorptions beyond 12 μm. Other biological or chemical agents such as serum, milk, butter and gasoline are also chosen for exploration of the potential application in daily life.

3.2 Glass selection, synthesis, purification and characterization

3.2.1 Selection of the glass composition

According to the results shown in chapter 2, the thermal analysis, at a heating rate of 10°C/min, have shown that $(GeTe_4)_{100-x}AgI_x$ (x=10, 15 and 20) glasses do not exhibit any obvious crystallization peak. Moreover, by heat treatment at 30°C above T_g of the $(GeTe_4)_{90}AgI_{10}$ glass, the first Te crystalline peaks appeared only after 40 hours (Figure 3.1) [20]. This experiment result confirms a very good stability against crystallization of these new pure tellurium glasses. Thus, this Te-Ge-AgI glass system is a potential proper amorphous material for infrared fiber preparation.

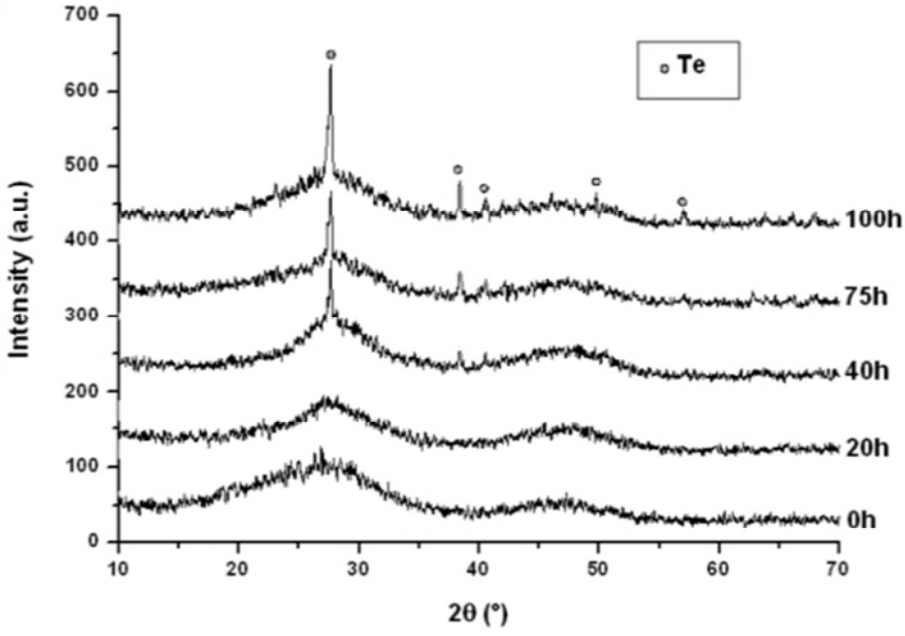

Figure 3.1 XRD diagrams of $(GeTe_4)_{90}AgI_{10}$ annealed glasses at Tg + 30°C.

It has been shown in both Te-Ge-Ga[10] and Te-Ge-Se[19] glass systems that the most stable compositions are usually slightly richer in germanium compared to the ideal stoichiometry corresponding to four chalcogens per germanium. This is also the fundamental reason for us to set the composition of our Te-Ge-Se glasses to be $Ge_{21}Te_{79-x}Se_x$ (x=3, 3.5 and 8), containing germanium slightly higher than the ideal stoichiometry which acts as stabilization agent. Therefore, in this chapter, $(Ge_{0.21}Te_{0.79})_{100-x}AgI_x$ (x=10, 15, and 20) glasses were chosen for single index far-infrared preparation and named as TG-AgI10, TG-AgI15 and TG-AgI20 respectively.

3.2.2 Synthesis of the bulk glass

Similar to Te-Ge-Se glass system, for obtaining optical fibers with limited defects and impurities, high purity Te-Ge-AgI glass preforms should be prepared. Based on previous study on the purification of Te-Ge-Se glasses in Chapter 1, two-steps chemical-distillation purification will be directly used here to purify Te-Ge-AgI glasses. To justify the effectiveness of the two-steps purification method, Ge-Te-AgI glass was also prepared by simply melting the raw elements in a sealed vacuum silica tube, the bulk transmittance spectra of glasses with and without purification will be compared.

3.2.2.1 Glass synthesis without purification

To prepare unpurified Te-Ge-AgI glasses, silver iodine (5N, Alfa Aesar), germanium and pre-purified tellurium were weighted and settled in a cleaned 7 mm quartz tube under a controlled atmosphere of argon in a glove box. After a few hours under vacuum (10^{-5} millibar) to remove the last traces of water and oxygen, the silica ampoule was sealed, and the melt-quenching method was applied. The detailed preparation procedure was thoroughly explained in Chapter 1, and the schematic diagram is shown in Figure 1.6.

The sealed quartz tube containing the raw elements is placed into a rocking furnace. After homogenization at 800˚C for 10 hours, the furnace is inclined to induce a separation between melts and bubbles inside the melt. After cooling to 450°C, the melt is quenched in water and annealed at 145˚C for 3 hours in a chamber furnace. The synthesis parameters are listed in Figure 3.2.

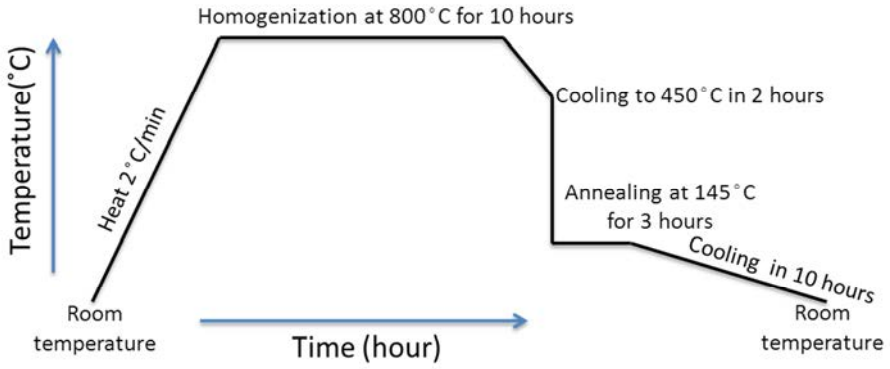

Figure 3.2 Thermal profile for the synthesis of Te-Ge-AgI glasses.

3.2.2.2 Synthesis of the glass with a by two-steps purification process

To prepare high quality optical fiber with low optical losses, it should be known that, due to the long-distance light transmission in fiber, any tiny absorption caused by the presence of impurities in bulk glass can be significantly amplified in fiber. Therefore, preforms with high purity have to be prepared. This is the key operation, of course for the optical quality of the glass, but also to avoid any nucleation of microcrystals in the steps of shaping the preform.

As introduced before, germanium purification is difficult owning to high melting temperatures of both Ge and GeO_2. As a result, extra purification during glass preform preparation procedure should be executed. Silver iodine is a photosensitive compound which can decompose into silver and iodine under ultraviolet. But it could be considered stable at the time scale of the experiment. Moreover, AgI shows much less tendency to react with O_2 and H_2O in air compared with Ge and Te. Meanwhile, due to its intrinsic high purity of 5N, AgI needs no special purification.

From the study of different glass purification methods in Chapter 1, it has been shown that the two-steps chemical-distillation method is an effective purification technique. So, this method was applied to the following compositions TG-AgI10, TG-AgI15, and TG-AgI20

During the chemical purification step, Te (6N), Ge (5N) were weighed in the adequate proportion and melted with 100 ppm of Al at 800 °C for 10 hours. The aluminum acts as an oxygen getter and traps the oxygen of the oxide during the homogenization period. After cooling the melt at 500˚C, the amorphous material was obtained by quenching, and then annealed at 150˚C for 3 hours.

During the distillation step, the mixture of Te, Ge and Al_2O_3 previously obtained was distilled [23,24] through a filter to reaction silica tube containing AgI (5N). By this way, the

alumina generated can be separated from Te and Ge, and left in the chamber. The reaction tube was then sealed under vacuum and homogenized at 800 ˚C for 10 hours. After cooling to 450˚C, the melt was quenched in water and annealed at 145˚C for 3 hours. A typical glass preform, with its diameter and length to be around 7 and 150 mm respectively, was obtained. To obtain high quality glass preforms without bubbles inside or at the surface of the glass, the rocking furnace should be kept at a vertical position for 1 hour at 800 ˚C before it drops to the quenching temperature. The distillation procedure, thermal profile for Te-Ge-AgI glass synthesis and a typical Te-Ge-AgI glass preform obtained are shown in Figure 3.3. The glass obtained after annealing could be used directly for single index fiber drawing.

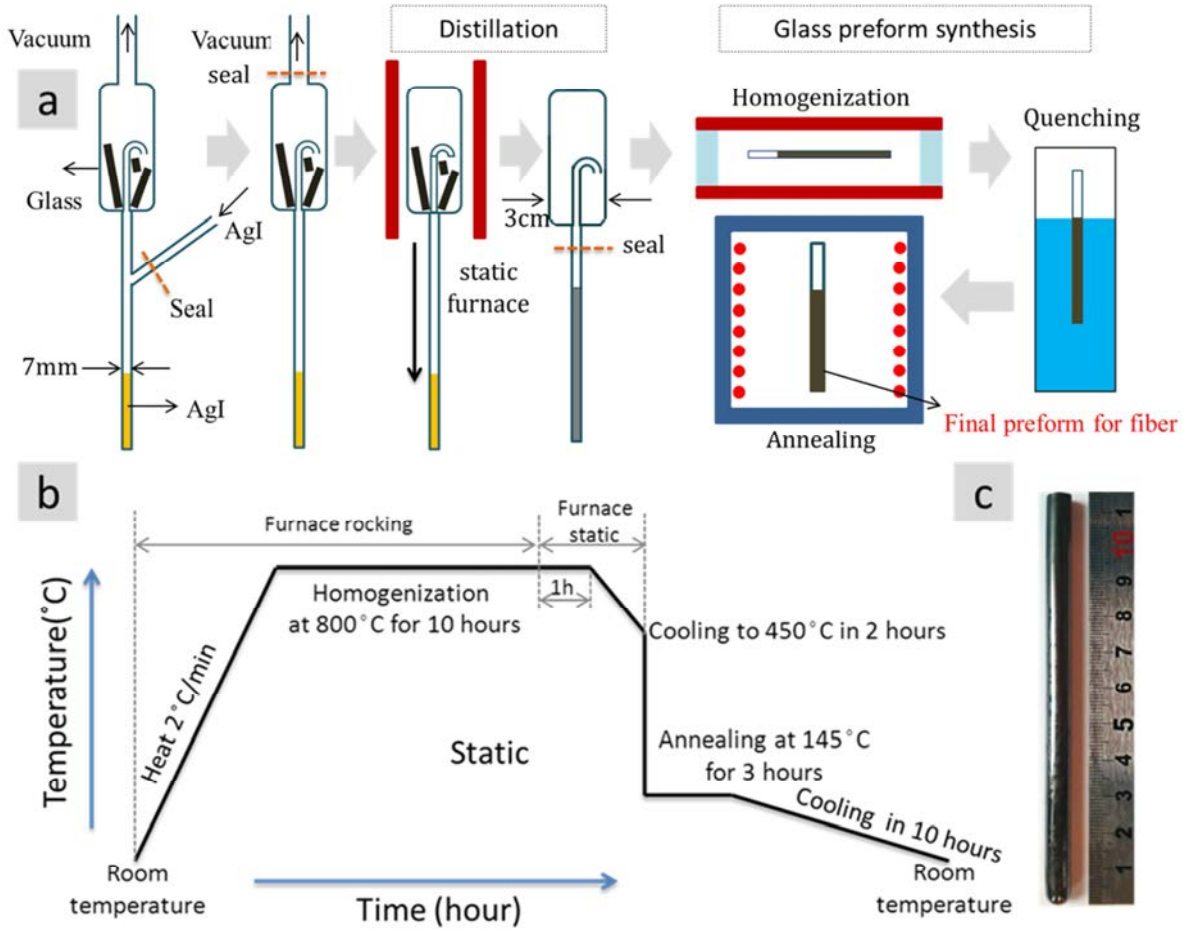

Figure 3.3 The distillation procedure (a), thermal profile (b) for Te-Ge-AgI glass synthesis and a typical macroscopic image of Te-Ge-AgI glass preform.

3.2.3 Characterization of bulk glass

To prepare a high-quality glass preform for fiber drawing, a compromise must be found between efficient purification and conservation of the stoichiometry of the glass. The recent results obtained by V.S. Shiryaev[19] showed that complicated multi-steps purification

procedure could greatly alter the real content of AgI in the glass, and as a result destroy the glass thermal stability. Therefore, the energy-dispersive X-ray spectroscopy (EDS) was executed to control the actual glass composition. The Differential Scanning Calorimetry (DSC) was also performed at a heating rate of 10˚C/min up to 320°C to verify the glass preform stability. Finally, optical transmittance of bulk glasses with and without purification was also applied to ensure the effectiveness of purification.

3.2.3.1 Elemental analysis of Te-Ge-AgI glasses by EDS

EDS was used to analyze the real composition of TG-AgI10, TG-AgI15, and TG-AgI20 glass preforms (Table 3.1). Different regions in the center (point 2) or at the edge of the cross-section (point 1 and 3) were analyzed to verify the homogeneity of Te-Ge-AgI glasses. All the preforms are obtained after two-steps purification.

Table 3.1 Elemental Analysis of Te-Ge-AgI Glasses

Composition	TG-AgI10	TG-AgI15	TG-AgI20
Point 1	$Ge_{17.7}Te_{65.1}Ag_{8.8}I_{8.4}$	$Ge_{15.2}Te_{59.6}Ag_{14.1}I_{11.1}$	$Ge_{13.5}Te_{53.2}Ag_{17.9}I_{15.4}$
Point 2	$Ge_{15.6}Te_{66.6}Ag_{9.0}I_{8.8}$	$Ge_{15.5}Te_{58.9}Ag_{14.2}I_{11.4}$	$Ge_{12.9}Te_{53.7}Ag_{18.1}I_{15.3}$
Point 3	$Ge_{17.6}Te_{64.5}Ag_{9.3}I_{9.0}$	$Ge_{15.6}Te_{58.9}Ag_{14.1}I_{11.4}$	$Ge_{13.9}Te_{52.4}Ag_{18.1}I_{15.6}$
Average comp.	$Ge_{17.0}Te_{65.4}Ag_{9.0}I_{8.6}$	$Ge_{15.4}Te_{59.2}Ag_{14.1}I_{11.3}$	$Ge_{13.5}Te_{53.1}Ag_{18.0}I_{15.4}$
Theoretical comp.	$Ge_{17.2}Te_{64.6}Ag_{9.1}I_{9.1}$	$Ge_{15.5}Te_{58.4}Ag_{13.0}I_{13.0}$	$Ge_{14.0}Te_{52.7}Ag_{16.7}I_{16.7}$

Comparing the real compositions of 3 selected regions, it can be concluded that, taking into account the accuracy of EDS (~ 1%), the prepared glass preforms are homogeneous. Comparing with the Te-Ge-I glass system in Chapter 2 which has a large and unpredictable loss of iodine during synthesis, it is finally much more efficient to introduce iodine as a salt rather than in its elemental form, because the majority remains in the glass network and don't escape as previously observed. However, compared with the theoretical values, the concentrations of germanium and iodine are still a bit lower than the designed composition. Similar to $(GeTe_4)_{100-x}AgI_x$ glass system in Chapter 2, this could be explained by the generation of germanium iodide during synthesis process.

As a matter of fact, germanium (II) iodide (GeI_2) is a crystalline solid and can be sublimed at 240°C in a vacuum. Germanium (IV) iodide (GeI_4) is a crystalline solid with melting point 144°C and boiling point 440 °C. Consequently, during glass synthesis, although the majority of Ge and I were kept in the glass structure, there are still minor quantities of GeI_2 and GeI_4 which could escape due to their instability at high temperature. Indeed a yellow vapor could be observed on the top of glass liquid before quenching. During quenching, yellow crystals

are formed in the upper part of the silica tube. The analysis of this compound by EDS gives the following composition $Ge_{23.2}I_{76.8}$, which is very close to GeI_4.

3.2.3.2 Thermal stability of glasses

For two-steps purified AgI-doped glass preforms, due to the small glass component variations, it is necessary to confirm the glass stability. The DSC curves obtained from a DSC Q20 (TA Instruments) at a heating rate of 10˚C/min are shown in Figure 3.4.

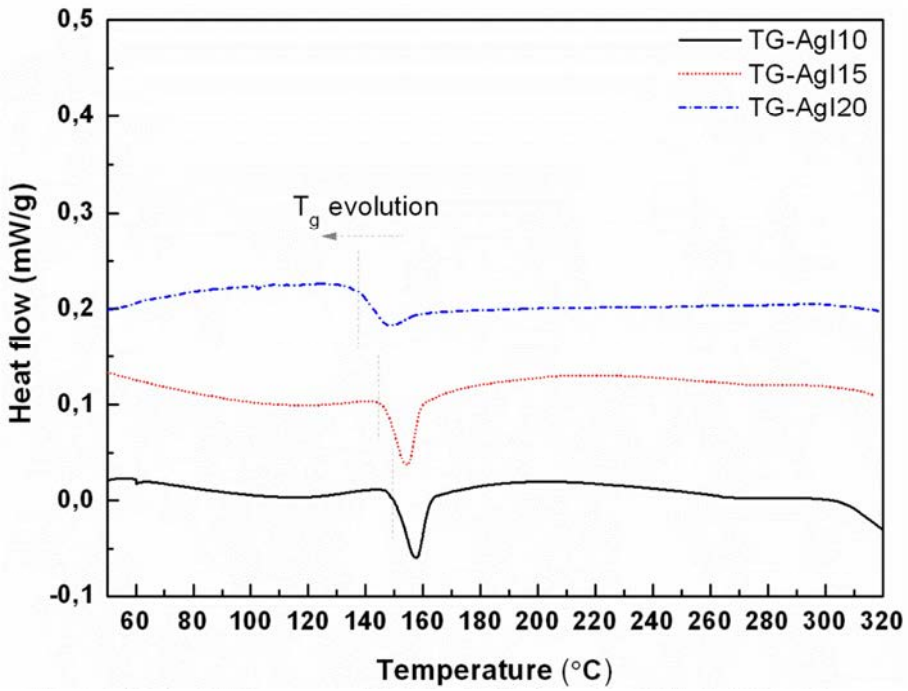

Figure 3.4 Thermal stability of two-steps purified TG-AgI glass preforms

Similar to $(GeTe_4)_{100-x}AgI_x$ (x=10, 15, and 20) glasses introduced in Chapter 2, the TG-AgI10, TG-AgI15 and TG-AgI20 glass preforms also show no visible crystallization peak up to 320°C. The small loss of Ge and I would not undermine the glass stability. Compared with Te-Ge-Se glass system introduced in Chapter 1, which shows a significant exothermic crystallization peak before 300 °C, the formability of the glasses from the Ge-Te-AgI system are more stable against crystallization.

Meanwhile, as AgI content increases, the glass transition temperature T_g also shows an obvious decrease, which is consistent with previous results. This phenomenon is caused by iodine, acting as a kind of glass structure terminator.

3.2.3.3 Optical transmittance

The bulk transmittance spectra of the TG-AgI10 glass with and without purification were tested and compared as an example in order to verify the efficiency of the chemical-distillation method (Figure 3.5).

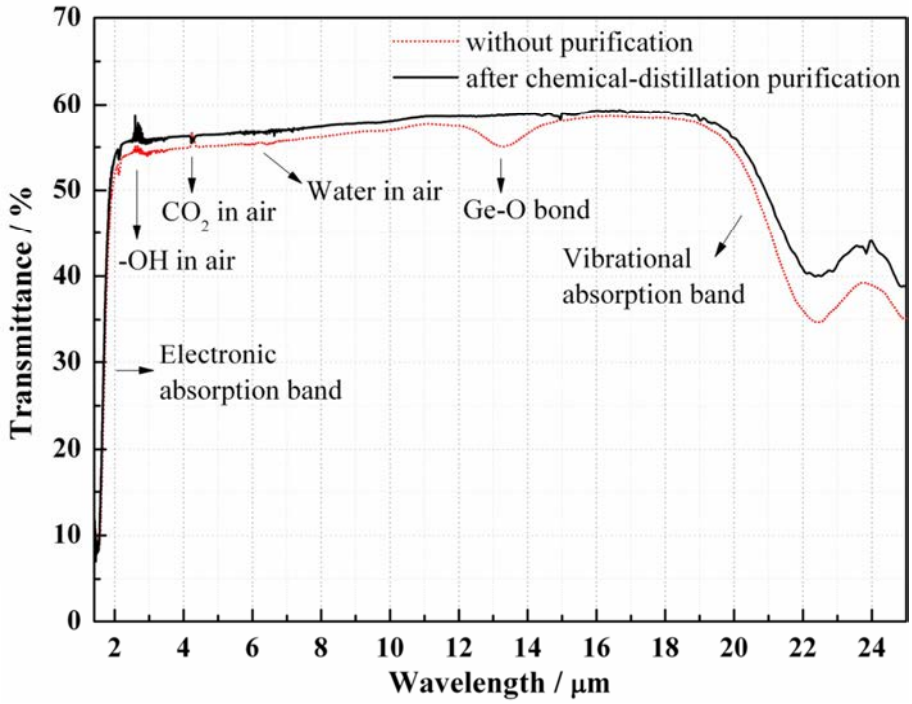

Figure 3.5 The bulk optical transmittance of TG-AgI10 glasses with (black line) and without (red dotted line) chemical-distillation purification.

After purifications, the Ge-O absorption peak located at 13.3 μm has been totally removed. This goal was achieved thanks to the introduction of aluminum in the batch. Indeed, as described before, Al acts as an oxygen getter and reacts with the oxygen in oxides and water. The Al_2O_3 generated has an intrinsic low equilibrium vapor pressure at high temperature, and is mostly kept in the distillation chamber. The peaks at 2.70, 4.26 and 6.30 μm are caused by the concentration differences of –OH, CO_2 and H_2O vapor in air between sample and reference tests. After purification, the glass shows a very flat transmission region from 2.2 to 19.0 μm. Here, it should be emphasized that the low transmittance, less than 60%, is caused by the Fresnel losses caused by the high refractive index of the glass.

3.3 Preparation of low attenuation single index fiber

3.3.1 Glass surface defects and its influence on light propagation

3.3.1.1 Glass surface defects formation mechanism

The surface of the Te-Ge-AgI glasses always showed lots of defects after annealing. In the past, this phenomenon has already been observed for glasses, especially for telluride glasses containing iodine. In this part, TG-AgI10 will be studied as an example in order to find out the causes of surface defects and its influence on light propagation of optical fiber.

After annealing, a deposition could be found in the gap between the glass preform and the silica tube. Some of them are attached to glass surface and cannot be removed easily. These micro-scale defects can be easily observed by optical microscopy (Figure 3.6 a). Moreover, EDS was used to determine the composition of this compound collected by slightly scraping the preform surface (Figure 3.6 b).

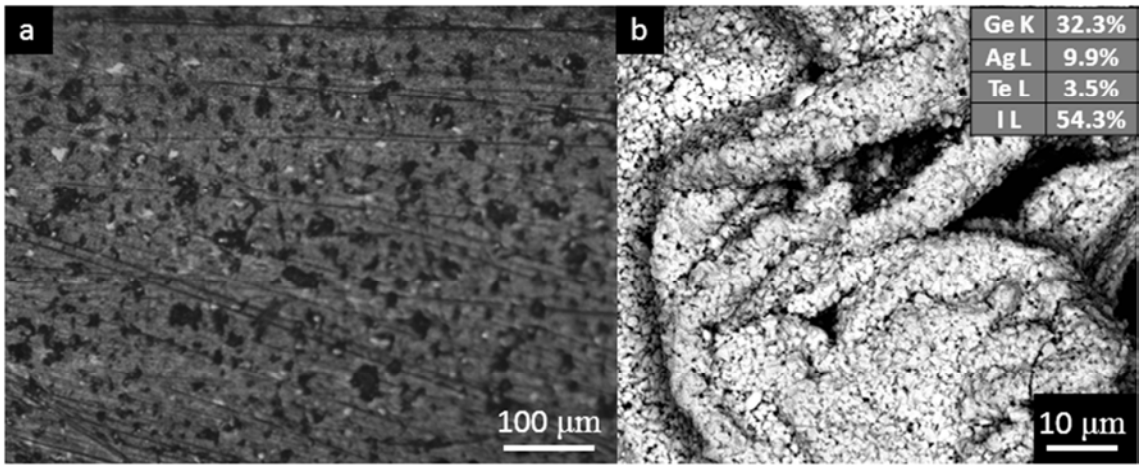

Figure 3.6 The optical microscope image of TG-AgI10 preform (a) and electron microscope image of deposition on preform (b).

As its main components are Ge and I, based on low melting point (T_m=144°C) of GeI_4, it is proposed that, during annealing at 145°C, the yellow GeI_4 crystal condensed after quench in the upper part of the silica tube became vapor and went into the gap between glass preform and silica tube and re-condensed as temperature decreasing. The crystal size is around 1 µm.

To confirm this proposal, the quenching and annealing should be separated. Thus, a TG-AgI10 glass was firstly quenched. Then the glass is transferred to a novel silica tube under vacuum for annealing (Figure 3.7).

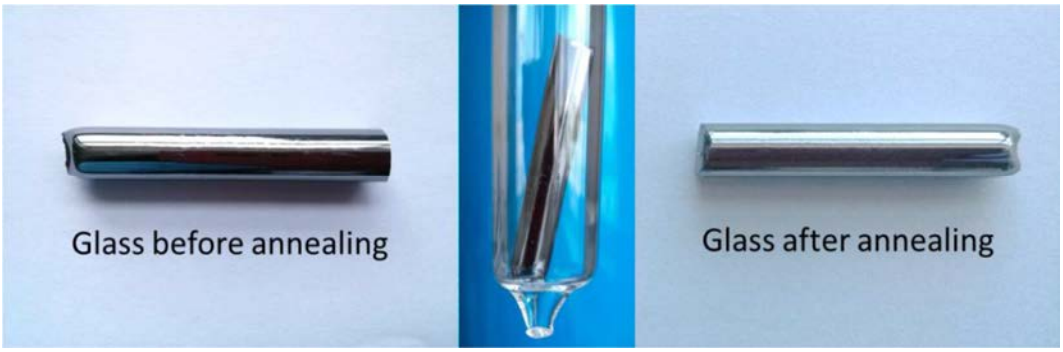

Figure 3.7 Images of TG-AgI10 glass before and after novel annealing treatment

The glass surface is shiny after quench. After annealing in a novel silica tube, no new deposition can be observed on glass and the glass surface is still shiny. This experiment proves that the deposition appears during the annealing phase of the synthesis. However, the glass was exposed in air during the transfer from original to new silica tube, and the glass should be pumped under vacuum at least 1 hour before sealing and starting the annealing phase. The risks of the oxidation and the cracks caused by tension inside the glass before the annealing make this method difficult to be applied in preform preparation.

3.3.1.2 Influence of fiber surface defects on light propagation

In order to study the fiber surface defects on light propagation property, a single index fiber was drawn from the original TG-AgI10 preform with surface deposition.

Similar to Te-Ge-Se glass fiber preparation, the fabrication of the fibers from Te-Ge-AgI preforms were carried out under a He controlled atmosphere thanks to a home-made fiber tower. During the drawing step, the diameters of the fiber were controlled to be 350 μm by using the fixed preform feed speed and coordinating drum speed. The detailed fiber drawing parameters are listed in Table 3.2.

Table 3.2 Typical parameters for TG-AgI fiber drawing

Preform and fiber size			
Diameter of rod:	7.0mm	Diameter of fiber:	350μm
Parameters before fiber drawing			
Flow of argon:	3L/min	Flow time:	2 hours
Parameters during fiber drawing			
Flow of helium:	3L/min	Water elimination temp.	120°C
Heating rate:	10°C/min	Fiber drawing temperature:	280°C
Preform speed:	2mm/min	Drum speed:	0.80m/min
Fiber tension:	15 grams		

Compared with Te-Ge-Se fiber (Table 1.3), the Te-Ge-AgI fiber drawing parameters was slightly adjusted, such as the flow of helium and fiber drawing temperature. Actually, the

fiber drawing requirement of Te-rich glasses is very demanding. Several degrees of temperature alteration may cause significant viscosity change. As a result, the processing parameters are hard to be optimized. This is also one of the difficulties in Te-rich glass fiber drawing.

After fiber drawing, the surface morphology variation from preform (a) to shrinkage part (b to e) to fiber (f) was monitored by an optical microscope (Figure 3.8).

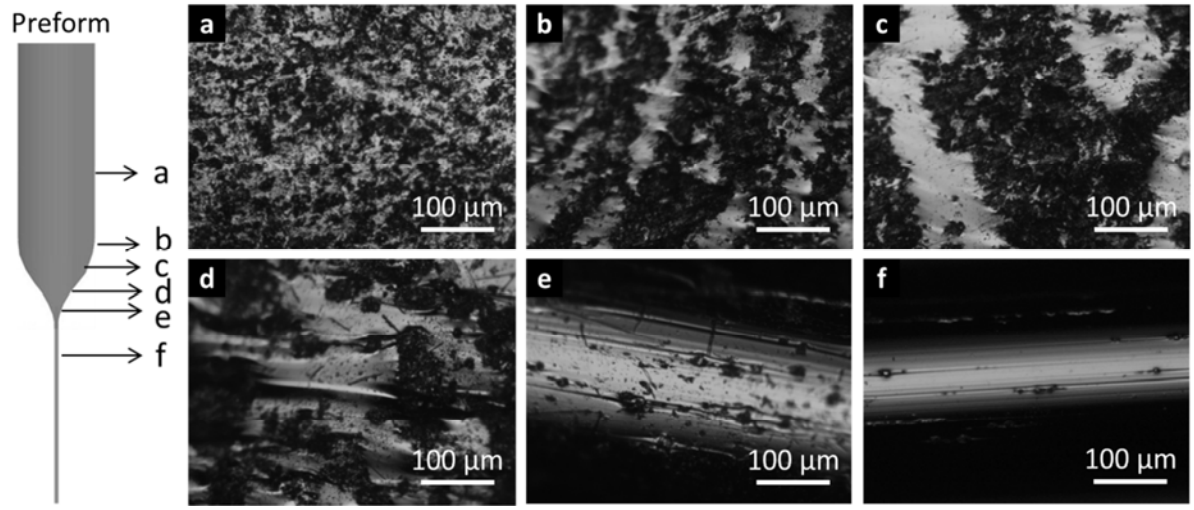

Figure 3.8 Optical microscope images of TG-AgI10 glass surface variation during fiber drawing process (from a to e) and the surface morphology of the fiber obtained (f).

It can be obtained from Figure 3.8 that during fiber drawing process, due to the increase of surface area, fresh shiny glass without deposition appeared more and more. The homogeneous deposition film on glass preform started to show a “zebra pattern”, then gradually turned into numerous isolated small areas, and finally became micro-scale surface defects on the obtained optical fiber. Indeed, the surface defects could also act as nucleating agents and accelerate surface crystallizations when the preform is heated during the fiber drawing process for example.

It has been concluded by a number of researchers[25] that surface roughness is the primary influence preventing waveguides from achieving their theoretical limits. Actually, the surface roughness can be described as perturbations in the shape of the waveguide on a size scale similar to the wavelength of the transmitted light. In ray optic terms, the disruption of specular reflection by a rough surface explains the increased attenuation. Even the nano-scale defects can have a profound impact on the transmission of a waveguide due to the large number of reflections over the length of the guide.

Therefore, it can be predicted that due to distortion of the glass-air interface, the surface diffraction could be introduced and as a result generate an extra attenuation. The optical loss of the fiber prepared was measured using cutback technique by Bruker Tensor 27 FT-IR spectrometer with a mercury cadmium telluride (MCT) detector. The attenuation curve is shown in Figure 3.9.

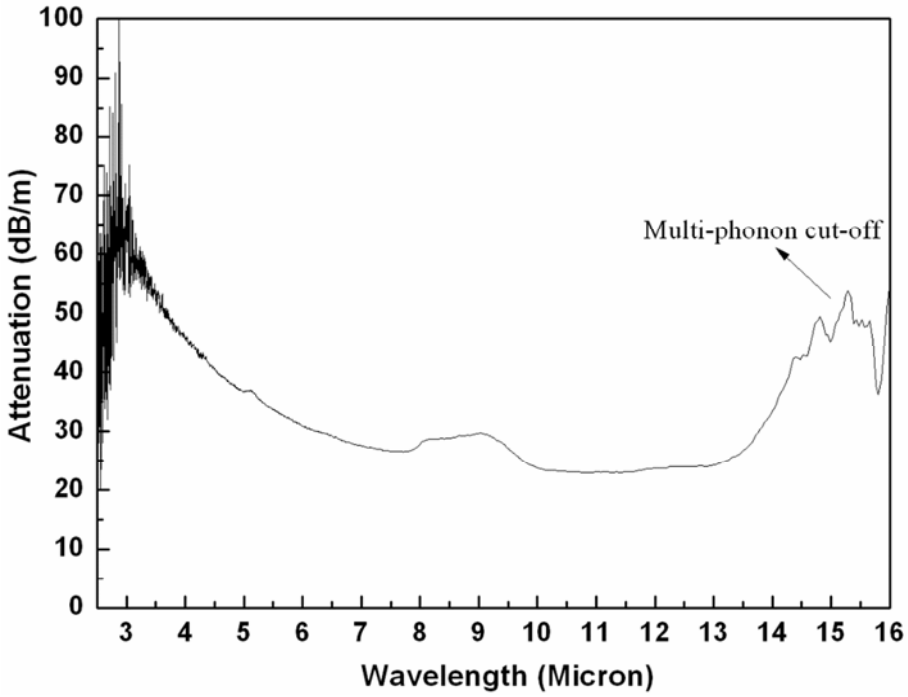

Figure 3.9 Optical loss of TG-AgI10 single index fiber obtained from original preform

This Te-based glass fiber shows a large transmission window up to 16 μm. However, the minimum attenuation value is around 23 dB/m between 10 and 12 μm, which is unacceptable for any application. Based on the previous analysis of Figure 3.8, it is believed that besides intrinsic optics loss, the majority sources of loss in fiber optics can be categorized as a large light scattering from surface roughness during the reflection at the glass-air interface. Thus, the glass surface defects should be removed using a proper technique.

3.3.2 Preparation of low attenuation fiber

3.3.2.1 Selection of proper polishing parameters

To obtain high quality optical fibers, the surface defects of the preforms should be thoroughly removed before fiber drawing. Usually, chemical etching and mechanical polishing are the two main treatment methods used for improving the quality of the preform surfaces.

Research on chemical etching

The key point in chemical etching is to keep the bulk glass composition constant. So, it is necessary to develop a corrosion process which eliminates all the elements with the same rate. In this part of the work, strong acid H_2SO_4 (98%, 100ml) with a strong oxidant H_2O_2 (30%, 30ml) was used as an oxidizing agent. This solution is famous for its application in etching of the Te-As-Se glass fiber in the aim of elaborating tapered fiber probe[26].

For TG-AgI10 preform, one end was etched for just 30 seconds. The other end was etched for 30 minutes and its surface morphology was checked every 2 minutes (Figure 3.10).

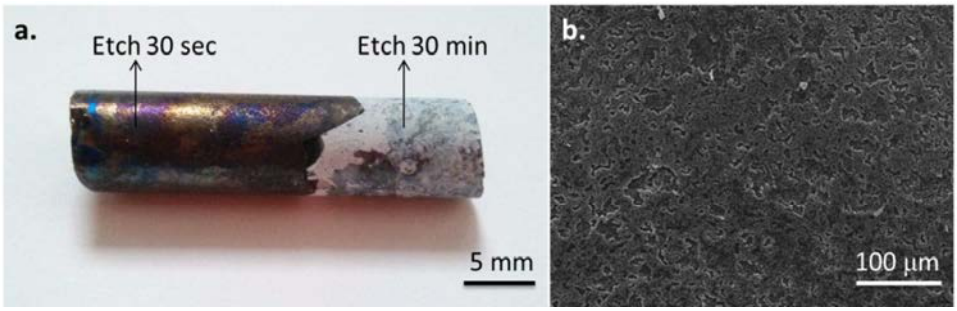

Figure 3.10 The macroscopic photo of glass preform after etching for 30 seconds and 30 minutes (a) and the SEM image of the white membrane generated (b).

No significant change could be observed after 30 seconds of etching. However, as etching time going on, a kind of white membrane started to form and became thicker. The composition of this membrane, studied by EDS, is a mixture of TeO_2, GeO_2 and a small amount of Ag_2O. Therefore, this method is not proper for Te-Ge-AgI glasses.

Research on mechanical polish

Therefore, the mechanical polishing has also been tried. The TG-AgI10 preform was firstly polished using polishing papers of 1200 and 4000 grits. After polish, the surface defects were totally removed (Figure 3.11 a). However, during fiber drawing process, an obvious crystallization could be obviously observed on both the preform shrinkage part (b to d) and the fiber (e).

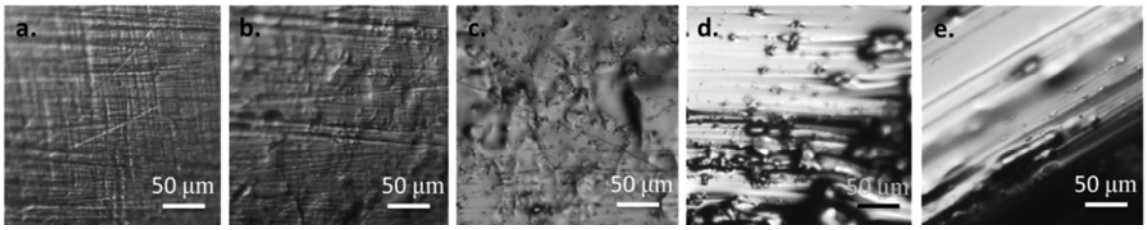

Figure 3.11 Optical microscope images of TG-AgI10 glass surface morphology variation from preform (a) to fiber (e).

Note that after polish, a new surface roughness could also be induced depending on the particles sizes of polish paper. This surface roughness is associated with surface free energy. Indeed, the surface energy of a solid is a function of the broken bond energy of exposed atoms. Thus, inadequate polish can induce a higher surface free energy and in this way contributes to faster kinetics of nucleation. Thus, owning to the high surface free energy and the additional energy provided by ring furnace, surface crystallization occurred. This led to a large quantity of defects on fiber surface (e), which can cause extra losses and greatly decrease its mechanical strength. As a result, polishing parameters need to be precisely controlled to prevent the acceleration of nucleation induced by excessive surface free energy.

After several trials, the Ge-Te-AgI glass preform with a perfect shiny surface was successfully obtained by polishing using polishing papers (1200 and 4000 grits) and alumina powder step by step. The images of TG-AgI10 glass preform before and after proper mechanical polishing are shown in Figure 3.12. After polish, the preform surface became shiny again. All the deposition has been confirmed to be totally removed by optical microscope. Some tiny scratches caused by polishing still can be observed. During fiber drawing, these scratches could be removed by surface tension.

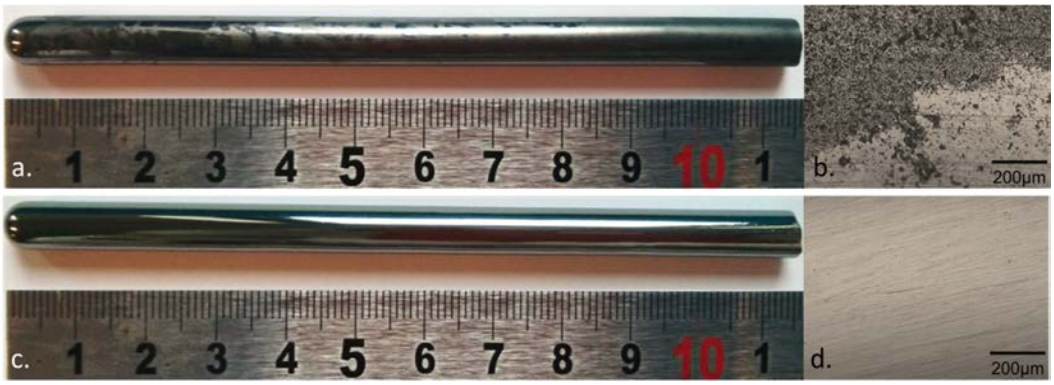

Figure 3.12 Macroscopic and optical microscopic photos of TG-AgI10 glass preform before (a and b) and after (c and d) proper mechanical polishing

3.3.2.2 Low attenuation fiber preparation from optical polished preform

The fabrication of the fibers from polished preforms were carried out under a He controlled atmosphere. The detailed fiber drawing parameters have already been listed in Table 3.2. The images of TG-AgI10 fiber and preform after drawing are shown in Figure 3.13. All the glass preform, first drop and the single index fiber obtained are maintained shiny after fiber drawing, indicating the effectiveness of mechanical polishing.

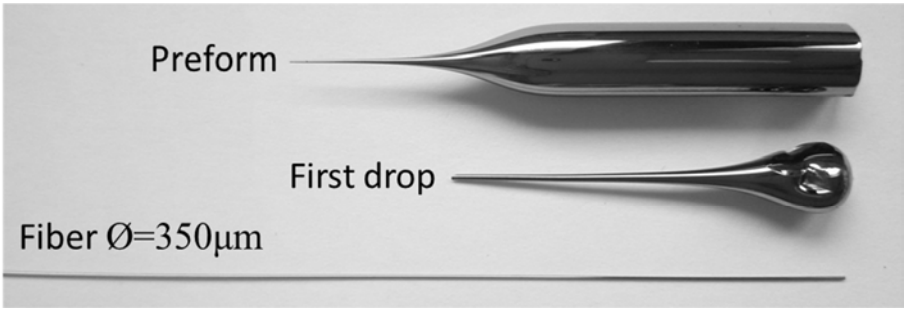

Figure 3.13 Photograph of TG-AgI10 fiber and preform after drawing

As mentioned above, any tiny defect on fiber surface could be greatly amplified due to the long-distance propagation of light. As a result, the measurement of fiber optical loss is the most direct way to evaluate the quality of the fiber surface. The optical losses of TG-AgI10 optical fiber are shown in Figure 3.14. For comparison, the attenuation curve of a previous fiber, without polishing, is also shown for comparison.

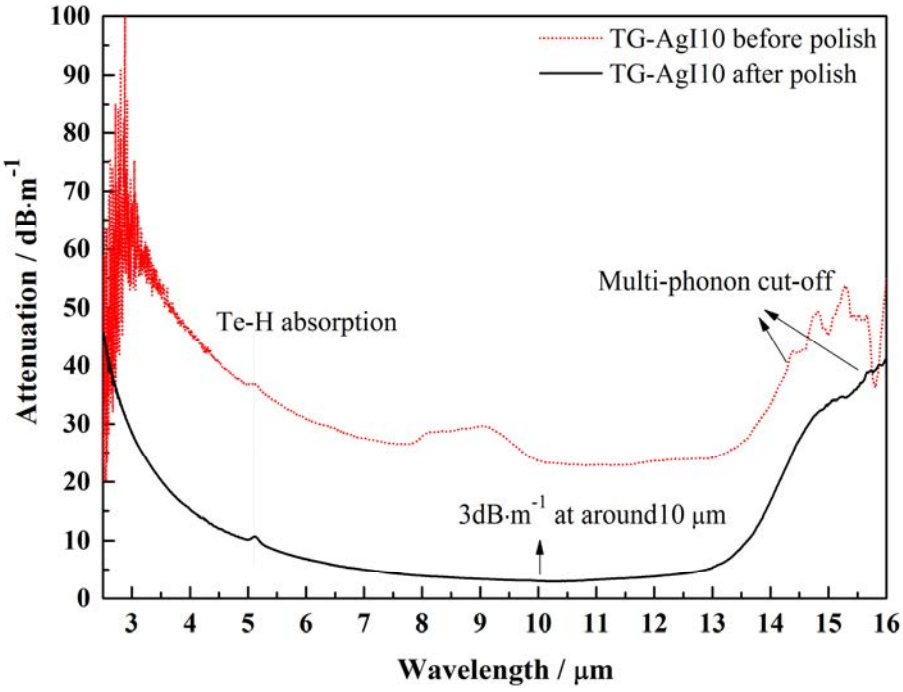

Figure 3.14 The optical losses of TG-AgI10 single index fibers obtained from the preforms with (black line) and without (red dotted line) optical polishing.

By polishing, the optical loss has been significantly reduced. The minimum attenuation value is 3 dB/m at around 10 μm. Note that previous pure telluride glass fibers exhibit minimum optical losses larger than 20 dB/m[27]. Thus fiber attenuation and is up to now the minimum value ever measured for a telluride glass.

The residual optical absorptions in the transmitting range are due to the charge carriers' concentration inherent to the semi-conducting behavior of the tellurium. As electronegative

element, it is clear that iodine plays a benefit role to trap the electronic charges[11,12], which was one motivation to introduce AgI in the glass composition. The small absorption peak at 5.1 μm is caused by Te-H bonds. The hydrogen could be introduced by the water molecules attached to the surface of the elements during the distillation when Al reacted with H_2O and generated Al_2O_3. Another possible source is the hydrogen absorbed on silica set-up by chemical bond during the tube fabrication and cleaning process. Such impurities are also classically observed in selenide glasses (Se-H bonds) and are difficult to be totally removed by vacuum drying.

The attenuation curves of theTG-AgI15 and TG-AgI20 fibers (Figure 3.15) have been also measured.

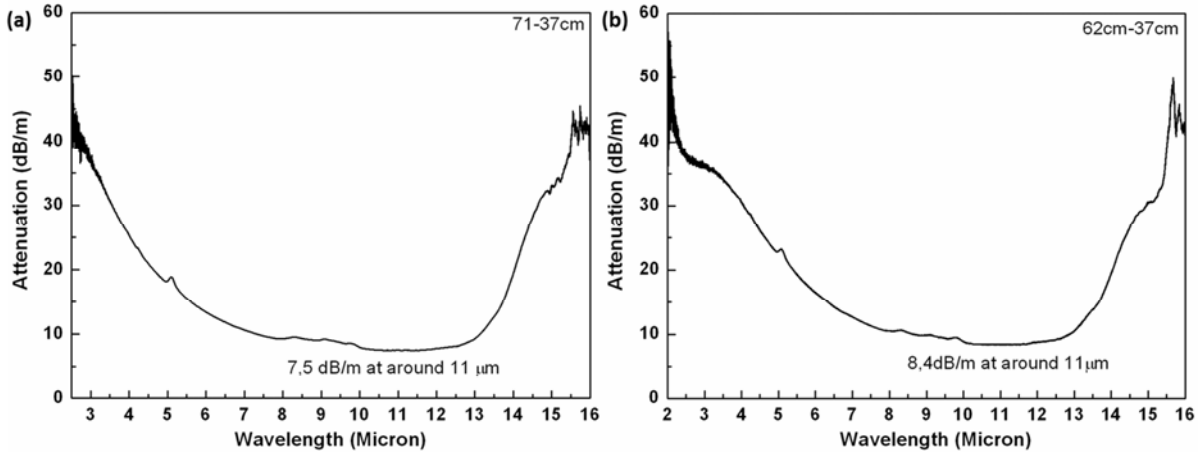

Figure 3.15 Optical losses of TG-AgI15 (a) and TG-AgI20 (b) optical fibers (fiber diameters are 350μm).

Even though the free electron concentration of these fibers is lower due to a larger content of AgI, their optical losses are still a bit higher than the TG-AgI10 fiber. These results show that the mechanical polishing is a delicate stage of the rod preparation. To obtain a fiber without surface crystallization after a mechanical polishing is not so obvious. This is mainly caused by the following two reasons. Firstly, during fiber drawing process, any tiny polishing defect will cause nucleation, which will expand rapidly on the surface. Moreover, due to the tiny amount of water inside silver iodide and the generation of high-volatilized germanium iodide, there are frequently lots of pores remaining on the preform surface, which could be sources of nucleation.

3.3.2.3 Cutoff wavelength verification of Te-Ge-AgI fiber by MCT and DTGS

It has been proved in Chapter 2 that glasses in the Te-Ge-AgI system show a wide infrared transmission region up to 39 μm. For TG-AgI10 single index fiber, the light attenuation was measured by a liquid nitrogen cooled MCT detector. Compared with the deuterated triglycine sulfate (DTGS) room temperature detector, which is most commonly used for bulk transmittance measurement, the MCT detector shows a significantly higher sensitivity. Bruker Corporation has down series of experiments to check the infrared signal detection ability of both MCT and DTGS detectors[28]. The results have shown that the noise level with the DTGS detector is about 2 to 3 orders of magnitude higher than MCT collected. However, DTGS detector shows an intrinsic wider spectral range up to 28 μm.

In this work, to confirm the transparent region of the fiber, the absolute transmission beam of a short length (37cm) fiber was tested using both MCT and DTGS infrared detector. As DTGS detector exhibits larger detection region but less sensitivity, both the two transmittance spectrums are normalized and compared (Figure 3.16).

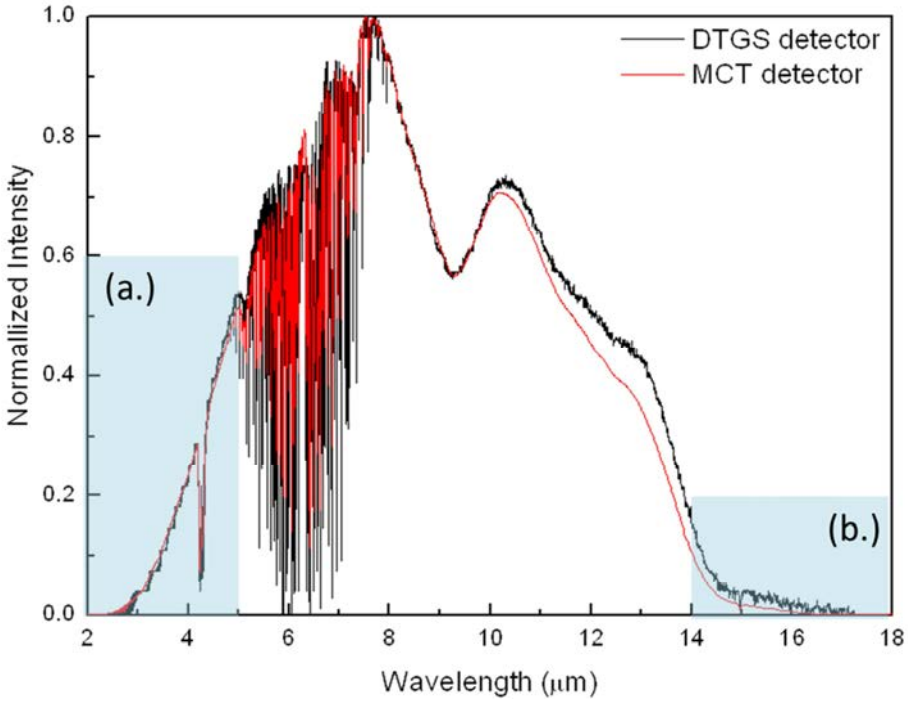

Figure 3.16 Normalized transmission beam of TG-AgI10 single index fiber detected by MCT and DTGS detectors

The two blue areas selected are enlarged to a more comfortable size and shown in Figure 3.17 to give a clearer view.

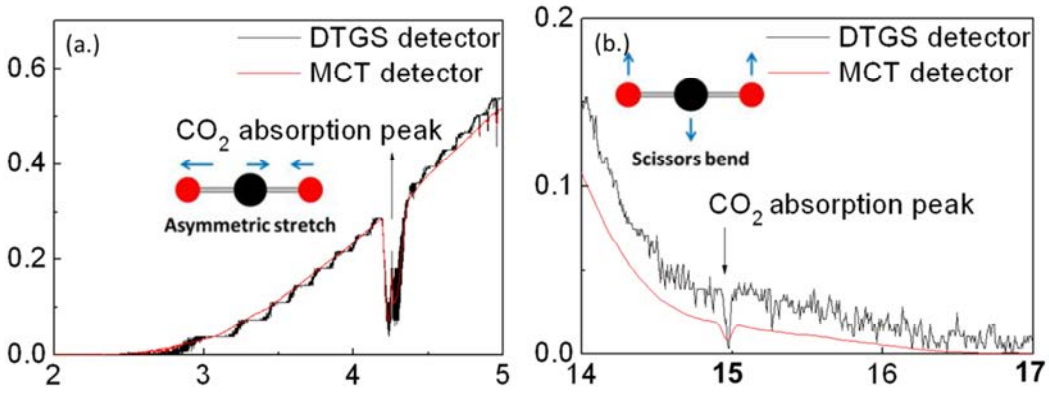

Figure 3.17 Enlarged images of Normalized transmission beam less than 5 µm (a) and beyond 14 µm (b).

The beams detected by MCT and DTGS are almost the same from 2 to 10 µm. When infrared radiation is beyond 10 µm, DTGS exhibits a higher resolution capacity. However, both spectra confirm this glass fiber can transmit signal from 2.5 µm up to at least 16 µm. This TG-AgI10 fiber is totally opaque beyond 17µm and no signal from source could be monitored. Due to existence of CO_2 in air, the asymmetric stretch absorption and scissors bend located at 4.3 µm and 15 µm separately are clearly visible. CO_2 in the Earth's atmosphere is at a concentration of approximately 390 ppm by volume, indicating the high fiber sensitivity for the infrared detection.

3.4 Biochemical sensing investigation on Te-Ge-AgI glasses

Since Compton[1] first reported chemical detection using chalcogenide glass fibers in 1988, this topic has been under investigation for more than 20 years. Based on previous results, Te-Ge-AgI glass fibers have shown their ability to observe the CO_2 absorption band spreading around 15 µm, providing their potential application as a sensing probe in the field of chemical detection. Thus, several chemical and biochemical products will be used to test the infrared sensing ability of Te-Ge-AgI fibers with different percentage of silver iodine.

3.4.1 Chalcogenide infrared sensors: principle

3.4.1.1 Fiber evanescent wave spectroscopy (FEWS)

Up to now, selenide glasses have been revealed as good candidates for the elaboration of special fibers to be implemented in optical sensors. They are especially suitable for sensors based on an original spectroscopic method named Fiber Evanescent Wave Spectroscopy (FEWS). This technique uses the evanescent field formed, as a beam propagates by internal

reflection, at the interface between the waveguide and the sample to test absorption peaks of the sample at specific wavelengths (Figure 3.18 a). The interference between the incident and the reflected waves gives rise to the generation of an evanescent field away from the fiber, which is perpendicular to the interface. When an absorbing sample is in contact with the fiber, the evanescent wave could be partially absorbed at specific wavelengths, causing the reflectivity lower than 1.This so-called attenuated total reflection (ATR) is the basic of the FEWS.

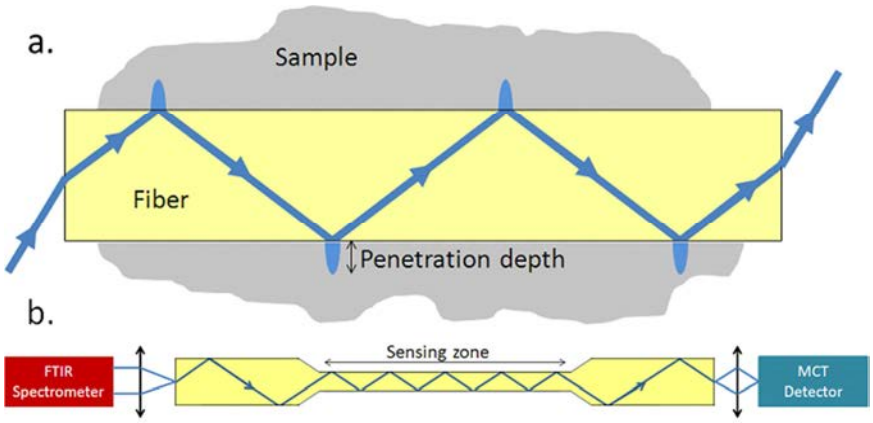

Figure 3.18 (a) Mechanism of fiber evanescent wave spectroscopy (FEWS); (b) General set up of FEWS and the scheme of a tapered fiber.

The FEWS method is quite simple to implement since the measurement necessitates only a standard spectrometer equipped with special kits to focus the light and a MCT detector (Figure 3.18 b). By dividing the signal collected before and after the sample is placed in contact with the fiber, the transmission spectrum can be obtained, similar to classical bulk transmission spectroscopy. Moreover, a large range of glass formulations is available to obtain suitable optical fibers with large infrared transparency ranges and low optical losses. Therefore, chalcogenide glass fibers for FEWS have drawn lots of attention in the last decades. The advantage of this technique is to perform remote, real-time and *in situ* analysis.

3.4.1.2 Factors that affect the sensitivity of the optical fiber

Penetration depth

The evanescent wave intensity decays exponentially with distance. Indeed, the wave intensity is mostly localized within 1 µm from the fiber surface. The penetration depth d_p, a function of refractive index and light wavelength, is defined as the depth at which the radiation intensity falls to 1/e of its original value. According to Equation (3.1), where λ, n_1,

n_2 and θ_i represent wavelength, refractive indices of glass and surrounding, and incident light angle respectively, d_p increases linearly with the wavelength. Therefore, the fiber shows a higher sensitivity at longer wavelength due to a penetration depth increase.

$$d_p = \frac{\lambda}{2\pi\sqrt{n_1^2 \sin^2 \theta_i - n_2^2}} \quad \textbf{(3.1)}$$

Influence of fiber diameter and contact length on sensivity

To improve fiber sensitivity, an effective approach is to increase the quantity of internal reflections which result in many absorption events at the glass/sample interface. Actually, the reflections number N depends on the fiber diameter according to the formula

$$N = L * \frac{\tan(90 - \theta_i)}{d} \quad \textbf{(3.2)}$$

Here, L, θ_i, and d represent contact length between the fiber and the sample, incident angle and fiber diameter at sensing zone respectively. Clearly, the probe sensitivity is directly proportional to the immersed light length L and the reciprocal of diameter $1/d$ [29].Actually, the diameter could locally be reduced from 400 μm to 100μm in the sensing zone by two operating routes[30]: etching[26] and reduction on-line by precise adjustment of fiber drawing speed[31].

Glass hydrophobicity

For FEWS, the Beer–Lambert law, which relates the absorption of light to the properties of the material through which the light is traveling, can also be applied to qualify the sensitivity of the fiber. The absorbance $A(\lambda)$ can be written as a product of the wavelength-dependent molar absorptivity $\varepsilon(\lambda)$, the path length l, and the analyte concentration c.

$$A(\lambda) = \varepsilon(\lambda) \cdot l \cdot c \quad \textbf{(3.3)}$$

This implies that the absorbance of evanescent field absorption has a linear relationship with the analytes concentration. Indeed, for chalcogenide glass fiber, this linear relationship has already been observed[2]. However, deviation from the Beer–Lambert law has also been observed in some aqueous solutions of non-polar molecules[32]. This is attributed to the hydrophobic character of chalcogenide glasses, linked to the essentially covalent nature of chemical bonds in the glass fiber. Thus, surface bonds are softly polarized, which favors contact with non-polar targeted molecules.

3.4.1.3 Advantages of chalcogenide glass for FEWS application

The modes of molecular vibrations including stretching and bending occur in the mid and far infrared region (3 to 20 μm). This region is sometimes referred to as the "fingerprint" region of the electromagnetic spectrum, since many effluents and gases have distinctive absorption features used in their identification. Chalcogenide glass waveguides, due to their large transmission window, are especially proper to monitor these characteristic absorptions.

For the FEWS technique, a higher refractive index contrast between waveguide and sample contacted could induce a smaller evanescent wave penetration depth and thereby decrease fiber sensitivity (Equation 3.1). This is detrimental for telluride glasses due to their high refractive index (n>3). However, as fiber sensitivity could be greatly enhanced by reducing fiber diameter[29] or increasing contact length[33] between fiber and sample, fibers with small diameter and long contact length can compensate this disadvantage.

At this time, selenide glass fiber has been proved to be suitable for capturing vibrations of most of chemical and biological molecules. Applications such as detection of molecules[34], or pollutants for environmental purposes[35] and follow-up of in-situ chemical reactions[4] have been explored by a close contact between fiber and specimen.

However, due to its light atom weights, selenide glass fibers are totally opaque beyond 12 μm, making it is impossible to test the vibration absorption band located at longer wavelength, such as the strongest absorption peaks of chloroform[15] and benzene[14], for example. Thus, Te-Ge-AgI optical fibers are especially proper for testing the signal located between 12 μm and 16 μm.

3.4.2 Te-Ge-AgI tapered fiber: an infrared sensor probe

3.4.2.1 Preparation of Te-Ge-AgI tapered fiber optic sensors

To prepare high sensitivity fiber infrared sensor probes, tapered Te-Ge-AgI fibers were obtained by a sudden drum speed increase during the drawing process. By coordinating the drum speed, tapered fibers with different diameters at the sensing zone were successfully prepared. The parameters of all the fibers with and without tapered sensing zones are listed in Table 3.3.

Table 3.3 The parameters of Te-Ge-AgI fibers with and without a tapered sensing zone.

Composition	Diameter (μm)	Diameter at sensing zone (μm)
TG-AgI10	450	--
	350	--
	350	160
	350	174
	350	200
TG-AgI15	350	--
	350	120
	350	150
	350	170
TG-AgI20	350	--
	350	180

3.4.2.2 Experimental setup of Te-Ge-AgI infrared sensor

In order to check the fiber sensing properties, especially the limit absorption wavelength as well as the relationship between sensitivity and sensing zone diameter, a home-made infrared sensor with Te-Ge-AgI fiber (Figure 3.19) was used to carry out measurements on chemical and biological specimens in situ and in real time.

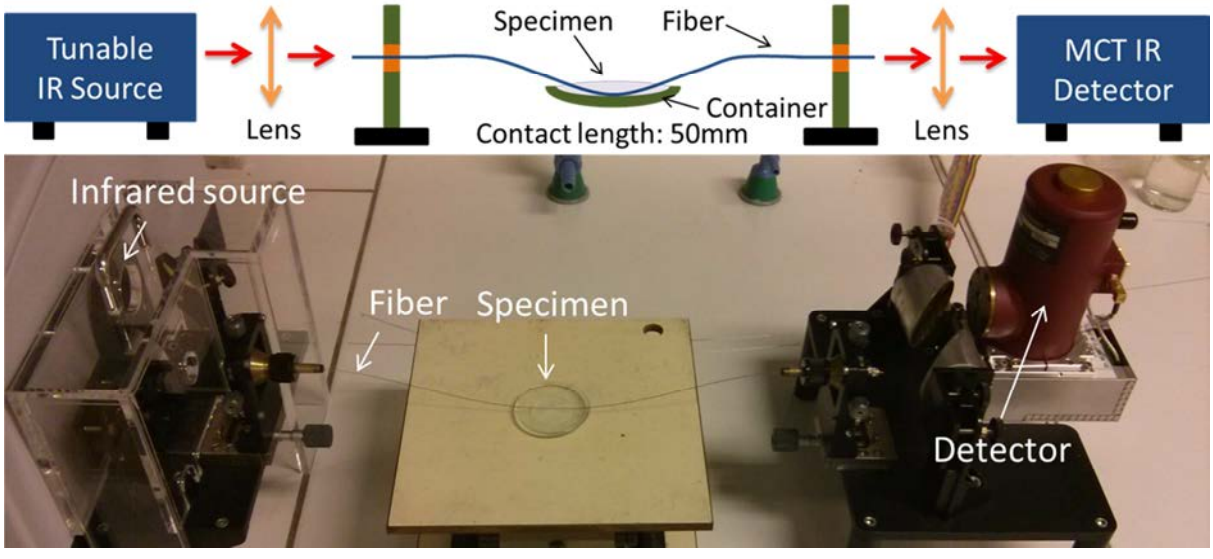

Figure 3.19 Setup for infrared sensing measurement.

To measure the attenuated total reflection (ATR) spectroscopy, chemical and biological specimens were put in contact with the fiber sensing zone having a contact length of 50 mm . By focusing a continuous infrared source into a single index Te-Ge-AgI fiber, the characteristic absorption peaks of the specimen could be monitored by liquid nitrogen cooled MCT detector.

Based on this simple apparatus, the influence of the sensing zone fiber diameter and analyte concentration on absorbance will be studied by monitoring the spectroscopy variation of dichloromethane (CH_2Cl_2), chloroform ($CHCl_3$) and toluene (C_7H_8). The potential applications of Te-Ge-AgI fiber on medicine, energy, and other areas related to daily life will also be explored.

3.4.3 The impact of sensing zone diameter on fiber sensitivity

In view of the broad transmission window up to 16 μm, the Te-Ge-AgI single index glass fibers have a distinct advantage for monitoring absorptions beyond 12 μm compared with Se-based glass fibers. In this part, the molecules having their vibration bands between 12 and 16 μm will be chosen and investigated.

3.4.3.1 The sensing property of dichloromethane (CH_2Cl_2)

Dichloromethane (CH_2Cl_2), due to its strong asymmetric and symmetric CCl_2 stretch vibration beyond 12 μm, was first chosen. The sensing spectra obtained using TG-AgI10 and TG-AgI15 fibers with and without taper are compared in Figure 3.20. The sensing zone and total length of the fiber is controlled to be 50 mm and 40 cm respectively.

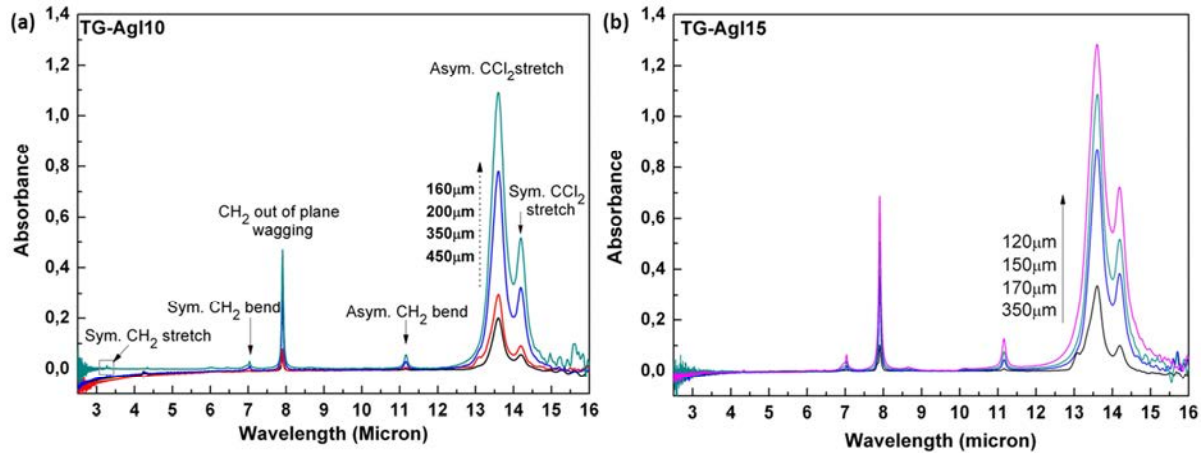

Figure 3.20 The dichloromethane absorbance spectra obtained with TG-AgI10 (a) and TG-AgI15 (b) fibers with different sensing zone diameters.

Clearly, Te-Ge-AgI single index fibers can successfully monitor the symmetric CH_2 stretch at 3.3 μm up to the symmetric CCl_2 stretch at 14.2 μm, which is, by the way, another evidence of the fiber broader transmission range. When the fiber diameter is reduced, the sensitivity of the sensor is obvious increased by increasing the reflection number N. The use of fiber taper for increasing detection sensitivity is therefore proved.

To determine the dependence of the absorbance of asymmetric C-Cl stretch on fiber sensing zone diameter, the relationship between absorbance and $1/d$ are shown in Figure 3.21.

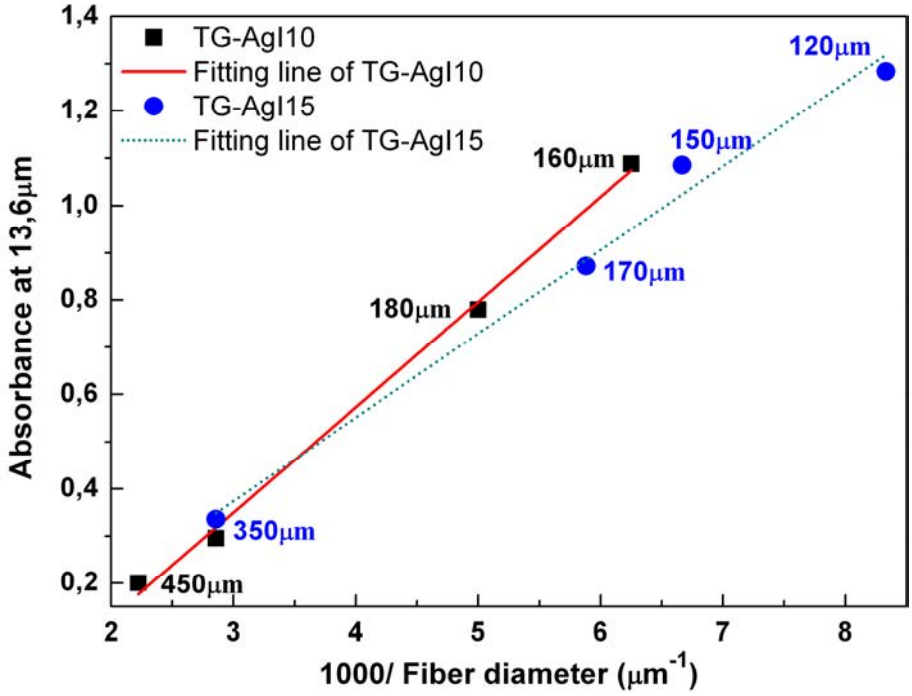

Figure 3.21The relationship between C-Cl asymmetric stretch vibration absorbance and the reciprocal of sensing zone diameter of TG-AgI10 and TG-AgI15 fibers.

Linear relationships could be clearly observed, in consistent with Equation (3.2). Although the optical loss of TG-AgI15 fiber is twice more than TG-AgI10 fiber owning to the surface defects diffraction during long-distance light propagation, its sensitivity is just lightly reduced. That is because for short-distance sensing application, optical loss is limited. Meanwhile, the vast majority of fiber surface at sensing zone has no defect. For comparison, the infrared spectrum of CH_2Cl_2 obtained by measuring liquid transmittance with a path length around 3 μm (NIST Chemistry WebBook) is also shown in Figure 3.22.

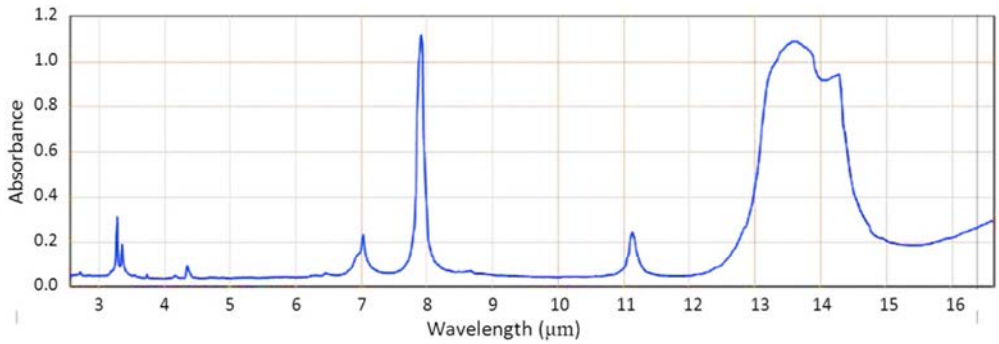

Figure 3.22 Infrared spectrum of liquid CH_2Cl_2 from the Coblentz Society's evaluated infrared reference spectra collection

By comparing the absorbance of CH_2 wagging at 7.9 μm and CCl_2 asymmetric stretch at 13.6 μm of the two spectra, it can be observed that owning to the influence of wavelength on evanescent field penetration depth, the fiber shows a higher sensitivity at longer wavelength. As a result, Te-Ge-AgI glass fiber is especially proper for far infrared sensing beyond 12 μm. Meanwhile, traditional transmittance measurement is quite complicated and time-consuming. Fiber sensing has an advantage of performing remote, real-time and *in situ* analysis.

3.4.3.2 The sensing property of chloroform ($CHCl_3$)

To study the infrared sensing limit of the Te-Ge-AgI glass fibers, and at the same time to explore the possibility of these fibers to be applied in Darwin project for CO_2 detection at 14.9 μm, molecules having an IR vibrational absorption peak at longer wavelength should be selected. Chloroform was selected due to its strong C-Cl stretching and C-Cl bending absorption peaks located at 13.3 μm and 14.9 μm respectively.[15] Pure chloroform (2N) was put in contact with the sensing zone of a tapered Te-Ge-AgI glass fiber in a silica evaporating dish.

Figure 3.23 shows the related FEWS absorbance spectra of chloroform. The sensitivities of the fibers TG-AgI10 and TG-AgI15 with different sensing zone diameters were studied and also compared with TAS glass optical fiber.

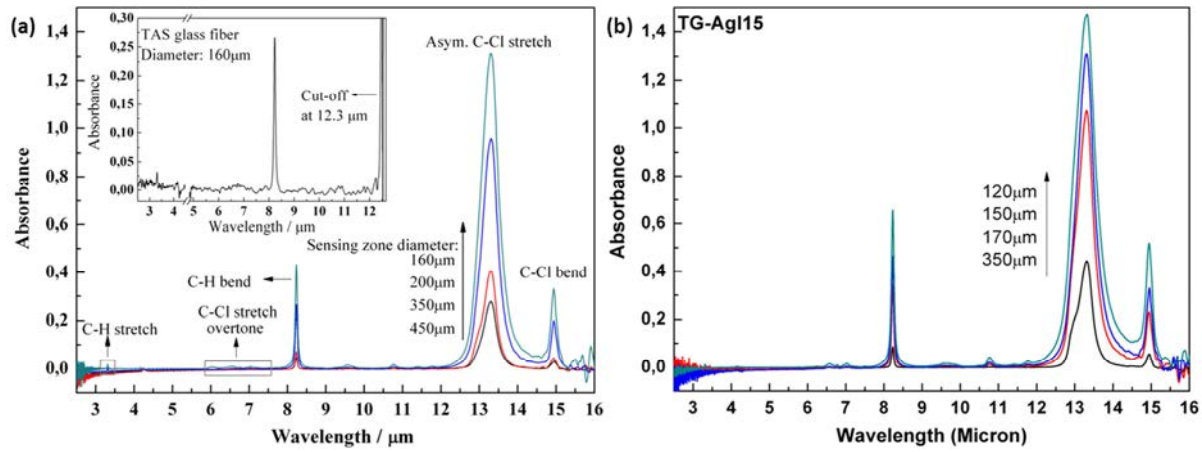

Figure 3.23 The chloroform absorbance spectra recorded with TG-AgI10 (a) and TG-AgI15 (b) fibers having different sensing zone diameters. The inset is the chloroform absorbance spectrum recorded with a Te20As30Se50 (TAS) fiber for comparison.

It can be observed from the spectra that the Te-Ge-AgI glass fibers are able to monitor the chloroform absorption peaks at 3.3 μm, 8.2 μm, 13.3 μm and 14.9 μm at the same time, showing a potential to work in the second (12-20 μm) infrared window and detect the

signature of CO_2 in Darwin mission (European Space Agency) or Terrestrial Planet Finder (National Aeronautics and Space Administration).

For comparison, the equivalent chloroform FEWS spectrum collected by a $Te_{20}As_{30}Se_{50}$ (TAS) fiber with the same tapered sensing zone diameter, 160 µm, as TG-AgI10 fiber is also presented in the inset of Figure 3.23a. As expected, the largest transmission windows of the TG-AgI fibers compared with TAS fibers give access to absorption bands beyond 12 µm. Moreover, it is noticeable that for the C-H bending absorption at 8.2 µm, the Te-Ge-AgI fiber even shows a higher absorbance value than the TAS fiber. This indicates again that the optical attenuation value of the fiber, which is around 1µm for the TAS fiber, in the transmitting domain does not have a direct consequence on the sensitivity of FEWS experiments which are short distance applications.

This sensitivity also depends on the chemical nature of the optical glass fiber. Clearly the physical interaction between the fiber and the liquid sample is very good, as shown by the very high signal to noise ratio of the FEWS spectra.

Besides, as the fiber diameter at the sensing zone decreases, the sensitivity increases significantly due to the much larger number of internal reflections that results in more absorptions at the interface between the glass and the sample. The absorbance at 13.3 µm of both TG-AgI10 and TG-AgI15 fibers are shown in Figure 3.24.

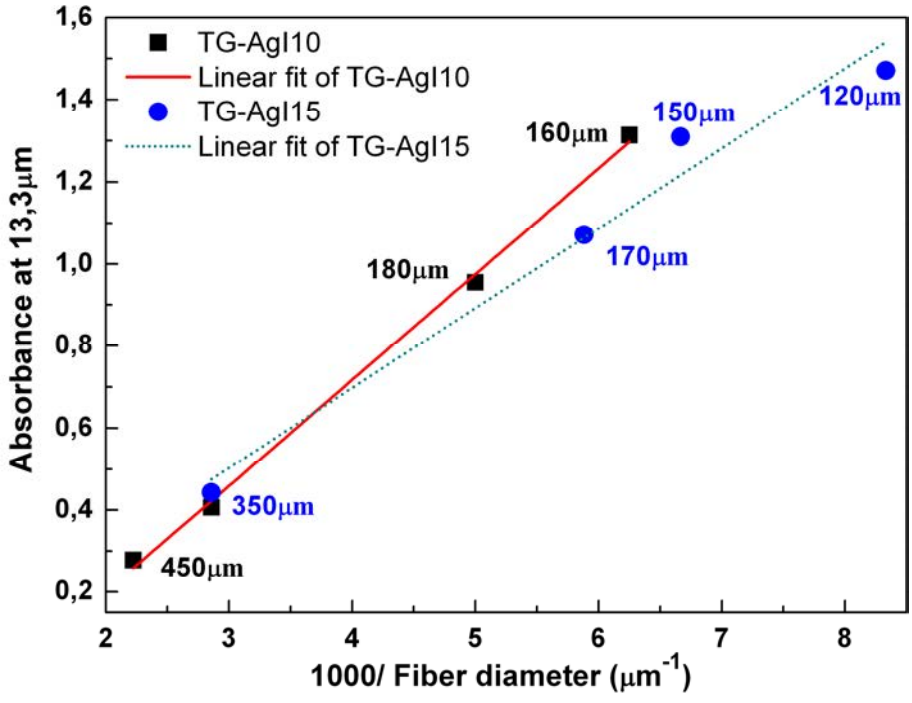

Figure 3.24The relationship between absorbance caused by asymmetric C-Cl stretch and the reciprocal of fiber sensing zone diameter of TG-AgI10 and TG-AgI15 fibers.

Absorbance shows a linear relationship with *1/d*, in agreement with previous theoretical models and observation, which definitively validates the benefit of such geometry for the sensing device.

3.4.4 Fiber optic sensor for liquid quantitative analysis

For potential applications in daily life, beside rapid identification of substance category using evanescent-wave interactions, the capability of Te-Ge-AgI fibers for analyte concentration monitoring should also be explored. Toluene has two strong out-of-plan C-H deformation bands located at around 13.7 and 14.4 μm, and is selected for concentration measurement.

As a gasoline additive, toluene acts as an antiknock agent to boost octane rating, which is similar to benzene. Thus, this concentration-dependent absorbance study of toluene will be beneficial to the further studies on benzene. 2,2,4-trimethylpentane, also known as isooctane, as itself has negligible absorption in this region, is used as solvent.

TG-AgI10 and TG-AgI20 tapered fibers with their sensing zone diameters to be 174μm and 180μm respectively are chosen as sensing probes to measure the toluene absorption variations along with concentration (vol%). The results are shown in Figure 3.25 and Figure 3.26.

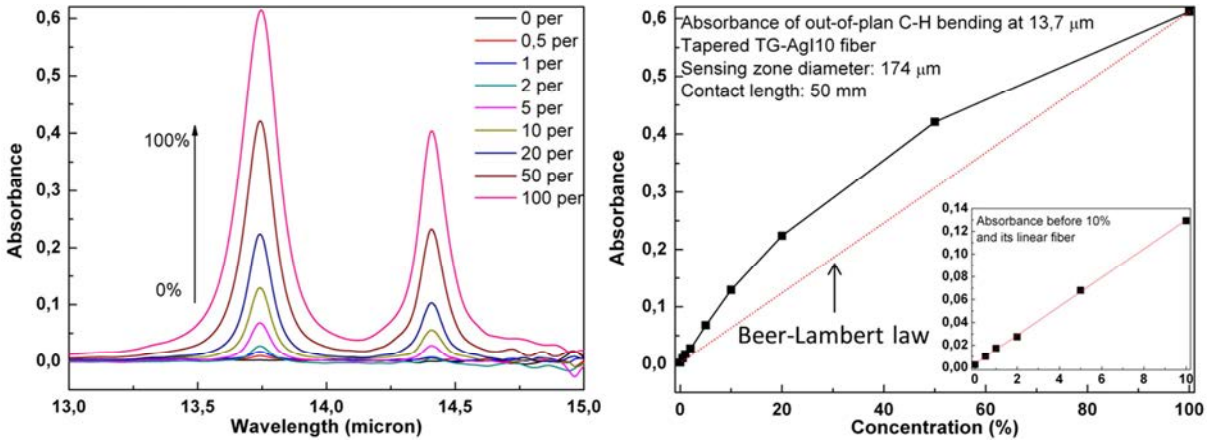

Figure 3.25 Toluene FEWspectra as a function of concentration in isooctane solution registered with a TG-AgI10 tapered fiber (a). Evolution of the toluene absorbance as a function of concentration (b). The inset is the evolution of the absorption for a concentration lower than 10% and its linear fit.

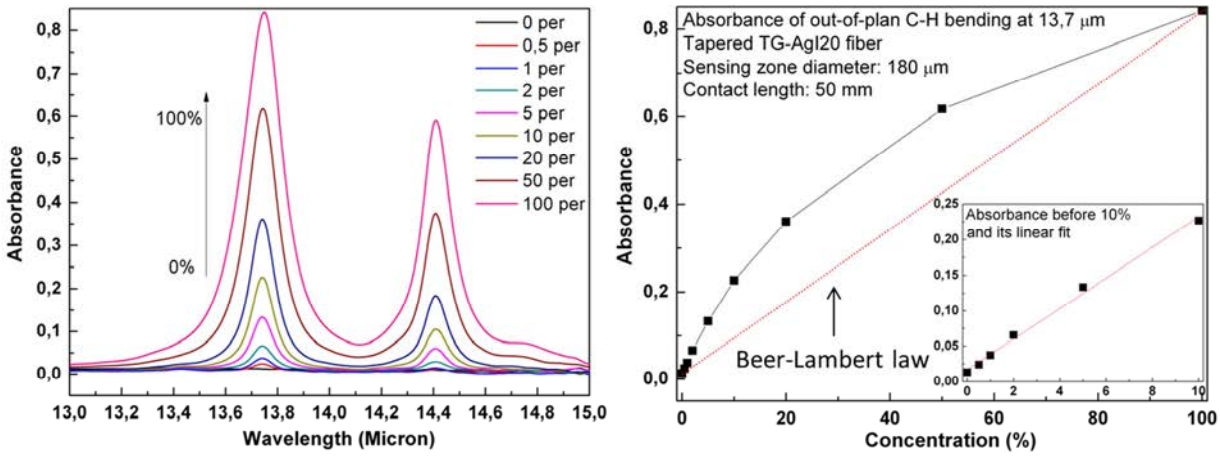

Figure 3.26 Toluene FEWspectra as a function of concentration in isooctane solution registered with a TG-AgI20 tapered fiber (a). Evolution of the toluene absorbance as a function of concentration (b). The inset is the evolution of the absorption for a concentration lower than 10% and its linear fit.

For TG-AgI10 and TG-AgI20 fibers, the out-of-plan C-H bending absorptions at 13.7 and 14.4 μm both grow with toluene concentration. However, the evolution of the intensity of the toluene absorption band at 13.7 μm versus concentration does not follow the pseudo-Beer-Lambert law. This result is perhaps attributed to the surface polarization of chalcogenide glasses. Indeed, the essentially covalent nature of chemical bonds in the glass fiber can make the surface bonds softly polarized. This slightly polarized fiber surface favors contact with molecules having similar polarity index. 2,2,4-trimethylpentane, due to its symmetrical structure, is a typical non-polar molecule with an extremely low polarity index (around 0.1). The polarity index of toluene is about 2.4, which is more likely to be closer to fiber surface polarization value. Thus, the greater interaction of toluene with the Te-Ge-AgI fiber surface leads to a concentration gradient of toluene at the glass surface where the evanescent wave is most intense. This results in selective detection of solution in isooctane solvent using FEWS.

Nevertheless, for both TG-AgI10 and TG-AgI20 fibers, when the concentration of toluene is less than 10%, a linear calibration curve with a coefficient of determination R^2 larger than 0.99 could be clearly observed. Moreover, the minimum detectable concentration of toluene is around 0.5 vol.%, which is the first concentration-dependent absorption result obtained from a tellurium based glass fiber.

Based on previous results, the Te-Ge-AgI glass fibers have shown their high-sensitive infrared sensing capability, and are proper for potential application in quantitative analysis, especially in low analyte concentration measurement.

3.4.5 Exploration of potential applications of Te-Ge-AgI fibers

3.4.5.1 Analysis of serum in medical diagnosis

Metabolic abnormalities due to diseases can be detected in serum. FEWS using glass fibers can characterize biochemical components such as glucose, cholesterol, and triglyceride at the same time, providing an extensive view of the serum species levels. For selenide glass fibers, FEWS combined with unsupervised analysis technique such as Principle Component Analysis (PCA) has been shown to be efficient to discriminate tissues types [22], differentiate ill and healthy serum[36,37], and others bio-medical applications[38].

In this part, fresh serum of calf was used for infrared analysis to explore new absorptions beyond 12 μm (Figure 3.27). To obtain the infrared spectrum, 5 ml of serum was put in contact with the fiber in a watch glass with a contact length to be 50 mm. The setup for infrared sensing measurement has already been shown in Figure 3.19.

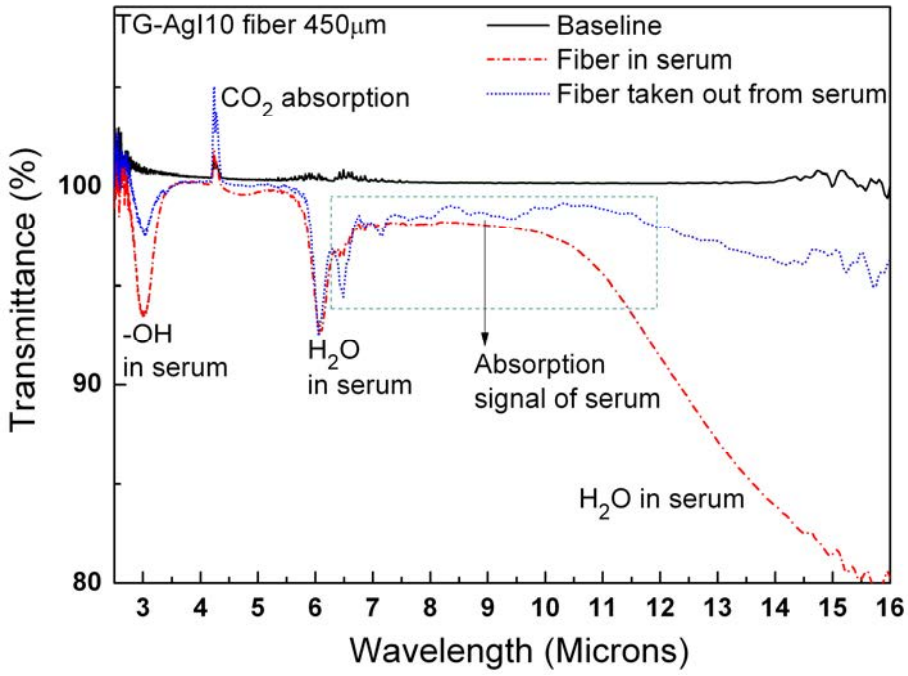

Figure 3.27 Calf serum infrared sensing spectrum tested by TG-AgI10 glass fiber.

Chalcogenide fibers have been shown to have an apparent hydrophobic surface characteristic, which induces partitioning of the organics towards the fiber surface where the evanescent wave is most intense and results in detection enhancement for organic species in aqueous solutions[39,40]. The mechanism of this phenomenon is based on a much smaller polarity indices difference between glass and organic molecules than between glass and water, generating a stronger interaction between the organic species and the glass surface.

This specific property of chalcogenide fibers is particularly important for applications in infrared spectroscopy where spectra are often saturated with water fingerprints, which hide the vibration bands of the samples being studied. This is exactly the case for the infrared spectroscopy study on calf serum using TG-AgI10 glass fiber with its diameter to be 450 μm.

In Figure 3.27, due to large amount of water, the spectrum recorded with the fiber immersed in the serum, is saturated with the water fingerprint. After the fiber was taken out of the serum, the attached water molecules would be repelled and evaporate in air thanks to fiber surface hydrophobic characteristic. Thus, the absorption peaks of the biochemical components of the serum could be clearly observed. However, as most of the IR vibrational absorption peaks are located before 12 μm, Se-based optical fibers are sufficient for such application.

3.4.5.2 Applications in food safety

Food safety and medical diagnosis has become hot issues in recent decades. Selenide glass optical fibers have already been successfully used to monitor the contamination of food by pathogens [41] In order to show the potential of Te-Ge-AgI optical fibers for rapid *in-situ* monitoring of food quality, the FEWS spectra of different kinds of calf milk and butter were collected from 2 μm to 16 μm.

Rapid identification of the type of milk

Fatty acid content in cow milk having different percentages of lipids is studied using FEWS. The label ingredients which could be detected by infrared spectroscopy are listed in Table 3.4. Therefore, the type of milk can be simply identified by the lipid absorption peaks due the significant content difference.

Table 3.4 The label ingredients of different types of cow milk

Nutrition (g/100ml)	Full-cream milk Carrefour	Semi-skimmed milk Carrefour	Skimmed milk Carrefour
Protein	3.2	3.2	3.2
Carbohydrates	4.8	4.8	4.8
Lipid	3.6	1.55	0.05

The infrared spectra for full-cream, semi-skimmed and skimmed cow milk are shown in Figure 3.28. The TG-AgI10 fiber with its total length, specimen contact length and sensing zone diameter to be 40 cm, 50 mm and 350 μm respectively, was used as a sensing probe. The main absorption bands identified [42,43] are shown in Table 3.5.

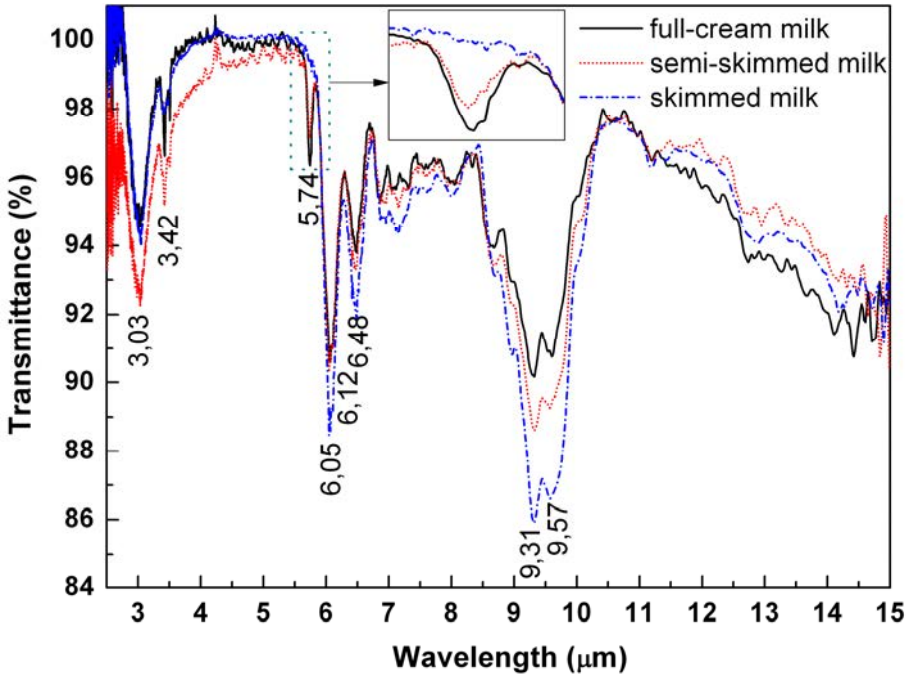

Figure 3.28 IR spectra for full-cream, semi-skimmed, and skimmed milk using a TG-AgI10 fiber. The sensing zone diameter is 350 μm.

Due to the influence of water fingerprint saturation on spectrum, the TG-AgI10 fiber should be taken out of cow milk before infrared sensing. The absorption of proteins, carbohydrates and lipids can be clearly observed in Figure 3.28 thanks to fiber surface hydrophobicity. The C=O stretch absorption band of esters at 5.74 μm show an obvious increase with the lipid concentration.

Table 3.5 The bands assignment of the IR vibrational absorption spectrum of milk.

Wavelength [μm]	Assignment
3.03	N-H from protein & O-H from water
3.42	CH_2 asymmetric stretch from fatty acid
5.74	C=O stretch from esters
6.05	O-H bend from water
6.12	C=O & N-H from protein amide I and amide II
6.48	
9.31	C-O from polysaccharides
9.57	

Besides, a very interesting phenomenon has also been noticed. From Table 3.4, it can be seen that the label ingredients of carbohydrates in different cow milks are the same, 4.8 g per 100 ml. Actually, skimmed milk has a higher percentage of carbohydrates, which is obtained by comparing the absorption band intensities of C-O from polysaccharides. Therefore, besides rapid identification of food category, Te-Ge-AgI fiber can also be applied in food safety and quality control.

Butter species identification

The FEWS spectra of butter (with around 80% wt. butterfat) and light butter (with around 15% wt. butterfat) were also collected from 2 μm to 16 μm and are compared in Figure 3.29. The band assignment of the IR vibrational absorption peaks of butter are listed in Table 3.6.

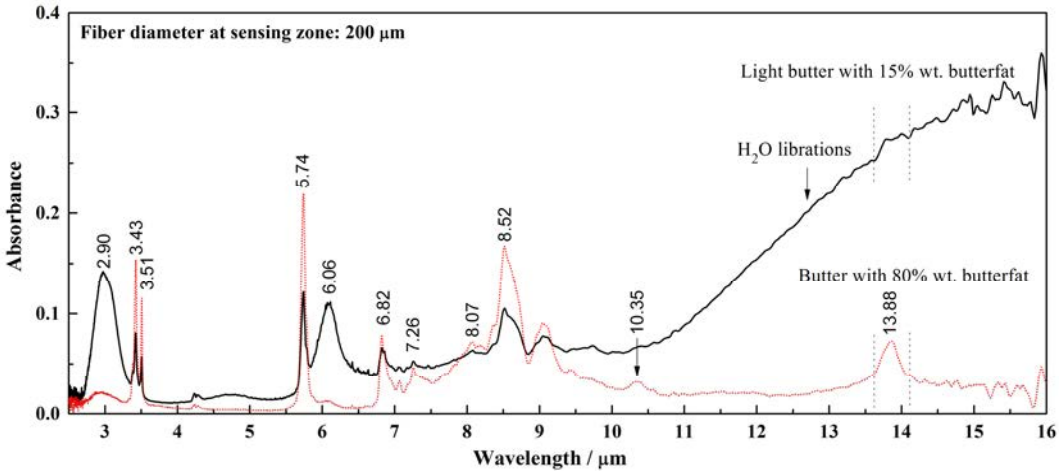

Figure 3.29 The infrared absorption spectra of butter (80% wt. butterfat) and light butter (15% wt. butterfat) obtained from a TG-AgI10 fiber sensor.

Table 3.6 The bands assignment of the IR vibrational absorption spectrum of butter.

Wavelength [μm]	Assignment
2.90	O-H stretch
3.43	CH_2 asymmetric stretch
3.51	CH_2 symmetric stretch
5.74	C=O stretch
6.06	O-H bend
6.82	CH_2 scissor
7.26	CH_3 scissor
8.07	CH_2 bend (out of plane)
8.52	CO-O-C stretch
10.35	-CH=CH- bend
13.88	CH_2 rock

It can be observed that due to a large butterfat and water content difference between the regular butter and the light butter, the absorbance beyond 12 μm of the two shows an obvious dissimilarity. Normal butter, due to its high butterfat content, has a distinct absorption peak at 13.8 μm caused by CH_2 rocking. On the contrary, light butter shows a wide absorption shoulder owning to the librations of liquid water due to the restrictions imposed by hydrogen bonding[44]. Therefore, by collecting additional infrared signal beyond 12 μm, we clearly get richer information on a complex biological material such as butter which could be benefit for controlling the chemical content and the quality of food. More generally, this permits to focus

on the potential of the Te-Ge-AgI glass optical fiber for food identification and quality verification based on FEWS which could be extended to various applications in the health field.

3.4.5.3 Potential applications of fiber sensor in energy industry

Ever since the industrial revolution took off in the 18th century, gasoline has been used to power the economy and deliver unprecedented affluence to huge numbers of people. It is a liquid mixture of aliphatic hydrocarbons derived from fractional distillation of petroleum which is then enhanced with a variety of additives including antiknock agent and a series of other additives, such as ethanol, methanol, formaldehyde, xylene, 1,3-butadiene, methyl tertiary butyl ether and hexane.

Tetraethyl lead was used as an additive in early model cars to boost the octane rating of gasoline and to help reduce engine knocking. Due to concerns over air pollution and health risks, this type of gas was slowly phased out[45]. Nowadays, as a substitute, unleaded gasoline is commonly used. However, at least 15 hazardous chemicals including benzene and toluene are still used as additives. As an antiknock agent, the concentration of benzene in gasoline should be strictly controlled due to its carcinogenicity. Regulations are in place in many countries to limit its concentration in gasoline to level of 1% or less. Therefore, a method quantifying benzene at the concentration level is required. At present, the two methods most widely used are capillary gas chromatography with flame ionization detection and capillary chromatography - mass spectrometry, both of which are complicated and time-consuming. IR spectroscopy due to its simplicity is an ideal method for benzene analysis in gasoline by monitoring the distinctive C-H out-of-plane deformation band at around 14.8 μm.

A Te-Ge-AgI tapered fiber has already shown its potential to monitor chloroform absorptions at 14.9 μm. Meanwhile, the toluene concentration detection limit using Te-Ge-AgI tapered fiber is 0.5%. On this basis, we can predict that the characteristic band of benzene in gasoline can be clearly observed using Te-Ge-AgI tapered fiber sensing probe. To validate our prediction, tapered TG-AgI15 and TG-AgI20 fibers are used to detect gasoline (95E10, TOTAL) infrared spectra (Figure 3.30). The C-H out-of-plane bending absorptions of both toluene (<30% mass) and benzene (<1% vol.) in gasoline are clearly shown in spectra, located at 13.7, 14.0, and 14.8 respectively. Especially for benzene, the absorption band increases as the fiber sensing zone diameter decreases from 170 to 120 μm. As a result,

Te-Ge-AgI optical fibers have shown their great potential to be applied to rapid identification of gasoline components in energy industry.

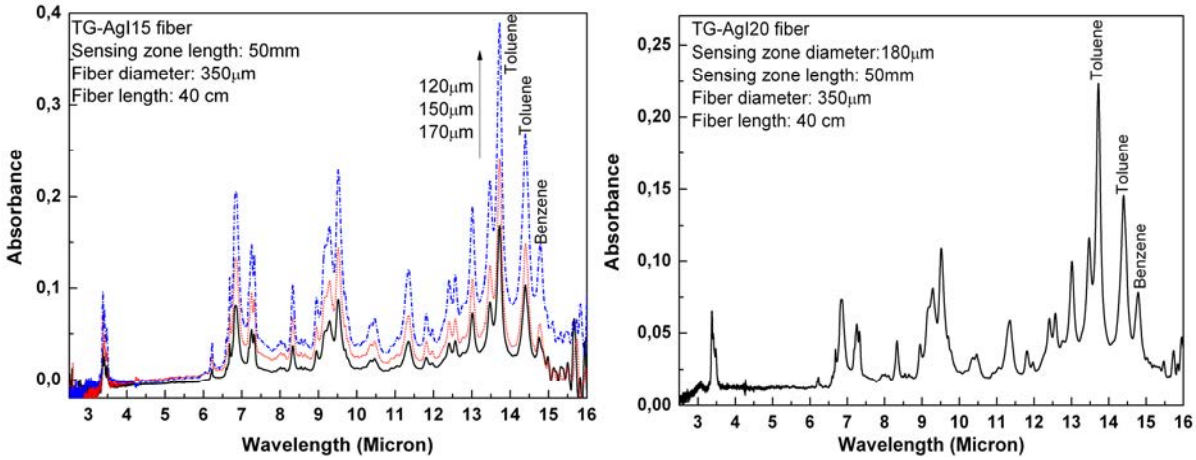

Figure 3.30 The 95E10 gasoline infrared spectra obtained by tapered Te-Ge-AgI fiber

3.5 Conclusion

The aim of this chapter was to change the status of pure tellurium-based glass from curiosity for material scientist toward effective functional material for mid and far-infrared optical devices.

To achieve this goal, high-purified $(Ge_{0.21}Te_{0.79})_{100-x}AgI_x$ (x=10, 15, and 20) glasses (named as TG-AgI10, TG-AgI15 and TG-AgI20 respectively) showing no obvious crystallization peak in DSC curves were synthesized using two-steps chemical-distillation method. The bulk transmittance comparison of the glasses with and without purification verified the effectiveness of this purification technique. From EDS, the preform has proved to be homogeneous. Compared with previous fibers containing iodine in the Te-Ge-I system, it is much more efficient to introduce iodine as a salt rather than in its elemental form, because it remains in the glass network and would not have the tendency to escape during the synthesis.. By a careful operation of polishing, the preform surface defects caused by germanium iodide re-condensation during the annealing process have been totally removed, permitting to obtain Te-Ge-AgI high quality glass preforms.

On this basis, some optical fibers having optical losses lower than 10 dB/m have been prepared. Note that previous pure telluride glass fibers exhibit minimum optical losses higher than 20 dB/m. Thus the fiber attenuation has been significantly reduced. The minimum attenuation value is 3 dB/m around 10 μm for 350 μm diameter TG-AgI10 single index fiber, which is up to now the minimum value ever measured for a telluride glass.

By tapering them, the fibers were designed for mid-IR FEWS experiments. To compare the sensing ability with the currently in-service optical fibers made from selenium based glasses, dichloromethane, chloroform, and toluene with vibrational band beyond 12 μm were chosen as examples. By measuring dichloromethane and chloroform infrared spectra, the tapered fiber-based sensors show an enhanced sensing ability as sensing zone diameter decreases. In term of sensitivity, these new telluride glass fibers supplant the selenium based glasses optical fibers. Above all, they give access to a range of wavelengths that was previously inaccessible with chalcogenide glass fibers.

Besides, the experiment using toluene-isooctane solution show a toluene concentration detection limit of Te-Ge-AgI fiber to be 0.5 vol.%, which is the first concentration-dependent absorption result obtained from Te-based glass fiber.

On this basis, Te-Ge-AgI fibers will be essential for mid-infrared spectroscopy in particular for applications involving complex bio-molecules for which the 12 to 16 µm spectroscopic range could be rich in information. Thus, the infrared spectra of calf serum, milk, butter and gasoline, taking as examples of complex organic system, have been carried on for the exploration of potential applications of Te-Ge-AgI fiber.

Results show that infrared sensor using Te-Ge-AgI fiber sensing probe is an ideal tool due to its simplicity and efficiency for the identification and quantification of complex system in food safety, medicine, energy, and other areas related to daily life. Also, due to its large infrared sensing range, Te-Ge-AgI fiber is also applicable in aerospace, such as CO_2 analysis in the Darwin project.

Reference

[1] D.A.C. Compton, S.L. Hill, N.A. Wright, M.A. Druy, J. Piche, W.A. Stevenson, D.W. Vidrine. In Situ Ft-IR Analysis of a Composite Curing Reaction Using a Mid-Infrared Transmitting Optical Fiber. Appl. Spectrosc. 1988, 42 (6): 972-979

[2] J. Heo, M. Rodrigues, S.J. Saggese, G.H. Sigel Jr. Remote Fiber-Optic Chemical Sensing Using Evanescent-Wave Interactions in Chalcogenide Glass Fibers. Applied optics. 1991, 30 (27): 3944-3951

[3] J. Sanghera, F. Kung, P. Pureza, V. Nguyen, R. Miklos, I.D. Aggarwal. Infrared Evanescent-Absorption Spectroscopy with Chalcogenide Glass Fibers. Applied optics. 1994, 33 (27): 6315-6322

[4] D. Le Coq, K. Michel, J. Keirsse, C. Boussard-Plédel, G. Fonteneau, B. Bureau, J.-M. Le Quéré, O. Sire, J. Lucas. Infrared Glass Fibers for *in-situ* Sensing, Chemical and Biochemical Reactions. Comptes Rendus Chimie. 2002, 5 (12): 907-913

[5] B.J. Eggleton, B. Luther-Davies, K. Richardson. Chalcogenide Photonics. Nat. Photonics. 2011, 5 (3): 141-148

[6] V.Q. Nguyen, J.S. Sanghera, B. Cole, P. Pureza, F.H. Kung, I.D. Aggarwal. Fabrication of Arsenic Sulfide Optical Fiber with Low Hydrogen Impurities. J. Am. Ceram. Soc. 2002, 85 (8): 2056-2058

[7] M.F. Churbanov, G.E. Snopatin, V.S. Shiryaev, V.G. Plotnichenko, E.M. Dianov. Recent Advances in Preparation of High-Purity Glasses Based on Arsenic Chalcogenides for Fiber Optics. J. Non-Cryst. Solids. 2011, 357 (11–13): 2352-2357

[8] J.S. Sanghera, I.D. Aggarwal. Active and Passive Chalcogenide Glass Optical Fibers for IR Applications: A Review. J. Non-Cryst. Solids. 1999, 256–257 (0): 6-16

[9] C. Conseil, Q. Coulombier, C. Boussard-Plédel, J. Troles, L. Brilland, G. Renversez, D. Mechin, B. Bureau, J.L. Adam, J. Lucas. Chalcogenide Step Index and Microstructured Single Mode Fibers. J. Non-Cryst. Solids. 2011, 357 (11–13): 2480-2483

[10] S. Danto, P. Houizot, C. Boussard-Plèdel, X.H. Zhang, F. Smektala, J. Lucas. A Family of Far-Infrared-Transmitting Glasses in the Ga-Ge-Te System for Space Applications. Adv. Funct. Mater. 2006, 16 (14): 1847-1852

[11] A.A. Wilhelm, C. Boussard-Plédel, Q. Coulombier, J. Lucas, B. Bureau, P. Lucas. Development of Far-Infrared-Transmitting Te Based Glasses Suitable for Carbon Dioxide Detection and Space Optics. Adv. Mater. 2007, 19 (22): 3796-3800

[12] Z. Yang, P. Lucas. Tellurium Based Far Infrared Transmitting Glasses. J. Am. Ceram. Soc. 2009, 92 (12): 2920-2923

[13] X. Zhang, H. Ma, C. Blanchetière, J. Lucas. Low Loss Optical Fibres of the Tellurium Halide-Based Glasses, the TeX Glasses. J. Non-Cryst. Solids. 1993, 161: 327-330

[14] W. Chen, F. Cazier, F. Tittel, D. Boucher. Measurements of Benzene Concentration by Difference-Frequency Laser Absorption Spectroscopy. Appl. Opt. 2000, 39 (33): 6238-6242

[15] N.B. Colthup, L.H. Daly, S.E. Wiberley. Introduction to Infrared and Raman Spectroscopy. San Diego, CA, USA: Academic Press, 1990

[16] P. Houizot, C. Boussard-Plédel, A.J. Faber, L.K. Cheng, B. Bureau, P.A. Van Nijnatten, W.L.M. Gielesen, J. Pereira do Carmo, J. Lucas. Infrared Single Mode Chalcogenide Glass Fiber for Space. Opt. Express. 2007, 15 (19): 12529-12538

[17] S. Maurugeon, B. Bureau, C. Boussard-Plédel, A.J. Faber, X.H. Zhang, W. Geliesen, J. Lucas. Te-Rich Ge-Te-Se Glass for the CO_2 Infrared Detection at 15μm. J. Non-Cryst. Solids. 2009, 355 (37–42): 2074-2078

[18] S. Maurugeon, C. Boussard-Plédel, J. Troles, A.J. Faber, P. Lucas, X.H. Zhang, J. Lucas, B. Bureau. Telluride Glass Step Index Fiber for the Far Infrared. J. Lightwave Technol. 2010, 28 (23): 3358-3363

[19] S. Maurugeon, B. Bureau, C. Boussard-Plédel, A.J. Faber, P. Lucas, X.H. Zhang, J. Lucas. Selenium Modified $GeTe_4$ Based Glasses Optical Fibers for Far-Infrared Sensing. Opt. Mater. 2011, 33 (4): 660-663

[20] C. Conseil, J.-C. Bastien, C. Boussard-Plédel, X.-H. Zhang, P. Lucas, S. Dai, J. Lucas, B. Bureau. Te-Based Chalcohalide Glasses for Far-Infrared Optical Fiber. Opt. Mater. Express. 2012, 2 (11): 1470-1477

[21] X. Wang, Q. Nie, G. Wang, J. Sun, B. Song, S. Dai, X. Zhang, B. Bureau, C. Boussard, C. Conseil, H. Ma. Investigations of Ge-Te-AgI Chalcogenide Glass for Far-Infrared Application. Spectrochim. Acta, Part A. 2012, 86 (0): 586-589

[22] S. Hocdé, O. Loréal, O. Sire, C. Boussard-Plédel, B. Turlin, J. Keirsse, P. Leroyer, J. Lucas, B. Bureau. Metabolic Imaging of Tissues by Infrared Fiber-Optic Spectroscopy: An Efficient Tool for Medical Diagnosis. J. Biomed. Opt. 2004, 9 (2): 404-407

[23] X.H. Zhang, H. Ma, J. Lucas. Evaluation of Glass Fibers from the Ga-Ge-Sb-Se System for Infrared Applications. Opt. Mater. 2004, 25 (1): 85-89

[24] S. Zhang, X.H. Zhang, M. Barillot, L. Calvez, C. Boussard, B. Bureau, J. Lucas, V. Kirschner, G. Parent. Purification of $Te_{75}Ga_{10}Ge_{15}$ Glass for Far Infrared Transmitting Optics for Space Application. Opt. Mater. 2010, 32 (9): 1055-1059

[25] H.-J. Kim, O.-J. Kwon, Y.-G. Han. Effect of Surface Roughness Variation on the Transmission Characteristics of D-Shaped Fibers with Ambient Index Change. J. Korean Phys.Soc. 2010, 56 (4): 1355-1358

[26] D. Le Coq, K. Michel, G. Fonteneau, S. Hocde, C. Boussard-Pledel, J. Lucas. Infrared Chalcogen Glasses: Chemical Polishing and Fibre Remote Spectroscopy. International Journal of Inorganic Materials. 2001, 3 (3): 233-239

[27] P. Lucas, C. Boussard-Pledel, A. Wilhelm, S. Danto, X.-H. Zhang, P. Houizot, S. Maurugeon, C. Conseil, B. Bureau. The Development of Advanced Optical Fibers for Long-Wave Infrared Transmission. Fibers. 2013, 1 (3): 110-118

[28] Bruker Biosciences Corporation. FT-IR Microscopy Using Dtgs Detectors.

[29] K. Le Foulgoc, L. Le Neindre, X.H. Zhang, J. Lucas. Tapered Tex Glass Optical Fibers for Remote IR Spectroscopic Analysis. Presented at the Chemical, Biochemical, and Environmental Fibers sensors VIII, Denver, Colorado, 1996: 26-36

[30] S. Hocdé, C. Boussard-Plédel, G. Fonteneau, D. Lecoq, H.-L. Ma, J. Lucas. Recent Developments in Chemical Sensing Using Infrared Glass Fibers. J. Non-Cryst. Solids. 2000, 274 (1–3): 17-22

[31] B. Bureau, X.H. Zhang, F. Smektala, J.-L. Adam, J. Troles, H.-l. Ma, C. Boussard-Plèdel, J. Lucas, P. Lucas, D. Le Coq, M.R. Riley, J.H. Simmons. Recent Advances in Chalcogenide Glasses. J. Non-Cryst. Solids. 2004, 345–346 (0): 276-283

[32] K. Michel, B. Bureau, C. Boussard-Plédel, T. Jouan, J.L. Adam, K. Staubmann, T. Baumann. Monitoring of Pollutant in Waste Water by Infrared Spectroscopy Using

Chalcogenide Glass Optical Fibers. Sensors and Actuators B: Chemical. 2004, 101 (1–2): 252-259

[33] S. Hocdé, C. Boussard-Plédel, G. Fonteneau, J. Lucas. Chalcogens Based Glasses for IR Fiber Chemical Sensors. Solid State Sciences. 2001, 3 (3): 279-284

[34] F. Charpentier, J. Troles, Q. Coulombier, L. Brilland, P. Houizot, F. Smektala, C. Boussard-Plédel, V. Nazabal, N. Thibaud, K. Le Pierrès, G. Renversez, B. Bureau. CO_2 Detection Using Microstructured Chalcogenide Fibers. Sensor Letters. 2009, 7 (5): 745-749

[35] K. Michel, B. Bureau, C. Pouvreau, J.C. Sangleboeuf, C. Boussard-Plédel, T. Jouan, T. Rouxel, J.L. Adam, K. Staubmann, H. Steinner, T. Baumann, A. Katzir, J. Bayona, W. Konz. Development of a Chalcogenide Glass Fiber Device for in Situ Pollutant Detection. J. Non-Cryst. Solids. 2003, 326–327 (0): 434-438

[36] M.-L. Anne, C. Le Lan, V. Monbet, C. Boussard-Plédel, M. Ropert, O. Sire, M. Pouchard, C. Jard, J. Lucas, J.L. Adam, P. Brissot, B. Bureau, O. Loréal. Fiber Evanescent Wave Spectroscopy Using the Mid-Infrared Provides Useful Fingerprints for Metabolic Profiling in Humans. Journal of Biomedical Optics. 2009, 14 (5): 054033-054033

[37] J. Keirsse, B. Bureau, C. Boussard-Pledel, P. Leroyer, M. Ropert, V. Dupont, M.L. Anne, C. Ribault, O. Sire, O. Loreal, J.L. Adam. Chalcogenide Glass Fibers Used for *in-situ* Infrared Spectroscopy in Biology and Medicine. Presented at the Optical Sensing, Strasbourg, France, 2004: 61-68

[38] M.-L. Anne, J. Keirsse, V. Nazabal, K. Hyodo, S. Inoue, C. Boussard-Pledel, H. Lhermite, J. Charrier, K. Yanakata, O. Loreal. Chalcogenide Glass Optical Waveguides for Infrared Biosensing. Sensors. 2009, 9 (9): 7398-7411

[39] P. Lucas, M.R. Riley, M.A. Solis, C. Juncker, J. Collier, D.E. Boesewetter. Hydrophobic Chalcogenide Fibers for Cell-Based Bio-Optical Sensors. In: Biomedical Optics 2005: International Society for Optics and Photonics, 2005: 104-114

[40] P. Lucas, M.A. Solis, D.L. Coq, C. Juncker, M.R. Riley, J. Collier, D.E. Boesewetter, C. Boussard-Plédel, B. Bureau. Infrared Biosensors Using Hydrophobic Chalcogenide Fibers Sensitized with Live Cells. Sensors and Actuators B: Chemical. 2006, 119 (2): 355-362

[41] M.-L. Brandily, V. Monbet, B. Bureau, C. Boussard-Plédel, O. Loréal, J.-L. Adam, O. Sire. Identification of Foodborne Pathogens within Food Matrices by IR Spectroscopy. Sens. Actuators, B. 2011, 160 (1): 202-206

[42] N. Nicolaou, R. Goodacre. Rapid and Quantitative Detection of the Microbial Spoilage in Milk Using Fourier Transform Infrared Spectroscopy and Chemometrics. Analyst. 2008, 133 (10): 1424-1431

[43] N. Nicolaou, Y. Xu, R. Goodacre. Fourier Transform Infrared Spectroscopy and Multivariate Analysis for the Detection and Quantification of Different Milk Species. Journal of dairy science. 2010, 93 (12): 5651-5660

[44] F.N. Keutsch, R.J. Saykally. Water Clusters: Untangling the Mysteries of the Liquid, One Molecule at a Time. Proc. Natl. Acad. Sci. 2001, 98 (19): 10533-10540

[45] R.C. Gupta. Reproductive and Developmental Toxicology. Academic Press, 2011: 309

Chapter 4.

Te-Based Glass: a New Class of Material for Thermoelectric Application

4.1 Introduction

Thermoelectric (TE) phenomena provide the direct conversion of applied temperature gradient into electricity or electricity into temperature difference. A thermoelectric device can create voltage when there is a temperature difference at the both sides. Conversely, using an applied voltage, it creates a temperature difference. Indeed, many common materials, including metals and semiconductors, have a certain thermoelectric effect. The thermoelectric materials mentioned here show their thermoelectric effect in a strong and/or convenient form.

Thermoelectricity has been investigated for about two hundred years since Seebeck effect and Peltier effect were discovered by T. J. Seebeck[1] and J. C. A. Peltier[2] separately. By the 1950's, A. F. Ioffe and his colleagues [3,4] had developed the theory of thermoelectric conversion using the concept of figure of merit zT. This formed the basis of all modern thermoelectric theory and accelerated a wide research focused on developing materials with high figure-of-merit in 1950s and 1960s. However, thermoelectric have long been too inefficient to be cost-effective in most applications[5].

In early 1990s, the development of "phonon-glass electron-crystal" (PGEC) concept by G. Slack[6] led to a better understanding of the mechanism. In a good thermoelectric material, the phonons should be disrupted like in a glass but the electrons should have high mobility like they do in crystalline semiconductors. Since mid-1990s, the need of new renewable energy sources has driven a resurgence of interest when theoretical predictions suggested that thermoelectric efficiency could be greatly enhanced through nano structural engineering. This led to experimental efforts to demonstrate the proof-of-principle and high-efficiency materials [7-11]. At the same time, complex bulk materials (such as skutterudites [12], clathrates[13], and Zintl phases[14]) have been explored and found. All of these developments make it possible to obtain TE materials with high efficiencies[15].Compared with conventional electric generator, the reliability and simplicity of thermoelectricity enables niche applications for this solid-state technology even while conventional processes are more efficient.

Thermoelectric material can be applied in a variety of applications[16]. The most well-known is thermocouple for temperature measurement[17]. Besides thermocouples, the need for reliable and remote power sources provides some niche applications for thermoelectric power generation based on Seebeck effect. A typical application is radioisotope thermoelectric generators[18] which can provide electric power for spacecraft and satellites. Besides,

thermoelectric devices could also convert waste heat[19] from thermal power plant and automobile into useful electricity. Moreover, Peltier coolers based on thermoelectric materials, due to its lack of moving parts or circulating liquid, near-infinite life and invulnerability to potential leaks, and its small size and flexible shape, have occupied a small but stable industry[20].

According to the microscopic mechanism, good TE materials ask for high electrical conductivity and low thermal conductivity. The chalcogenide glasses have intrinsic poor thermal conductivity (about $0.5 W/m^{-1}K^{-1}$) and high Seebeck coefficient (more than 500μV/K). Telluride glasses are those with the highest electrical conductivity. A.P.Gonçalves [21-23], P. Lucas[24], et al. have already done lots of work on the investigation of TE properties of Te-based glasses. The Cu-Ge-Te, Cu-Si-Te, Cu-Ga-Te and Cu-As-Te glassy systems have already been developed for TE application. Up to now, the most conductive tellurium-based glass is $Cu_{30}As_{15}Te_{55}$ prepared by melt spinning with its electrical conductivity around 0.1 Ω·cm[22]. Compared with the commonly used TE material bismuth telluride, the main aim of this work is to increase the electrical conductivity of the telluride glasses without a significant destruction of its high Seebeck coefficient and low thermal conductivity.

Indeed, preliminary results get on the conductivity of telluride glasses are promising.. The aim of this chapter is to explore new glass composition to hopefully improve again the electronic conductivity.

4.2 Basic thermoelectric principle

4.2.1 Thermoelectric effect

The thermoelectric effect is a kind of direct conversion from temperature differences to electric voltage and vice versa. Thermoelectric devices can create voltage when there are different temperatures on each side. Conversely, when apply a voltage, a gradient of temperature appeared in the material. This effect can be used to generate electricity, measure temperature or change the temperature of objects. The term "thermoelectric effect" encompasses three separately identified effects: the Seebeck effect, Peltier effect and Thomson effect.

4.2.1.1 Seebeck effect

The Seebeck effect is the conversion of temperature differences directly into electricity and is named after German physicist T. J. Seebeck, who discovered this phenomenon in 1821[1].

Different metals (or semiconductors) have different free electron densities. When two different materials contact with each other, the electron diffusion will occur at the interface to eliminate electron density difference. Meanwhile, the electron diffusion rate is proportional to the temperature at interface. Therefore, as long as the temperature difference between the two materials is maintained, electron diffusions will be continuous, generating a stable voltage.

In the following circuit (Figure 4.1),

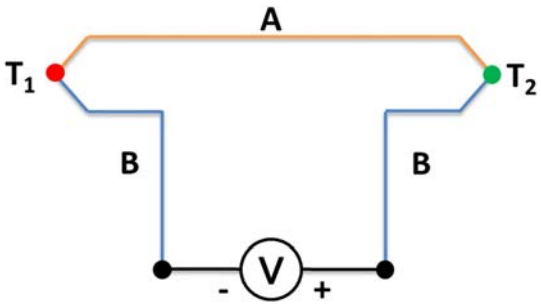

Figure 4.1 Seebeck effect circuit

voltage generated by the Seebeck effect can be expressed as:

$$V = \int_{T_1}^{T_2} \left(S_B(T) - S_A(T)\right) dT \quad \textbf{(4.1)}$$

where S_A and S_B are Seebeck coefficients (S), T_1 and T_2 are temperatures at interface. If Seebeck coefficient in the experiment temperature range can be treated as constant, the above equation can be approximated as:

$$V = (S_B - S_A)(T_2 - T_1) \quad \textbf{(4.2)}$$

Actually, Seebeck coefficient depends largely on the temperature and the microstructure of the material. One way to define the Seebeck coefficient is to divide the voltage built up (ΔV) by the small temperature gradient applied to the material (ΔT):

$$S = -\Delta V/\Delta T \quad \textbf{(4.3)}$$

By the analysis of charge carrier mobility, it can be got that n-type semiconductors have negative Seebeck coefficients, the ones of p-type materials are positive. To ensure that the Seebeck coefficient is large, there should only be a single type of carrier. Mixed n-type and p-

type conduction in one material will lead to both charge carriers moving to the cold end, cancelling out the induced Seebeck voltages.

Based on Seebeck effect, many applications have been explored, such as thermocouple using metallic junctions and thermoelectric generator using semiconductor junctions.

4.2.1.2 Peltier effect

Peltier effect is named after French physicist Jean-Charles Peltier, who discovered it in 1834[2]. This effect is the presence of the heating at one electrified junction and the cooling at the other when electric current is maintained in a circuit of material consisting of two dissimilar conductors (Figure 4.2). The effect is even stronger in circuits containing dissimilar semiconductors. If the current is reversed, heat generated by current flowing in one direction is absorbed. This effect can be explained from carrier energies.

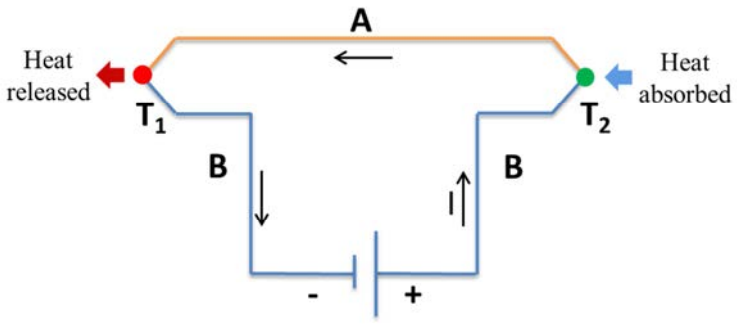

Figure 4.2 Peltier effect circuit

Electron conductors are analyzed as an example. For a metallic conjunction, the energy levels of electrons in different metals are different. In Figure 4.2, if the electron energy level of metal A is lower than metal B, due to the existence of electric potential in a circuit, the electrons are pulled out from metal A to metal B at the green point. At this upper junction, the kinetic energy of electron will convert to potential energy and electrons will move slower. Since the temperature is just a representation of the average speed of the random movements of the particles, the temperature at the upper junction will decrease. On the contrary, potential energy will convert to kinetic energy at the lower junction (red point), releasing heat.

For semiconductor conjunctions, the electrons of the n-type and p-type semiconductors are above and below Fermi level respectively. Similar to metallic conjunction, the directional movement of charge carriers can generate thermal effects (endothermic or exothermic phenomenon) at the interface. In Figure 4.2, the Peltier heat generated per unit time Q at the junction of conductor A and B (red point) is equal to,

$$Q = (\prod_A - \prod_B) \times I \quad \textbf{(4.4)}$$

where $\prod_A$ ($\prod_B$) is Peltier coefficient of conductor A (B) and I is electric current from A to B.

Due to Peltier effect, the TE conjunctions can be used in applications ranging from travel coolers/warmers to laboratory instruments and communications systems. The advantage is its lack of moving parts or circulating fluid, and its small size and flexible shape. By cascading or pyramiding Peltier devices, quite large temperature differences can be generated.

4.2.1.3 Thomson effect

The Thomson effect was predicted and subsequently observed by W. Thomson in 1854. It describes the heating or cooling of a current-carrying conductor with a temperature gradient.

Any current-carrying conductor (except for a superconductor) with a temperature difference between two points either absorbs or emits heat, depending on the material. If a current density J passes through a homogeneous conductor, the heat production Q per unit volume is:

$$Q = \rho J^2 - \mu J \frac{dT(x)}{dx} \quad \textbf{(4.5)}$$

where ρ is material resistivity; μ is Thomson coefficient; dT/dx is the temperature gradient along the wire; and the first item is Joule heating.

Compared with the other two thermoelectric effects, Thomson effect is directly measurable for any unique material.. On the contrary, no direct method exists for determining absolute Seebeck or Peltier coefficients for one material.

4.2.1.4 Kelvin relations

Indeed, the three thermoelectric coefficients mentioned above are not independent of each other. In 1854, Lord Kelvin found relationships among them, implying that the Thomson, Peltier, and Seebeck effects are different manifestations of one effect (uniquely characterized by the Seebeck coefficient).

The first Kelvin relation is,

$$\mu = TdS/dT \quad \textbf{(4.6)}$$

and the second Kelvin relation is,

$$\Pi = S \times T \quad \textbf{(4.7)}$$

where T is the absolute temperature. This relation expresses a subtle and fundamental connection between S, Π, and μ.

4.2.2 Thermoelectric converters

A metallic conjunction, due to the intrinsic high thermal conductivity, cannot provide high S or Π thus cannot generate high conversion efficiency as a thermoelectric converter. Semiconductors with sufficient S (or Π), are good candidates.

The electrical conductivity of a material is due to the mobility of charge carriers therein. In semiconductors, these carriers are of two different types. If conduction is ensured mainly by electrons, the material is n-type. In the opposite case, when electrons are deficient, the conduction is provided by the holes, the material is p-type. By convention, the n-type materials have a negative S (or Π) and the p-type materials a positive one.

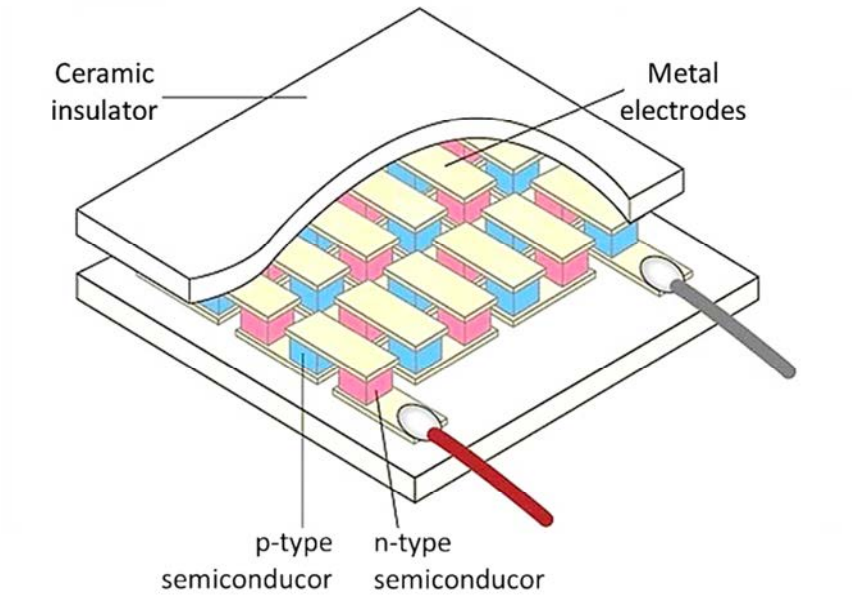

Figure 4.3 Diagram of a typical thermoelectric converter

A thermoelectric module is composed of an array of heavily doped p-type and n-type semiconductor legs (Figure 4.3). The legs are electrically connected by metal electrodes in series but thermally connected in parallel. Then the top and bottom of this array are affixed to ceramic substrates to provide electrical insulation and good thermal conductivity.

To examine how the heat transfer occurs, the charge carriers flowing property through one pair of p-type and n-type elements within the thermoelectric module was studied and shown in Figure 4.4.

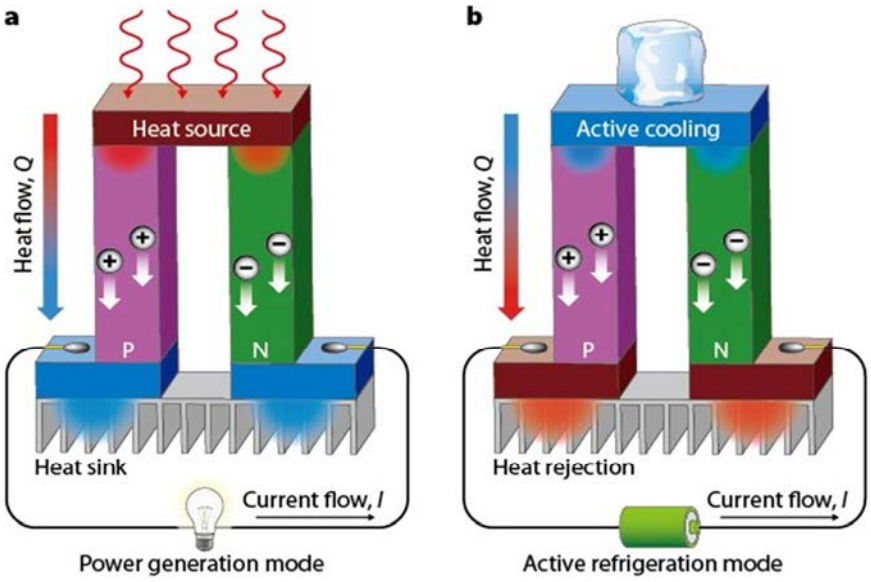

Figure 4.4 Diagram of a thermoelectric module. a) Thermoelectric generator. b) Peltier cooler.

When a temperature difference is imposed across the thermoelectric device, thanks to the thermo diffusion of charge carriers, a difference in voltage will build up between the two sides based on Seebeck effect. This power source can provide power to the electrical circuits.

Conversely, if a current is applied to the thermoelectric device, electrons will be forced out of p-type semiconductor, passing through the metal and into the n-type semiconductor. As electrons need to pass through the energy barriers, this is an endothermic process. As a result, a difference in temperature will build up between the two sides due to Peltier effect. If the current flow direction is opposite, the hot or cold face will be changed.

Actually, a thermoelectric generator can also be used as a Peltier cooler. However, a well-designed Peltier cooler will be a mediocre thermoelectric generator and vice-versa, due to different design and packaging requirements.

4.2.3 Material selection criteria

4.2.3.1 Power factor

S or Π is not the only coefficient that determines the usefulness of a material in a thermoelectric converter. Under a given temperature difference, the ability of one thermoelectric material producing useful electrical power is evaluated by its power factor PF,

$$\mathrm{PF} = S^2\sigma \quad \textbf{(4.8)}$$

where S is the Seebeck coefficient, and σ is the electrical conductivity. One can see from this equation that S and σ of TE material should be as high as possible in order to obtain a high electrical power. However, many researches[25,26] showed that S and σ are not independent because they have a close relationship with carrier concentration. Figure 4.5 shows S, $\ln\sigma$, and $S^2\sigma$ as a function of the logarithm of the carrier concentration. Thus the higher power factors are obtained for semimetals or for heavily doped semiconductors. Hence, a compromise between large S and σ of TE material should be chosen to maximize the power factor.

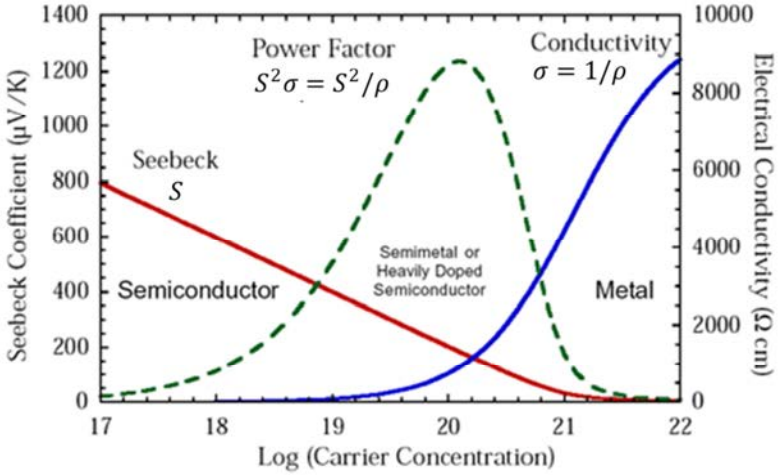

Figure 4.5 S, σ, and $S^2\sigma$ as a function of the logarithm of the carrier concentration[27,28]

4.2.3.2 Figure of merit

Materials with high power factor are able to generate more energy in a space-constrained application, but they are not necessarily efficient. The optimization of a compound or material to efficiently produce thermoelectric power mainly implies the maximization of a dimensionless figure of merit ZT given by,

$$\mathrm{ZT} = \frac{S^2 T\sigma}{\kappa_l + \kappa_e} \qquad \textbf{(4.9)}$$

where T is absolute temperature, σ is electrical conductivity, $(\kappa_l + \kappa_e)$ is thermal conductivity caused by phonon (κ_l) and electron (κ_e).

A potential material usable for applications in the field of thermoelectric must have the highest ZT value as possible. From Equation (4.9), it is clear that a material with interesting thermoelectric properties must have together high Seebeck coefficient, electrical conductivity, and low thermal conductivity. As electrons which participate in electrical

conduction also take part in the transfer of heat, it is understandable that the exploration of new TE material is a process of compromise and optimization.

4.2.3.3 Thermoelectric device efficiency

Typically, the maximum ZT value can be found in semimetals or heavily doped semiconductors with a carrier concentration between 10^{19} and 10^{21} per cm^3.

The thermoelectric device efficiency for electricity generation, η, is defined as the ratio of energy provided to the load and heat energy absorbed at hot junction. In an actual thermoelectric module using both p-type and n-type thermoelectric materials, the maximum efficiency η_{max} is defined as,

$$\eta_{max} = \frac{T_H - T_C}{T_H} \frac{\sqrt{1+zT}-1}{\sqrt{1+zT}+\frac{T_C}{T_H}} \tag{4.10}$$

Here, T_H and T_C are temperatures at the hot and cold junctions respectively. Figure 4.6 shows the calculated maximum thermoelectric efficiency. From both Eq. (4.10) and Figure 4.6, we can see that η_{max} depends on the ZT. A remarkable high value of efficiency could be obtained if the value of ZT is enhanced. When ZT approaches infinity, the η_{max} approaches the Carnot limit. However, up to now, no known TE materials have a ZT larger than 3[15].

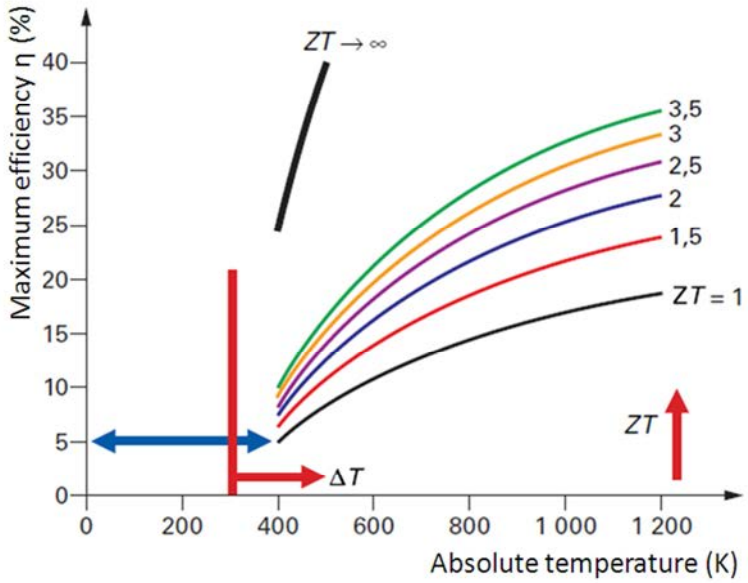

Figure 4.6 Maximum thermoelectric device efficiency

4.3 Design and synthesis of Te-based glass

4.3.1 Glass composition design

P-type and n-type bismuth telluride (Bi_2Te_3) are current commercial TE materials for low-temperature applications. Compared with the current commercial Bi_2Te_3-based bulk low-temperature TE materials, telluride glasses exhibit larger Seebeck coefficient and ultra-low thermal conductivity due to its amorphous state and low carrier concentration.

For vitreous solids, the temperature-dependent thermal conductivities often has a similar magnitude when scaled by material parameters[29]. The thermal conductivity of chalcogenide glass is quite low[30] (0.2~0.3 W/m·°C) because of their highly disordered structure as well as the relatively low phonon energy resulting from heavy atoms like Te[31,32]. Studies show that it is mainly contributed by lattice (phonon) thermal conductivity[33,34].

Besides, as semiconductors, chalcogenide glasses have narrow band gap between 1eV and 3eV. Glasses with large fractions of Te (~70%) tend to have small band gap energies (E_g<1eV)[35], making them the most electrically conductive glass. The electrical conductivity σ of As_2Te_3 glass with its band gap to be 0.3 eV is 10^{-4} S·cm^{-1}.[36] However, this electrical conductivity is still not enough for TE application.

Therefore, in order to optimize the value of ZT, the aim is to enhance σ. Nevertheless, once carrier concentration is enhanced to get a higher σ, thermal conductivity caused by electrons (κ_e) will also increase. On the other hand, a higher S results in decreased carrier concentration and decreased electrical conductivity[37]. Therefore, there is a compromise to find between σ, κ and S, as already shown in Figure 4.5.

On this basis, Te-based glasses which are more electrically conductive should be explored without destroying too much their S and κ. In the following works, As_2Te_3 glass was chosen as the starting composition. In order to decrease the electrical resistivity, many glass systems doped with different metal elements (e.g. Ag, Cu, Sb, Bi) were explored. Several percent of Se was also added into the glass by substitution of Te to maintain glass stability.

4.3.2 Experimental procedure

4.3.2.1 Starting elements purification

Compared with glasses for optical applications, Te-based glass for TE applications is expected to be not sensitive to impurities. Traces of M-O (metal oxide) and M-H (metal

hydrogen bond) existing in synthesized glass would not induce a noticeable variation of σ, κ and S. Thus, a high-purified glass is not essential here. All the raw elements used in TE material research have a purity of 5N and only the purification of starting elements will be enough. The selenium purification method has been introduced in Chapter 1. Here, only the purification of tellurium and arsenic will be presented.

Purification of Tellurium

Note that it is not necessary to use ultra-pure tellurium (6N) for TE research. Te with a purity of 5N can be used after purification by distillation. Due to the vapor pressure difference caused by the melting temperature difference between the Te (449.51°C) and TeO_2 (733 °C), TeO_2 and Te can be separated. The purification process is shown in Figure 4.7.

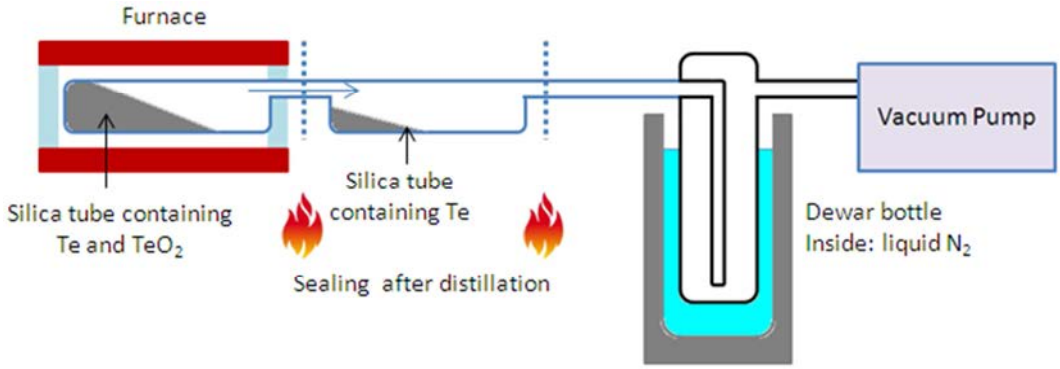

Figure 4.7 Tellurium purification scheme

The silica distillation chamber containing Te was heated until 500 °C and maintained for 4 hours. At this temperature, the vapor pressure of liquid Te is around 100 Pa[38,39], making it quite easy to become vapor and condense at the cold chamber. Then the chamber was sealed at both ends and opened in the glove box under the protection of argon.

Purification of Arsenic

Arsenic was purified by heat treatment since the vapor pressure of its oxide (6.56 kPa at 300°C) is higher than that of metal[40,41] (160 Pa at 300 °C). To do this, arsenic was firstly introduced into a pre-cleaned and dried distillation chamber in a glove box. The assembly is then evacuated using a pump equipped with a filter. Once vacuum reached the requirements (10^{-5} mbar), the dynamic distillation can be performed by introducing the setup in an upright furnace. The oven temperature is then raised to 300 °C and maintained for 15h. During this distillation procedure, As_2O_3 vapor was drawn by pumping and condensed on the silica tube. The ampoule was then sealed and opened in the glove box.

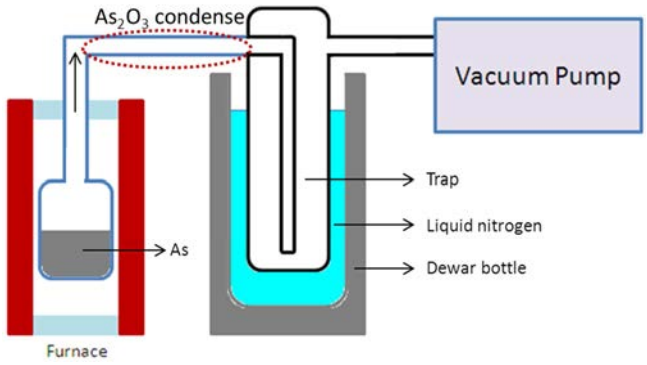

Figure 4.8 Arsenic purification scheme

The purification scheme is shown in Figure 4.8. Compared with selenium purification, the ampoule used here is quite similar. However, one can find that a nozzle between distillation chamber and silica tube do not exist here. This is because, according to our experience, As_2O_3 is quite adhesive to silica tube and would not fall back to the distillation chamber.

4.3.2.1 Glass preparation

Compared to tellurium-based glasses for infrared sensing, the glass preparation processes for TE applications are much easier. The pre-purified elements (5N) weighted according to their stoichiometry were sealed into quartz ampoules under vacuum (10^{-5} mbar) and heated at around 800˚C for 10 hours in a rocking furnace. Using melt quenching technique, the glasses were obtained after annealing 3 hours at several degrees below T_g.

4.4 Glass characterization for TE application

Compared to commercially TE materials, such as bismuth telluride, the main drawback of Te-based glass is its low electrical conductivity. In this chapter, several glass systems will be explored to obtain a stable chalcogenide glass with a higher electrical conductivity.

Te-As-Cu glasses have been proved to be potential candidates in the quest for new high-performance thermoelectric materials. The glass $Cu_{30}As_{15}Te_{55}$ prepared by melt spinning has shown a maximum $s^2\sigma$ value of around 100μWK^{-2}m^{-1}.[21] The glass pieces should be pressed to bulk materials by hot-pressing or spark plasma sintering (SPS) for actual applications. Owing to the limited ΔT between T_g and T_x, sintering process may induce a high tendency of crystallization. Thus, it seemed interesting to explore new compositions in this system for the preparation of thermoelectric bulk material.

In this work, several Te-based glass systems have been explored. DSC and X-ray diffraction (XRD) measurements were performed, respectively, by TA Instruments Auto

Q20, with a heating rate of 10˚C/min, and PANalytical X'Pert PRO, in the range of 5° to 90°. T_g and T_x were obtained from DSC curves using the intersection of tangents. The resistivity was measured by four point probe resistivity probing equipment S-302 from Lucas Labs at room temperature.

4.4.1 Study of Te-As-Cu glasses system

In this part, ternary $(Te_{60}As_{40})_{100-x}Cu_x$ glasses (x=0, 10, 20, 25, 30) (named as L1, L2, L3, L4, and L5 respectively) were explored and characterized. It has already been shown that this ternary system could be interesting for thermoelectric with the initial ratio $Te_{55}As_{45}$[24]. The aim here is to try to improve by focusing on a different stoichiometry.

4.4.1.1 Glassy state confirmation by XRD

The glasses ternary phase diagram and XRD patterns are shown in Figure 4.9.

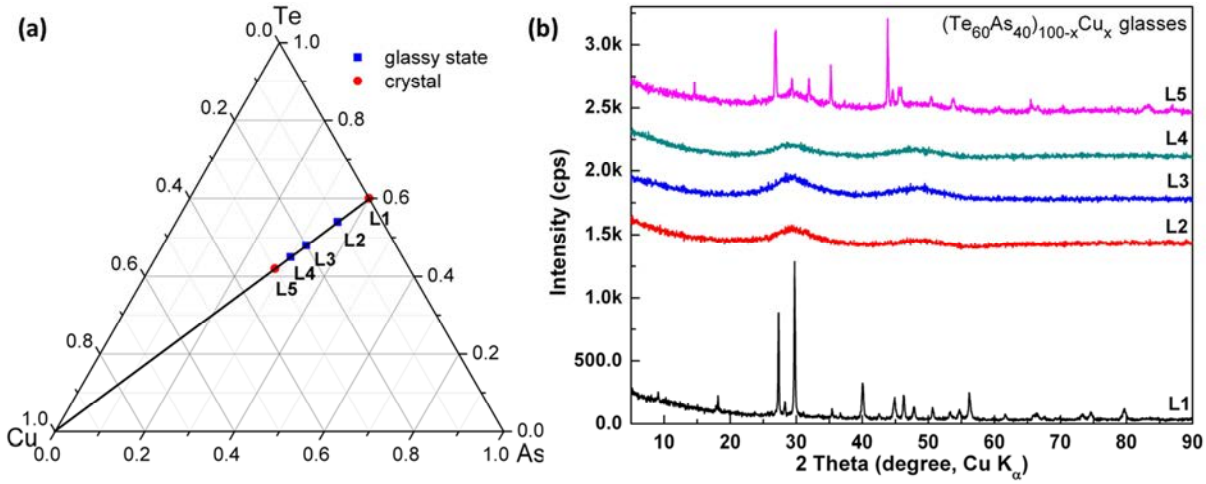

Figure 4.9 Ternary diagram and XRD patterns of $Te_{60-0.6x}As_{40-0.4x}Cu_x$ glasses

Both samples without (L1) or with 30% of Cu (L5) cannot form glass. The precipitated crystalline phases are As_2Te_3 [01-080-0328] and Cu_7Te_5 [00-026-1117] respectively. Thus, the maximum Cu content in this glass system is around 25%. Indeed, Cu, with the electron configuration of [Ar] $3d^{10}$ $4s^1$, shows a preference to bind with tellurium[42], and can enhance the glass stability to some extent. However, free electron density enhanced by too much copper dopant can destroy glass stability. As a result, L5 with 30% of Cu was crystallized.

4.4.1.2 Glass stability study

To evaluate Te-As-Cu glasses thermal stability, DSC curves of L2, L3 and L4 glasses are compared in Figure 4.10.

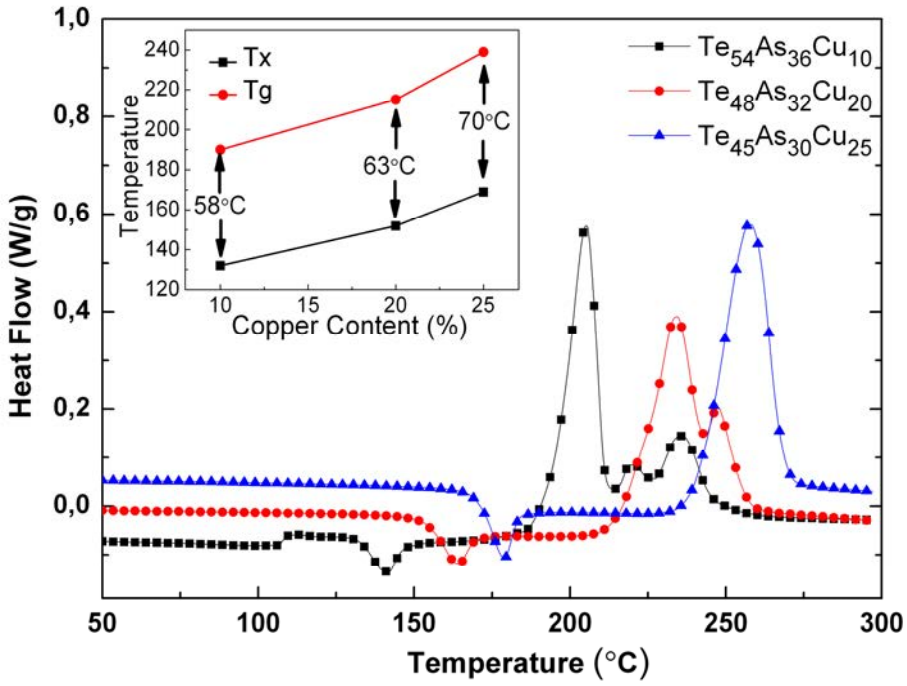

Figure 4.10 DSC curves and ΔT values (inset) of Te-As-Cu glasses

It can be got from DSC curves that both T_g and T_x increase as copper content increased. Copper plays a positive effect on the enhancement of glass stability to some extent. The inset shows that ΔT increases gradually from 58˚C to 70˚C as copper content rises from 10% to 25%. Indeed, to obtain a chalcogenide glass successfully, sufficiently high cooling rate should be given. Owning to the low thermal conductivity of silica glass (1.38 $W \cdot m^{-1}K^{-1}$), L2 glass with its ΔT value to be 58°C is quite difficult to be obtained by melt quenching technique in silica tube. Even for L4 glass, ΔT is still too small to get glassy state easily.

4.4.1.3 Evolution of glass electrical resistivity

Cu has the best electrical conductivity of any metal after silver. In this glass, due to its [Ar] $3d^{10}$ $4s^1$ electron structure and the electronegativity difference between Cu (1.90), As (2.18) and Ge (2.10), Cu easily give up its valence electron under a weakly charged field, and share it with other atoms. As a result, electrical resistivity evolution of glasses with different percentage of copper should be verified.

From Table 4.1, an obvious ρ value decrease can be observed. The minimum resistivity of about 15Ω·cm was achieved. Compared with ρ of As_2Te_3 glass (~10^4 Ω·cm) in reference[36], Cu addition up to 25% molar fraction results in an electrical resistivity decrease of more than 3 orders of magnitude. To explain the mechanism of the ρ decrease caused by copper, glass structure and atom coordination environment should be taken into account.

Table 4.1 Electrical resistivity evolution of Te-As-Cu glasses

Glass composition	Electrical resistivity ρ [Ω·cm]
$Te_{54}As_{36}Cu_{10}$ (L2)	590
$Te_{48}As_{32}Cu_{20}$ (L3)	40
$Te_{45}As_{30}Cu_{25}$ (L4)	15

The local structure analysis of Te-Ge-Cu glasses [42,43] using EXAFS confirmed that Cu occupies the free space of the host matrix without strongly distorting the network of Ge and Te atoms. In this glass system[42], Cu binds mostly to Te when its content is low (~5%). Cu-Cu bonding starts to be significant as Cu content increase (~8%). The coordination number of Cu is always around 2.5.

For Te-As-Cu glass system, the Cu_7Te_5 precipitation in L5 proved again the preference of Cu to stay with Te. Besides, the edges EXAFS studies of $Te_{50-x}As_{50-x}Cu_x$ (x=0~20) glasses (which are still ongoing) show that the valence state of all elements are rather 0. This indicates that mobile electrons are shared over many nuclei. In the Te-As-Cu glass, copper is rather expected to connect to Te, give one free electron to the glass network and as a result increase glass electrical conductivity. However, the σ value obtained is still not sufficient for effective thermoelectric devices manufacture. In addition, more stable glass systems need to be explored also.

4.4.2 Study of Se-As-Cu glasses system

4.4.2.1 Glass composition design

To our knowledge, selenium-based glasses are much more stable compared with tellurium-based glass. This is owing to more non-metallic property of selenium and higher Se-Se bond energy (332.6±0.4kJ/mol) compared with Te-Te bond (259.8±5kJ/mol). Up to now, selenium based glass has already been used as infrared single mode[44,45] and multimode fiber[46] due to its high stability.

Although Se based glass has an intrinsic high electrical resistivity, the glass could be attractive if it can bear a higher copper concentration, which would compensate the side effect of selenium. Therefore, a large scale of compositions in Se-As-Cu glass system was explored (Figure 4.11). The correspondence sample names and compositions are listed in Table 4.2.

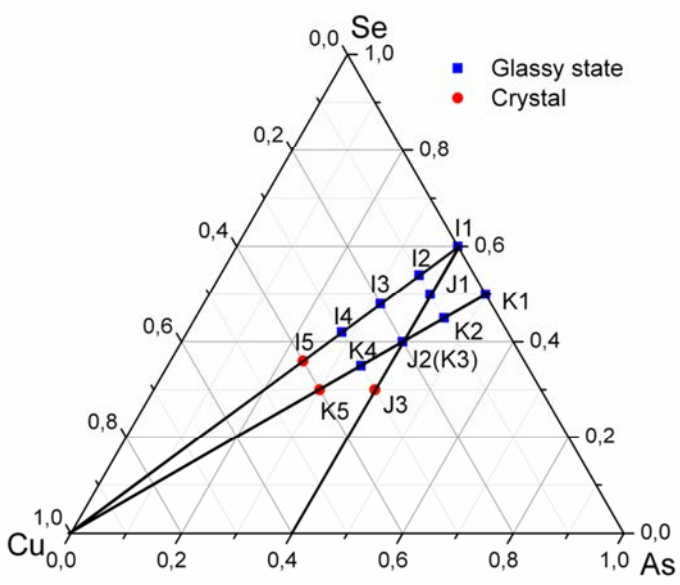

Figure 4.11 Ternary diagram and glass-forming region of Se-As-Cu glass system

Table 4.2 Correspondence of Se-As-Cu glasses names and compositions

No.	Composition	No.	Composition	No.	Composition
I1	$Se_{60}As_{40}$	K1	$Se_{50}As_{50}$	J1	$Se_{50}As_{40}Cu_{10}$
I2	$Se_{54}As_{36}Cu_{10}$	K2	$Se_{45}As_{45}Cu_{10}$	J2	$Se_{40}As_{40}Cu_{20}$
I3	$Se_{48}As_{32}Cu_{20}$	K3	$Se_{40}As_{40}Cu_{20}$	J3	$Se_{30}As_{40}Cu_{30}$
I4	$Se_{42}As_{28}Cu_{30}$	K4	$Se_{35}As_{35}Cu_{30}$		
I5	$Se_{36}As_{24}Cu_{40}$	K5	$Se_{30}As_{30}Cu_{40}$		

Series I and K are designed to compare the influence of Se/As ratio on electrical resistivity. Series J is to explore the influence of Se substitution by Cu on glass performance.

4.4.2.2 Glass property characterization: XRD, DSC, and Resistivity

To identify the glassy state of Te-As-Cu samples and characterize their thermal stability and electron transport properties, XRD, DSC and Resistivity measurements were executed.

XRD

The glass forming region in Figure 4.11 was obtained by measuring the XRD patterns of each composition. In Figure 4.12, the diffraction curves of series I, K and J3 were listed.

Compared with previous Te-As-Cu system, this Se-As-Cu system can support more Cu. More than 30% of copper can be introduced in series I and K. For I5 and K5, too much dopant (40%) starts to induce a crystallization of Cu_2Se. For series J, as the substitution of Se by Cu can decrease the glass stability, when dopant concentration is 30% (J3), Cu_2Se crystals start to appear. XRD patterns show that Cu-doped Se-based glasses possess a higher thermal

stability than previous Te-based glass. In addition, the Cu_2Se crystals precipitation indicates Cu also prefer to bind with chalcogenide element, Se, in Se-As-Cu glass system.

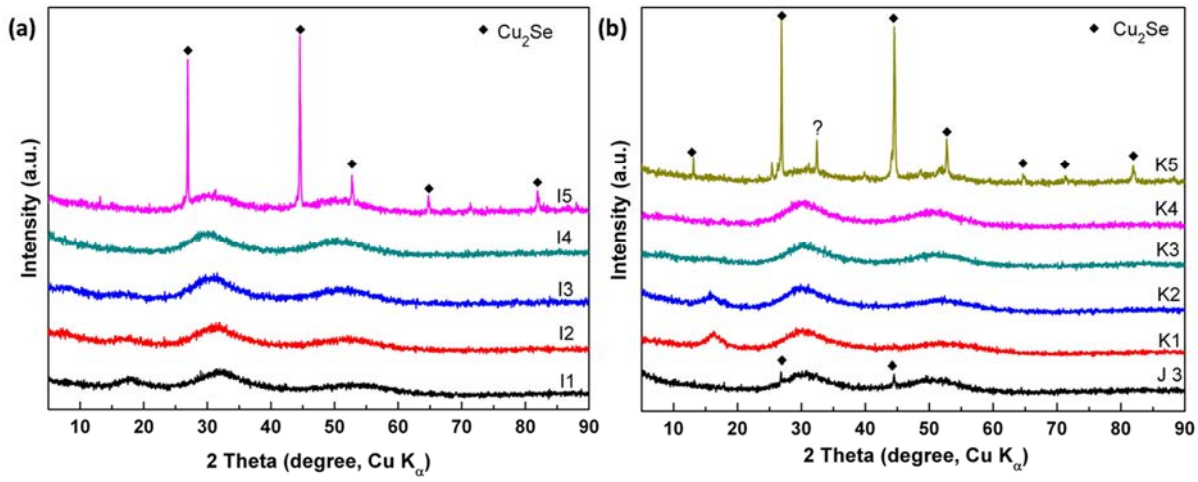

Figure 4.12 XRD patterns of Se-As-Cu samples

DSC

DSC curves of I2 and L2 glasses are compared in Figure 4.13. All the T_g and T_x values of the Se-As-Cu glasses are listed in **Erreur ! Source du renvoi introuvable.**. The crystallized I5, K5 and J3 samples are not included in this table. '--' symbol means the glass is very stable and show no crystallization peak in DSC curves.

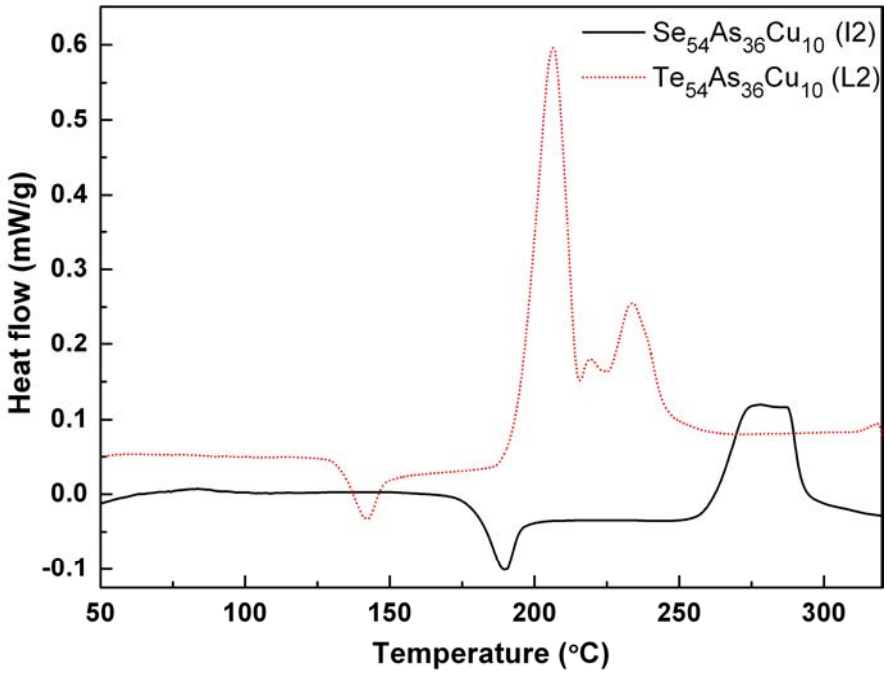

Figure 4.13 Comparison of $Se_{54}As_{36}Cu_{10}$ and $Te_{54}As_{36}Cu_{10}$ glasses stability

L2 glass has an obvious exothermic crystallization peak, indicating the glass thermal instability. In contrast, I2 glass show a large ΔT (103 °C) between T_g and T_x, and the T_x peak

height is much smaller. These two features signify that, as expected, Se-based glass is much more stable.

Table 4.3 Glass transition and crystallization temperatures of Se-As-Cu glasses

Sample	T_g[°C]	T_x[°C]	ΔT[°C]	Sample	T_g[°C]	T_x[°C]	ΔT[°C]	Sample	T_g[°C]	T_x[°C]	ΔT[°C]
I1	179	--	--	K1	170	--	--	J1	181	304	123
I2	179	282	103	K2	191	--	--	J2	206	314	108
I3	190	265	75	K3	206	314	108				
I4	215	267	52	K4	242	326	84				

When Cu concentration reached 30%, both I4 (ΔT=52°C) and K4 (ΔT=84°C) became unstable. J3 batch is too rich in Cu and do not form glass. By comparing Series I and K, it appears that As also plays a benefit role in the enhancement of glass stability. The maximum Cu content is around 30%, which is higher than for pure tellurium glasses.

Electrical resistivity

As more Cu can be introduced in Se-based glass, the electrical resistivity ρ should be measured to evaluate the possibility of Se-based glasses to be used as TE materials (Table 4.4). '--' symbol means ρ is too high and out of the specified measurement range of the four probe resistivity equipment.

Table 4.4 Electrical resistivity of Se-As-Cu glasses

Sample	Resistivity ρ [Ω·cm^{-1}]	Sample	Resistivity ρ [Ω·cm^{-1}]	Sample	Resistivity ρ [Ω·cm^{-1}]
I1	--	K1	--	J1	8.0×10^5
I2	1.5×10^7	K2	4.7×10^6	J2	1.0×10^5
I3	1.0×10^5	K3	1.0×10^5		
I4	3.1×10^3	K4	3.4×10^3		

Selenide glass exhibits a really high electrical resistivity. For example, although sample I4 contains 5% of Cu more than $Te_{45}As_{30}Cu_{25}$ (L4) glass; its electrical resistivity is almost 200 times larger. That means that pure selenide glasses are not all suitable for TE application. The highest Cu rate does not compensate the insulating behavior inherent to this glass family. Therefore, investigation of the resistivity evolution according with Te/Se ratio is a quite interesting issue.

4.4.3 Study of Te-Se-As-Cu glasses system

4.4.3.1 Glass composition design

In this part, the glass systems $(Te_{15}Se_{85})_{60-0.6x}As_{40-0.4x}Cu_x$ (Series G), $(Te_{85}Se_{15})_{60-0.6x}As_{40-0.4x}Cu_x$ (Series A), $(Te_{85}Se_{15})_{50-0.5x}As_{50-0.5x}Cu_x$ (Series F) and $Te_{50-0.5x}As_{50-0.5x}Cu_x$ (Series D) are explored. It has already been shown that the introduction of Se into the system enables to

stabilize the initial tellurium glass and permit to increase the Cu rate introduced in the batch[24]. These first works have been carried out in the frame of a previous PhD in Rennes, in collaboration with the University of Arizona in Tucson. Up to now, the most conductive tellurium-based glass prepared by melt quenching technique is $Cu_{30}As_{10}Te_{54}Se_6$ with its electrical conductivity around 1Ω·cm[23]. Here, the motivation is to further improve glass conductivity by modifying the ratio between Te/Se/As.

The purpose is to choose the proper glass system which combines high thermal stability and low electrical resistivity for further TE material development. As a result, the names and compositions of the samples, and their DSC, XRD and electrical resistivity measurement were all listed in Table 4.5. Note that all the compositions listed in this table were confirmed to be vitreous by XRD. The '--' symbol in G1 means the glass is quite stable and no T_x appears, meanwhile ρ is too high to be measured.

Table 4.5 Performance parameters of Te-Se-As-Cu glass systems

Sample	Composition	T_g(˚C)	T_x(˚C)	ΔT(˚C)	ρ [Ω·cm]
G1	$(Te_{15}Se_{85})_{60}As_{40}$	159	--	--	--
G2	$(Te_{15}Se_{85})_{54}As_{36}Cu_{10}$	161	280	119	4.3×10^6
G3	$(Te_{15}Se_{85})_{48}As_{32}Cu_{20}$	185	258	73	4.3×10^4
G4	$(Te_{15}Se_{85})_{42}As_{28}Cu_{30}$	208	295	87	1.1×10^3
A1	$(Te_{85}Se_{15})_{60}As_{40}$	130	195	65	1.0×10^5
A2	$(Te_{85}Se_{15})_{54}As_{36}Cu_{10}$	136	220	84	2.9×10^3
A3	$(Te_{85}Se_{15})_{50}As_{33.3}Cu_{16.7}$	150	250	100	2.9×10^2
A4	$(Te_{85}Se_{15})_{48}As_{32}Cu_{20}$	155	253	98	2.9×10^2
A5	$(Te_{85}Se_{15})_{45}As_{30}Cu_{25}$	168	267	99	35
F1	$(Te_{85}Se_{15})_{50}As_{50}$	145	272	127	4.3×10^5
F2	$(Te_{85}Se_{15})_{49}As_{49}Cu_2$	140	263	123	2.3×10^5
F3	$(Te_{85}Se_{15})_{45}As_{45}Cu_{10}$	150	280	130	4.3×10^3
F4	$(Te_{85}Se_{15})_{40}As_{40}Cu_{20}$	167	275	108	1.8×10^2
D1	$Te_{50}As_{50}$	142	241	99	3.4×10^4
D2	$Te_{49}As_{49}Cu_2$	137	240	103	2.7×10^4
D3	$Te_{45}As_{45}Cu_{10}$	153	259	106	9.0×10^2
D4	$Te_{40}As_{40}Cu_{20}$	171	280	109	56
D5	$Te_{37.5}As_{37.5}Cu_{25}$	192	261	69	18

4.4.3.2 Glass property characterization: DSC, and electrical resistivity

DSC

For the 4 glass series, as Cu content grew, the T_g values were greatly increased. This phenomenon had also been observed in previous Te-As-Cu and Se-As-Cu glasses. Based on previous structure analysis on Te-As-Cu glasses, it can be proposed that in both Te-based and Se-based chalcogenide glasses, Cu occupies the interstices or voids in glass and connects to Se or Te without breaking glass network. This behavior can increase the average coordination number [47-49] and make the glass structure more rigid.

For Series G, as the majority chalcogenide element is Se, the glass without doping G1 is already quite stable, showing no crystallization peak up to 350°C. As the Cu content increases, some free electrons are provided to the glass structure, decreasing the glass thermal stability. Apart from this series, all the other Te-based glass series show a quite complicated ΔT evolution: ΔT value first increases and then decreases. This observation confirms the complex role played by Cu in the structure. In one hand it tends to increase the T_g by reticulating the network, which could also delayed the crystallization process. But on the other hand, the highest rate of Cu brought too much free electrons to the network, which is detrimental to its stability.

Comparing ΔT of Series A and Series F, it can also be drawn that arsenic rather improves the glass stability. The same result has been observed for the Se-As-Cu glasses.

Electrical resistivity

On the other hand, Cu played a vital role in reducing glass resistance. In Table 4.5, the resistivities ρ decreased 3 or 4 orders of magnitude for each series with the addition of copper. In order to have a more intuitive view on the electrical resistivity alteration, electrical resistivity of different glass series were compared in Figure 4.14.

For a Cu content constant, Se-based glasses have a much higher electrical resistance compared to Te-based glasses. As the Te/Se ratio changes from Series I, to Series G, Series A, and Series L, the ρ value increased significantly. This phenomenon was also observed in Series D and F. Figure 4.14 b shows that substitution of 15% of Te by Se causes several times of ρ increase. Thus, a compromise has to be found on the Te/Se balance, since selenium decreases the free electron concentration and block the electron mobility, but also extend the vitreous domain and the stability of the glasses. In addition, the sublimation of arsenic during

glass preparation should be also taken into account. In glassy state, Te and As prefer to form short-range order of As_2Te_3. During the synthesis of glasses in Series F and D, the extra unstable arsenic would escape from the glass and condense on the top of the silica tube, which has been confirmed by XRD. As a result, the final glass compositions are difficult to be controlled. On this basis, even though arsenic rather improves the glass stability, Series F and D are still not good candidates. $(Te_{85}Se_{15})_{45}As_{30}Cu_{25}$ (A5) glass from series A combines both the performance of high stability and low resistance, and shows its potential to be a great candidate for following investigation.

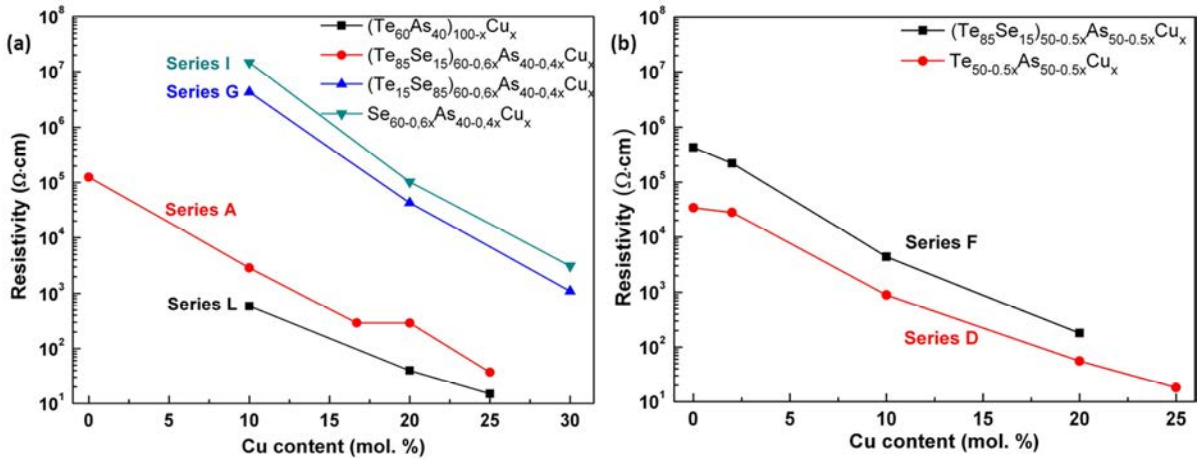

Figure 4.14 Resistance comparison of Te-As-Cu, Te-Se-As-Cu and Se-As-Cu glasses

4.4.4 Exploration of Te-Se-As-Ag and Te-Se-As/(Sb,Bi)-Cu glasses

According to the previous paragraph, $(Te_{85}Se_{15})_{45}As_{30}Cu_{25}$ is among the most interesting candidate for TE. However, the value of electrical resistivity 35Ω·cm is still too high. Therefore, the substitution of Cu by Ag or As by a small amount of Sb/Bi was tried in order to decrease the electrical resistivity.

4.4.4.1 Study of Te-Se-As-Ag system

Compared to copper, silver has similar electronic structure and electronegativity, but has a lower electrical resistivity and larger radius (Table 4.6). Actually, silver has the lowest resistance of any known natural material.

Table 4.6 Property and structure comparison of copper and silver

	Copper	**Silver**
Electron structure	[Ar] $3d^{10}$ $4s^1$	[Kr] $4d^{10}$ $5s^1$
Electrical resistivity	(20 °C) 16.78 nΩ·m	(20 °C) 15.87 nΩ·m
Atomic radius	128 pm	144 pm
Electronegativity	1.90 (Pauling scale)	1.93 (Pauling scale)

The glass compositions were designed using the same Te/Se and As ratio as for Cu-doped glasses. The explored compositions are shown in the following ternary phase diagram (Figure 4.15). The glassy state was confirmed by XRD.

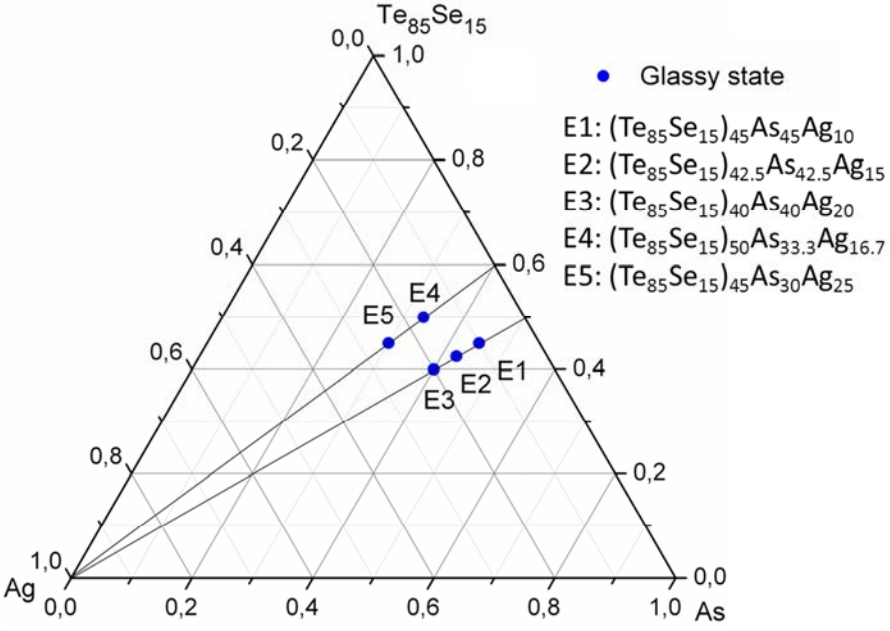

Figure 4.15 Ternary phase diagram of Te-Se-As-Ag glass system

The ρ value comparison between Cu and Ag doped glasses is shown in **Figure 4.16**.

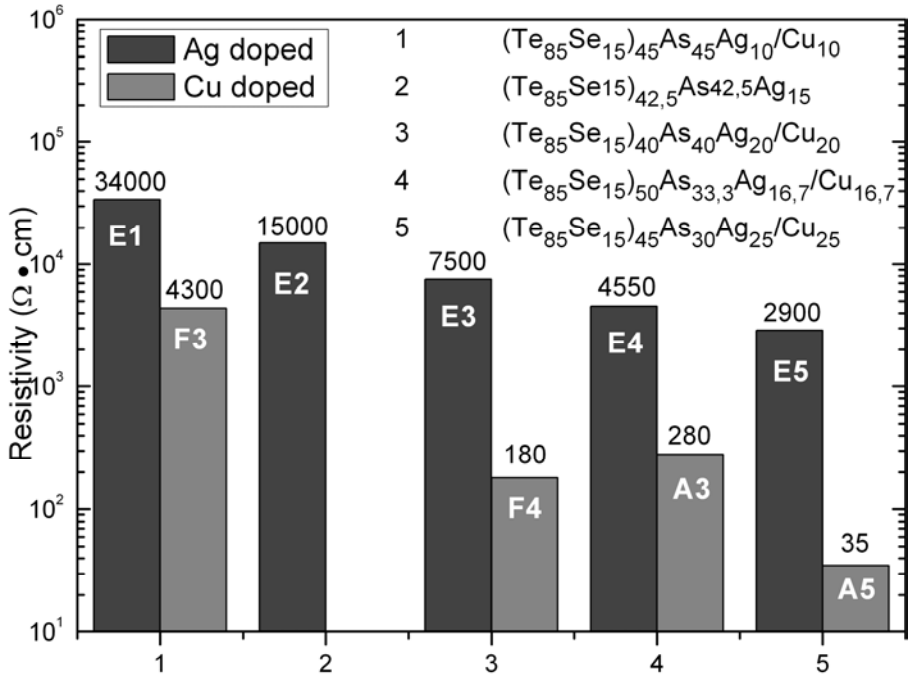

Figure 4.16 Electrical resistivity of silver- and copper-doped tellurium based glasses

With the increase of Ag content, the ρ value declined from E1 to E3 and from E4 to E5. The same phenomenon was also observed in previous research on the Te-As-Ag glass

system [50]. However, ρ of Ag-doped glasses are much higher than that of Cu-doped glasses, disqualifying them for TE. Actually, it is also well known that Ag-doped telluride glasses are rather good candidates for ionic conduction[51].

4.4.4.2 Study of Te-Se-As/(Sb,Bi)-Cu glasses system

Sb and Bi are two elements in the same column of the periodic chart as arsenic, they have the similar atomic structure but are more metallic compared to As. As a result, we predict that a small amount substitution of As by Sb or Bi may make the glass more conductive. The compositions explored are listed in Table 4.7.

Table 4.7 Correspondence of Te-Se-As/(Sb,Bi)-Cu glasses names and compositions

	Sample	Composition		Sample	Composition
Series B	B1	$(Te_{85}Se_{15})_{45}As_{29}Cu_{25}$-$Sb_1$	Series C	C1	$(Te_{85}Se_{15})_{45}As_{29}Cu_{25}$-$Bi_1$
	B2	$(Te_{85}Se_{15})_{45}As_{28}Cu_{25}$-$Sb_2$		C2	$(Te_{85}Se_{15})_{45}As_{28}Cu_{25}$-$Bi_2$
	B3	$(Te_{85}Se_{15})_{45}As_{27}Cu_{25}$-$Sb_3$		C3	$(Te_{85}Se_{15})_{45}As_{27}Cu_{25}$-$Bi_3$
	B4	$(Te_{85}Se_{15})_{45}As_{26}Cu_{25}$-$Sb_4$		C4	$(Te_{85}Se_{15})_{45}As_{26}Cu_{25}$-$Bi_4$

DSC curves of glasses with different dopant concentration (Figure 4.17) show that only a small amount of Sb and Bi can greatly increase the energy released during crystallization and make the system unstable.

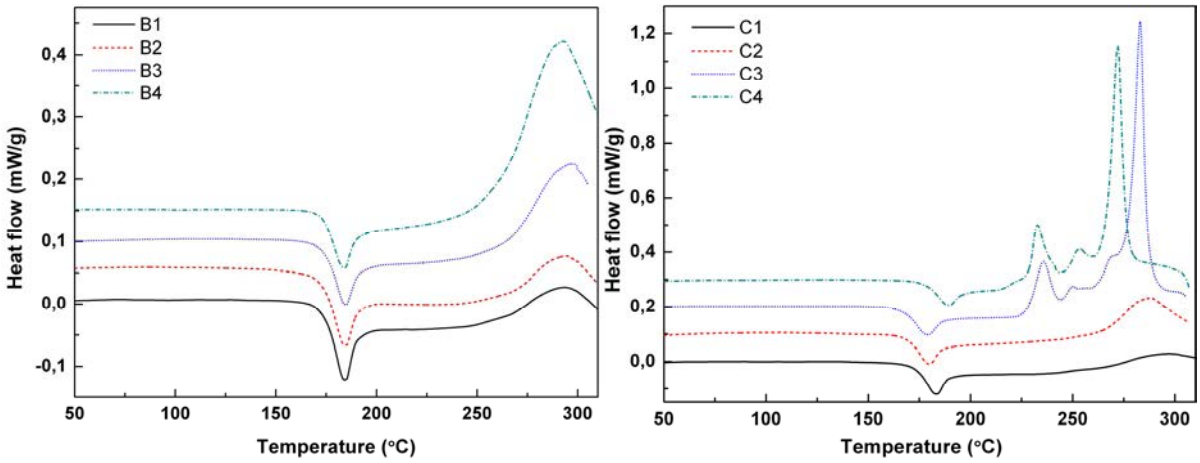

Figure 4.17 DSC curves of Sb (left) and Bi (right) doped Te-based glasses

For Series B, although ΔT has no significant decline, the bulk glass formability has been destroyed by Sb and all the glasses break into small pieces after annealing. For Series C, ΔT exhibits a remarkable decrease when the Bi concentration increases. For C4 sample, BiSeTe crystals were precipitated. As a result, the glass composition was changed, inducing an increase of T_g value. However, both the resistivities of Series B and C measured by four point probe method shows no significant change (around 30 Ω·cm).

4.5 Te-based glasses crystallization investigation

As a commonly used TE material, bismuth telluride has a quite low ρ around $1.0 \times 10^{-5}\Omega$·m. Regarding this, the minimum ρ (~15 Ω·cm) obtained for the glass is still too high for any thermoelectric application. New method to decrease ρ value should be explored.

Controllable crystallization would be an applicable way[52]. Crystals nucleation and growth could provide a large quantity of free electrons, meanwhile, the microstructure formed by glassy state and crystal in the glass-ceramics could raise boundary phonon scattering at a micro scale. Therefore, $(Te_{85}Se_{15})_{45}As_{30}Cu_{25}$ (A5) glass was firstly selected for heat treatment at various temperatures and during different times due to the combination of its high stability and low resistance. $Te_{45}As_{30}Cu_{25}$ (L4), as the most conductive glass in this work was also chosen for crystallization.

Actually, compared to a crystallized state, more energy is stored in glassy state. Glass structure can have a certain degree of flexibility when its temperature is higher than T_g. Atoms in glass can cross the energy barrier and slowly rearrange into organized crystal patterns thanks to the energy provided by heat treatment.

In this part, the glass slices were heat treated tens of degrees higher than T_g in air atmosphere. The categories of predicated crystals and glass ρ variation were verified by XRD and 4-probe technique respectively.

4.5.1 Crystallization of $(Te_{85}Se_{15})_{45}As_{30}Cu_{25}$ glass

The A5 glass $(Te_{85}Se_{15})_{45}As_{30}Cu_{25}$ was first selected for heat treatment. The heat treatment was first set to be at T_g+10°C from 10 hours up to 90 hours. The glass samples were also heat treated at T_g+40°C and at T_g+60°C for 15 hours.

4.5.1.1 Glass heat treatment and XRD measurement

The first trial was set to be at T_g+10°C during 10 to 90 hours for the purpose of monitoring crystal precipitation procedure. To exclude the influence of surface oxidation caused by O_2 in air, all samples were re-polished before XRD measurement. The polish depth was around 0.1 mm. XRD patterns shown that all samples remain vitreous after heat treatment. As a result, heat treatments at T_g+40 °C and T_g+60 °C were subsequently executed. However, even heat-treated at T_g+60 °C for 15 hours, the glass is only slightly crystallized (Figure 4.18 a), showing that this glass composition is definitively very stable.

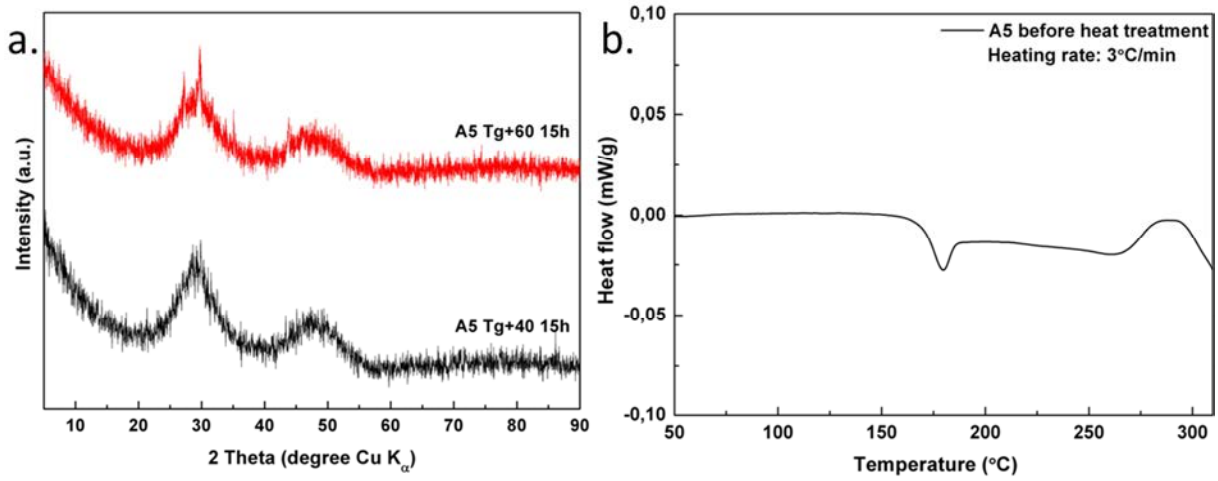

Figure 4.18 (a.) X-ray diffraction pattern of sample $(Te_{85}Se_{15})_{45}As_{30}Cu_{25}$ after heat treatment at T_g+40 and T_g+60°C for 15 hours. (b.) DSC curve of $(Te_{85}Se_{15})_{45}As_{30}Cu_{25}$ glass without heat treatment using a heating rate of 3°C/min.

DSC curve of A5 glass could explain this stability. In Figure 4.18 b, the exothermic peak caused by glass crystallization is really small confirming that the driving force of crystallization during heat treatment is really limited.

4.5.1.2 Electrical resistivity and surface crystallization

Another interesting phenomenon after heat treatment in air atmosphere is the appearance of thin film showing a purple color on all the sample surfaces. To identify the reasons, ρ of samples before and after polishing were also compared (Figure 4.19).

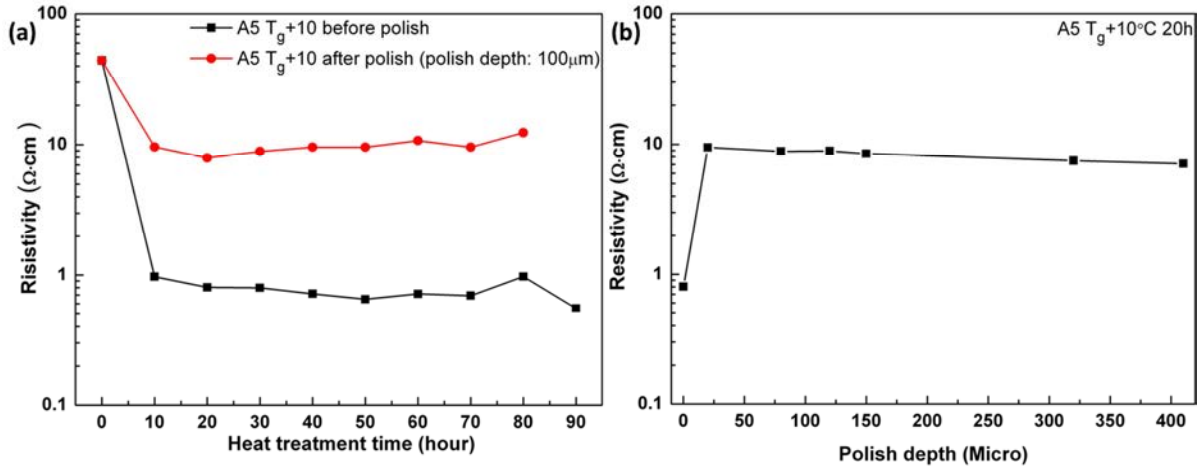

Figure 4.19 Resistivities of $(Te_{85}Se_{15})_{45}As_{30}Cu_{25}$ (A5) samples (a) heat treated at T_g+10°C for different hours before and after polish (b) with polish depth after heat treatment at 178°C for 20 hours.

ρ of glass without heat treatment is 35 Ω·cm. After heat treatment at T_g+10°C for 10 hours, the resistivity of polished glass samples is about 10Ω·cm. This value doesn't change when the heat treatment time increases. The ρ difference before and after heat treatment was probably caused by the release of stress inside the sample during the heating. Besides, ρ values are quite different before and after polishing. Unpolished samples always exhibit a lower ρ value than polished samples. To verify this phenomenon, A5 sample, heat treated at T_g+10°C for 20 hours, was polished step by step. The polish depth (measurement error is ± 10 μm) and electrical resistivity after each polish were measured and their relationship are reported in Figure 4.19b.

Before polish, ρ is around 0.8 Ω·cm. After a first polishing for only 20 μm, the value is greatly increased to 10 Ω·cm and remains stable with the polish depth increases up to 0.4mm. This ρ evolution confirms that the surface presents a specific behavior and that the bulk is homogeneous. However, the ρ decrease at surface could not be explained by surface oxidation, and very probably surface crystallization occurred. To check this assumption, XRD of unpolished surface of A5 sample after heat treatment at T_g+10°C for 90 hours were measured (Figure 4.20).

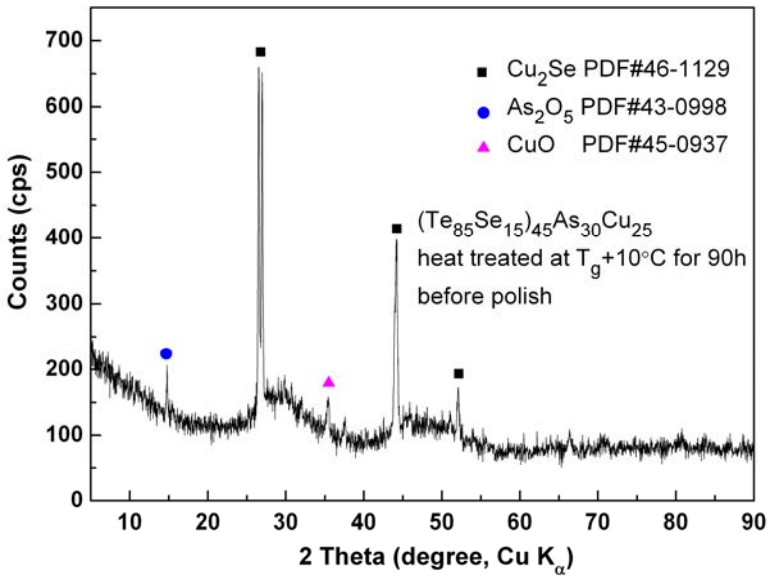

Figure 4.20 XRD pattern of $(Te_{85}Se_{15})_{45}As_{30}Cu_{25}$ surface after heat treatment at T_g+ 10°C for 90 hours

This XRD pattern confirmed that beside As_2O_3 and CuO, Cu_2Se crystals also nucleated on surface, explaining a lower resistivity value for the surface. This surface crystallization is caused by the high surface energy induced by the broken bonds and impurities. This kind of non-uniform crystallization is often observed during the fiber drawing process of telluride

glasses (e.g. Figure 3.11). On this basis, it can be concluded that in Figure 4.19b, 20 hours of heat treatment at T_g+10°C can cause surface crystallization with a thickness less than 50 μm.

4.5.2 $Te_{45}As_{30}Cu_{25}$ glass and glass-ceramics

4.5.2.1 Heat treatment and characterization: XRD and resistivity

DSC of the $Te_{45}As_{30}Cu_{25}$ (L4) glass at a heating rate of 3°C/min was executed to obtain an accurate T_g value for the heat treatment (Figure 4.21).

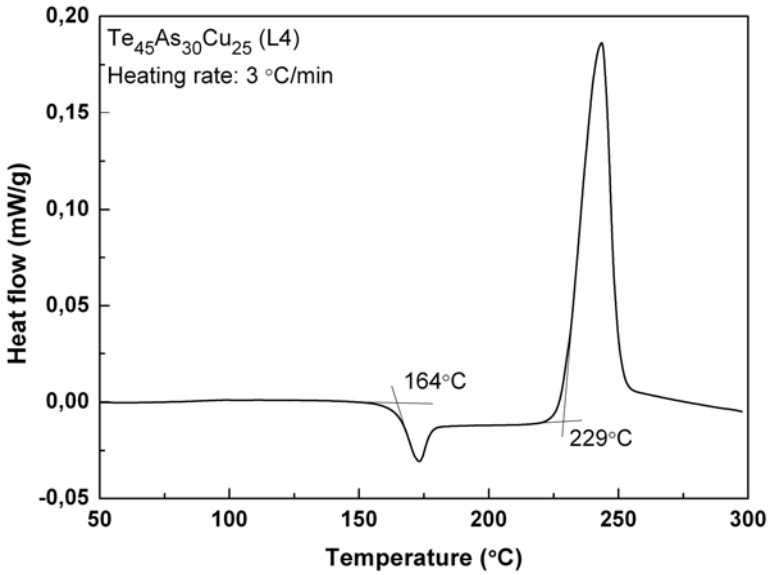

Figure 4.21 DSC curve of $Te_{45}As_{30}Cu_{25}$ glass at heating rate: 3˚C/min

This glass has a large exothermic crystallization peak and should be much easier to crystallize than A5 glass. Based on DSC curve, the heat treatment conditions were designed and listed in. The phase of sample after heat treatment was also measured using XRD.

Table 4.8 The heat treatment condition of $(Te_{85}Se_{15})_{45}As_{30}Cu_{25}$ glass

Temperature [°C]	Time [hour]	Sample phase	Temperature [°C]	Time [hour]	Sample phase
$T_g + 10$	15	Glass	$T_g + 30$	75	Partially crystallized
$T_g + 20$	15	Glass	$T_g + 40$	15	Partially crystallized
$T_g + 30$	15	Glass	$T_g + 50$	15	Crystallized
$T_g + 30$	45	Partially crystallized	T_x	0.5	Crystallized

In order to get controllable nano-sized crystals, the heat treatment should be between T_g and T_x and not be too high to avoid the rapidly growth of crystal size. As example, even 30 minutes of heat treatment at T_x can induce obvious nucleation of crystals. The corresponding XRD pattern is shown in Figure 4.22.The crystalline phases As_2Te_3, $Cu_{2.72}Te_2$, Cu_2Te and algodonite are identified and the samples is no longer vitreous. Therefore, a proper heat treatment temperature should be determined.

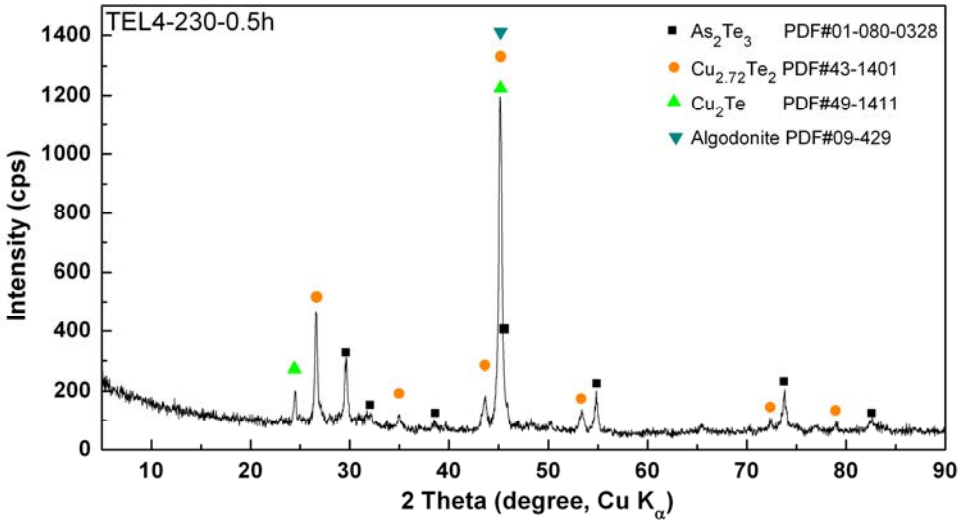

Figure 4.22 XRD of $Te_{45}As_{30}Cu_{25}$ after the heat treatment at 230°C for 0.5 hour

From Figure 4.23, it can be concluded that heat treatment at different temperature (from T_g+30°C to T_g+50°C) for 15 hours and at T_g+30°C for different time (15h, 45h, and 75h) can both nucleate crystals gradually. As heat treatment time or temperature increasing, the crystallinity rate became higher. Compared with A5 glass, the crystallization of L4 glass is easier to be controlled.

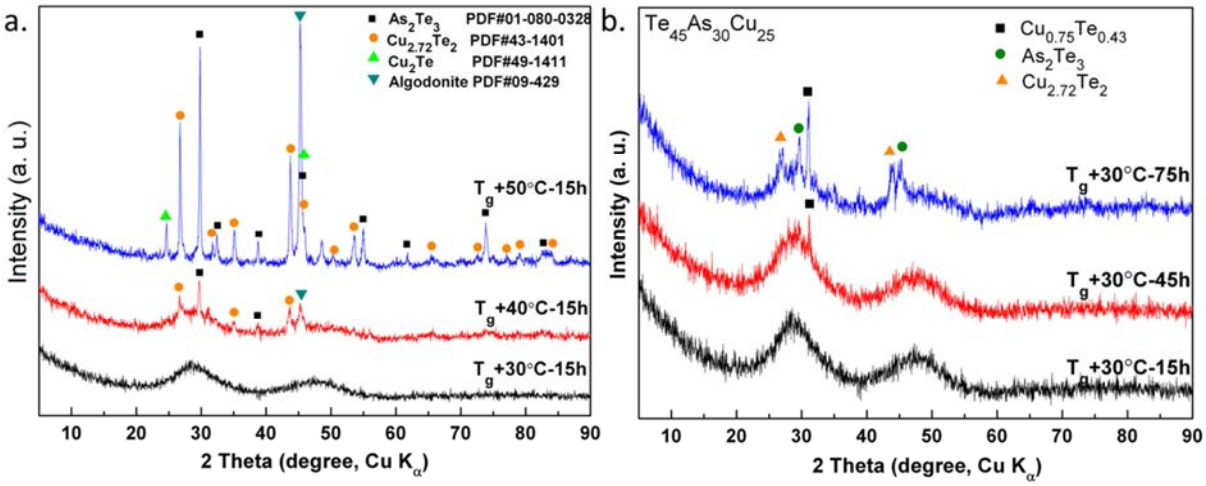

Figure 4.23 XRD of $Te_{45}As_{30}Cu_{25}$ after heat treatment at different temperature for 15 hours (a.) and at T_g+30°C for different time (b.)

The electrical resistivities of re-polished sample slices after heat treatment were also measured. For samples which are still vitreous, their ρ values are all around 6Ω·cm. Even ρ of partial crystallized sample after heat treatment at T_g+30°C for 45 hours is still the same as that of the glass. As crystallinity increasing, ρ of samples after heat treatment at T_g+30°C for 75 hours and T_g+40°C for 15 hours declined to 2Ω·cm. Hopefully, by controlling the crystallization process, it is possible to control the resistivity.

4.5.2.2 Surface crystallization

However, during the preparation of glass-ceramics sample for Seebeck measurement, new problem was found. The sample heat treated at T_g+40°C for 15 hours was taken as an example. After heat treatment, glass rod, with its diameter and length to be 7 and 10 mm respectively, was polished in order to get the sample (2×2×10 mm) for Seebeck measurement (inset A of Figure 4.24). The electrical resistivity was controlled during the polishing. By polishing, the sample exhibits a great change of resistivity value.

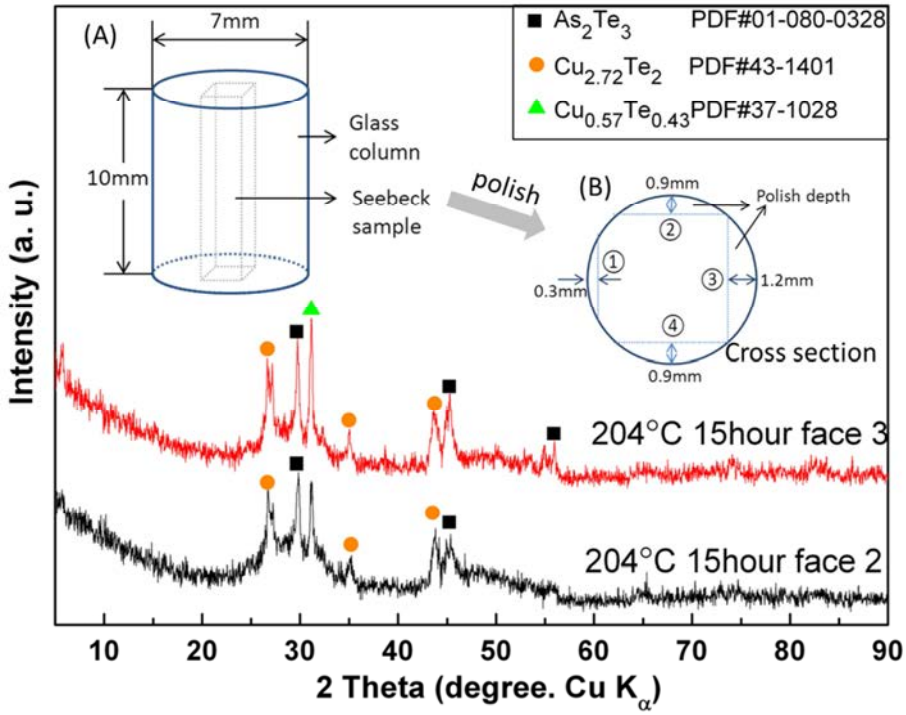

Figure 4.24 XRD of different faces of $Te_{45}As_{30}Cu_{25}$ rod after polish. The sample is heat-treated at 204°C for 15 hours

Inset B of Figure 4.24 shows the cross section of glass rod after polish. The polish depths from 1 to 4 were 0.9, 0.9, 0.3 and 1.2 mm respectively. However, ρ values had two orders of magnitude difference varies from 0.023 Ω·cm (face 3) up to 4.3 Ω·cm (face 1). Comparing the XRD patterns of both face 2 and face 3 in Figure 4.24, it can be found that the diffraction peaks of face 3 are higher than face 2. This signifies the existence of crystallinity gradient from rod surface to the center. These measurements confirm that the crystallization process is not homogeneous. As expected, the resistivity is lower in regions where the nuclei are numerous and large sizes. Therefore, alternative ways have to be devised for preparing homogeneous samples of glass ceramics.

4.6 Conclusion

In this chapter the basic principles useful for understanding the thermoelectric phenomena: Seebeck effect, Peltier effect and Thomson effect have been introduced. It has been also shown that the composition and phase design of the material is a compromise among the physical quantities electrical conductivity, Seebeck coefficient and thermal conductivity in order to get the maximum figure of merit.

In fact, materials for thermoelectric applications should possess very low thermal conductivities, which is the advantage of telluride glass. However, the figure of merit of telluride glass is too low due to insufficient electrical conductivity. In order to increase the conductivity, we have explored Te-As-Se-Cu glass systems with Te/Se ratio varies from 0/100 up to 100/0. $(Te_{85}Se_{15})_{45}As_{30}Cu_{25}$ glass could be an intersting candidate with a combination of high stability (ΔT=99 °C) and low resistance (ρ=35 Ω·cm). However, as it stands, the ρ value 35Ω·cm is still too high for any TE application. It is even much higher than previous results obtain in our lab[24] and other reference[23]. Therefore, the substitution of Cu by Ag or As by a small amount of Sb/Bi was tried in this part of the work in order to decrease the electrical resistivity. None of these both strategies has proved to be convincing.

Finally the last way which was explored to decrease the resistivity consisted in the preparation of glass ceramics[52]. The best results were obtained from the $Te_{45}As_{30}Cu_{25}$ glass. It is possible to control the nucleation growth process by heating, in order to decrease the resistivity from 15 Ω·cm down to 2 Ω·cm. Unfortunately, it is difficult to get some homogeneous samples in term of nuclei spreading over the glassy matrix. That is a real problem because the ρ values are directly connected to the crystallinity rate.

Therefore, new method for preparing glass ceramics or composites should be explored. That is the purpose of the next chapter.

Reference

[1] T.J. Seebeck. Ueber Die Magnetische Polarisation Der Metalle Und Erze Durch Temperaturdifferenz. Annalen der Physik. 1826, 82 (3): 253-286

[2] P. JCA. Nouvelle Experiences Sur La Caloricité Des Courants Électriques. In: Annales de chimie et physique, 1834: 371-387

[3] A.F. Ioffe. Semiconductor Thermoelements and Thermoelectric Cooling. 1957

[4] M. Vedernikov, E. Iordanishvili. Af Ioffe and Origin of Modern Semiconductor Thermoelectric Energy Conversion. In: Thermoelectrics, 1998. Proceedings ICT 98. XVII International Conference on: IEEE, 1998: 37-42

[5] D.M. Rowe. Thermoelectrics Handbook: Macro to Nano. Boca Raton, Florida: CRC press, 2005

[6] G.A. Slack. New Materials and Performance Limits for Thermoelectric Cooling. CRC Handbook of Thermoelectrics. 1995, 407

[7] M.S. Dresselhaus, G. Chen, M.Y. Tang, R.G. Yang, H. Lee, D.Z. Wang, Z.F. Ren, J.P. Fleurial, P. Gogna. New Directions for Low-Dimensional Thermoelectric Materials. Advanced Materials. 2007, 19 (8): 1043-1053

[8] G. Chen, M.S. Dresselhaus, G. Dresselhaus, J.P. Fleurial, T. Caillat. Recent Developments in Thermoelectric Materials. International Materials Reviews. 2003, 48 (1): 45-66

[9] T.M. Tritt. Recent Trends in Thermoelectric Materials Research. In: Semiconductors and Semimetals San Diego: Academic Press, 2000

[10] T.M. Tritt, G.S. Nolas, M. Kanatzidis, G. Mahan, D.G. Mandrus. New Materials for Small Scale Thermoelectric Refrigeration and Power Generation Applications. Warrendale PA: Materials Research Society, 2000

[11] T.M. Tritt, G. Mahan, H.B. Lyon, M.G. Kanatzidis. Thermoelectric Materials - New Directions & Approaches. San Francisco, CA: Materials Research Society, 1997

[12] G.S. Nolas, D.T. Morelli, T.M. Tritt. Skutterudites: A Phonon-Glass-Electron Crystal Approach to Advanced Thermoelectric Energy Conversion Applications. Annual Review of Materials research. 1999, 29: 89-116

[13] B.B. Iversen, A.E.C. Palmqvist, D.E. Cox, G.S. Nolas, G.D. Stucky, N.P. Blake, H. Metiu. Why Are Clathrates Good Candidates for Thermoelectric Materials? Journal of Solid State Chemistry. 2000, 149 (2): 455-458

[14] S.M. Kauzlarich, S.R. Brown, G. Jeffrey Snyder. Zintl Phases for Thermoelectric Devices. Dalton Transactions. 2007 (21): 2099-2107

[15] K. Biswas, J. He, I.D. Blum, C.-I. Wu, T.P. Hogan, D.N. Seidman, V.P. Dravid, M.G. Kanatzidis. High-Performance Bulk Thermoelectrics with All-Scale Hierarchical Architectures. Nature. 2012, 489 (7416): 414-418

[16] S.B. Riffat, X. Ma. Thermoelectrics: A Review of Present and Potential Applications. Applied Thermal Engineering. 2003, 23 (8): 913-935

[17] P.A. Kinzie. Thermocouple Temperature Measurement. Wiley New York, 1973

[18] H. Xi, L. Luo, G. Fraisse. Development and Applications of Solar-Based Thermoelectric Technologies. Renewable and Sustainable Energy Reviews. 2007, 11 (5): 923-936

[19] L.E. Bell. Cooling, Heating, Generating Power, and Recovering Waste Heat with Thermoelectric Systems. Science. 2008, 321 (5895): 1457-1461

[20] I. Hatcher, K.L. Reed. Compact Thermoelectric Refrigerator: Google Patents, 1982

[21] A.P. Gonçalves, G. Delaizir, E.B. Lopes, L.M. Ferreira, O. Rouleau, C. Godart. Chalcogenide Glasses as Prospective Thermoelectric Materials. Journal of Electronic Materials. 2011, 40 (5): 1015-1017

[22] A.P. Gonçalves, E.B. Lopes, G. Delaizir, J.B. Vaney, B. Lenoir, A. Piarristeguy, A. Pradel, J. Monnier, P. Ochin, C. Godart. Semiconducting Glasses: A New Class of Thermoelectric Materials? Journal of Solid State Chemistry. 2012, 193 (0): 26-30

[23] J.B. Vaney, A. Piarristeguy, A. Pradel, E. Alleno, B. Lenoir, C. Candolfi, A. Dauscher, A.P. Gonçalves, E.B. Lopes, G. Delaizir, J. Monnier, M. Ribes, C. Godart. Thermal Stability and Thermoelectric Properties of $Cu_xAs_{40-x}Te_{60-y}Se_y$ Semiconducting Glasses. Journal of Solid State Chemistry. 2013, 203 (0): 212-217

[24] P. Lucas, C. Conseil, Z. Yang, Q. Hao, S. Cui, C. Boussard-Pledel, B. Bureau, F. Gascoin, C. Caillaud, O. Gulbiten, T. Guizouarn, P. Baruah, Q. Li, J. Lucas. Thermoelectric Bulk Glasses Based on the Cu-As-Te-Se System. Journal of Materials Chemistry A. 2013, 1 (31): 8917-8925

[25] P. Zhu, Y. Imai, Y. Isoda, Y. Shinohara, X. Jia, G. Ren, G. Zou. Electrical Transport and Thermoelectric Properties of Pbte Prepared by Hpht. Materials transactions. 2004, 45 (11): 3102-3105

[26] N. Mateeva, H. Niculescu, J. Schlenoff, L. Testardi. Correlation of Seebeck Coefficient and Electric Conductivity in Polyaniline and Polypyrrole. Journal of Applied Physics. 1998, 83 (6): 3111-3117

[27] C. GODART. Materiaux a Effets Thermoelectriques. Éditions techniques de l'ingénieur 2009

[28] B. Lenoir, J.-P. Michenaud, A. Dauscher. Thermoelectricite: Des Principes Aux Applications. Éditions techniques de l'ingénieur 2010

[29] J. Freeman, A. Anderson. Thermal Conductivity of Amorphous Solids. Physical Review B. 1986, 34 (8): 5684

[30] J.S. Sanghera, I.D. Aggarwal. Active and Passive Chalcogenide Glass Optical Fibers for Ir Applications: A Review. J. Non-Cryst. Solids. 1999, 256–257 (0): 6-16

[31] A. Majumdar. Thermoelectricity in Semiconductor Nanostructures. Science. 2004, 303 (5659): 777-778

[32] D.G. Cahill, R. Pohl. Lattice Vibrations and Heat Transport in Crystals and Glasses. Annual Review of Physical Chemistry. 1988, 39 (1): 93-121

[33] M. Fadel, H.T. El-Shair. Electrical, Thermal and Optical Properties of $Se_{75}Ge_7Sb_{18}$. Vacuum. 1992, 43 (3): 253-257

[34] M. Afifi, H. Labib, M. El-Fazary, M. Fadel. Electrical and Thermal Properties of Chalcogenide Glass System $Se_{75}Ge_{25-x}Sb_x$. Applied Physics A. 1992, 55 (2): 167-169

[35] Z. Yang, O. Gulbiten, P. Lucas, T. Luo, S. Jiang. Long-Wave Infrared-Transmitting Optical Fibers. Journal of the American Ceramic Society. 2011, 94 (6): 1761-1765

[36] S.R. Elliott. Chalcogenide Glasses. Materials science and technology. 1991, 9: 375

[37] H. Goldsmid, A. Sheard, D. Wright. The Performance of Bismuth Telluride Thermojunctions. British Journal of Applied Physics. 1958, 9 (9): 365

[38] R.F. Brebrick. Tellurium Vapor Pressure and Optical Density at 370-615 Degree. The Journal of Physical Chemistry. 1968, 72 (3): 1032-1036

[39] R.E. Machol, E.F. Westrum Jr. Vapor Pressure of Liquid Tellurium. Journal of the American Chemical Society. 1958, 80 (12): 2950-2952

[40] E.S. Toberer, A.F. May, G.J. Snyder. Zintl Chemistry for Designing High Efficiency Thermoelectric Materials. Chemistry of Materials. 2009, 22 (3): 624-634

[41] R. Viennois, X. Tao, P. Jund, J.-C. Tedenac. Stability and Thermoelectric Properties of Transition-Metal Silicides. Journal of Electronic Materials. 2011, 40 (5): 597-600

[42] L. Rátkai, A.P. Gonçalves, G. Delaizir, C. Godart, I. Kaban, B. Beuneu, P. Jóvári. The Cu and Te Coordination Environments in Cu-Doped Ge–Te Glasses. Solid State Communications. 2011, 151 (21): 1524-1527

[43] M. Sakurai, F. Kakinuma, E. Matsubara, K. Suzuki. Partial Structure Analysis of Amorphous $Ge_{15}Te_{80}M_5$ (M= Cu, Ag and in). Journal of Non-Crystalline Solids. 2002, 312: 585-588

[44] P. Toupin, L. Brilland, C. Boussard-Plédel, B. Bureau, D. Mechin, J.-L. Adam, J. Troles. Comparison between Chalcogenide Glass Single Index and Microstructured Exposed-Core Fibers for Chemical Sensing. J. Non-Cryst. Solids. 2013 (0)

[45] D.A.C. Compton, S.L. Hill, N.A. Wright, M.A. Druy, J. Piche, W.A. Stevenson, D.W. Vidrine. In Situ FT-IR Analysis of a Composite Curing Reaction Using a Mid-Infrared Transmitting Optical Fiber. Appl. Spectrosc. 1988, 42 (6): 972-979

[46] M.L. Anne, E.L.G.L. Salle, B. Bureau, J. Tristant, F. Brochot, C. Boussard-Plédel, H.L. Ma, X.H. Zhang, J.L. Adam. Polymerisation of an Industrial Resin Monitored by Infrared Fiber Evanescent Wave Spectroscopy. Sensors and Actuators B: Chemical. 2009, 137 (2): 687-691

[47] K. Liang, A. Bienenstock, C. Bates. Structural Studies of Glassy $Cuasse_2$ and $Cu\text{-}As_2Se_3$ Alloys. Physical Review B. 1974, 10 (4): 1528

[48] J. Conejo, N. De La Rosa-Fox, L. Esquivias, R. Jiménez-Garay. Tetrahedral Bonding in the Glassy Semiconductor $Cu_{15}As_{34}Se_{51}$. Materials Letters. 1986, 4 (11): 481-484

[49] J. Liu, P. Taylor. Absence of Photodarkening in Bulk, Glassy As_2S_3 and As_2Se_3 Alloyed with Copper. Physical review letters. 1987, 59 (17): 1938

[50] A. Giridhar, S. Mahadevan. Silver as a Dopant and as a Constituent in As-Ag-Te Glasses: Electrical Conductivity. Journal of Non-Crystalline Solids. 1996, 197 (2–3): 228-234

[51] S. Hocdé, C. Boussard-Plédel, G. Fonteneau, D. Lecoq, H.-L. Ma, J. Lucas. Recent Developments in Chemical Sensing Using Infrared Glass Fibers. J. Non-Cryst. Solids. 2000, 274 (1–3): 17-22

[52] J. Vaney, G. Delaizir, E. Alleno, O. Rouleau, A. Piarristeguy, J. Monnier, C. Godart, M. Ribes, R. Escalier, A. Pradel. A Comprehensive Study of the Crystallization of Cu–As–Te Glasses: Microstructure and Thermoelectric Properties. Journal of Materials Chemistry A. 2013, 1 (28): 8190-8200

Chapter 5.

Synthesis of Thermoelectric Composites by Hot Pressing and Spark Plasma Sintering

5.1 Introduction

A material efficient for thermoelectricity (TE) should have complex structure and be based on heavy elements. Te-based glasses have proved to be potential thermoelectric materials due to their relatively low electrical resistivity. Besides low electrical resistivity, good TE material also asks for high Seebeck coefficient and low thermal conductivity. It has been known that glassy material in general exhibits a quite low thermal conductivity (~0.5W/$m^{-1}K^{-1}$). Actually, thermal conductivity of noncrystalline solids is several orders of magnitude smaller than that of crystalline substance. It decreases monotonically with decreasing temperature, and is almost independent of the chemical composition[1,2]. The typical thermal conductivity of Te glasses is of the order of ~$10^{-1}WK^{-1}m^{-1}$ [3](0.12 $WK^{-1}m^{-1}$ for Ge–Te–Se[4], 0.35 $WK^{-1}m^{-1}$ for Pb–Ge–Se[5], and ~0.3 $WK^{-1}m^{-1}$ for As–Te–Se–Cu[3]). Meanwhile, the chalcogenide glass has an intrinsic high Seebeck coefficient [6-8] (more than 500μV/K).

Currently, bismuth telluride is still the best commercial TE material near room temperature. Both p-type [9-13] and n-type[12-15] bismuth telluride exhibit high electrical conductivity (~1.2×10^5 $S\cdot m^{-1}$) and Seebeck coefficient (±180~220μV/K). Unlike the majority of crystalline compounds, Bi_2Te_3 shows a really low thermal conductivity[11,16] (~1.2 $W\cdot m^{-1}K^{-1}$), which makes the ZT value higher than 1.

Compared to these commercial materials[11,17], besides Seebeck coefficient and thermal conductivity, the electrical conductivity of the Te-As-Se-Cu glass is still too high for potential application. In order to overcome the low electrical conductivity of glassy material, and prepare a kind of material with good thermoelectric performance and high formability, composites based on both Te-As-Se-Cu glass and Bi_2Te_3 crystals were designed. In this chapter, different ratios of the $(Te_{85}Se_{15})_{45}As_{30}Cu_{25}$ glass and bismuth telluride powder will be mixed together and sintered using hot pressing technique or spark plasma sintering (SPS). Characterizations including electrical resistivity, Seebeck coefficient, thermal diffusivity, density, XRD and SEM were implemented in order to evaluate the thermoelectric performance of these glass-ceramics composites.

5.2 Thermoelectric material prepared by hot pressing

5.2.1 Glass-ceramics powder mixture preparation

To obtain homogeneous glass-ceramics composites, $(Te_{85}Se_{15})_{45}As_{30}Cu_{25}$ glass and Bi_2Te_3 bulk materials were firstly obtained separately using the traditional melt quenching technique

in sealed silica tube. Glass preparation was already detailed in Chapter 4. The Bi_2Te_3 synthesis procedure is presented in Figure 5.1. Bi and Te were firstly homogenized at 750 °C for 10 hours in a silica tube. The melt was then cooled down and maintained at tens of degrees (560°C) below the melting point (585°C) for two hours for fully crystallization. The figure of merit ZT of this Bi_2Te_3 is 0.75 at room temperature.

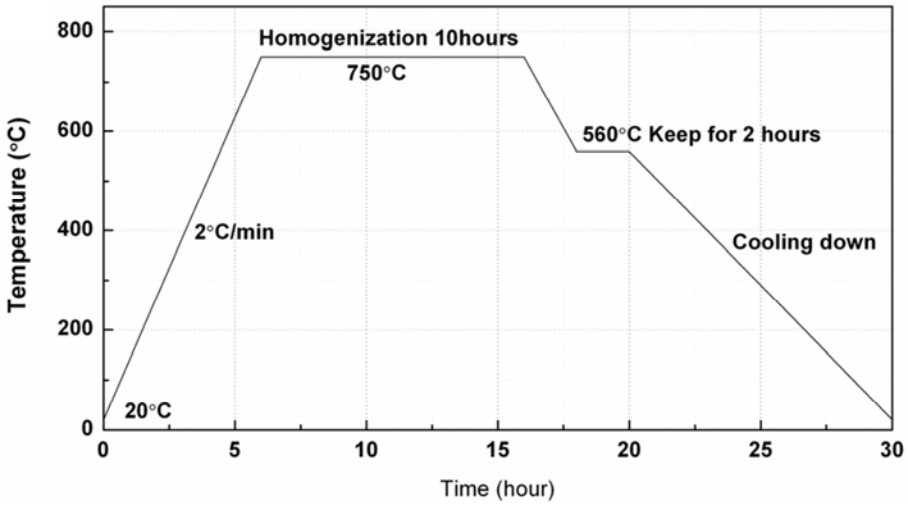

Figure 5.1 Synthesis procedure of Bi_2Te_3

The obtained bulk glass and Bi_2Te_3 were accurately weighted according to their atomic ratio (10:0, 9:1, 7:3, and 3:7) and introduced into the milling tank. The tank was positioned into a planetary ball mill (Retsch PM100). Rotation cycles of 3 min at 300 rpm were scheduled with direction reversal and a pause of 3min between each cycle. The homogeneous glass and glass-ceramics powders were obtained after 4 hours of milling. To reduce potential contaminations by oxygen and water, all the manipulations mentioned here were performed in the glove box under the protection of argon.

5.2.2 Synthesis of glass-ceramics composites by hot pressing

5.2.2.1 Hot pressing technique

Hot pressing is an efficient tool to prepare alloy steels or specific ceramics from powders at a temperature high enough to induce sintering by the simultaneous application of heat and pressure in a mold. This technology is frequently used for the manufacturing of various materials which are difficult to prepare via liquid phase processing or which cannot be sufficiently densified by using powder technology such as pressing and sintering.

Hot pressing technique also has its application limitations. It can only manufacture bulks with simple shapes like plates, blocks, cylinders, and is not proper for cases where a pore-free

state is required. Nevertheless, as thermoelectric materials do not require complex shapes and free of defects, both the two restrictions are not a matter for thermoelectric application.

For the present work, a home-made hot pressing machine was used, schematized in Figure 5.2. In the preparation process, pressure was applied on the top of the hot press die and heat was provided by a heater at the bottom. A typical cycle time is several hours.

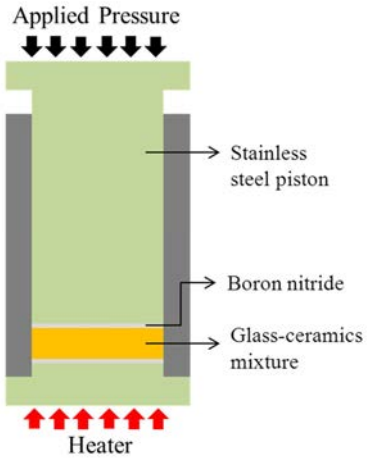

Figure 5.2 Schematic diagram of hot pressing machine

5.2.2.2 Sintering process and parameters introduction

The bulk sample was prepared by introducing 5 grams of the powder in a stainless steel die of 20 mm inner diameter. The walls of the die were previously covered with a layer of boron nitride (Alfa Aesar, 99.5%) powder to avoid sticking of the chalcogenide powder together with the die. Boron nitride powder was diluted in laboratory grade acetone and the solution was applied with a paintbrush over the walls of the die. The die was then left to dry in air atmosphere, leaving a thin and uniform layer of boron nitride powder on the surface. The die with glass-ceramics powder was then introduced into a hot uniaxial press evacuated by primary vacuum pump (10^{-3} mBar). The temperature was raised up to 300 °C in 28 min (heating rate of 10°C/min) without applying pressure. In order to obtain a stable temperature field, the die was kept at 300 °C for 15 min. Then a pressure of 30MPa was applied and released after 7 hours of sintering. After consolidation process, the temperature was slowly decreased to 210°C with a cooling rate of 10°C/min and kept for 2 hours for annealing. The die together with the ball mill then decreased to room temperature gradually (Figure 5.3).

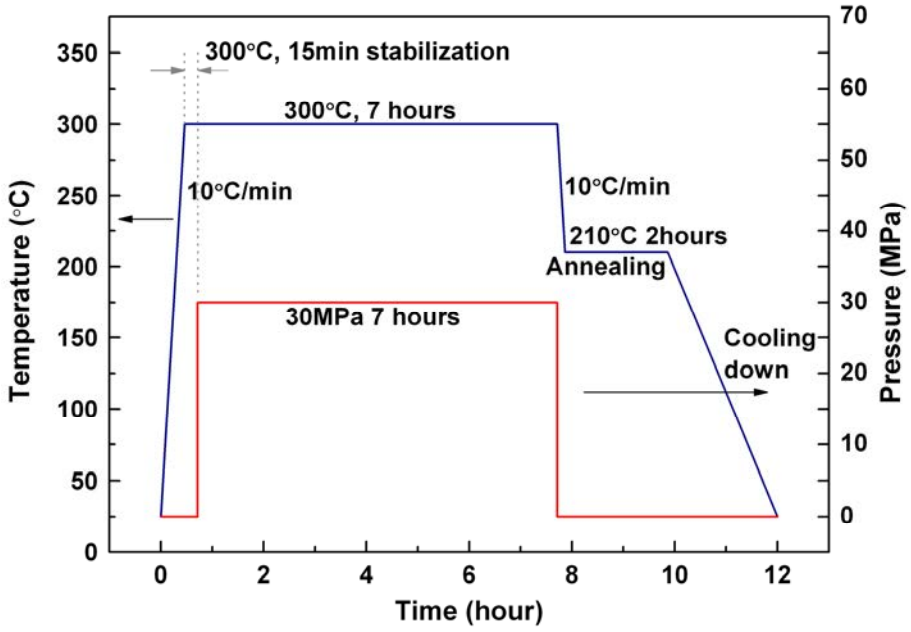

Figure 5.3 Hot pressing procedure of $(Te_{85}Se_{15})_{45}As_{30}Cu_{25}/Bi_2Te_3$ composites

5.2.2.3 Temperature distribution in the furnace

Actually, the applied sintering and annealing temperatures were chosen based on the actual temperature distribution (Figure 5.4) and DSC curve of $(Te_{85}Se_{15})_{45}As_{30}Cu_{25}$ glass. The sintering temperature should be located between the glass transition temperature T_g and crystallization temperature T_x. From Figure 5.4, the actual temperature of sample located at 1 cm above bottom is about 40~50 °C lower than the setting temperature.

In order to find the proper temperature, a series of sintering temperatures from 270°C up to 310 °C were applied and the optical microscope image was used to monitor the consolidation procedure. 300 °C is proved to be the proper sintering temperature. Indeed, due to the existence of only one heat source provided in the hot pressing machine and the low thermal conductivity of glass (0.1-0.3 $WK^{-1}m^{-1}$) and bismuth telluride (1.0-1.2 $WK^{-1}m^{-1}$), heat transfer was thwarted during sintering and a temperature gradient was generated from the bottom to the top of the sample. When the sintering temperature is too low (e.g. sintering at 280°C shown in Figure 5.5), the material cannot be homogeneously sintered. Glass powders and small bulks which are not well sintered can be clearly observed on the top surface. On the other hand, when the temperature is too high (e.g. sintering at 310°C), As_2Te_3 crystallization can be generated at the bottom face, which is confirmed by XRD. Thus, 300 °C was used as sintering temperature as $(Te_{85}Se_{15})_{45}As_{30}Cu_{25}$ glass can be well sintered without inducing extra crystallization, which will be shown in paragraph 5.2.3.1.

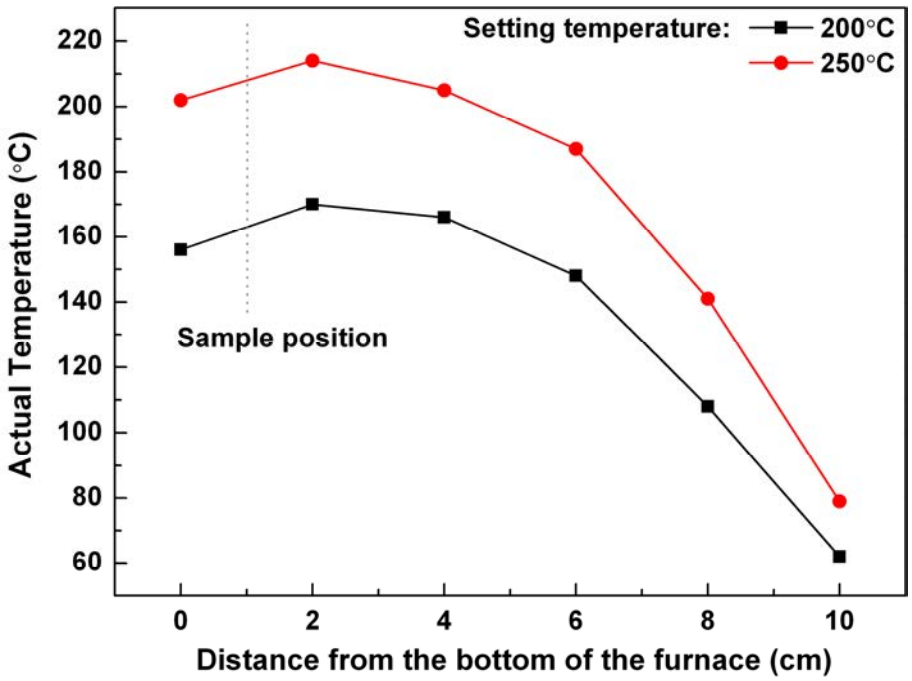

Figure 5.4 Actual furnace temperature distribution curves

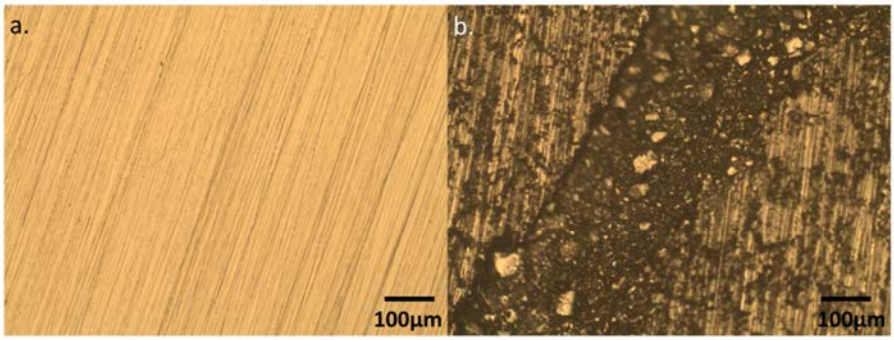

Figure 5.5 Optical microscope images of polished top (a) and bottom (b) face of pure $(Te_{85}Se_{15})_{45}As_{30}Cu_{25}$ glass sintered at 280°C for 7 hours.

5.2.2.4 Glass and glass-ceramic composites preparation

Pure $(Te_{85}Se_{15})_{45}As_{30}Cu_{25}$ glass was firstly sintered. The relative densities of prepared glass disc was 99.25% (Actual $\rho_{density}$: 5.985g/cm^3 Theoretical $\rho_{density}$: 6.03g/cm^3), which is almost the limit of hot-pressing technique. The electrical resistivity of this hot-pressed $(Te_{85}Se_{15})_{45}As_{30}Cu_{25}$ glass was also confirmed to be 3×10^5 μΩ·m a by four-point probe resistivity equipment (S-302, Lucas Labs). This value is consistent with the bulk $(Te_{85}Se_{15})_{45}As_{30}Cu_{25}$ glass (3.5×10^5 μΩ·m) prepared by traditional melt quenching technique.

On this basis, $(Te_{85}Se_{15})_{45}As_{30}Cu_{25}$ glass with 10%, 30% and 70% of Bi_2Te_3 were then prepared and named as BT10, BT30 and BT70 respectively. Several polished glass and glass-ceramics discs were shown in Figure 5.6. After polish, all the glass and glass-ceramics

samples show a flat shiny mirror-like surface, indicating no micro-scale defect between the glass-glass and glass-ceramic interface. This phenomenon predicted the well consolidation of the composites. The density tests also proved our prediction. The relative density between actual density and theoretical density of each sample is higher than 98%.

Figure 5.6 Images of pure glass, BT30 and BT70 discs prepared by hot-pressing

5.2.3 Characterization of glass-ceramic composites

5.2.3.1 Crystal structure analysis by X-ray diffraction

X-ray diffraction (XRD) was used for unambiguously determining the state of $(Te_{85}Se_{15})_{45}As_{30}Cu_{25}$ glass, BT10, BT30, and BT70 (Figure 5.7).

After hot-pressing, the pure glass sample still remains in a vitreous state. XRD patterns of both top and bottom faces of glass disc showed a wide range of high reflected intensities, which are typical diffraction patterns of amorphous materials.

BT10, BT30 and BT70 composites show the diffraction peaks of Bi_2Te_3. However, among these composites, only BT70 showed no new diffraction peaks. Indeed, BT10 and BT30 exhibit As_2Te_3 diffraction peaks, indicating the crystallization of $(Te_{85}Se_{15})_{45}As_{30}Cu_{25}$ glass during sintering. In addition, the bottom face of the sintered disc showed more severe glass crystallization due to its smaller distance from the heat source. Similar results have also been found in the electrical resistivity measurement. The electrical resistivities of the top and bottom surfaces of BT10 are 0.31 Ω·cm and 0.095 Ω·cm respectively. For BT30, the resistivities are 0.28 Ω·cm (bottom face) and 0.095 Ω·cm (top face). Clearly, the resistance of bottom was much smaller.

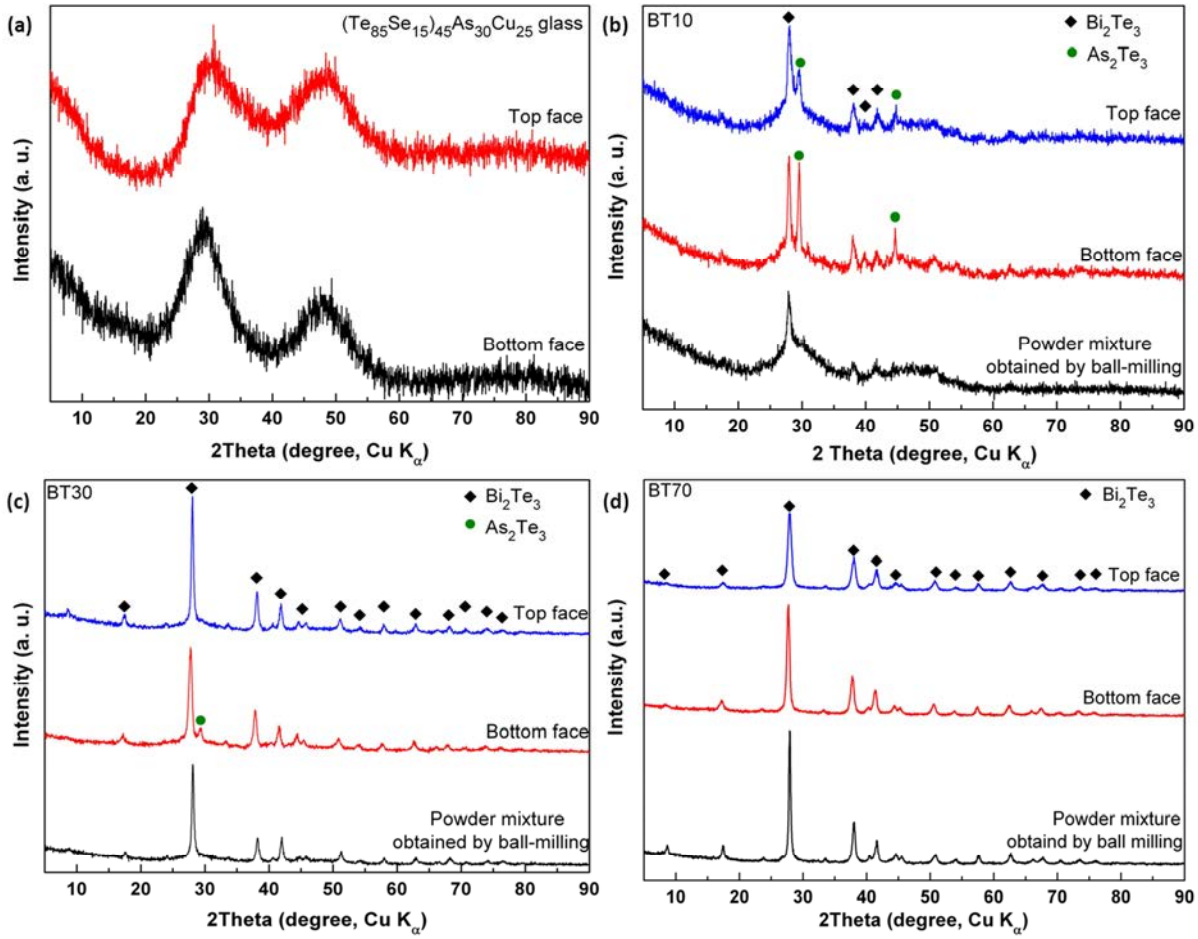

Figure 5.7 XRD of (a) $(Te_{85}Se_{15})_{45}As_{30}Cu_{25}$ glass, (b) BT10, (c) BT30, and (d) BT70.

5.2.3.2 Thermal analysis by DSC

DSC curves of bulk $(Te_{85}Se_{15})_{45}As_{30}Cu_{25}$ glass, glass and BT10, BT30, and BT70 powders obtained after ball-milling were measured and compared (Figure 5.8) to find the root cause of the unexpected crystallization.

For comparison, the $(Te_{85}Se_{15})_{45}As_{30}Cu_{25}$ glass powder was also obtained by hand-grinding in an agate mortar for 30 minutes under the protection of Ar. In Figure 5.8, bulk $(Te_{85}Se_{15})_{45}As_{30}Cu_{25}$ glass showed a good thermal stability. In comparison, both ball-milled and hand-grinded glass powder have a lower thermal stability. This phenomenon is easy to be understood. During the grinding process, there were defects, distortions and especially large quantities of breaking chemical bonds generated on the surface of micro-scale glass powder, causing a significant increase of surface energy. In the heating process of DSC test, this surface energy could accelerate the crystallization and decrease ΔT value between T_g and T_x.

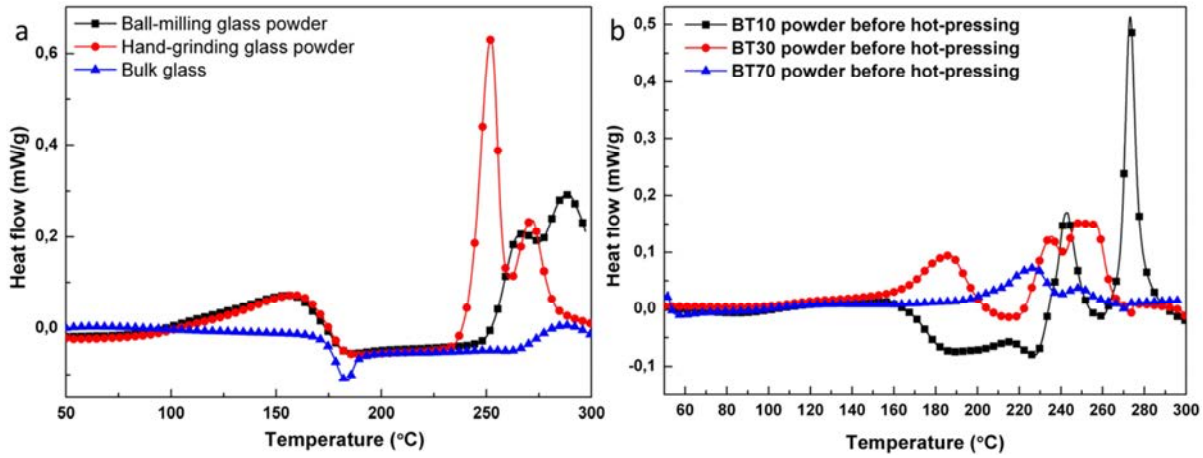

Figure 5.8 DSC of bulk, ball-milling and hand-grinding $(Te_{85}Se_{15})_{45}As_{30}Cu_{25}$ glass (a) and ball-milled BT10, BT30 and BT70 powder (b).

For BT10, BT30 and BT70, the decrease of thermal stability could be caused by the following two reasons. Firstly, the micro-scale Bi_2Te_3 crystals in $(Te_{85}Se_{15})_{45}As_{30}Cu_{25}$ glass could act as nucleating agents, and accelerated the crystallization rate by decreasing the surface free energy barrier hindering nucleation. Secondly, high-energy ball milling procedure could generate lots of collision between glass and ceramic particles. This could change the glass composition, and as a result destroy the thermal stability. It can also be observed that from BT10 to BT70, the heat flow per unit mass became smaller. This is caused by the rising of Bi_2Te_3 percentage. Indeed, Bi_2Te_3 exhibits no obvious endothermic and exothermic phenomenon before its melting point.

As a result, it can be concluded that, due to the uneven temperature distribution in hot-pressing furnace and the glass stability destruction caused by ball-milling with Bi_2Te_3, new inhomogeneous crystallization was inevitable during sintering. So, new mixture preparation and sintering methods should be taken into account.

5.3 Thermoelectric material prepared by Spark plasma sintering

In this part, the main work was done in Nanoforce Technology Ltd in London. The equipments, such as Spark Plasma Sintering (SPS), Seebeck and laser flash thermal diffusivity measurements were provided by Prof. Michael J. Reece. The composites between $(Te_{85}Se_{15})_{45}As_{30}Cu_{25}$ glass and Bi_2Te_3 or $Bi_{0.5}Sb_{1.5}Te_3$ were prepared and characterized.

5.3.1 Synthesis of glass-ceramics composites

5.3.1.1 Glass-ceramics mixture preparation

In order to avoid the thermal destruction of $(Te_{85}Se_{15})_{45}As_{30}Cu_{25}$ glass during mechanical milling with crystals, glass, Bi_2Te_3, and $Bi_{0.5}Sb_{1.5}Te_3$ powders were prepared separately. $(Te_{85}Se_{15})_{45}As_{30}Cu_{25}$ glass and Bi_2Te_3 bulk materials were firstly prepared in sealed silica tube and then crushed to power separately using planetary ball milling technique (300rpm, 4 hours) under the protection of argon. $Bi_{0.5}Sb_{1.5}Te_3$ (BST), provided by H. Ning in Queen Mary University of London, was synthesized by ball-milling raw elements (5N) at 350 rpm for 10 hours. For further experiments, the grain size of all the glass and crystal powders was selected to be less than 50 μm using a sieve.

On this basis, the mixtures of glass with different ratios of Bi_2Te_3 or BST (10%, 30%, 50%, 70%, and 90%) were prepared by magnetic stirring at 200 rpm in ethanol (3N) solution at 70°C for 30 minutes and dried at 80°C for 30 minutes in a drying oven. Here, ethanol was chosen based on its high removability. The sieved pure glass, Bi_2Te_3 and BST powders (<50μm) were also stored for future preparation.

5.3.1.2 Preparation of glass-ceramics bulk samples using SPS technique

Spark plasma sintering technique

Spark Plasma Sintering (SPS) is a high-speed powder consolidation technology capable of processing a large variety of both novel and traditional materials. The main characteristic of SPS is that a high-energy, low-voltage pulse DC current directly passes through the powder compact and generates Joule heating and electrical field diffusion effect in fine local areas between particles. Compared to conventional sintering technique, the heat generation in SPS is internal, and Joule's heating effect results in achieving near theoretical density at lower sintering temperature. Moreover, the high heating rate (up to 1000 K/min) and fast sintering process (within a few minutes) provide a potential of near total densification with little grain growth.

Sample preparation

To prepare glass or glass-ceramics composites using SPS technique, a series of parameters should be optimized. For example, to avoid the crystallization of the glassy phase and the leakage of toxic elements such as arsenic during sintering process, the temperature should be

precisely controlled. This asks for lower electric current, power and heating rate, and as a result prolongs sintering time. Meanwhile, cooling rate after sintering should also be controlled in order to provide an annealing to the glass. According to series of trials, the proper parameters were chosen and the process is shown in Figure 5.9 a.

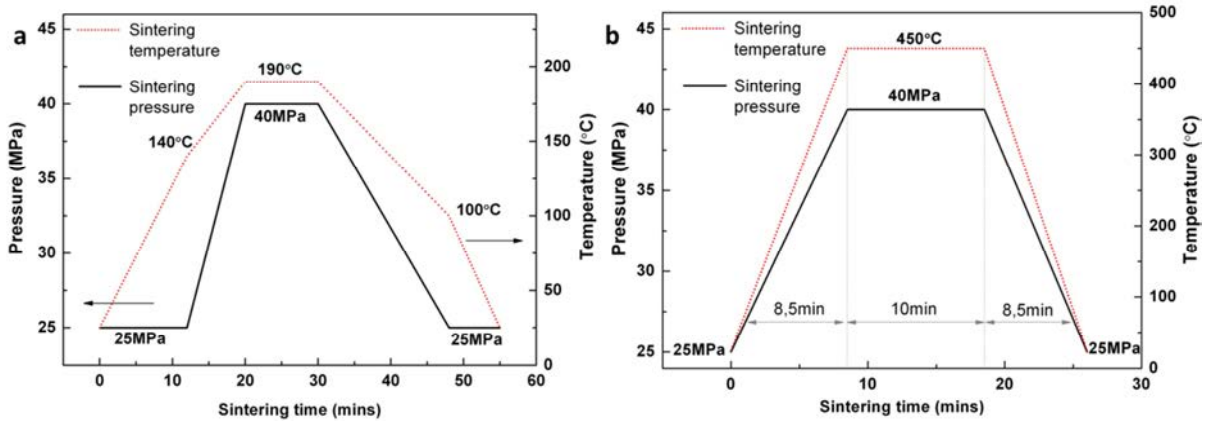

Figure 5.9 SPS preparation procedures of glass and glass-ceramics (a), and pure Bi_2Te_3/BST samples (b).

Compared with traditional hot pressing technique, the sintering time of SPS is greatly reduced. In addition, pure Bi_2Te_3 and BST samples were also prepared by SPS at 450°C. The preparation procedure is shown in Figure 5.9 b. Compared with samples with vitreous phase, the heating and cooling rate can be much faster and the sintering time was greatly decreased.

5.3.2 Characterization of $(Te_{85}Se_{15})_{45}As_{30}Cu_{25}$ / Bi_2Te_3 composites

The following samples were prepared and characterized : $(Te_{85}Se_{15})_{45}As_{30}Cu_{25}$ glass, glass with 0%, 10%, 30%, 50%, 70%, 90% and 100% of Bi_2Te_3 (atomic ratio), named as SPS-BT0, SPS-BT10, SPS-BT30, SPS-BT50, SPS-BT70, SPS-BT90, SPS-BT100 respectively.

Indeed, the ability of a given material to efficiently produce thermoelectric power is related to its dimensionless figure of merit (ZT) given by:

$$zT = \frac{S^2 T}{\rho \kappa} \quad \textbf{(5.1)}$$

which depends on the Seebeck coefficient S, thermal conductivity κ, electrical resistivity ρ, and temperature T. As a result, S, κ, and ρ should be studied separately.

5.3.2.1 X-ray diffraction

After SPS, XRD were performed by the PANalytical X'Pert MRD PRO set-up from 5˚ to 90˚ (Figure 5.10) in order to have a comparison with the composites prepared by hot-pressing technique.

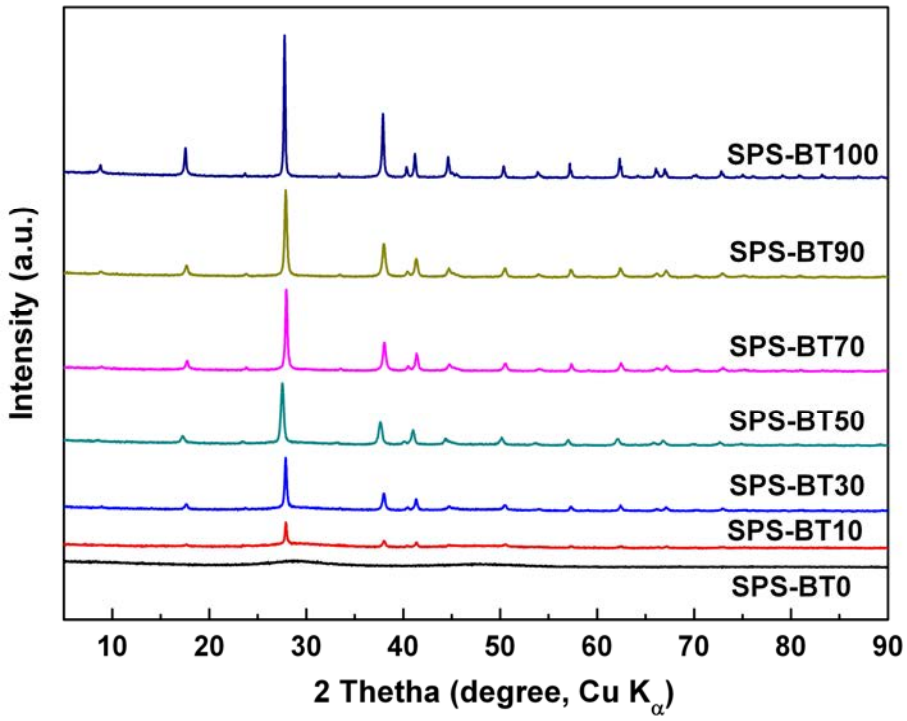

Figure 5.10 XRD of $(Te_{85}Se_{15})_{45}As_{30}Cu_{25}$ glass with different percentage of Bi_2Te_3.

Unlike hot-pressing samples, the glass in all the composites still remains in a glassy state and all the diffraction peaks belong to Bi_2Te_3. This proves an intrinsic advantage of SPS technique in preparing novel materials without introducing nucleation and crystal growth. As expected, the diffraction intensity was enhanced as Bi_2Te_3 content increasing.

5.3.2.2 Seebeck coefficient

The Seebeck effect (S) corresponds to the conversion of temperature differences directly into electricity. It has been introduced in the section 4.2.1 of the Chapter 4. Thus the Seebeck coefficient is a very important parameter to determine the efficiency of a thermoelectric material. If the temperature difference between the two ends of a material is small, S of a material could be defined approximately as,

$$S = -\frac{V_1 - V_2}{T_1 - T_2} \quad \textbf{(5.2)}$$

Based on this equation, S can be easily measured using the principle shown in Figure 5.11.

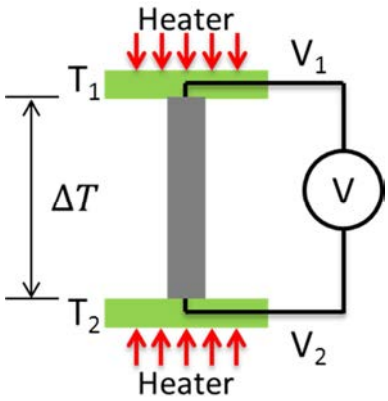

Figure 5.11 The Seebeck coefficient test principle.

By the analysis of charge carrier mobility, it can be got that n-type semiconductors have negative Seebeck coefficients, while the ones of p-type materials are positive[18]. The Seebeck coefficient of pure glass and glass-ceramics composites were measured using two different home-made systems depending on their measuring scales and shown in Figure 5.12. The samples were cut into 2×2×10 mm bars for measurements. The Seebeck coefficient of SPS-BT0 was measured from 160 K up to 380 K using one home-made system. For other samples, Seebeck coefficients were tested using another home-made system around 300K, 330K, 370K, 410K and 440K (Figure 5.12). To avoid glass crystallization, the highest test temperature was controlled to be 440K, several degrees lower than the glass transition temperature (443K).

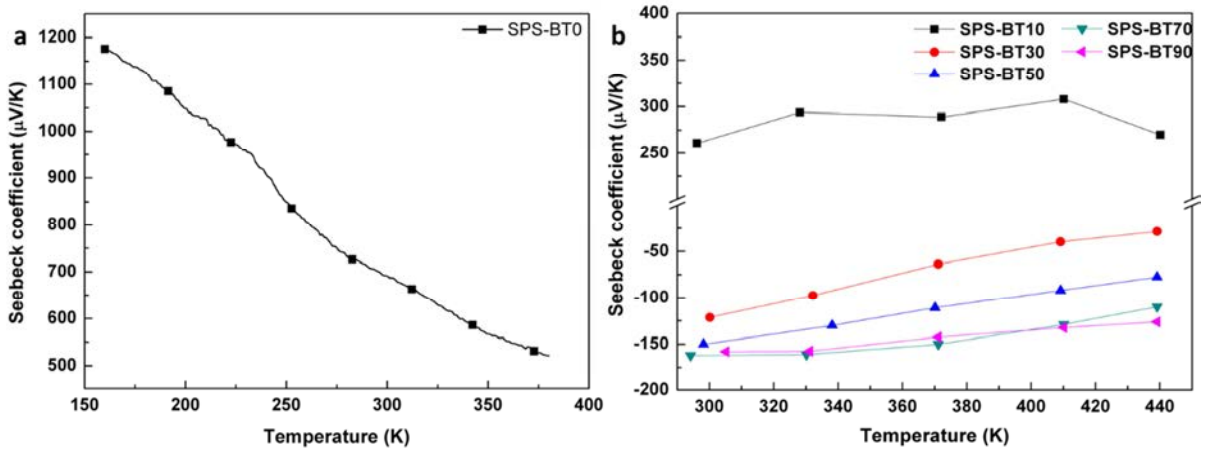

Figure 5.12 Seebeck coefficients of pure $(Te_{85}Se_{15})_{45}As_{30}Cu_{25}$ glass (a) and $(Te_{85}Se_{15})_{45}As_{30}Cu_{25}$ / Bi_2Te_3 composites (b).

SPS-BT0, as pure glass, has a really limited charge carrier concentration. According to previous discussion in 4.2.3 of Chapter 4, it should possess a high Seebeck coefficient. This is exactly the result shown in Figure 5.12a with values extending from 1170 μV/K to 520 μV/K.

As SPS-BT0 is p-type, and SPS-BT100 is n-type, there was an obvious carrier type change as Bi_2Te_3 content increased from 10% to 90%. As the quantity of electrons in Bi_2Te_3 crystal is much larger than holes in SPS-BT0, the composite became n-type when Bi_2Te_3 content was more than 30%. The best one is SPS-BT90, where the glass acts only as a kind of "binder" among Bi_2Te_3 particles. Nevertheless SPS-BT70 presents almost the same Seebeck values and could also be an interesting compromise. For comparison, Seebeck coefficient of SPS-BT100 is around 153 $\mu V \cdot K^{-1}$ at room temperature.

5.3.2.3 Electrical resistivity

As an efficient thermoelectric material does not only ask for a high Seebeck coefficient, but also a low electrical resistivity (ρ), the electrical resistivities were tested by four probe method using a home-made system. With four probes well contacted with the regular quadrangular prism sample, the volume resistivity can be automatically calculated using the values of current, voltage, distance between the two probes and the sample size (Figure 5.13). Resistivities at various temperatures are compared in Figure 5.14.

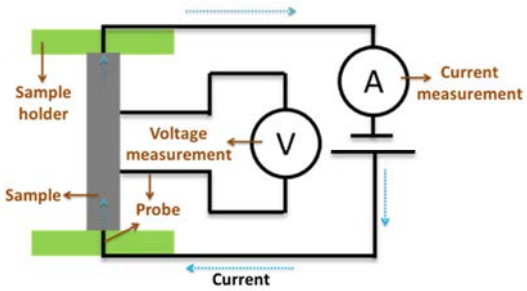

Figure 5.13 Schematic diagram of resistivity measurement device.

ρ of SPS-BT100 is confirmed to be 8.9 $\mu\Omega \cdot m$ at room temperature. By adding Bi_2Te_3, the resistivities of glass-ceramics composites decreases gradually. For SPS-BT10, as majority of the composite is still glassy, Bi_2Te_3 micro crystals are isolated between each other. Hence, charge carriers are difficult to come across the glass barriers and as a result generate a much higher resistivity value compared with the ones with more Bi_2Te_3. In all samples, the resistance decreases when temperature is increased. That is because $(Te_{85}Se_{15})_{45}As_{30}Cu_{25}$ glass and Bi_2Te_3 are both semiconductors, and higher temperature could provide enough energy to free electrons from valence band to conduction band and therefore generate a lower resistance. For comparison, ρ of SPS-BT0 is 3×10^5 $\mu\Omega \cdot m$ at room temperature.

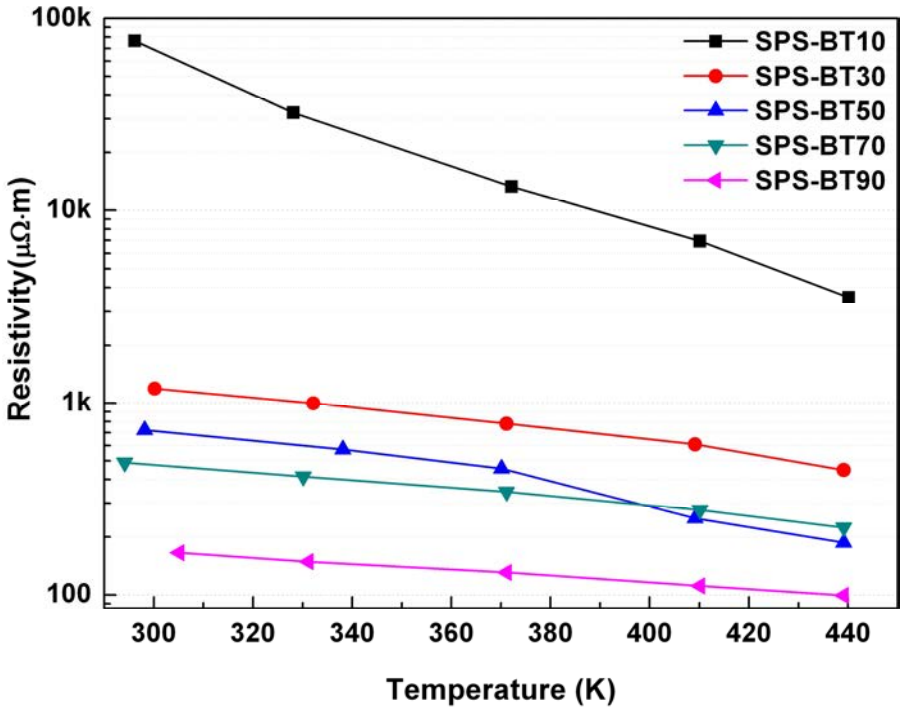

Figure 5.14 Electrical resistivities of $(Te_{85}Se_{15})_{45}As_{30}Cu_{25}$ / Bi_2Te_3 composites

5.3.2.4 Power factor

Under a given temperature difference, the ability of a material to produce useful electrical power is quantified by its power factor. In this work, power factor of SPS-BT composites were calculated from S and ρ using Equation (4.8) (Figure 5.15).

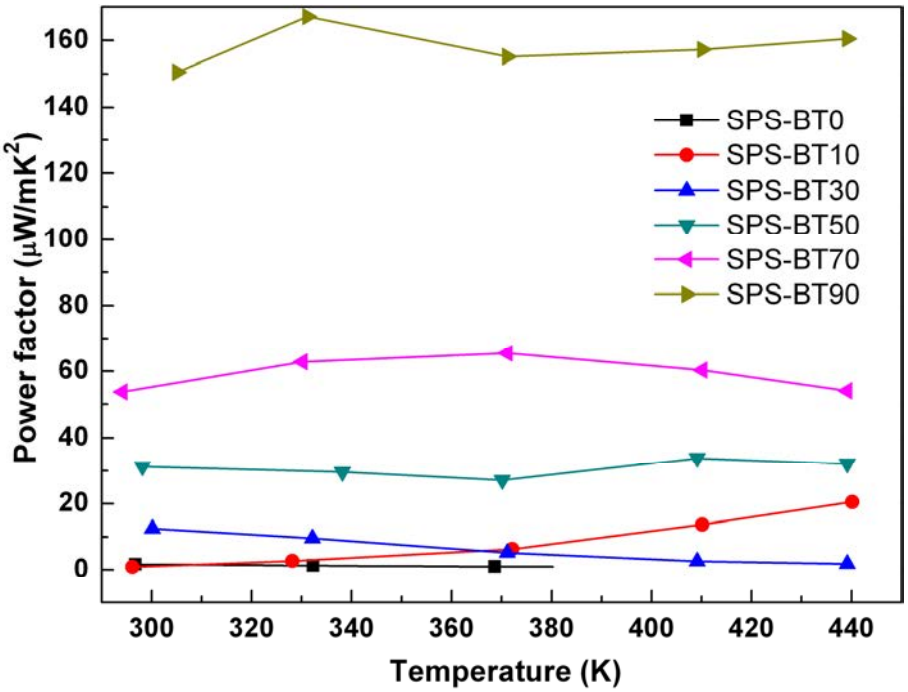

Figure 5.15 Power factors of $(Te_{85}Se_{15})_{45}As_{30}Cu_{25}$ / Bi_2Te_3 composites

For SPS-BT0, due to the lack of resistivity data at higher temperature, the power factor at higher temperature was estimated using its room temperature resistance.

From Figure 5.15, it is proved that adding Bi_2Te_3 into $(Te_{85}Se_{15})_{45}As_{30}Cu_{25}$ is an efficient method to improve material TE performance. SPS-BT90, due to its lower electrical resistivity and rather high Seebeck coefficient, generates the largest power factor value. Note that materials with high power factor are able to generate more energy. Nevertheless, it does not mean they are efficient in the conversion of a temperature gradient into electricity.

5.3.2.5 Thermal conductivity

Thermal conductivity κ is the property of a material that indicates its ability to conduct heat. In heat transfer analysis, thermal conductivity is obtained by multiplying the thermal diffusivity α, density $\rho_{density}$ and specific heat capacity c_p.

$$\kappa = \alpha \rho_{density} c_p \quad \textbf{(5.3)}$$

Thermal diffusivity

To calculate the thermal conductivity, thermal diffusivity α at different temperatures were tested (Figure 5.16) using the laser flash method (NETZSCH, LFA457, Germany).

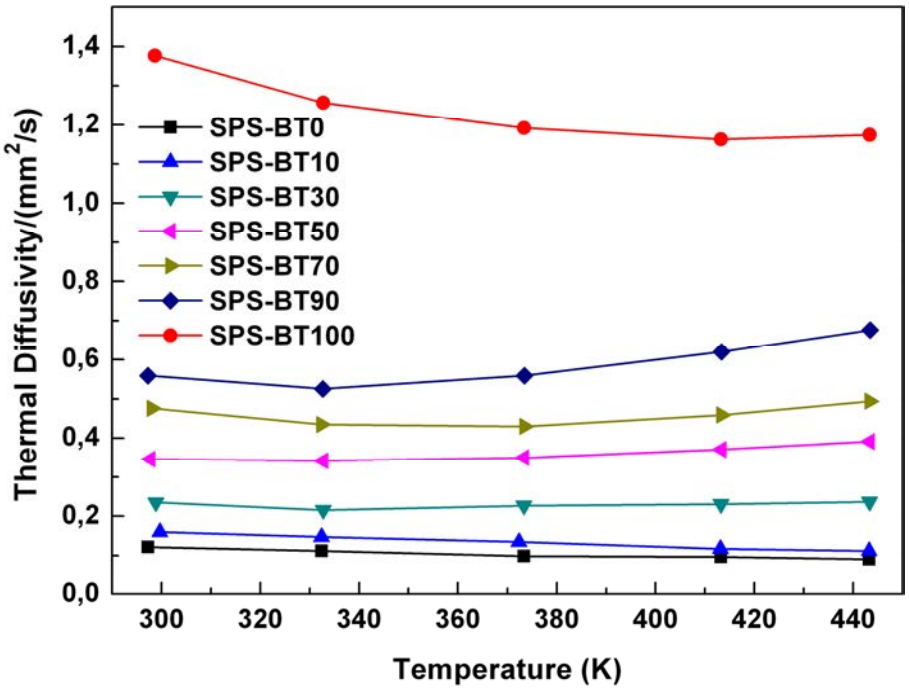

Figure 5.16 Thermal diffusivities of $(Te_{85}Se_{15})_{45}As_{30}Cu_{25}$ / Bi_2Te_3 composites

As expected, pure glass exhibits the lowest thermal diffusivity. This phenomenon is caused by the intrinsic disordered structure of glass which limits the free path of a phonon[2].

Comparing the values of SPS-BT90 and SPS-BT100, it can be drawn that just 10% of glass can decrease the thermal diffusivity a lot. This is perhaps caused by the scattering at the interface between Bi_2Te_3 crystal and $(Te_{85}Se_{15})_{45}As_{30}Cu_{25}$ glass.

Density

In order to obtain the thermal conductivity, density ($\rho_{density}$) of the composites were also measured using Archimedes' principle and compared with theoretical density calculated from $\rho_{density}$ of glass and pure Bi_2Te_3 (Figure 5.17).

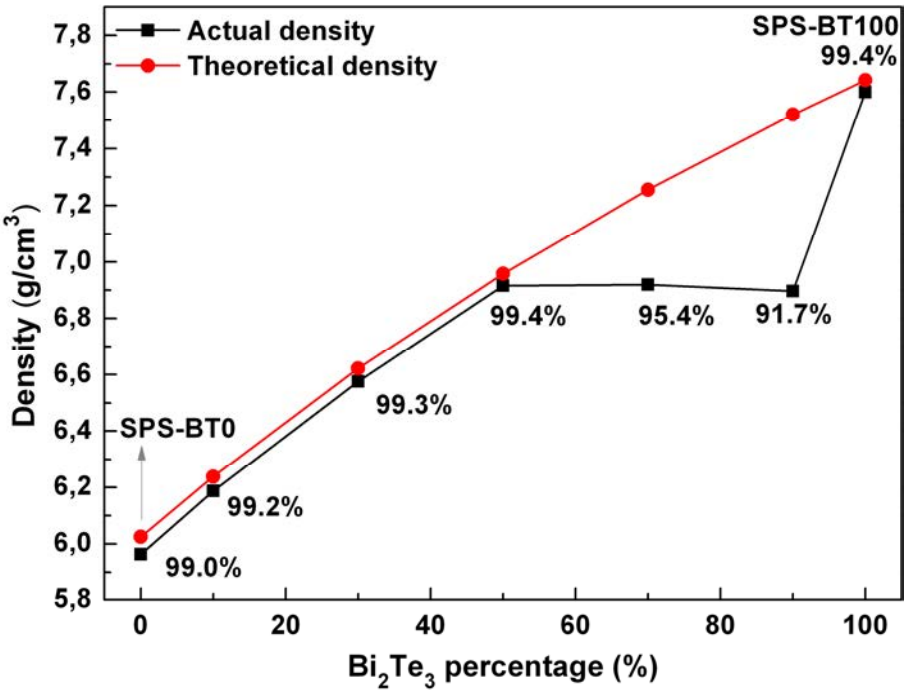

Figure 5.17 Densities of $(Te_{85}Se_{15})_{45}As_{30}Cu_{25}$ / Bi_2Te_3 composites at room temperature

From SPS-BT0 to SPS-BT50, during the SPS process, the glass with certain fluidity could fill the space between Bi_2Te_3 crystals and generate a high condensed slide. The relative density between actual density and theoretical density is more than 99%. When Bi_2Te_3 content increases, $(Te_{85}Se_{15})_{45}As_{30}Cu_{25}$ glass is not enough to fill all the pores between crystals and therefore the relative densities of SPS-BT70 and SPS-BT90 decrease to 95.4% and 91.7% respectively.

Specific heat capacity

Specific heat capacity (c_p) is the ratio between the heat added to per unit mass of a material and the resulting temperature change. c_p was measured and calculated (Figure 5.18) from 300K up to 420K by DSC 1 STARe System (Mettler Toledo).

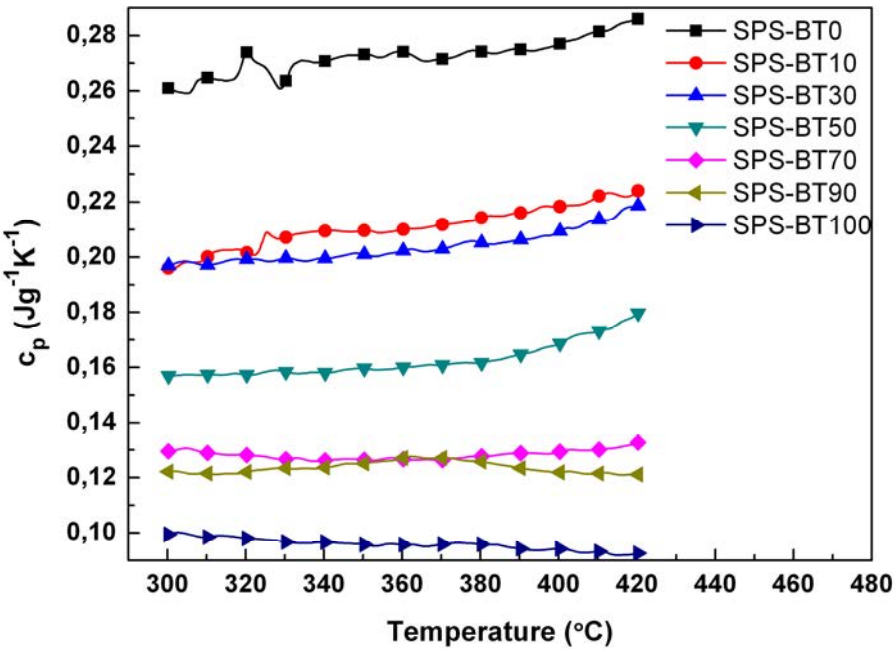

Figure 5.18 Specific heat capacity of $(Te_{85}Se_{15})_{45}As_{30}Cu_{25}$ / Bi_2Te_3 composites.

From Figure 5.18, it can be concluded that as Bi_2Te_3 content increased the specific heat capacity gradually decreased. This phenomenon could be explained by Dulong-Petit law.

Dulong-Petit law is a thermodynamic rule proposed in 1819 by French physicists Pierre Louis Dulong and Alexis Thérèse Petit. It is a classical law describing the specific heat capacity of crystalline solids caused by lattice vibrations. This law has proved to be also applicable for vitreous materials [19-21]. Thus, regardless of the nature of the substance or crystal, Dulong-Petit law provides a direct correlation between the heat capacity and the molar mass of the compounds:

$$c_p = \frac{3R}{M} \tag{5.4}$$

where R is the gas constant (8.314 JK^{-1}mol^{-1}) and M is the molar mass. From SPS-BT0 to SPS-BT100, M increased from 92.5 g·mol^{-1} to 160.152 g·mol^{-1}, generating a decrease of c_p value. The measured c_p values are in correct agreement with the value expected from the Dulong-Petit law.

Thermal conductivity

Based on Equation (5.3), thermal conductivities were calculated and are shown in Figure 5.19. Note that the density variation of a solid material with temperature is typically small. $\rho_{density}$ at room temperature have been used here for thermal conductivity calculation.

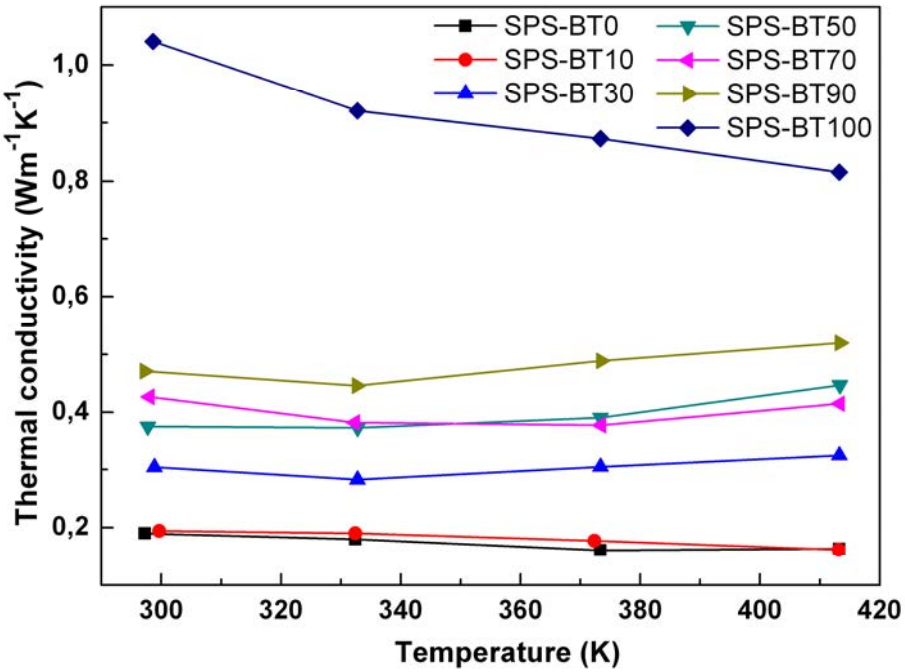

Figure 5.19 Thermal conductivities of $(Te_{85}Se_{15})_{45}As_{30}Cu_{25}$ / Bi_2Te_3 composites.

SPS-BT100 has a much higher thermal conductivity than SPS-BT0. Thus, the substitution of glass by Bi_2Te_3 enhanced the thermal conductivity gradually. Meanwhile, a big value difference between SPS-BT100 and SPS-BT90 could be observed. This phenomenon indicates that only a few percentage of glass distributed among Bi_2Te_3 micro-crystals causes significant boundary phonon scattering, thwarting thermal conductivity.

5.3.2.6 Figure of merit (ZT)

According to Equation (5.1), the figure of merit (ZT) values were calculated and are shown in Figure 5.20.

The ZT value of SPS-BT0 was calculated to be around 0.002. Although the Seebeck coefficient was interestingly high for the pure glass, the consequence of the too large electrical resistivity is an insurmountable handicap preventing to get a good figure of merit. This observation confirms that this resistivity is the relevant parameter that has to be drastically decreased to improve the TE properties of such materials. By adding Bi_2Te_3, ZT value shows a significant increasing tendency. Nevertheless, ZT values of glass-ceramics from SPS-BT10 to SPS-BT90 are all much larger than pure glass. SPS-BT90 sample, which is not fully densified, has a ZT value varies from 0.095 to 0.125 by increasing temperature. For comparison, the ZT value of SPS-BT100 is calculated to be 0.75 at room temperature from S, ρ, and κ.

However, it can be predicted that by adjusting the powder mixing method and sintering parameters, glass-ceramics well compacted could be obtained with a comparable figure of merit value and much lower sintering temperature compared with Bi_2Te_3. Moreover, as explained in section 5.3.2.2, due to the existence of both positive and negative charge carriers provided by p-type $(Te_{85}Se_{15})_{45}As_{30}Cu_{25}$ glass and n-type Bi_2Te_3, the Seebeck voltages of these composites have been partially cancelled out.

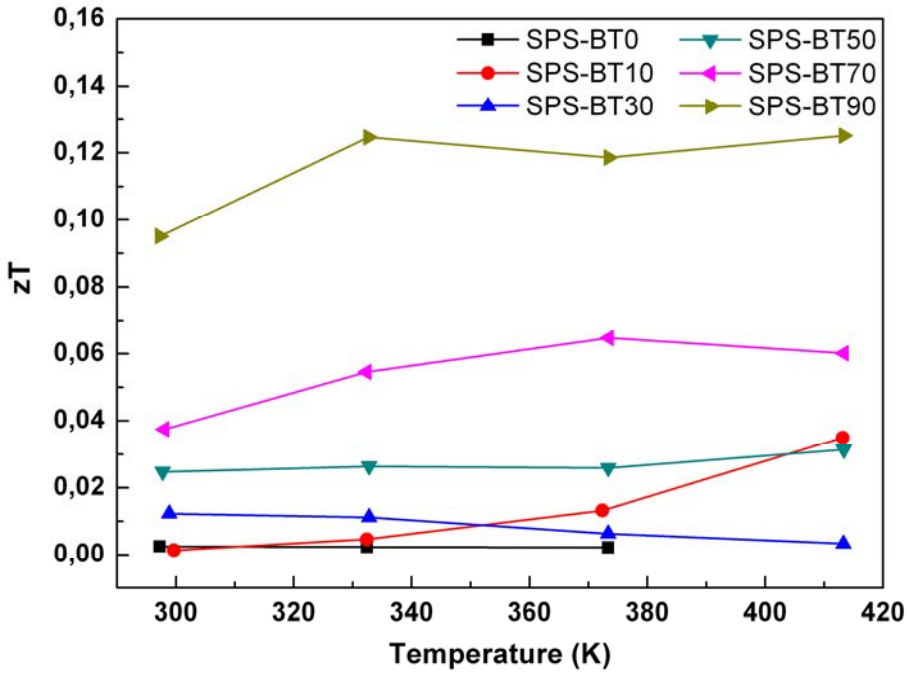

Figure 5.20 Figure of merit of $(Te_{85}Se_{15})_{45}As_{30}Cu_{25}$ / Bi_2Te_3 composites.

5.3.3 Characterization of $(Te_{85}Se_{15})_{45}As_{30}Cu_{25}$ / BST composites

To ensure that the Seebeck coefficient is large, there should only be a single type of carrier. Mixed n-type and p-type conduction in one material lead to both charge carriers moving to the cold end, cancelling out the induced Seebeck voltages. As $Bi_{0.5}Sb_{1.5}Te_3$ (BST) is a typical p-type thermoelectric material and is used commercially for a long time, the composites of $(Te_{85}Se_{15})_{45}As_{30}Cu_{25}$ glass with 10%, 30%, 50%, 70% and 90% BST were prepared using SPS technique (190°C 10mins) and named as SPS-BST10, SPS-BST30, SPS-BST50, SPS-BST70 and SPS-BST90 respectively. Pure glass (SPS-BST0) and pure BST (SPS-BST100) were also prepared by SPS for comparison (Figure 5.21). The mixture preparation procedure, the sintering parameters and the characterization implemented have already been described in section 5.3.1. Note that SPS-BST0 is exactly the same sample as the SPS-BT0 discussed above.

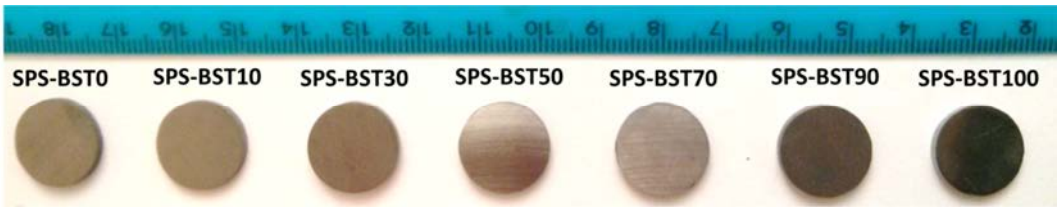

Figure 5.21 The samples prepared by SPS technique.

5.3.3.1 X-ray diffraction

XRD patterns of all the SPS-BST glass-ceramics composites are shown in Figure 5.22.

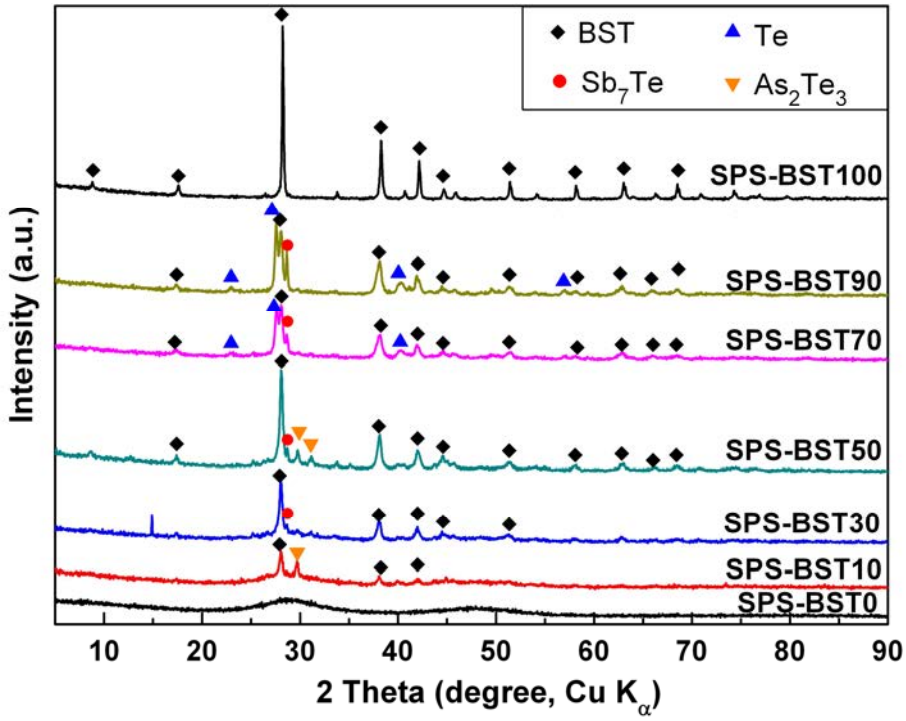

Figure 5.22 XRD of $(Te_{85}Se_{15})_{45}As_{30}Cu_{25}$ / $Bi_{0.5}Sb_{1.5}Te_3$ composites.

Besides the peak of BST, new diffraction peaks, which are assigned to be arsenic telluride (PDF#39-1043), appeared for SPS-BST10, SPS-BT30, and SPS-BT50. For SPS-BST70 and SPS-BST90, the three peaks located at around 28° are belonged to tellurium (PDF#36-1452), $Bi_{0.5}Sb_{1.5}Te_3$ (PDF#49-1713) and Sb_7Te (PDF#46-1068) respectively. Indeed, the BST powder was synthesized by mechanical milling. Compared with traditional high temperature sintering, extra peaks of other phases can be quite often observed if the mechanical alloying is not complete. Note that the BST powder used for SPS-BST70 and SPS-BST90 preparation was obtained from a different round of mechanical milling. Thus, the existence of Te and Sb_7Te indicates an incomplete reaction during mechanical milling.

To confirm this, XRD pattern of the BST powder used for SPS-BST70 and SPS-BST90 preparation was carried out and shown in Figure 5.23. As for SPS-BST70 and SPS-BST90, the diffraction peaks of Sb_7Te and Te can also be observed.

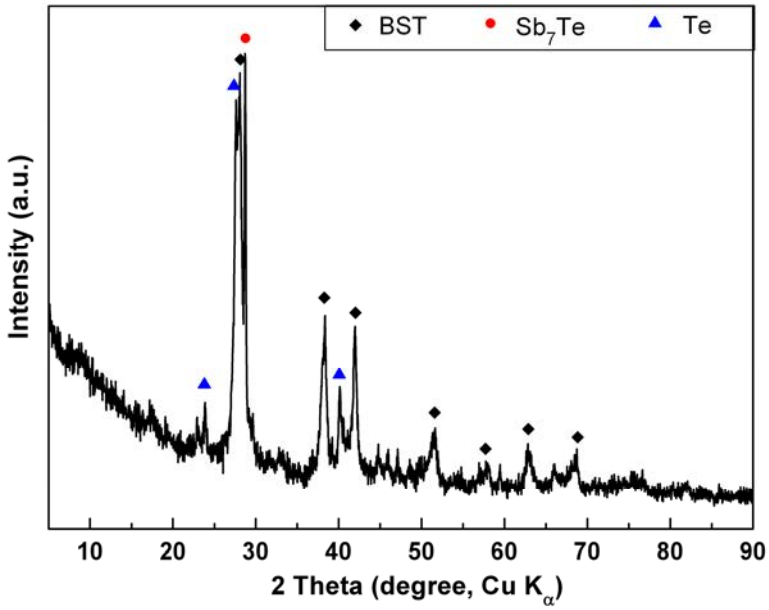

Figure 5.23 XRD pattern of $Bi_{0.5}Sb_{1.5}Te_3$ powders used for SPS-BST70 and SPS-BST90

5.3.3.2 Seebeck coefficient

For ZT calculation, Seebeck coefficients were measured and the results are shown in Figure 5.24.

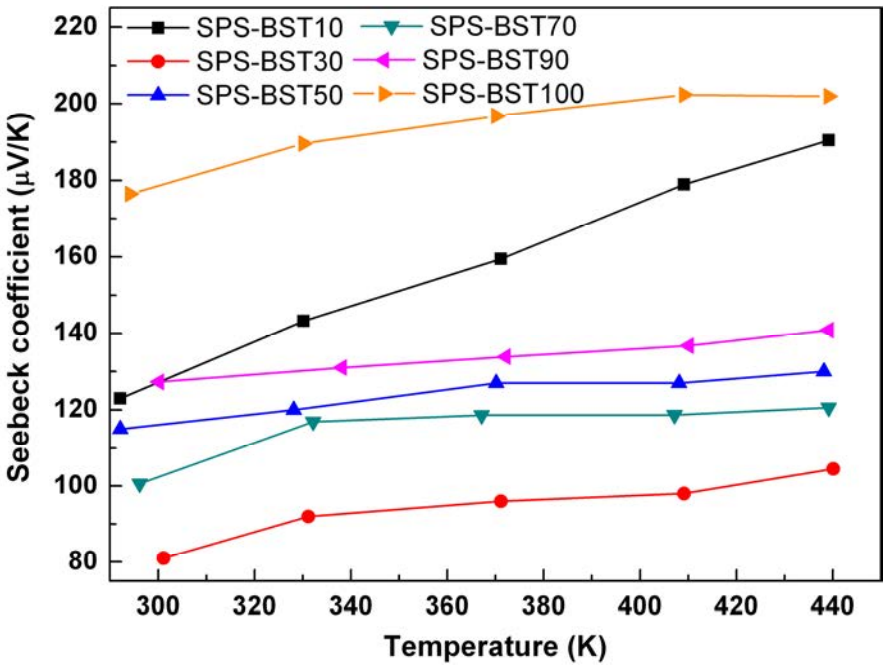

Figure 5.24 Seebeck coefficients of $(Te_{85}Se_{15})_{45}As_{30}Cu_{25}$ / $Bi_{0.5}Sb_{1.5}Te_3$ composites.

All the specimens are p-type semiconductor materials. By adding BST, the Seebeck coefficient was firstly decreased from SPS-BST0 (the same as SPS-BT0, see Figure 5.12a) to SPS-BST30. To explain this, it is important to note that a material's Seebeck coefficient is inversely related to its carrier density. Therefore, insulators tend to have higher Seebeck coefficients, while metals have lower values due to their high carrier concentrations. $(Te_{85}Se_{15})_{45}As_{30}Cu_{25}$ glass, as a p-type semiconductor, exhibits a much lower hole concentration compared to BST. Hence, from SPS-BST0 to SPS-BST30, the sudden increase of hole concentration induced by BST can significantly decrease the Seebeck coefficient.

Then, from SPS-BST30 to SPS-BST90, the Seebeck coefficient rises again and tends to converge to a mean value equal to 120 $\mu V \cdot K^{-1}$. The Seebeck coefficient of SPS-BST100 varies from 175 $\mu V \cdot K^{-1}$ at 300K to 200 $\mu V \cdot K^{-1}$ at 440K. The big difference between SPS-BST90 and SPS-BST100 is most likely caused by the incomplete mechanical alloying.

5.3.3.3 Electrical resistivity

The electrical resistivities were also measured at different temperatures (Figure 5.25a).

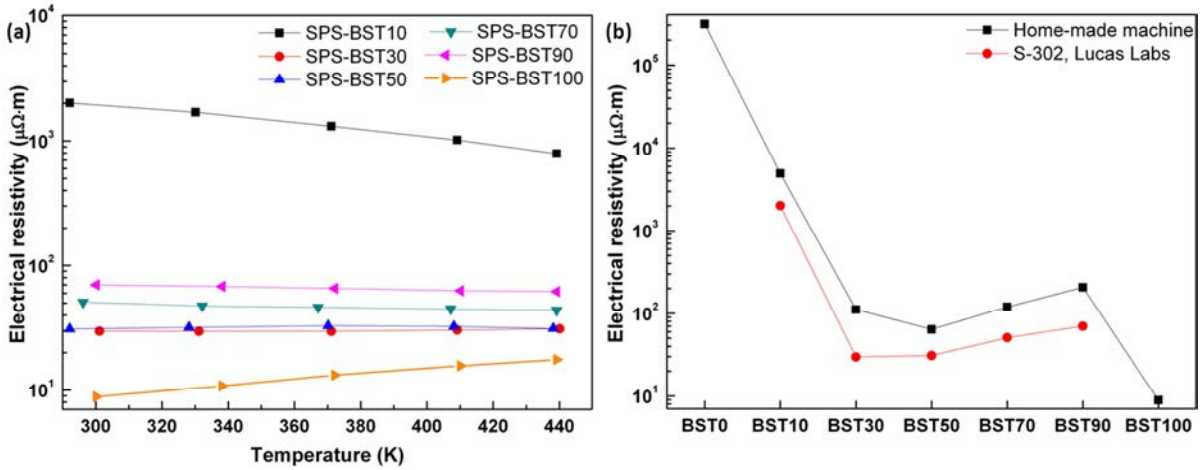

Figure 5.25 Electrical resistivities of $(Te_{85}Se_{15})_{45}As_{30}Cu_{25}$ / $Bi_{0.5}Sb_{1.5}Te_3$ composites (a) at different temperatures and (b) measured by two equipment at room temperature.

It can be found that BST plays an obvious role in reducing electrical resistivity. However, an abnormal increase of resistivity value can be found for SPS-BST70 and SPS-BST90. To confirm this phenomenon, electrical resistivities at room temperature were also measured using another manual four point resistivity probing equipment (S-302, Lucas Labs) for comparison (Figure 5.25b). The resistivities at room temperature obtained by the two equipment have the same order of magnitude, suggesting the reliability of test results. It is also consistent with the non-monotonous evolution observed for the Seebeck. These

observations could be largely caused by bad compaction and the existence of Sb_7Te and Te phases in the initial BST.

5.3.3.4 Power factor

Power factor of SPS-BST composites was calculated based on their Seebeck and electricity resistivity measurements and are shown in Figure 5.26.

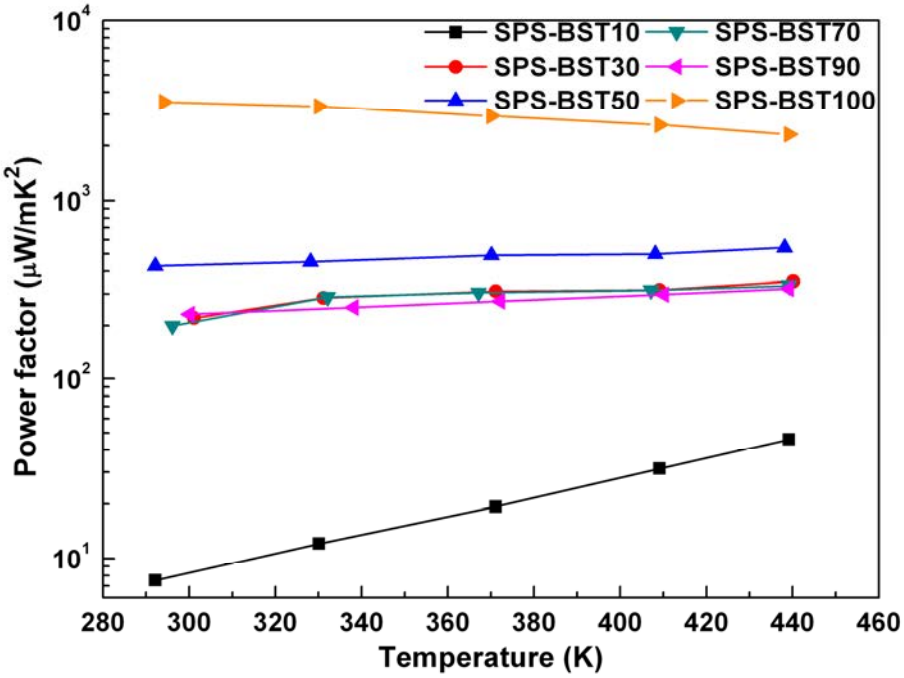

Figure 5.26 Power factor of $(Te_{85}Se_{15})_{45}As_{30}Cu_{25}$ / $Bi_{0.5}Sb_{1.5}Te_3$ composites.

By comparing thermoelectric power factor of SPS-BST10, SPS-BST30 and SPS-BST50, it can be concluded that BST can significantly improve the thermoelectric properties of materials. In addition, as both BST and $(Te_{85}Se_{15})_{45}As_{30}Cu_{25}$ glass are p-type semiconductors, the glass-ceramics composites, particularly SPS-BST50 (540 μW/mK^2 at 440K), show a much larger power factor than the best (SPS-BT90) of previous $(Te_{85}Se_{15})_{45}As_{30}Cu_{25}/Bi_2Te_3$ samples (160 μW/mK^2 at 440K). For SPS-BST70 and SPS-BST90, owning to the defects of the composites themselves, an abnormal electrical resistivity increase induced a lower power factor compared to SPS-BST50. SPS-BST100, whose power factor is around 2000 μW/mK^2, is also listed for comparison.

5.3.3.5 Thermal conductivity

Based on Equation (5.3), thermal diffusivity α, density $\rho_{density}$, and specific heat capacity c_p need to be measured for the calculation of thermal conductivity κ.

Density

The densities of SPS-BST composites were measured and reported in Figure 5.27.

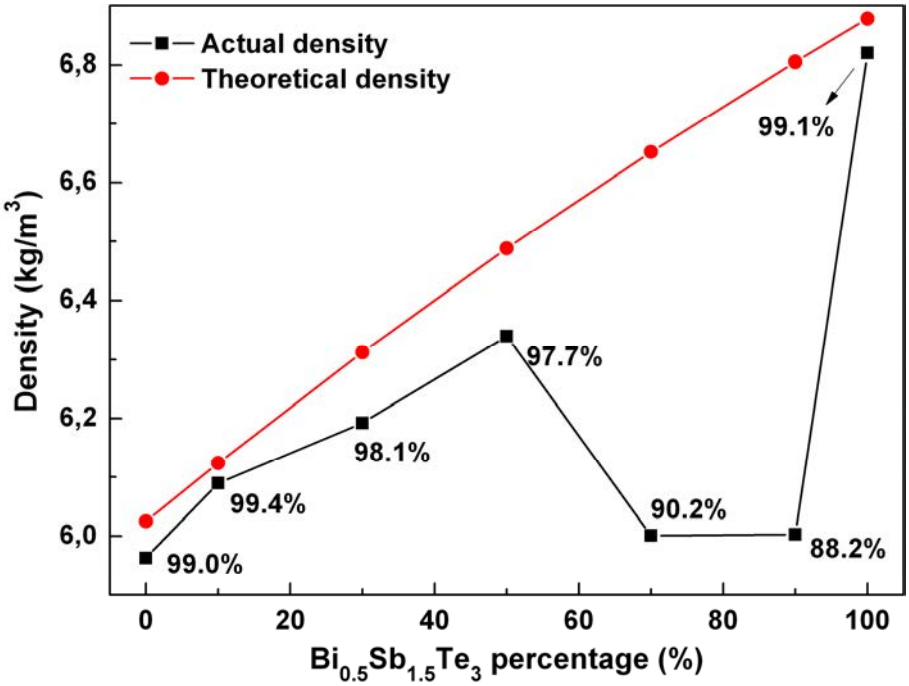

Figure 5.27 Densities of $(Te_{85}Se_{15})_{45}As_{30}Cu_{25}/Bi_{0.5}Sb_{1.5}Te_3$ composites at room temperature

Compared to the expected densities, a discrepancy is observed especially when BST content is less than 50%. For SPS-BST70 and SPS-BST90, due to the lack of glass and its limited fluidity, pores among BST crystals cannot be totally filled during sintering, inducing a much lower relative density.

To confirm previous analysis, scanning electron microscope (SEM), as a method for high-resolution imaging of surfaces, was used to observe sample cross section. The images are shown in Figure 5.28.

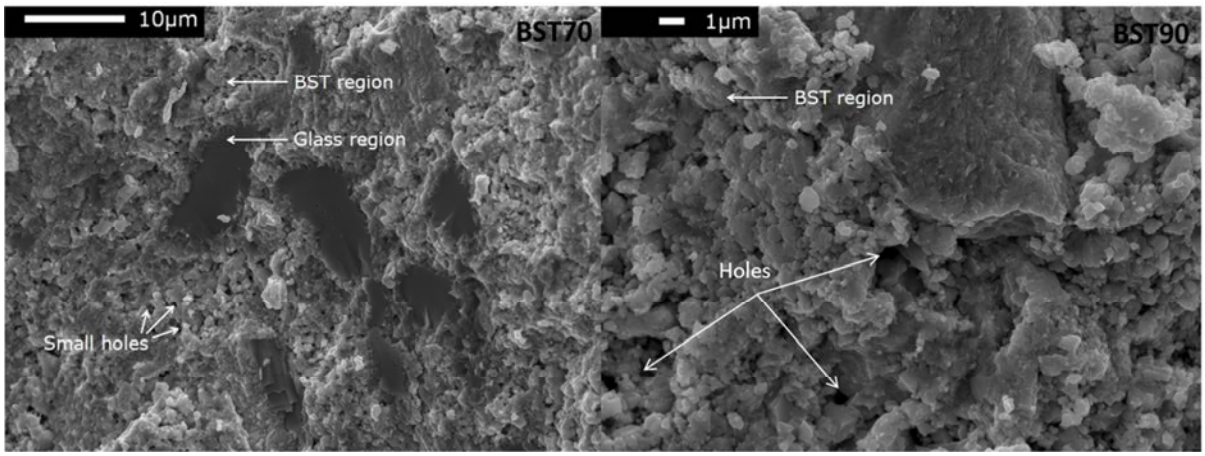

Figure 5.28 SEM images of SPS-BST70 and SPS-BST90 composites.

In both images, large quantities of small holes could be observed; this phenomenon is direct evidence of the abnormal density decrease in SPS-BST70 and SPS-BST90. These micro scale defects should also thwart the electron mobility and explain the erratic measurement of the Seebeck and of the resistivity.

Thermal diffusivity

The thermal diffusivities were also measured at different temperatures (Figure 5.29).

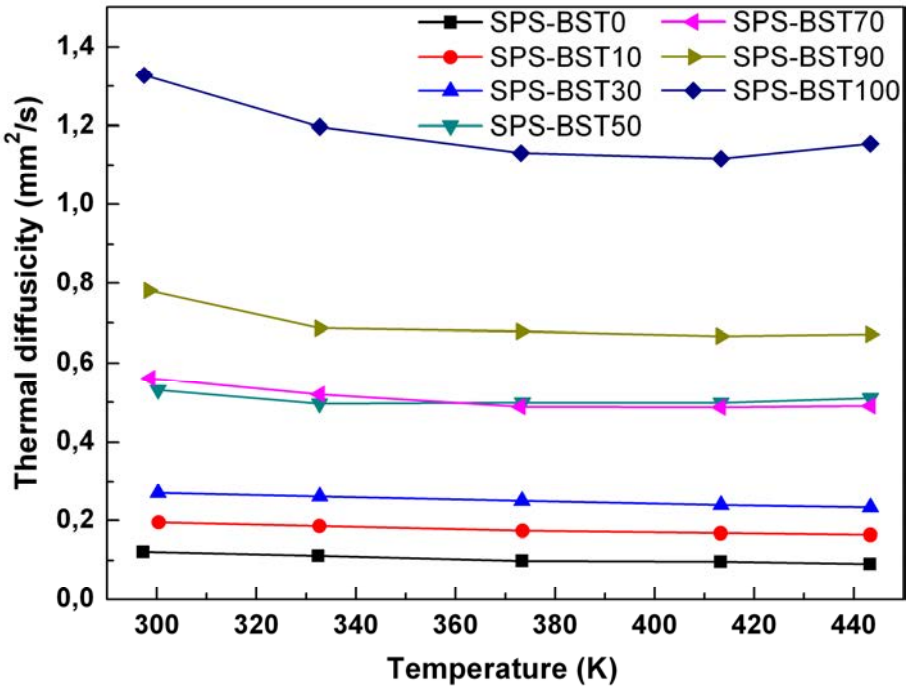

Figure 5.29 Thermal diffusivities of $(Te_{85}Se_{15})_{45}As_{30}Cu_{25}/Bi_{0.5}Sb_{1.5}Te_3$ composites.

In Figure 5.29, pure glass exhibits the lowest thermal diffusivity. By increasing the BST content, thermal diffusivity was gradually increased. Comparing SPS-BST90 and SPS-BST100, it can be drawn that just 10% of glass can decrease the thermal diffusivity a lot. Note that the evolution of the diffusivity is almost monotonous, and seems not be disturbed by the inhomogeneities pointed out in the previous section.

Specific heat capacity

The specific heat capacity, c_p was also measured (Figure 5.30). As $Bi_{0.5}Sb_{1.5}Te_3$ content increased, c_p more or less gradually decreased. According to Dulong-Petit law, this c_p decrease can be attributed to the increase of molecular mass from SPS-BST0 (92.5 $g \cdot mol^{-1}$) to SPS-BST100 (133.986 $g \cdot mol^{-1}$).

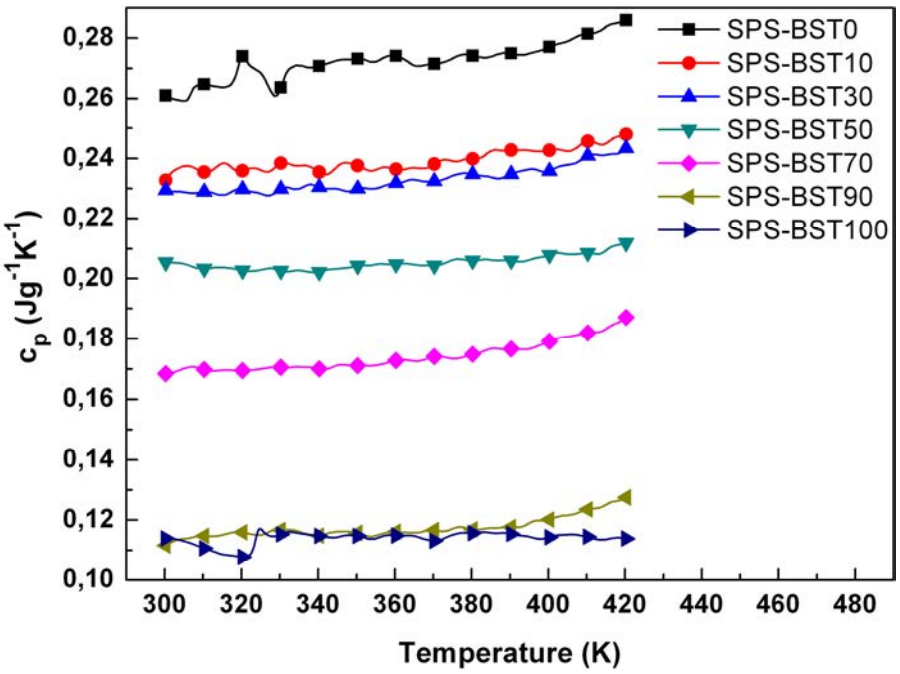

Figure 5.30 Specific heat capacity of $(Te_{85}Se_{15})_{45}As_{30}Cu_{25}/Bi_{0.5}Sb_{1.5}Te_3$ composites.

Thermal conductivity

Based on Equation (5.3), thermal conductivity κ of SPS-BST composites was calculated by multiplying the thermal diffusivity α, density ρ and specific heat capacity c_p (Figure 5.31).

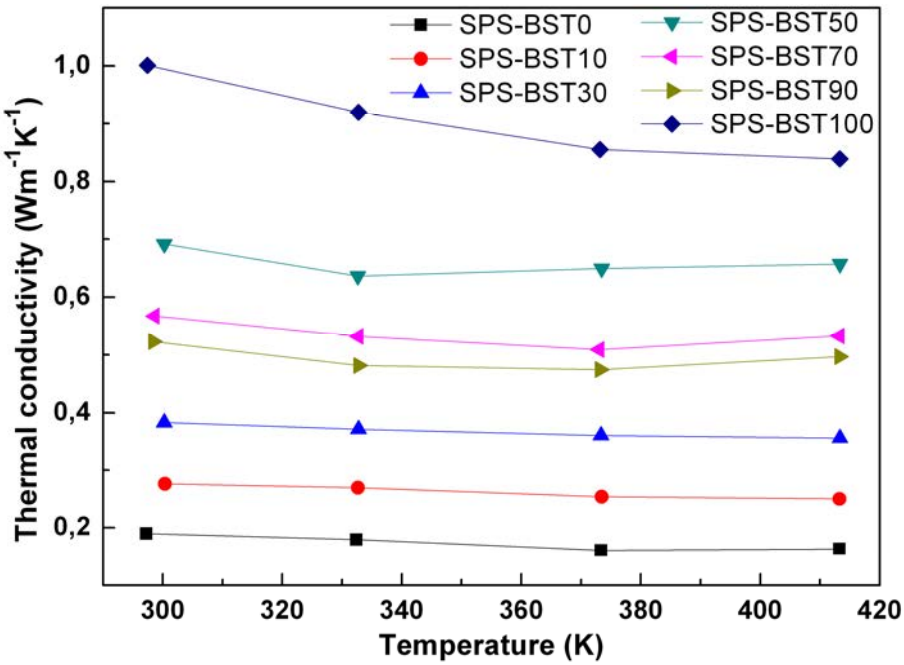

Figure 5.31 Thermal conductivities of $(Te_{85}Se_{15})_{45}As_{30}Cu_{25}/Bi_{0.5}Sb_{1.5}Te_3$ composites.

Due to a much higher κ of SPS-BST100 than SPS-BST0, the substitution of glass by BST made κ increasing gradually from 0.2 to 1.0. However, κ of both SPS-BST70 and SPS-

BST90 exhibit an irregular decrease which has to be correlated to the density measurements which reflect themselves the homogeneity defects of the materials (section 5.3.3.5).

5.3.3.6 Figure of merit (ZT)

According to Equation (5.1), the figure of merit (ZT) values of the composites were calculated from power factor, temperature, and thermal conductivity (Figure 5.32).

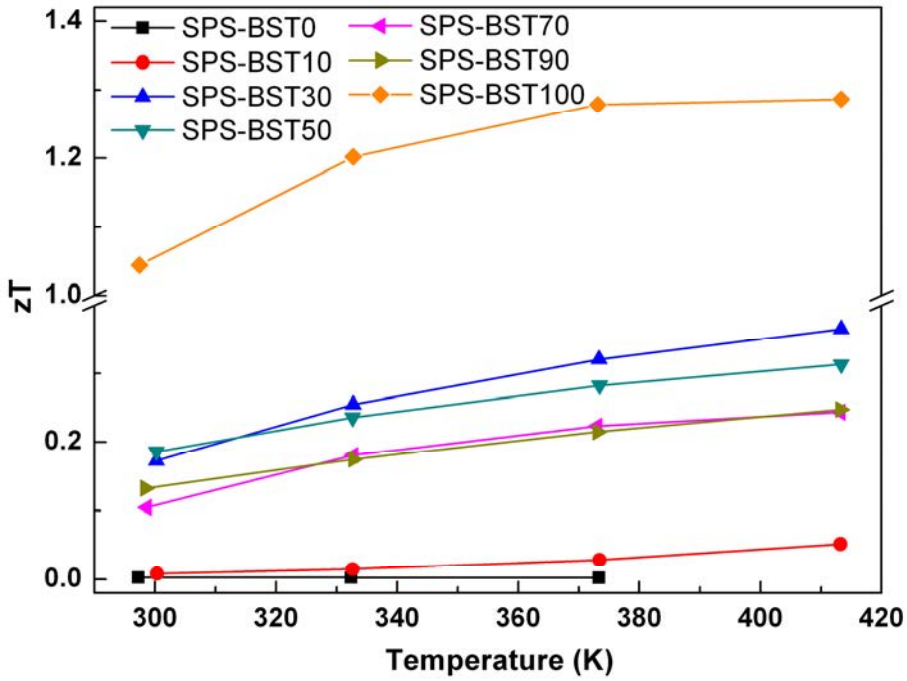

Figure 5.32 Figure of merit of $(Te_{85}Se_{15})_{45}As_{30}Cu_{25}/Bi_{0.5}Sb_{1.5}Te_3$ composites.

The ZT value of SPS-BST0 was around 0.002. By adding 10% of BST, ZT value of SPS-BST10 shows a significant increase. The ZT values of SPS-BST30 and SPS-BST50 are around 0.18 at room temperature. As temperature increase, ZT increased gradually and even reached the values of 0.365 and 0.313 at 413 K respectively. SPS-BST70 and SPS-BST90, due to the incomplete reaction during ball-milling and the bad compaction during SPS sintering, have ZT values lower than SPS-BST30 and SPS-BST50. Compared with SPS-BST100 (ZT>1.0), extra effort should be made for the enhancement of ZT value of $(Te_{85}Se_{15})_{45}As_{30}Cu_{25}$/BST composites.

Nevertheless, it is predictable that by adjusting BST ball-milling time, powder mixing method and SPS parameters, well-compacted glass-ceramics could be obtained with a comparable figure of merit value and much lower sintering temperature compared with p-type bismuth telluride.

5.4 Conclusions

In this chapter, in order to overcome low electrical conductivity of glassy material, and prepare a kind of material with good thermoelectric performance and high formability, $(Te_{85}Se_{15})_{45}As_{30}Cu_{25}$ glass was firstly doped with Bi_2Te_3. The powder mixture was prepared by ball-milling glass and ceramics together. Hot-pressing was used to sinter the glass and glass-ceramics powder mixture. However, the thermal stability of the composite is greatly deteriorated after ball-milling due to the addition of extra surface energy and nucleation agent. During several hours of hot-pressing, inhomogeneous crystallization was generated.

On this basis, the glass-ceramics mixture was prepared using ethanol as a solution, and spark plasma sintering (SPS) was used for sample synthesis. The percentage of Bi_2Te_3 varies from 10% up to 90%. After SPS sintering, no extra diffraction peak could be observed for all samples, indicating a proper synthesis parameter. Due to its relatively high electrical resistivity, the ZT value of $(Te_{85}Se_{15})_{45}As_{30}Cu_{25}$ glass was calculated to be around 0.002. By adding Bi_2Te_3, the thermoelectric conversion capacity was greatly enhanced. SPS-BT90 has a ZT value varies from 0.095 to 0.125 by increasing temperature from room temperature to 423 K. In this composite, glass acts as an adhesive between crystals and generates phonon scattering. However, this ZT value is still far from ZT of pure Bi_2Te_3, which is aroun 0.75 at room temperature. Note that $(Te_{85}Se_{15})_{45}As_{30}Cu_{25}$ glass and Bi_2Te_3 are p-type and n-type TE material respectively. Due to the existence of both positive and negative charge carriers, the Seebeck voltage has been partially cancelled out. As a result, p-type bismuth telluride ($Bi_{0.5}Sb_{1.5}Te_3$) was selected for further investigation.

Thus, powder mixtures of $(Te_{85}Se_{15})_{45}As_{30}Cu_{25}$ glass and $Bi_{0.5}Sb_{1.5}Te_3$ with the same ratio variation as previous were sintered using SPS. The ZT values of SPS-BST30 and SPS-BST50 are around 0.18 at room temperature. As temperature increasing, ZT increased gradually and even reached the values of 0.365 and 0.313 at 413K respectively. SPS-BST70 and SPS-BST90, due to the incomplete reaction during ball-milling and the bad compaction during SPS sintering, have lower ZT. Nevertheless, it is predictable that by preparing high quality $Bi_{0.5}Sb_{1.5}Te_3$ powder and adjusting synthesis parameters, well-compacted glass-ceramics could be obtained hopefully with better ZT comparable to pure $Bi_{0.5}Sb_{1.5}Te_3$ (ZT>1.0). In addition, the great benefit of the $(Te_{85}Se_{15})_{45}As_{30}Cu_{25}/Bi_{0.5}Sb_{1.5}Te_3$ composites compared with pure $Bi_{0.5}Sb_{1.5}Te_3$ is a higher formability and a much lower sintering temperature. The shaping of such samples together with their stabilities has to be checked in the future.

Reference

[1] R. Zeller, R. Pohl. Thermal Conductivity and Specific Heat of Noncrystalline Solids. Physical Review B. 1971, 4 (6): 2029

[2] C. Kittel. Interpretation of the Thermal Conductivity of Glasses. Physical Review. 1949, 75 (6): 972-974

[3] P. Lucas, C. Conseil, Z. Yang, Q. Hao, S. Cui, C. Boussard-Pledel, B. Bureau, F. Gascoin, C. Caillaud, O. Gulbiten. Thermoelectric Bulk Glasses Based on the Cu–As–Te–Se System. Journal of Materials Chemistry A. 2013, 1 (31): 8917-8925

[4] S.-N. Zhang, J. He, T.-J. Zhu, X.-B. Zhao, T.M. Tritt. Thermal Conductivity and Specific Heat of Bulk Amorphous Chalcogenides $Ge_{20}Te_{80-x}Se_x$ (x= 0, 1, 2, 8). Journal of Non-Crystalline Solids. 2009, 355 (2): 79-83

[5] J. Philip, R. Rajesh, C.P. Menon. Carrier-Type Reversal in Pb–Ge–Se Glasses: Photopyroelectric Measurements of Thermal Conductivity and Heat Capacity. Applied Physics Letters. 2001, 78 (6): 745-747

[6] A.P. Gonçalves, E.B. Lopes, O. Rouleau, C. Godart. Conducting Glasses as New Potential Thermoelectric Materials: The Cu–Ge–Te Case. Journal of Materials Chemistry. 2010, 20 (8): 1516-1521

[7] C. Seager, D. Emin, R.K. Quinn. Electrical Transport and Structural Properties of Bulk As-Te-I, As-Te-Ge, and As-Te Chalcogenide Glasses. Physical Review B. 1973, 8 (10): 4746

[8] A.P. Gonçalves, E.B. Lopes, G. Delaizir, J.B. Vaney, B. Lenoir, A. Piarristeguy, A. Pradel, J. Monnier, P. Ochin, C. Godart. Semiconducting Glasses: A New Class of Thermoelectric Materials? Journal of Solid State Chemistry. 2012, 193 (0): 26-30

[9] J. Navratil, Z. Starý, T. Plechacek. Thermoelectric Properties of P-Type Antimony Bismuth Telluride Alloys Prepared by Cold Pressing. Materials Research Bulletin. 1996, 31 (12): 1559-1566

[10] Y. Ma, Q. Hao, B. Poudel, Y. Lan, B. Yu, D. Wang, G. Chen, Z. Ren. Enhanced Thermoelectric Figure-of-Merit in P-Type Nanostructured Bismuth Antimony Tellurium Alloys Made from Elemental Chunks. Nano Letters. 2008, 8 (8): 2580-2584

[11] B. Poudel, Q. Hao, Y. Ma, Y. Lan, A. Minnich, B. Yu, X. Yan, D. Wang, A. Muto, D. Vashaee. High-Thermoelectric Performance of Nanostructured Bismuth Antimony Telluride Bulk Alloys. Science. 2008, 320 (5876): 634-638

[12] S.D. Bhame, D. Pravarthana, W. Prellier, J.G. Noudem. Enhanced Thermoelectric Performance in Spark Plasma Textured Bulk N-Type $BiTe_{2.7}Se_{0.3}$ and P-Type $Bi_{0.5}Sb_{1.5}Te_3$. Applied Physics Letters. 2013, 102 (21): 211901

[13] H.J. Goldsmid. Bismuth Telluride and Its Alloys as Materials for Thermoelectric Generation. Materials. 2014, 7 (4): 2577-2592

[14] O. Yamashita, S. Tomiyoshi. High Performance N-Type Bismuth Telluride with Highly Stable Thermoelectric Figure of Merit. Journal of Applied Physics. 2004, 95 (11): 6277-6283

[15] L. Hu, X. Liu, H. Xie, J. Shen, T. Zhu, X. Zhao. Improving Thermoelectric Properties of N-Type Bismuth-Telluride-Based Alloys by Deformation-Induced Lattice Defects and Texture Enhancement. Acta Materialia. 2012, 60 (11): 4431-4437

[16] H. Goldsmid. The Thermal Conductivity of Bismuth Telluride. Proceedings of the Physical Society. Section B. 1956, 69 (2): 203

[17] H. Goldsmid. The Electrical Conductivity and Thermoelectric Power of Bismuth Telluride. Proceedings of the Physical Society. 1958, 71 (4): 633

[18] F.P. Incropera, D.P. DeWitt. Introduction to Heat Transfer. USA: John Wiley & Sons, 2011

[19] L. Leuzzi, T.M. Nieuwenhuizen. Thermodynamics of the Glassy State. CRC Press, 2007: 287

[20] M. Mézard, G. Parisi. Thermodynamics of Glasses: A First Principles Computation. Journal of Physics: Condensed Matter. 1999, 11 (10A): A157

[21] S.V. Nemilov. Thermodynamic and Kinetic Aspects of the Vitreous State. CRC Press, 1994: 70

General Conclusion

This work deals with the development of tellurium-based glass for applications in the mid-infrared sensing and thermoelectric fields.

The tellurium-based glasses are of interest because of their transparency in the mid- and far-infrared range. Thus, the first part of this work concerns the development of stable tellurium-based glasses and optical fibers for detection of chemical species both in the daily life and in the atmosphere detection of terrestrial planets, which is a continuation of the previous work of Glasses and Ceramics team.

To monitor the terrestrial planets and analyze the possibility of extraterrestrial life, Darwin mission (European Space Agency) ask for the development of single mode fiber to detect infrared signatures of H_2O (6 µm), O_3 (9 µm), and CO_2 (15 µm). Up to now, single mode fiber working in the first window (6-12 µm) has been successfully developed based on selenium-based glass. Thus, the aim of Chapter 1 is seeking the manufacturing technology of single mode optical fibers working in the second infrared window (12-18 µm). To reach this aim, highly purified Te-Ge-Se ternary glasses with limited Se content ($\leq$ 8%) were obtained using a newly developed two-steps chemical-distillation purification method, which provide a good contact between raw material and oxygen absorbers. In addition, a new way to make the preform, called capillary method, has also been developed alternatively to the classical rod in tube method for the preparation of fiber with a small core. On this basis, high purity $Te_{76}Ge_{21}Se_3/Te_{71}Ge_{21}Se_8$ double index fiber which can transmit light up to 16 µm has been successfully fabricated. Its minimum attenuation is 11.5dB/m at 10.7 µm. The intensity profile of the output light exhibit a Gaussian shape, showing an obvious experimental single mode character. It is the first single-mode fiber ever prepared working so far in the infrared.

Besides military application, in order to test the fundamental vibrations (stretching and bending) of molecules and biomolecules beyond 12 µm, optical sensor of high selectivity and sensitivity should be developed based on telluride glass. Te-Ge-AgI glasses are particularly stable against crystallization, showing no crystallization peak.

So, in Chapter 2, a series of $(GeTe_4)_{100-x}M_x$ (M is Ag, I, or AgI) glasses were synthesized to explore the effect of Ag, I separately and AgI as a salt in $GeTe_4$ glass on glass properties. To achieve this goal, glass physical properties were investigated, including thermal stability, density, electrical and ionic conductivity. Also, a glass structural model is proposed thanks to XRD and EXAFS measurement and a reverse Monte Carlo studied carried out in close collaboration with Pal Jovari (Wigner Research Centre for Physics, Hungarian Academy of Sciences). According to these works, it is confirmed that iodine acts as an electron absorber

and a glass network terminator. By adding AgI, the glass network is opened up gradually. When AgI is less than 15%, silver acts as glass former, embedded in the covalent network, rather bonded to Te. When AgI is beyond 15%, silver start to act as modifier, occupy the interstices of the network, engaged rather ionic bond with iodine. Meanwhile, the ion diffusion channels are large enough and the glass shows a clear transition from electron conductor to ionic conductor. Based on the structural features, the high thermal stability of the glass could be explained by the switches of tellurium from two to three fold coordinated and the charge interactions between iodine and silver atoms blocking the trapped electron going back to glass network.

In addition, $(GeTe_4)_{100-x}AgI_x$ glasses have shown a wide optical transmittance from 2μm up to more than 35μm (collaboration Pascal Masselin at the Université du Littoral). To our knowledge, they are the first glass transmitting so far in the infrared. Thus, these glasses are very promising materials both as optical fibers for the mid-infrared means, and as lenses for the far-infrared range.

On this basis, Chapter 3 focus on the exploration of far infrared sensing probe based on $(Ge_{0.21}Te_{0.79})_{100-x}AgI_x$ (x=10, 15, and 20) glasses. By a careful operation of polishing, the surface defects of the purified preform caused by germanium iodide re-condensation during annealing process have been totally removed. By this treatment, the fiber attenuation has been significantly reduced from more than 20dB/m to less than 10dB/m. The minimum attenuation value is 3dB/m around 10 μm for $(Ge_{0.21}Te_{0.79})_{90}AgI_{10}$ single index fiber, which is up to now the minimum value ever measured for a telluride glass. By tapering them, the fibers were designed for FEWS experiments up to 16μm. By measuring dichloromethane and chloroform infrared spectra, the tapered fiber-based sensors show an enhanced sensing ability as sensing zone diameter decreases. Besides, the experiment using toluene-isooctane solution show a toluene concentration detection limit of Te-Ge-AgI fiber to be 0.5 vol.%. Moreover, the infrared spectra of calf serum, milk, butter and gasoline, taking as examples of complex organic system, have been also carried out. Results show that infrared sensor using $(Ge_{0.21}Te_{0.79})_{100-x}AgI_x$ fiber sensing probe is an ideal tool due to its simplicity and efficiency for the identification and quantification of complex system. This development will have some clear benefit to carry out FEWS experiments in biology or medicine for example.

The second axe of this work concerns the potential of tellurium-based glasses in thermoelectricity. The chalcogenide glasses have intrinsic poor thermal conductivity (about

$0.5 W/m^{-1}K^{-1}$) and high Seebeck coefficient (more than 500µV/K). Telluride glasses are those with the highest electrical conductivity.

In Chapter 4, the originality of the present work lies in the method of synthesis of melt-quenched glasses in the form of bulk samples. Te-As-Se-Cu glasses with Te/Se ratios and Cu percentage have been explored in order to further improve the electrical conductivity. It has been shown that by introducing copper, the conductivity increases by several orders of magnitude. Other glass systems, including Te-As-Se-Ag and Te-As (Sb, Bi)-Se-Cu were also been tried without success. $(Te_{85}Se_{15})_{45}As_{30}Cu_{25}$ glass seems to be the most interesting composition for TE with a combination of a sufficient stability (ΔT=99 °C) and low resistance (ρ=35 Ω·cm). Still, this resistance value is not sufficiently low for commercial application. Thus, glass-ceramics were prepared via heat treatment. Unfortunately, due to the high surface energy induced by the broken bond and impurities, the crystallization is not homogeneous and uncontrollable.

In Chapter 5, to further increase the electrical conductivity, hot-pressing was first used to prepare glass-ceramics composites from ball-milled $(Te_{85}Se_{15})_{45}As_{30}Cu_{25}$ glass and Bi_2Te_3 mixture. However, due to several hours of hot-pressing process with inhomogeneous temperature field, extra inhomogeneous crystallization was generated. Thus, spark plasma sintering was carried out for the preparation of $(Te_{85}Se_{15})_{45}As_{30}Cu_{25}/Bi_2Te_3$ and $(Te_{85}Se_{15})_{45}As_{30}Cu_{25}/Bi_{0.5}Sb_{1.5}Te_3$ composites. Characterizations, such as electrical resistivity, Seebeck coefficient, and thermal conductivity, were implemented for the calculations of figure of merit zT. $(Te_{85}Se_{15})_{45}As_{30}Cu_{25}/Bi_{0.5}Sb_{1.5}Te_3$ composites are quite promising. The zT values of SPS-BST30 and SPS-BST50 at 413K are 0.365 and 0.313 respectively, which is quite promising knowing that improvement in the synthesis process can be done.

Finally, all the works done in this thesis help to advance the state of knowledge of tellurium-based glasses. Many promising progresses have been obtained which will contribute to the improvement of their applications in the daily life.

Some achievements in optics will change the status of pure tellurium-based glass from curiosity for material scientist toward effective functional material for mid and far-infrared optical devices.

Perspective

Overall, although a lot of insightful researches have been done on the infrared sensing and thermoelectric properties of tellurium-based glass, many more works will be done in the future. For example, the following points can be mentioned,

a) Effort will focus on the preform polishing in order to limit crystallization effect during the fibering process for the preparation of single mode fiber.
b) Microstructure optical fibers with a hexagonal lattice of air holes will be explored based on $(Ge_{21}Te_{79})_{100-x}AgI_x$ glass for the preparation of single mode fiber.
c) To prepare well-compacted thermoelectric composites, high quality $Bi_{0.5}Sb_{1.5}Te_3$ powder and a find adjustment of spark plasma sintering parameters are essential.

Résumé

Les verres de tellures sont des matériaux récemment remis au goût du jour pour des applications en optiques. Certaines compositions permettent en effet de transmettre la lumière loin dans l'infrarouge au-delà de 20 µm, mais leur tendance naturelle à recristalliser rend difficile la fabrication d'objet pour la photonique telle que des fibres optiques.

Des verres du système Te-Ge-Se ont été développés dans le cadre du projet Darwin de l'Agence Spatiale Européenne permettant de détecter la bande d'absorption du CO_2 à 15 µm. La première fibre optique monomode a été obtenue à partir d'une nouvelle méthode de fabrication de préforme par moulage. Les verres de tellure du système Te-Ge-AgI sont les seuls à ne pas présenter de pic de cristallisation en analyse thermique. Leur stabilité a été mise à profit pour développer des fibres optiques avec un niveau très bas de pertes optiques, de l'ordre de 3 $dB \cdot m^{-1}$, ce qui constitue un record. Ces fibres ont été utilisées pour mettre en œuvre des expériences de spectroscopie par ondes évanescentes permettant d'accéder à une gamme de longueurs d'onde encore jamais atteinte de 2 à 16 µm. Ce gain sera de première importance pour la mise en service de ces fibres en biologie ou médecine.

Par ailleurs, les verres de tellure sont les verres présentant les conductivités électroniques les plus élevées jamais mesurées. Il s'agit donc de matériaux potentiellement intéressants pour la thermoélectricité. Certaines compositions du système (Te/Se)-(As/Sb/Bi)-(Cu/Ag) ont été synthétisées et caractérisées. Des matériaux composites obtenus par broyage et compression de poudres de verre et de $Bi_{0.5}Sb_{1.5}Te_3$ cristallisé ont été préparés. Ces derniers présentent un ZT = 0.365 à 413°K, ce qui est encourageant pour l'avenir.

Abstract

The tellurium-based glasses are of interest because of their transparency in the mid- and far-infrared range. Tellurium-based glasses and optical fibers can be used for the detection the atmosphere of terrestrial planets in Darwin project and the identification of chemical species in the daily life.

For the detection of CO_2 (15 µm) on exoplanet, high purity Te-Ge-Se experimental single mode fiber which can transmit light up to 16 µm has been successfully fabricated based on a new preform molding process. Moreover, Te-Ge-AgI glasses, which present no crystallization peak and far infrared transmittance beyond 30 µm (as bulk), are also candidates for infrared sensing. A structural model proposed in this work provides some explanations on their good thermal stability. Low-loss single index fibers drawn from these glasses have shown their capabilities to collect mid-infrared spectra from 2 to 16 µm. To the best of our knowledge, it is the first fiber evanescent wave spectra collected on such a wide range. This achievement will be essential for future medical applications.

Otherwise, tellurium-based glasses, due to the intrinsic poor thermal conductivity and high Seebeck coefficient, are good candidates as new materials in the thermoelectricity field. Te-As-Se-Cu glass with the introduction of copper up to 25% has been explored. By sintering this glass with $Bi_{0.5}Sb_{1.5}Te_3$, glass-ceramic composites were also obtained exhibiting maximum zT values equal to 0.365 at 413 K.